

MULTISCALE CONTINUUM MODELING OF
PIEZOELECTRIC SMART STRUCTURES

A Dissertation

Submitted to the Faculty

of

Purdue University

by

Ernesto Camarena

In Partial Fulfillment of the

Requirements for the Degree

of

Doctor of Philosophy

May 2019

Purdue University

West Lafayette, Indiana

THE PURDUE UNIVERSITY GRADUATE SCHOOL
STATEMENT OF DISSERTATION APPROVAL

Dr. Wenbin Yu, Co-Chair

School of Aeronautics and Astronautics

Dr. Andres Arrieta Diaz, Co-Chair

School of Mechanical Engineering

Dr. Tyler N. Tallman

School of Aeronautics and Astronautics

Dr. William A. Crossley

School of Aeronautics and Astronautics

Approved by:

Dr. Weinong Chen

Head of the Departmental Graduate Program

ACKNOWLEDGMENTS

First and foremost, I must acknowledge God the Father, Jesus the God-Man, and God the Holy Spirit for creating all things; piezoelectricity included. I thank Him also for appointing me the desire and ability to complete this monumental work in my life.

Furthermore, I am pleased to thank the people that have loved me the most in my life: my parents. Thank you for your unquestioning support of my time at Purdue. You are one of the greatest blessings I have ever received! Mom, I feel your love so strongly when you are so eager to hear and learn about what I am studying and how I am progressing. Gracias, Papá por su orientación sobre cómo pensar creativamente en el contexto de las matemáticas. Gracias también por darme buenos consejos de trabajo.

I would also like to thank Kristi, my wife. Thank you for being the closest person that has understood my many joys and frustrations with this work. I am thankful for all of your support and encouragement—from the qualifying exams to the preliminary exam to the defense. Thank you!

Additionally, I am beyond privileged to have been advised by Dr. Wenbin Yu. Thank you for your generosity, integrity, technical know-how, and an outstanding work ethic. You are a mentor I will always be fond of remembering. I also am thankful for the feedback I received from each committee member during my preliminary exam. Many thanks also to Dr. Weinong Chen and Purdue's School of Astronautics and Aeronautics for providing most of my financial support.

I'd also like to give special thanks to Cary and Terri Davis along with Allen and Carmen Gilbert for your love and support these past few years! Collectively, you gave us many meals, helped us with various chores, and opened up your home to us on countless occasions.

Last but not least, thanks to my student colleague Xin Liu for the many micromechanical discussions we had. Thanks also to him and Bo Peng for providing a starting point for the RVE scripts. I am also thankful to have worked with and known my colleagues Fei Tao, Ankit Deo, Ning Liu, Liang Zhang, Orzuri Rique, Diane Aloisio, Ronald Agyei, Tejas Pant, Nitin Dhamankar, and Andrea Nicolas.

TABLE OF CONTENTS

	Page
LIST OF TABLES	viii
LIST OF FIGURES	x
SYMBOLS	xiii
ABBREVIATIONS	xvi
ABSTRACT	xviii
1 INTRODUCTION	1
1.1 Micromechanical Basics	1
1.2 A Primer for Piezoelectrics	3
1.2.1 Polarization of Piezoelectrics	3
1.2.2 Piezoelectric Field Variables	5
1.2.3 Piezoelectric Constitutive Equations	7
1.2.4 Piezoelectric Devices and Piezocomposites	16
1.2.5 Unit Conversions for Piezoelectricity	19
1.3 Review of the Micromechanics of Piezocomposites.	20
1.3.1 General Micromechanical Theories	23
1.3.2 Uniform Field Assumption Methods	25
1.3.3 Mean-Field Theories	29
1.3.4 Other Techniques and Aspects of Homogenization	29
1.4 Piezoelectric Smart Structures	31
1.5 Multiscale Modeling of Macro Fiber Composites	32
1.6 Review: Analytical Homogenization of MFCs	37
1.6.1 Step-1: Fiber Layer Homogenization	40
1.6.2 Step-2: Stack of Homogeneous Layer Methods	41
1.7 Review: Numerical Homogenization of MFCs	43
1.8 Dissertation Motivation: Towards Improved Micromechanical Analysis of Piezocomposite Patches with the Mechanics of Structure Genome . .	46
1.8.1 MSG Analytical	47
1.8.2 RVE Analysis for In-plane Periodic Piezocomposite Patches . .	48
1.8.3 Local Fields Recovery	50
1.8.4 Direct Numerical Simulations	50
2 ANALYTICAL HOMOGENIZATION OF THE MFC	52
2.1 Piezoelectric Homogenization with Mechanics of Structure Genome . .	52
2.2 Stack of Homogeneous Layers	55

	Page
2.3 Hybrid Rule of Mixtures for MFCs	61
2.3.1 HRM1: Fiber Layers (Step-1)	61
2.3.2 HRM2: Stack of Homogeneous Layers (Step-2)	61
2.4 Analysis and Results	64
2.4.1 Assumed Microstructural Details of the MFC	64
2.4.2 Comparison of Homogenized Fiber Layer Methods (Step-1 Ho- mogenization)	65
2.4.3 HRM2 Device Properties and Verification	72
2.4.4 Comparison of Analytical Homogenization Methods for the Full MFC (Step-2 Homogenization)	81
2.4.5 Discussion	90
2.4.6 Limitations	90
3 MIXED BOUNDARY CONDITIONS FOR FINITE THICKNESS EFFECTS	92
3.1 Theory Development for Active Layers	92
3.2 RVE Analysis for In-plane Periodic Piezocomposites	92
3.2.1 Proposed Boundary Conditions	95
3.2.2 Mechanical BCs	96
3.2.3 Electrical BCs	100
3.3 Rectification of the PBCs	105
3.4 Post-Processing for Mixed BCs and PBCs	106
3.5 Results	107
3.5.1 Case A Example	107
3.5.2 Case B Example	119
3.6 Discussion	122
4 RVE ANALYSIS OF MACRO FIBER COMPOSITES	123
4.1 Homogenization	127
4.1.1 PBCs	127
4.1.2 MIX BCs	130
4.1.3 Nonuniform Polarization from IDEs	131
4.1.4 Volume Averaging Nuances for MFCs	132
4.2 Dehomogenization	136
4.3 Homogenization Results	137
4.3.1 P2 MFC	137
4.3.2 P2 MFC Verification	138
4.3.3 P1 MFC	140
4.3.4 P1 MFC Verification	143
5 UNIMORPH DIRECT NUMERICAL SIMULATIONS	146
5.1 DNS Details	147
5.1.1 Geometry	147
5.1.2 Material Models	148
5.1.3 Boundary Conditions	150

	Page
5.2 Details for Homogenized Models	150
5.3 Computing Resources	151
5.4 Results	153
5.4.1 Macroscopic Response	153
5.4.2 Comparison of Local Fields	162
6 SUMMARY AND RECOMMENDATIONS	166
6.1 Summary	166
6.2 Recommendations	169
A MATHEMATICA CODE FOR HRM2	171
B RVE ANALYSIS SCRIPTS FOR THE FULL MFC	184
C SCRIPTS FOR POLARIZING THE P1 MFC	209
REFERENCES	214
VITA	226

LIST OF TABLES

Table	Page
1.1 Unit conversion for multiscale piezoelectric analyses. Adapted from [21]. . .	20
1.2 Periodic boundary conditions presented in the literature for the MFC. . . .	43
1.3 Periodic boundary conditions implemented in Ref. [52] for the P2 MFC. . .	44
2.1 Mechanical and piezoelectric properties for SONOX P502 in the material coordinate system (y'_i). The 3-direction corresponds to the polarization direction. $\epsilon_0 = 8.854$ pF/m.	65
2.2 Isotropic MFC constituent material properties. $\epsilon_0 = 8.854$ pF/m.	65
2.3 Effective elastic properties for each MFC fiber layer. All moduli are in GPa.	67
2.4 Effective piezoelectric and dielectric properties for each MFC fiber layer. Piezoelectric strain constants are in pC/N.	68
2.5 The HRM2 effective piezoelectric and dielectric device properties for the full homogenized MFC in problem coordinates.	73
2.6 Macroscopic variable comparison between a DNS of the P1 MFC patch and the HRM2 effective behavior.	79
2.7 Macroscopic variable comparison between a DNS of the P2 MFC patch and the HRM2 effective behavior.	80
2.8 Effective elastic properties for the full MFC in the problem coordinate system.	83
2.9 Comparison of the modified HRM2 (with $E_3 = \bar{E}_3$ and $D_3 = \bar{D}_3/V^a$) effective piezoelectric and dielectric properties to the literature and the active layer in problem coordinates.	87
3.1 In-plane periodic boundary conditions for RVE analysis of thin piezocomposites.	103
3.2 Boundary Conditions for two DNSs that verify asymmetric piezoelectric shear coupling results from the proposed RVE analysis.	111
3.3 Effective elastic properties for uniformly poled MFC fiber layers. All moduli are in GPa.	118

Table	Page
3.4 Effective piezoelectric and dielectric properties for uniformly poled MFC fiber layers. Piezoelectric stain constants are in pC/N.	118
3.5 Comparison of Case B effective properties obtained from the periodic BCs and a mixture of periodic and homogeneous stress BCs at $V_f = 0.6$	121
4.1 Geometric parameters for the MFC RVEs.	124
4.2 Periodic boundary conditions for the full MFC (P1 and P2 MFC cases). .	127
4.3 Mixed boundary conditions for the full MFC (P1 and P2 MFC cases). . .	130
4.4 Boundary Conditions for poling the P1 MFC.	133
4.5 Boundary conditions P1 and P2 dehomogenization analyses.	136
4.6 Effective elastic properties for the full P2 MFC in the problem coordinate system.	137
4.7 Effective piezoelectric and dielectric properties for the full P2 MFC in problem coordinates.	138
4.8 Macroscopic variable comparison between a DNS of the P2 MFC Active Area and the MIX effective behavior.	139
4.9 Effective piezoelectric and dielectric properties for the full homogenized P1 MFC in problem coordinates.	140
4.10 MIX effective piezoelectric and dielectric properties for the full homogenized MFC in problem coordinates.	141
4.11 PBC effective piezoelectric and dielectric properties for the full homogenized MFC in problem coordinates.	142
4.12 Macroscopic variable comparison between a DNS of the P1 MFC patch and the MIX effective behavior considering the Mechanical Transform. .	144
4.13 Macroscopic variable comparison between a DNS of the P1 MFC patch and the MIX effective behavior considering the Full Transform.	145
5.1 Test matrix considered for the DNS studies.	147
5.2 Geometric parameters for the MFCs tested.	149
5.3 Total element and node count as well as resources used for each MFC patch.	154
5.4 Transverse tip deflection, u_3 , in [mm] at Centerline $(L_1, L_2/2, 0)$. Values in parentheses are the percent errors relative to the DNS in each respective case.	157

LIST OF FIGURES

Figure	Page
1.1 The poling process of polycrystalline ceramics.	4
1.2 Contrasting electrical boundary conditions.	8
1.3 Common electrode types and associated electrical activity.	18
1.4 A generic composite that features periodicity in three dimensions.	21
1.5 Periodic RVE face labels and edge lengths for an arbitrary microstructure.	22
1.6 Usual rod configurations for piezocomposite transducers.	27
1.7 A macro-fiber composite and its structural flexibility. Photograph courtesy of NASA.	33
1.8 A rendering the MFC highlighting the Active Area and the Active Area RVE.	35
1.9 Two-Step homogenization for the Macro Fiber Composite.	38
1.10 Relationship between problem coordinate system (CS) and the local PZT material CS for the MFC patch. y_i are the problem coordinates, y'_i are the material coordinates.	39
1.11 Electrode surfaces from [52] for the P2 MFCs.	44
1.12 A generic composite that features periodicity in two dimensions.	48
2.1 The domain of the active region and that of the full laminate.	56
2.2 Illustration of the electrical behavior of the HRM (Step-2); applicable to both MFC types.	63
2.3 Major errors found for fiber layers due to the plane-stress-like assumption. The vertical dashed line for fiber volume fractions relevant to MFC active layer.	70
2.4 Other active layer plane-stress errors.	71
2.5 Illustration of the numerical tests performed to verify the HRM2 device properties.	74
2.6 Perspective view of the MFC patch for numerical tests without a Passive Area and host substrates.	76

Figure	Page
2.7 Center volumes utilized to compute volume averaged quantities.	78
2.8 The effect of assuming $\varepsilon_{33} = E_1 = E_2 = 0$ in Step-1 on the in-plane Young's moduli in Step-2 at a variety of PZT and electrode volume fractions. The dashed curves are when the plane-stress assumption is used with dropped terms (Eq. (1.64)). The vertical dashed lines are at $V_{PZT}^f = 0.8654$ [47].	84
2.9 Overall transverse shear moduli comparison between HRM2 and FSDT (Eq. (1.68)) at a variety of PZT and electrode volume fractions. The solid curves are from HRM2 and the dashed curves are Eq. (1.68). The vertical dashed lines are at $V_{PZT}^f = 0.8654$ [47].	85
2.10 PZT and copper fiber volume fraction study with the HRM2 of the P1 MFC. Results with the recommended $D_3 = \bar{D}_3$ and $E_3 = \bar{E}_3/V^a$ are shown. The vertical dashed lines are at $V_{PZT}^f = 0.8654$	88
2.11 PZT and copper fiber volume fraction study with the HRM2 of the P2 MFC. Results with the recommended $D_3 = \bar{D}_3$ and $E_3 = \bar{E}_3/V^a$ are shown. The vertical dashed lines are at $V_{PZT}^f = 0.8654$	89
3.1 Symmetry examination of the piezoelectric strain coefficients for Case A composites.	108
3.2 Resultant of the scaled electric displacement ($\mu\text{C}/\text{mm}^2/\text{s}$) from BVPs in Table 3.1 plotted on the deformed shape. $V_f = 0.8$	110
3.3 The DNS of the active layer.	111
3.4 Boundary condition effects on the effective elastic moduli for Case A composites.	113
3.5 Boundary condition effects on the effective piezoelectric e-form coefficients for Case A composites.	114
3.6 Boundary condition effects on the effective piezoelectric d-form coefficients for Case A composites.	115
3.7 Deformed shapes that contrast the nonuniform transverse normal strain of the MIX BCs to the uniform result of the PBCs. $V_f = 0.8$	116
3.8 Deformed shapes that contrast a nonuniform transverse shear strain of the MIX BCs to the uniform result of the PBCs. $V_f = 0.8$	117
3.9 Case B meshes used with fiber aspect ratios of 1, 5, 10, 25, and 50 ($V_f = 0.6$).	120
4.1 Micromechanical analysis overview.	123
4.2 RVE mesh utilized throughout the work presented in this dissertation.	125

Figure	Page
4.3 Specification of the internal electrode faces (Γ) for both MFCs.	126
4.4 Top and side views of the internal electrode faces (Γ) for both MFCs. . .	126
4.5 Illustration of the poling process after convergence of the electric field. Figures from top to bottom: A central cross section of the RVE; scaled electric field resultant (V/mm/s); resulting element coordinate systems in the PZT.	134
5.1 In-plane size comparison of both MFC patches considered.	146
5.2 In-plane geometrical parameters for the Passive Area and the problem coordinate system location.	148
5.3 Specification of the internal electrode faces (Γ) and poling for the homogenized MFCs.	152
5.4 Macroscopic model illustration with the M2503-P1 case. Electrical potential [V/mm] shown for all but the plate model. a) DNS b) DNS w/o Passive Area c) HRM-Solid d) HRM-Plate.	155
5.5 Relative locations for macroscopic quantities of interest and definitions of “Centerline” and “Tip Line”.	156
5.6 Static displacement of the host for Case 1.	158
5.7 Static displacement of the host for Case 2.	159
5.8 Transverse displacement of the host for Case 3.	160
5.9 Other static displacements of the host for Case 3 along Tip Line.	161
5.10 Relative locations for microscopic quantities of interest and definitions of “Line A,” “Line B,” and “Line C”.	162
5.11 Contrasting the local fields obtained from Line A and Line B for Case 3.	164
5.12 Transverse electric displacement along Line C.	165

SYMBOLS

Roman Symbols

a, b, c, d, e_1 and e_2	Inactive area geometric parameters
C_{ijkl}	Elastic Stiffness
c_1, c_2, c_3, c_4	Arbitrary constants of integration
D_i	Electric displacement
d	Diameter
d_{kij}	Piezoelectric strain coefficients
E_i	Electric field
e_{kij}	Piezoelectric stress coefficients
G	Shear Modulus
g_{kij}	Piezoelectric voltage coefficients
H_α	In-plane length of MFC active area (as modeled)
h_a	Active layer thickness
h_i	RVE edge length
h_{kij}	Piezoelectric h-coefficients
J	Direction cosines
k_{ik}	Dielectric permittivity
L_α	Overall MFC patch length
l_t	Electrode distance in Chapter 2, $t = 1, 3$
m	Arbitrary constants
m_1, m_2, m_3	Arbitrary constants of integration
N	Total number integration points in a RVE
N_a	Total number integration points in the active layer of a RVE
N_α	Number of RVEs along x_α
n_i	Unit normal vector

n_i^p	Unit normal poling direction vector
P^r	Remnant polarization
q	Free charge density
R_ε and R_σ	Transformation matrices for Engineering notation
S	Compliance
S_m	RVE boundary
s	Scaling factor, 10^{10}
T	Temperature
t_i	Traction
u_i	Mechanical displacement
V	Voltage
V_a	Volume of the active layer in a RVE
V^f	Fiber volume fraction
V_{Cu}^f	Copper fiber volume fraction in an electrode layer
V_{PZT}^f	PZT fiber volume fraction in the active layer
V_m	Volume of microstructure or RVE
$V^{(p)}$	Volume of integration point, p
x_i	Macroscale coordinates
X_i	RVE boundary face
Y	Elastic Modulus
y_i	Microscale coordinates
y'_i	Material coordinates

Greek Symbols

α	Coefficient of thermal expansion
β	Dielectric susceptibility
Γ	Electrode surface
Δ	Difference operator
δ_{ij}	Kronecker delta
ϵ	Small parameter

ε_{ij}	Strain tensor
ε_{ij}^r	Remnant strain
ε_{ij}^T	Temperature strain
ζ	Electrical fluctuating function
ν	Poisson's ratio
Π	Piezoelectric macro homogeneity condition
Π_{Active}	Piezoelectric enthalpy in electrically active regions
Π_{Passive}	Strain energy in electrically passive regions
ρ	Mass density
σ_{ij}	Stress tensor
ϕ	Electric potential
χ_i	Mechanical fluctuating function

Accent Marks

$(\)^a$	Active layer quantity
$(\)^0$	Applied quantity
$(\)^*$	Homogenized quantity
$(\)_{,i}$	Partial differentiation
$(\)'$	Property or variable in a new coordinate system
$(\)^-$	Quantity associated to a negative boundary surface
$(\)^+$	Quantity associated to a positive boundary surface
$(\)^{(p)}$	Quantity evaluated at integration point, p
$(\)_{(i,j)}$	Symmetric differentiation operator
$(\)^-$	Volume average
$\langle \ \rangle$	Volume average

ABBREVIATIONS

AFC	Active Fiber Composite
BVP	Boundary Value Problem
CFRP	Carbon Fiber Reinforced Polymer
CLPT	Classical Laminated Plate Theory
CPU	Central Processing Unit
CS	Coordinate System
DNS	Direct Numerical Simulation
DOF	Degree of Freedom
FE	Finite Element
FSDT	First-Order-Shear-Deformation-Theory
HRM1, HRM2	Step-1 and Step-2 Hybrid Rule of Mixtures, respectively
HSBC	Homogeneous Stress Boundary Conditions
MFC	Macro-Fiber Composite
MHT	Mathematical Homogenization Theory
MIX	In-plane PBCs and HSBC out-of-plane
MSG	Mechanics of Structure Genome
NASA	National Aeronautics and Space Administration
PBC	Periodic Boundary Condition
PMIL	Principle of Minimum Information Loss
PS	Plane-Stress-like
PSRM	Plane-Stress-like Rule of Mixtures
PZT	Lead Zirconate Titanate
RM	Rule of Mixtures
RVE	Representative Volume Element
SI	International System of Units

UFM	Uniform Field Model
VAM	Variational Asymptotic Method
VAMUCH	Variational Asymptotic Method for Unit Cell Homogenization

ABSTRACT

Camarena, Ernesto Ph.D., Purdue University, May 2019. Multiscale Continuum Modeling of Piezoelectric Smart Structures. Major Professor: Wenbin Yu.

Among the many active materials in use today, piezoelectric composite patches have enabled notable advances in emerging technologies such as disturbance sensing, control of flexible structures, and energy harvesting. The macro fiber composite (MFC), in particular, is well known for its outstanding performance. Multiscale models are typically required for smart-structure design with MFCs. This is due to the need for predicting the macroscopic response (such as tip deflection under a transverse load or applied voltage) while accounting for the fact that the MFC has microscale details. Current multiscale models of the MFC exclusively focus on predicting the macroscopic response with homogenized material properties. There are a limited number of homogenized properties available from physical experiments and various aspects of existing homogenization techniques for the MFC are shown here to be inadequate. Thus, new homogenized models of the MFC are proposed to improve smart-structure predictions and therefore improve device design. It is notable that current multiscale modeling efforts for MFCs are incomplete since, after homogenization, the local fields such as stresses and electric fields have not been recovered. Existing methods for obtaining local fields are not applicable since the electrodes of the MFC are embedded among passive layers. Therefore, another objective of this work was to find the local fields of the MFC without having the computational burden of fully modeling the microscopic features of the MFC over a macroscale area. This should enable smart-structure designs with improved reliability because failure studies of MFCs will be enabled. Large-scale 3D finite element (FE) models that included microscale features were constructed throughout this

work to verify the multiscale methodologies. Note that after creating a free account on cdmhub.org, many files used to create the results in this work can be downloaded from <https://cdmhub.org/projects/ernestocamarena>.

First, the Mechanics of Structure Genome (MSG) was extended to provide a rigorous analytical homogenization method. The MFC was idealized to consist of a stack of homogeneous layers where some of the layers were homogenized with existing rules of mixtures. For the analytical model, the electrical behavior caused by the interdigitated electrodes (IDEs) was approximated with uniform poling and uniform electrodes. All other assumptions on the field variables were avoided; thus an exact solution for a stack of homogeneous layers was found with MSG. In doing so, it was proved that in any such multi-layered composite, the in-plane strains and the transverse stresses are equal in each layer and the in-plane electric fields and transverse electric displacement are constant between the electrodes. Using this knowledge, a hybrid rule of mixtures was developed to homogenize the entire MFC layup so as to obtain the complete set of effective device properties. Since various assumptions were avoided and since the property set is now complete, it is expected that greater energy equivalence between reality and the homogenized model has been made possible. The derivation clarified what the electrical behavior of a homogenized solid with internal electrodes should be—an issue that has not been well understood. The behavior was verified by large-scale FE models of an isolated MFC patch.

Increased geometrical fidelity for homogenization was achieved with an FE-based RVE analysis that accounted for finite-thickness effects. The presented theory also rectifies numerous issues in the literature with the use of the periodic boundary conditions. The procedure was first developed without regard to the internal electrodes (*ie* a homogenization of the active layer). At this level, the boundary conditions were shown to satisfy a piezoelectric macrohomogeneity condition. The methodology was then applied to the full MFC layup, and modifications were implemented so that both types of MFC electrodes would be accounted for. The IDE case considered nonuniform poling and electric fields, but fully poled material was assumed. The in-

herent challenges associated with these nonuniformities are explored, and a solution is proposed. Based on the homogenization boundary conditions, a dehomogenization procedure was proposed that enables the recovery of local fields. The RVE analysis results for the effective properties revealed that the homogenization procedure yields an unsymmetric constitutive relation; which suggests that the MFC cannot be homogenized as rigorously as expected. Nonetheless, the obtained properties were verified to yield favorable results when compared to a large-scale 3D FE model.

As a final test of the obtained effective properties, large-scale 3D FE models of MFCs acting in a static unimorph configuration were considered. The most critical case to test was the smallest MFC available. Since none of the homogenized models account for the passive MFC regions that surround the piezoelectric fiber array, some of the test models were constructed with and without the passive regions. Studying the deflection of the host substrate revealed that ignoring the passive area in smaller MFCs can overpredict the response by up to 20%. Satisfactory agreement between the homogenized models and a direct numerical simulation were obtained with a larger MFC (about a 5% difference for the tip deflection). Furthermore, the uniform polarization assumption (in the analytical model) for the IDE case was found to be inadequate. Lastly, the recovery of the local fields was found to need improvement.

1. INTRODUCTION

Multi-physical structures have established a credible presence in science and engineering. The wonders of shape memory alloys, electrostriction, magnetostriction, piezoelectricity, pyroelectricity, and piezomagnetism have changed the outlook of what is possible for many engineering disciplines. Piezoelectricity, in particular, has found a sizable impact on everyday devices, such as gas igniters, to emerging technologies such as disturbance sensing, control of flexible structures, and energy harvesting.

A piezoelectric material is often combined with other materials and thus forming a piezoelectric composite (a.k.a piezocomposite). Much like ordinary composites such as carbon fiber reinforced polymers (CFRP), the major geometric features of piezocomposites are often microscopic. However, piezocomposite devices and associated structures are often much larger. Analysis and design of such devices quickly becomes computationally prohibitive when the microscopic features are explicitly incorporated. As such, many micromechanical theories which assume the continuum hypothesis have been extended from purely elastic to the piezoelectric case.

1.1 Micromechanical Basics

There are two objectives of micromechanics. The first one is to replace the heterogeneous body (*ie* the composite) with a homogeneous body that is equivalent in some sense [1, 2]. This is known as *homogenization*. The original boundary value problem (BVP) of the heterogeneous body is replaced by a simpler one where the heterogeneity has been replaced by a homogenized model. The second objective of micromechanics is to recover the local fields in the original heterogeneous body after solving the new BVP. This recovery of local fields is termed *dehomogenization* or

localization. Depending on the scope of the analysis, dehomogenization is not always required. However, the homogenization step precedes any dehomogenization.

A two-scale micromechanical analysis requires the definition of the microstructure as well as the targeted homogenized model. For example, this may be a question of whether an analysis considers fiber and matrix to obtain lamina properties or a stack of laminas being considered for the laminate behavior. Or the target model could be for a BVP of a different kind (beam or plate models). As demonstrated by the newly discovered Mechanics of Structure Genome (MSG) [3], the microstructure can be utilized to either obtain the effective material properties, the effective beam-stiffness, or the effective plate properties (ABD matrix). The constitutive information is then utilized in a solid model (3D elasticity), beam-theory, or plate/shell theory in the respective case. Finally, note, that it is often necessary to introduce idealizations into the definition of the microstructure for a given problem. For example, it is often sufficient to model continuous fiber reinforced composites with perfect square pack arrays and neglect any regions that are resin-rich.

So long as the separation of scales assumption is valid, more than two scales may be linked with the successive application of a micromechanics theory. For example, fiber and matrix can be homogenized to obtain the effective material properties of a lamina. Then a group of laminas can be homogenized to obtain effective properties of the group. Or for example, in textile composite, the fiber and matrix may be homogenized to obtain the effective yarn material properties and then various yarn configurations may be homogenized to obtain the effective material properties of the textile. The local fields at the original scale will only be available from a two-step dehomogenization (applied in the reverse order of the homogenization steps).

The remainder of the chapter presents a review of micromechanical methodologies for piezocomposites followed by the motivation of this dissertation. But first, a primer for piezoelectricity and piezoelectric devices is presented.

1.2 A Primer for Piezoelectrics

The *direct* piezoelectric effect was discovered by Jacques and Pierre Curie in 1880. They observed that when certain natural crystals undergo straining, a charge can be measured on its surface. The *converse* effect is when a strain is induced from an electric field and it was established only after defining piezoelectricity with rigorous tensor notation. These discoveries have been foundational to piezoelectric devices which provide a coupling between electricity and mechanics.

1.2.1 Polarization of Piezoelectrics

Piezoelectric materials are not usually piezoelectric until it is *polarized*. These materials are typically polymeric or ceramic. Polyvinylidene difluoride (PVDF, see [4] for example) is a common piezopolymer while lead zirconate titanate (PZT) and lead magnesium niobate-lead titanate (PMN-PT) are typical piezoceramics. Despite the use of lead, PZT is the most common piezoelectric material utilized for piezoelectric sensors and actuators [5]. It should be noted that lead-free piezoelectric materials are an enormously active area of research [6].

PZT is the focus of this dissertation and, therefore, only the polarization process of this material is described. When PZT wafers are formed (see [5] for an explanation of the process), they are usually polycrystalline as illustrated in Figure 1.1. Each single crystal (a.k.a. domain) consists of a local displacement of charges and thus forms local electrical dipoles. The dipole orientation is apparently random. Although each single crystal exhibits both piezoelectric effects, the misaligned domains result in no piezoelectricity when the averaged response of many crystals is considered (*ie* no piezoelectric effects at macroscopic scales). Fortunately, the orientation of these domains are reorientable and is known as *poling*. Bulk materials can be made piezoelectric through this process.

Poling for ceramics usually consists of elevating the temperature of the ceramic along with the application of a strong electric field for a period of time. Hot oil is

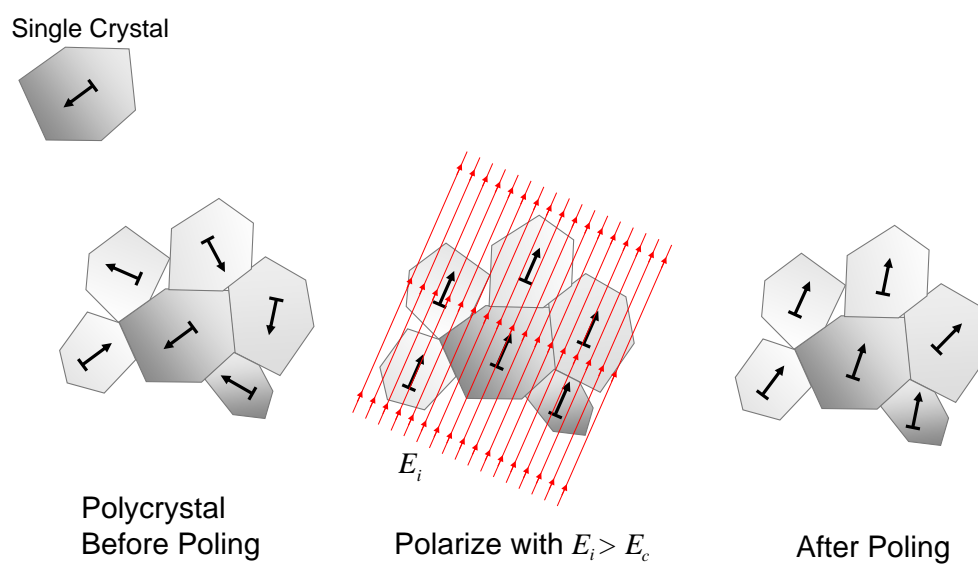


Figure 1.1: The poling process of polycrystalline ceramics.

used to raise the temperature and to provide electrical insulation [7,8]. The elevated temperatures make it easier to reorient the domains by lowering the coercive field [7]. Once the external electric field is removed, the domains lose some of their alignment but do have a preferential orientation as is also illustrated in Figure 1.1. It should be noted that depolarization is possible. Electrical depolarization occurs if a sufficiently high electric field is applied in another direction and mechanical depolarization is possible if certain strain components are excessive.

The *degree* to which the material is polarized depends on the electric field strength. If the applied electric field is lower than the coercive field value of the material, then poling will not occur. If the applied field is larger than the saturation field value, then the material will be fully polarized; at which point the piezoelectric effect of the material will be maximized. The material will be partially polarized if the applied field is between the coercive and saturation field values. Note that the applied electric field should be small enough to avoid dielectric breakdown of the material. The *poling direction*, which is in the direction of the applied field, is also important to note because various types of device behavior can be obtained for different poling directions. One should note that bulk single-crystal material is also available and can exhibit superior piezoelectric performance compared to polycrystalline material [9].

1.2.2 Piezoelectric Field Variables

Measuring charge or applying electric fields to a piezoelectric is usually facilitated with electrodes. Electrodes are electrically conductive materials that are typically nickel, gold, or copper. These materials are usually surface mounted to piezoelectrics in very thin films (*eg* via sputtering techniques). These electrodes are then wire-connected to other parts of a circuit (such as a multimeter) that can read voltage or charge for the direct effect. It is important to note that piezoelectric materials are dielectrics so none of their charges are mobile. This is in contrast to conductive materials (such as metals) where charges are free to move and therefore able to flow

current. When a conducting electrode is in mechanical contact with a piezoelectric, the free charge density at the interface (and in the conductor), q , can be found from

$$q = -D_i n_i \quad (1.1)$$

where D_i is the electric displacement (a.k.a electric flux intensity) at the interface (and in the piezoelectric) and n_i is the interface normal. Here and throughout this dissertation, index notation is utilized where Latin indices assume 1, 2, and 3 and Greek indices assume 1 and 2. Electric displacement in the piezoelectric represents the local flux of bound charges; thus the units are Coulomb/m² (C/m²). As for the converse effect, electrical fields can be applied through the piezoelectric either by specifying a voltage difference between the two electrodes or by specifying positive free charges on one electrode and negative free charges on the other. Finally, note that the electric displacement in a piezoelectric is governed by the first of Maxwell's equations [10]

$$D_{i,i} = q = 0 \quad (1.2)$$

where a comma indicates differentiation with respect to the Cartesian coordinates x_i . This equation is also referred to as Gauss' Law. Note that there is an absence of free charges in the piezoelectric so $q = 0$ everywhere in the piezoelectric domain. Finally, for purely elastic problems, the Cauchy stress tensor, σ_{ij} , is still governed by

$$\sigma_{ij,j} + b_i = \rho \ddot{u}_i \quad (1.3)$$

where b_i are body forces, ρ is the mass density, and \ddot{u}_i are accelerations. In the absence of body forces and inertia, one is left with

$$\sigma_{ij,j} = 0. \quad (1.4)$$

For mechanical displacement-based formulations, it is usual to incorporate the electrical potential to complete the primal field variables of piezoelectricity. The electrical potential, here denoted by ϕ , is a scalar field and Volt (V) is the unit. Electric fields can be defined as the negative gradient of the electric potential as

$$E_i = -\frac{\partial \phi}{\partial x_i} = -\phi_{,i}. \quad (1.5)$$

With the mechanical displacements denoted by u_i , the infinitesimal strain field is obtained from

$$\varepsilon_{i,j} = \frac{1}{2} \left(\frac{\partial u_i}{\partial x_j} + \frac{\partial u_j}{\partial x_i} \right) = \frac{1}{2} (u_{i,j} + u_{j,i}) = u_{(i,j)} \quad (1.6)$$

where the parenthesis in the subscripts indicates a symmetric operation. The stress tensor and the electric displacements can then be obtained from constitutive relations that utilize the material properties.

1.2.3 Piezoelectric Constitutive Equations

Material properties are often considered to be intrinsic to the material. However, unlike purely elastic behavior, some of the piezoelectric constitutive properties are obtained at specific boundary conditions. The material properties for a piezoelectric are defined from elastic, piezoelectric coupling, and dielectric properties. The elastic properties are obtained with specified electrical boundary conditions while the dielectric properties are obtained from constant mechanical boundary conditions.

Mechanical Properties at Specified Electrical Conditions

The electrical boundary conditions for the elastic properties are either *short-circuit* or *open-circuit*. These two conditions are illustrated in Figure 1.2. For the short-circuit condition, a wire connects the electrodes at opposing surfaces. This condition will have $E_3 = 0$. $E_\alpha = 0$ could also be obtained if the electrode conditions were also applied to the other faces. The mechanical properties obtained with short-circuit conditions should be specified with an E superscript (eg S_{ijkl}^E). Thus for $E_i = 0$, the short-circuit compliance can be obtained from

$$\varepsilon_{ij} = S_{ijkl}^E \sigma_{kl} + d_{kij} E_k \quad (1.7)$$

$$\Rightarrow \varepsilon_{ij} = S_{ijkl}^E \sigma_{kl} \quad \text{iff} \quad E_k = 0. \quad (1.8)$$

As for the open-circuit condition, the wire is disconnected and thus the voltages are unconstrained. This will produce $D_3=0$ [10]. These mechanical properties are

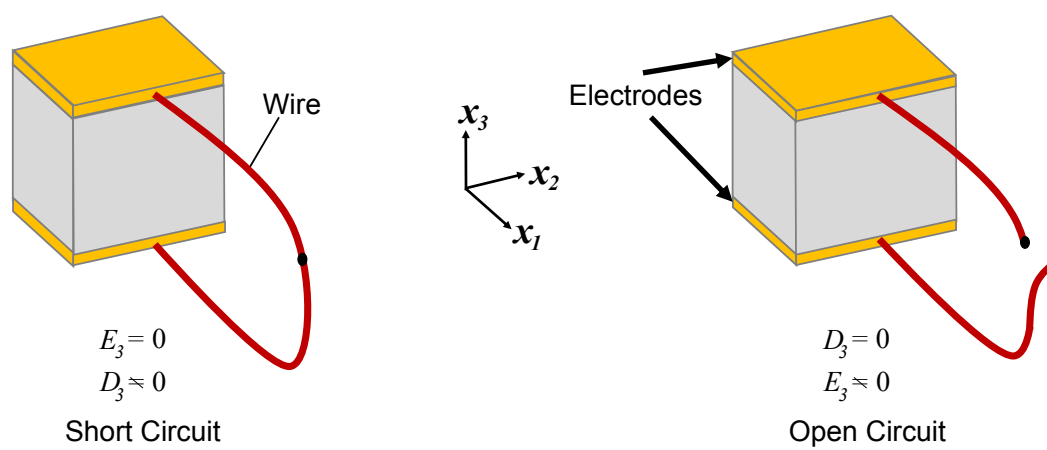


Figure 1.2: Contrasting electrical boundary conditions.

specified with a D superscript. When $D_i = 0$, the open-circuit compliance can be obtained from

$$\varepsilon_{ij} = S_{ijkl}^D \sigma_{kl} - g_{kij} \overrightarrow{D_k}^0 \quad (1.9)$$

$$\Rightarrow \varepsilon_{ij} = S_{ijkl}^D \sigma_{kl} \quad \text{iff} \quad D_k = 0. \quad (1.10)$$

Electrical Properties at Specified Mechanical Conditions

The mechanical boundary conditions on the dielectric properties are commonly referred to as either *free* or *blocked*. The dielectric properties can be given in terms of the permittivity k_{ij} (permittivity is often denoted by ε but here ε is reserved for strain). An illustration is not needed here because *free* means that the material is free to deform upon application of the electric field. *Blocked* refers to constraining any deformation under an applied electric field. Thus the free permittivity is obtained when $\sigma_{ij} = 0$ and is denoted by k_{ij}^σ . Thus for $\sigma_{ij} = 0$, the free permittivity can be obtained from

$$D_i = d_{ikl} \overrightarrow{\sigma_{kl}}^0 + k_{ij}^\sigma E_j \quad (1.11)$$

$$\Rightarrow D_i = k_{ij}^\sigma E_j \quad \text{iff} \quad \sigma_{ij} = 0 \quad (1.12)$$

The blocked permittivity, k_{ij}^ε , is obtained when $\varepsilon_{ij} = 0$ and thus

$$D_i = e_{ikl} \overrightarrow{\varepsilon_{kl}}^0 + k_{ij}^\varepsilon E_j \quad (1.13)$$

$$\Rightarrow D_i = k_{ij}^\varepsilon E_j \quad \text{iff} \quad \varepsilon_{ij} = 0. \quad (1.14)$$

It should be noted that, it is well known that the permittivity has a dependence on the field frequency and may have a complex value. The work presented herein is restricted to low frequencies and thus real values. It should also be noted that, in practice, the permittivities are obtained with capacitance measurements and other properties are often obtained dynamically with an impedance analyzer.

Constitutive Relations Summary

In summary, all the relations between E_i , D_i , σ_{ij} , and ε_{ij} are given by the following four equivalent constitutive relations.

$$\begin{aligned}\sigma_{ij} &= C_{ijkl}^E \varepsilon_{kl} - e_{kij} E_k \\ D_i &= e_{ikl} \varepsilon_{kl} + k_{ik}^\varepsilon E_k\end{aligned}\tag{1.15}$$

$$\begin{aligned}\varepsilon_{ij} &= S_{ijkl}^E \sigma_{kl} + d_{kij} E_k \\ D_i &= d_{ikl} \sigma_{kl} + k_{ik}^\sigma E_k\end{aligned}\tag{1.16}$$

$$\begin{aligned}\sigma_{ij} &= C_{ijkl}^D \varepsilon_{kl} - h_{kij} D_k \\ E_i &= -h_{ikl} \varepsilon_{kl} + \beta_{ik}^\varepsilon D_k\end{aligned}\tag{1.17}$$

$$\begin{aligned}\varepsilon_{ij} &= S_{ijkl}^D \sigma_{kl} + g_{kij} D_k \\ E_i &= -g_{ikl} \sigma_{kl} + \beta_{ik}^\sigma D_k\end{aligned}\tag{1.18}$$

C_{ijkl} denotes the elasticity tensor, S_{ijkl} denotes the compliance tensor, e_{ijk} are the piezoelectric stress coefficients, d_{ijk} are the piezoelectric strain coefficients, g_{ijk} are the piezoelectric voltage coefficients, h_{ijk} may be called the piezoelectric h-coefficients, β_{ik}^ε and β_{ik}^σ are the dielectric susceptibilities at constant stain and stress respectively.

It can be noted here that many model the polarization processes by including the remnant strain, ε_{ij}^r , and the remnant polarization P^r [11]. Temperature strains can also be included with ε_{ij}^T . Eq. (1.19) shows these terms below

$$\begin{aligned}\sigma_{ij} &= C_{ijkl}^E (\varepsilon_{kl} - \varepsilon_{kl}^T - \varepsilon_{kl}^r) - e_{kij} E_k \\ D_i &= e_{ikl} (\varepsilon_{kl} - \varepsilon_{kl}^T - \varepsilon_{kl}^r) + k_{ik}^\varepsilon E_k + P^r.\end{aligned}\tag{1.19}$$

Engineering Notation

It is often convenient to utilize Engineering (Matrix) notation of the constitutive equations. Below, Eq. (1.20) shows Eq. (1.16) in matrix form

$$\begin{pmatrix} \varepsilon_{11} \\ \varepsilon_{22} \\ \varepsilon_{33} \\ 2\varepsilon_{23} \\ 2\varepsilon_{13} \\ 2\varepsilon_{12} \\ D_1 \\ D_2 \\ D_3 \end{pmatrix} = \begin{bmatrix} S_{11}^E & S_{12}^E & S_{13}^E & S_{14}^E & S_{15}^E & S_{16}^E & d_{11} & d_{21} & d_{31} \\ & S_{22}^E & S_{23}^E & S_{24}^E & S_{25}^E & S_{26}^E & d_{12} & d_{22} & d_{32} \\ & & S_{33}^E & S_{34}^E & S_{35}^E & S_{36}^E & d_{13} & d_{23} & d_{33} \\ & & & S_{44}^E & S_{45}^E & S_{46}^E & d_{14} & d_{24} & d_{34} \\ & & & & S_{55}^E & S_{56}^E & d_{15} & d_{25} & d_{35} \\ & & & & & S_{66}^E & d_{16} & d_{26} & d_{36} \\ & & \text{Symm.} & & & & k_{11}^\sigma & k_{12}^\sigma & k_{13}^\sigma \\ & & & & & & & k_{22}^\sigma & k_{23}^\sigma \\ & & & & & & & & k_{33}^\sigma \end{bmatrix} \begin{pmatrix} \sigma_{11} \\ \sigma_{22} \\ \sigma_{33} \\ \sigma_{23} \\ \sigma_{13} \\ \sigma_{12} \\ E_1 \\ E_2 \\ E_3 \end{pmatrix} \quad (1.20)$$

Note that S_{ij}^E are the components of the 6×6 compliance matrix at constant electric field. The k_{ij}^σ are the components of the 3×3 dielectric permittivities at constant stress. d_{ij} are the components of the 6×3 piezoelectric strain coefficient matrix. Piezoelectrics are usually transversely isotropic with the axis of symmetry being aligned with the poling direction. In piezoelectric literature, the x_3 -axis is often reserved for the poling axis. Thus, piezoceramics are typically transversely isotropic with the x_3 -axis forming the axis of symmetry. Transverse isotropy along x_3 means that

$$S_{11}^E = S_{22}^E, S_{13}^E = S_{23}^E, S_{44}^E = S_{55}^E, d_{31} = d_{32}, d_{24} = d_{15}, \text{ and } k_{11}^\sigma = k_{22}^\sigma. \text{ Eq. (1.20)}$$

reduces to

$$\begin{Bmatrix} \varepsilon_{11} \\ \varepsilon_{22} \\ \varepsilon_{33} \\ 2\varepsilon_{23} \\ 2\varepsilon_{13} \\ 2\varepsilon_{12} \\ D_1 \\ D_2 \\ D_3 \end{Bmatrix} = \begin{bmatrix} S_{11}^E & S_{12}^E & S_{13}^E & & & & & & \\ & S_{11}^E & S_{13}^E & & & & & & \\ & & S_{33}^E & & & & & & \\ & & & S_{44}^E & & & & & \\ & & & & S_{44}^E & & d_{24} & & \\ & & & & & S_{66}^E & & & \\ & & & & & & k_{11}^\sigma & & \\ & & & & & & & k_{11}^\sigma & \\ & & & & & & & & k_{33}^\sigma \end{bmatrix} \begin{Bmatrix} \sigma_{11} \\ \sigma_{22} \\ \sigma_{33} \\ \sigma_{23} \\ \sigma_{13} \\ \sigma_{12} \\ E_1 \\ E_2 \\ E_3 \end{Bmatrix} \quad (1.21)$$

where empty spaces are null values. It is finally noted that piezoelectric material cannot be isotropic [12].

Material Property Transformations

Oftentimes, it is often necessary to transform the material properties to another coordinate system. Only if the material was poled uniformly along x_3 and x_3 corresponds to the global analysis coordinates, then material transformation would not be needed. If $[J]$ is the 3×3 direction cosine matrix, then the permittivity, $[k]$ (either k^σ or k^ε), can be transformed according to the usual transformation law of second order tensors

$$[k'] = [J][k][J]^T \quad (1.22)$$

where the prime denotes the transformed property. Either elastic compliance (S^E or S^D) will transform with

$$[S'] = [R_\varepsilon][S][R_\varepsilon]^T \quad (1.23)$$

where

$$[R_\epsilon] = \begin{bmatrix} J_{11}^2 & J_{12}^2 & J_{13}^2 & J_{12}J_{13} & J_{11}J_{13} & J_{11}J_{12} \\ J_{21}^2 & J_{22}^2 & J_{23}^2 & J_{22}J_{23} & J_{21}J_{23} & J_{21}J_{22} \\ J_{31}^2 & J_{32}^2 & J_{33}^2 & J_{32}J_{33} & J_{31}J_{33} & J_{31}J_{32} \\ 2J_{21}J_{31} & 2J_{22}J_{32} & 2J_{23}J_{33} & (J_{22}J_{33} + J_{23}J_{32}) & (J_{23}J_{31} + J_{21}J_{33}) & (J_{31}J_{22} + J_{21}J_{32}) \\ 2J_{11}J_{31} & 2J_{12}J_{32} & 2J_{13}J_{33} & (J_{13}J_{32} + J_{12}J_{33}) & (J_{11}J_{33} + J_{13}J_{31}) & (J_{11}J_{32} + J_{12}J_{31}) \\ 2J_{11}J_{21} & 2J_{12}J_{22} & 2J_{13}J_{23} & (J_{12}J_{23} + J_{13}J_{22}) & (J_{11}J_{23} + J_{13}J_{21}) & (J_{11}J_{22} + J_{12}J_{21}) \end{bmatrix}$$

Similarly, either elastic stiffness will transform with

$$[C'] = [R_\sigma][C][R_\sigma]^T \quad (1.24)$$

where $[R_\sigma]^T = [R_\epsilon]^{-1}$. Finally, the piezoelectric strain and stress coefficients, respectively, will transform according to

$$[d'] = [R_\epsilon][d][J]^T \quad [e'] = [R_\sigma][e][J]^T \quad (1.25)$$

Conversions Between Constitutive Relation Types

It is regularly needed to convert between the four forms of the constitutive equations from (1.15) to (1.18). The relations are shown below [10]

$$[S^E] = [C^E]^{-1} \quad (1.26)$$

$$[e] = [C^E][d] \quad (1.27)$$

$$[d] = [S^E][e] \quad (1.28)$$

$$[k^\sigma] = [k^\varepsilon] + [d]^T[e] \quad (1.29)$$

$$[\beta^\sigma] = [k^\sigma]^{-1} \quad (1.30)$$

$$[g] = [d][\beta^\sigma] \quad (1.31)$$

$$[S^D] = [S^E] - [g][d]^T \quad (1.32)$$

$$[C^D] = [S^D]^{-1} \quad (1.33)$$

$$[h] = [C^D][g] \quad (1.34)$$

$$[\beta^\varepsilon] = [\beta^\sigma] + [g]^T[C^D][g] \quad (1.35)$$

$$[k^\varepsilon] = [\beta^\varepsilon]^{-1} \quad (1.36)$$

$$[e] = [h][k^\varepsilon] \quad (1.37)$$

$$[C^E] = [C^D] - [h][e]^T \quad (1.38)$$

where a $[\bullet]^T$ indicates matrix transpose and a “ -1 ” superscript indicates matrix inversion.

Let ε and σ denote 6×1 vectors holding the strain and stress components in Engineering notation (see [2]). Also, let D , and E be 3×1 vectors holding the electric displacement and electric field respectively. In the process of converting from Eq. (1.15) to Eq. (1.16), the two matrix equations are

$$\sigma = [C^E]\varepsilon - [e]E \quad (1.39)$$

$$D = [e]^T\varepsilon + [k^\varepsilon]E. \quad (1.40)$$

Solving for ε in the first equation gives $\varepsilon = [C^E]^{-1} (\sigma + [e]E)$. Letting $[C^E]^{-1} = [S^E]$ as in Eq. (1.26) and then substituting ε into the second equation results in

$$\begin{aligned} D &= [e]^T [S^E] \sigma + [e]^T [S^E] [e] E + [k^\varepsilon] E \\ &= [e]^T [S^E] \sigma + ([k^\varepsilon] + [e]^T [S^E] [e]) E. \end{aligned} \quad (1.41)$$

Noting that $[S^E]^T = [S^E]$, the term $[e]^T [S^E]$ is recognized as $[d]^T$ where it is equivalently shown in Eq. (1.28). Then $([k^\varepsilon] + [e]^T [S^E] [e])$ is recognized as $[k^\sigma]$ from Eq. (1.29).

Next we convert from Eq. (1.16) to Eq. (1.18). The two matrix equations are

$$\varepsilon = [S^E] \sigma + [d] E \quad (1.42)$$

$$D = [d]^T \sigma + [k^\sigma] E. \quad (1.43)$$

Solving for E in the second equation gives $E = [k^\sigma]^{-1} (D - [d]^T \sigma)$. Letting $[k^\sigma]^{-1} = [\beta^\sigma]$ as in Eq. (1.30) and then substituting E into the first equation results in

$$\varepsilon = ([S^E] - [d] [\beta^\sigma] [d]^T) \sigma + [d] [\beta^\sigma] D. \quad (1.44)$$

The term $[d] [\beta^\sigma]$ is recognized as $[g]$ as in Eq. (1.31). Then $([S^E] - [d] [\beta^\sigma] [d]^T) = ([S^E] - [g][d]^T)$ which is recognized as $[S^D]$ from Eq. (1.32).

It is now shown how to convert from Eq. (1.18) to Eq. (1.17). This time, the two matrix equations are

$$\varepsilon = [S^D] \sigma + [g] D \quad (1.45)$$

$$E = -[g]^T \sigma + [\beta^\sigma]. \quad (1.46)$$

Solving for σ in the first equation gives $\sigma = [S^D]^{-1} (\varepsilon - [g] D)$. Letting $[S^D]^{-1} = [C^D]$ as in Eq. (1.33) and then substituting σ into the second equation results in

$$\begin{aligned} E &= -[g]^T [C^D] \varepsilon + [g]^T [C^D] [g] D + [\beta^\sigma] D \\ &= -[g]^T [C^D] \varepsilon + ([\beta^\sigma] + [g]^T [C^D] [g]) D. \end{aligned} \quad (1.47)$$

Noting that $[C^D]^T = [C^D]$, the term $[g]^T[C^D]$ is recognized as $[h]^T$ which is equivalently shown in Eq. (1.34). Then $([\beta^\sigma] + [g]^T[C^D][g])$ is recognized as $[\beta^\varepsilon]$ from Eq. (1.35).

Finally, the conversion from Eq. (1.17) to Eq. (1.15). This time, the two matrix equations are

$$\sigma = [C^D]\varepsilon - [h]D \quad (1.48)$$

$$E = -[h]^T\varepsilon + [\beta^\varepsilon]D. \quad (1.49)$$

Solving for D in the second equation gives $D = [\beta^\varepsilon]^{-1}(E + [h]^T\varepsilon)$. Letting $[\beta^\varepsilon]^{-1} = [k^\varepsilon]$ as in Eq. (1.36) and then substituting D into the first equation results in

$$\sigma = ([C^D] - [h][k^\varepsilon][h]^T)\varepsilon - [h][k^\varepsilon]E. \quad (1.50)$$

The term $[h][k^\varepsilon]$ is recognized as $[e]$ as in Eq. (1.37). Then $([C^D] - [h][k^\varepsilon][h]^T) = ([C^D] - [h][e]^T)$ which is recognized as $[C^E]$ from Eq. (1.38).

1.2.4 Piezoelectric Devices and Piezocomposites

Historically, it was not until the First World War that a technologically important piezoelectric device was formed; namely, the ultrasonic submarine detector by Paul Langevin [13]. Since then, many piezoelectric devices have been created such as sensitive pressure gauges, microphones, audio speakers, internal combustion engine monitoring, gas-grill igniters, and strain sensors [14] to name a few.

Electrodes: Uniform vs. Interdigitated

Since the electrodes in a device are often utilized to initially polarize the ceramic, the electrode type drastically affects the response of the device. The two electrode types that are commonly found are referred to as uniform electrodes and interdigitated electrodes (IDE). These electrodes are illustrated in Figure 1.3. Other electrode configurations can be devised (*eg* [15,16]) but uniform and IDEs are, by far, the most practical.

The uniform electrodes are the most basic electrode type. They often resemble that of a parallel plate capacitor. Neglecting the fringe fields near the edges, a uniform electric field, E_3 , is produced; where x_3 is usually through the device thickness. If polarization is performed under these conditions, then the ceramic will be polarized along x_3 . Constitutive Eq. (1.21) can then be utilized without transformation because x_3 will be the axis of material symmetry.

Bent *et al* [17] identified that devices with these conditions will produce isotropic sensing and actuation in the plane of the device. This is because $d_{31} = d_{32}$ and these link in-plane deformations with the electrical activity in the transverse direction. Furthermore, they noted that d_{33} is about 2.4 times higher than d_{31} for most piezoceramics. Thus, devices with uniform electrodes have a higher sensitivity for through-the-thickness effects than they do for in-plane effects. Polarizing piezoceramics with IDEs (as well as using them in service) enables the stronger d_{33} coefficient to take effect along, say x_1 (in-plane). Devices with these electrodes can produce comparatively higher actuation strain along x_1 .

However, recall from Section 1.2.1 that the poling direction and degree of poling depends on the applied electric field. Thus poling a ceramic with IDEs produces nonuniform poling. It is nonuniform in both the poling direction and degree. Recall that piezoelectric material properties are specified with the 3-axis corresponding to the poling direction. Therefore, a nonuniform poling direction implies that the material properties may need to be transformed so that the poling axis of symmetry is in the direction E_k at every point. As for variations in poling degree, there will be regions of unpoled material, and a possibility partially and fully poled material (see [18] for optimal electrode spacing studies). The unpolarized regions (and therefore not piezoelectric) are known as *dead-zones* (eg see [7, 18, 19]). They exist in regions near the electrodes. Since the constitutive Eq. (1.21) corresponds to transverse isotropy with the axis of symmetry corresponding to the polarization axis, and since the IDE case produces non-uniform electric fields, the material coordinate system for the material is a function of position.

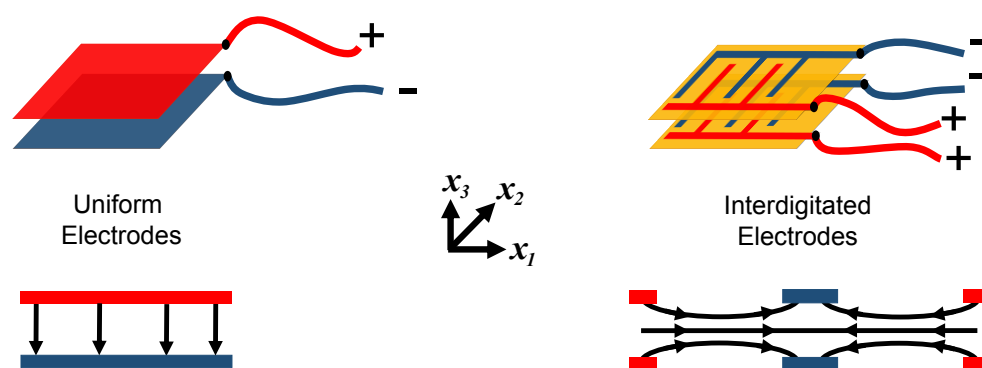


Figure 1.3: Common electrode types and associated electrical activity.

1.2.5 Unit Conversions for Piezoelectricity

Since the smallest heterogeneities (under the continuum hypothesis) of most piezoelectric devices are on the order of 10^{-6} meters, FE analyses of these devices need to properly account for these small scales. This would involve discretizing geometry at a microscopic scale. However, one should be aware of the limitations that geometry engines of commercial FE codes have. For example, the minimum size limit for Abaqus® is 10^{-6} (unitless). This means that the smallest element edge should be larger than this limit. Therefore it has been recommended that a part-size should be 10^{-3} or greater. Otherwise geometrical defects may occur [20]. It then becomes unlikely that standard unit systems, such as the International System of units (SI), can obtain reliable results. Since most codes do not accept explicit units, a solution to this problem is to represent the geometry in millimeters or even in microns. It is then only necessary to utilize consistent units among all quantities in the analysis.

It is relatively simple to ensure consistent units for purely mechanical analyses. For example, if the model geometry is in millimeters then, stresses and the elastic moduli can be converted from Pa to MPa (N/mm^2) by multiplying by 10^{-6} . Complications can arise from the electrical quantities in piezoelectric analyses. For example, the units of the piezoelectric stress coefficients are C/m^2 . However, a Coulomb is also a Nm/V . Thus the piezoelectric stress coefficients have the units of C/m^2 or N/(Vm) . A question becomes: how do you scale the piezoelectric stress coefficients so that they are based in millimeters? Do you multiply piezoelectric stress coefficients by 10^{-6} to convert from C/m^2 to C/mm^2 ; or should you use a factor of 10^{-3} to convert from N/(Vm) to N/(Vmm) ? The answer to this question comes by converting all problem variables to consistent units; not just the units that contain length. For example, Amperes (A) in the problem should be converted to μA . Table 1.1 shows the resulting unit conversions that are necessary for consistent piezoelectric units. The table also reveals that a factor of 1 should be used to convert C/m^2 to $\mu\text{C/mm}^2$;

the factor is neither 10^{-3} or 10^{-6} as discussed above. Conversions of other quantities are also found in the table.

Table 1.1: Unit conversion for multiscale piezoelectric analyses. Adapted from [21].

Parameter	MKS		Multiply		To	
	Unit	Dimension	By	Obtain	New	Dimension
Length	m	m	10^3	mm	mm	
Force	N	$\frac{\text{kg m}}{\text{s}^2}$	10^3	mN	$\frac{\text{kg mm}}{\text{s}^2}$	
Time	s	s	1	s	s	
Mass	kg	kg	1	kg	kg	
Stress	Pa	$\frac{\text{kg}}{\text{m s}^2}$	10^{-3}	kPa	$\frac{\text{kg}}{\text{mm s}^2}$	
Elastic Moduli	Pa	$\frac{\text{kg}}{\text{m s}^2}$	10^{-3}	kPa	$\frac{\text{kg}}{\text{mm s}^2}$	
Current	A	A	10^6	μA	μA	
Voltage	V	$\frac{\text{kg m}^2}{\text{A s}^3}$	1	V	$\frac{\text{kg mm}^2}{\mu\text{A s}^3}$	
Charge	C	A s	10^6	μC	$\mu\text{A s}$	
Capacitance	F	$\frac{\text{A}^2 \text{s}^4}{\text{kg m}^2}$	10^6	μF	$\frac{(\mu\text{A})^2 \text{s}^4}{\text{kg mm}^2}$	
Permittivity	F/m	$\frac{\text{A}^2 \text{s}^4}{\text{kg m}^3}$	10^3	$\mu\text{F}/\text{mm}$	$\frac{(\mu\text{A})^2 \text{s}^4}{\text{kg mm}^3}$	
Electric Field	V/m	$\frac{\text{kg m}}{\text{A s}^3}$	10^{-3}	V/mm	$\frac{\text{kg mm}}{\mu\text{A s}^3}$	
Electric Displacement	C/m ²	$\frac{\text{A s}}{\text{m}^2}$	1	$\mu\text{C}/\text{mm}^2$	$\frac{\mu\text{A s}}{\text{mm}^2}$	
Stress Coeff. e_{kij}	C/m ²	$\frac{\text{A s}}{\text{m}^2}$	1	$\mu\text{C}/\text{mm}^2$	$\frac{\mu\text{A s}}{\text{mm}^2}$	
Strain Coeff. d_{kij}	C/N	$\frac{\text{A s}^3}{\text{kg m}}$	10^3	$\mu\text{C}/\text{mN}$	$\frac{\mu\text{A s}^3}{\text{kg mm}}$	

1.3 Review of the Micromechanics of Piezocomposites.

Since the birth of piezocomposites, numerous piezoelectric homogenization techniques have emerged to enable simplified and efficient device design. It is desirable to replace the original, heterogeneous body with an equivalent homogeneous body. The challenge then is to find the effective properties that best resemble reality. The section

at present surveys existing homogenization techniques for heterogeneous piezoelectric media. The methods are categorized by various levels of approximation. Assumptions on the field variables are documented as well as assumptions about the microstructure.

Before proceeding further, it will now be useful to introduce notation that has been utilized throughout this dissertation. Figure 1.4 shows a 3D periodic structure and Figure 1.5 shows its Representative Volume Element (RVE). Figure 1.5 also shows the face labels X_i^+ and X_i^- , and edge lengths h_i . The plus and minus superscripts help establish quantities on a *positive* or *negative* RVE surface as shown in Figure 1.5.

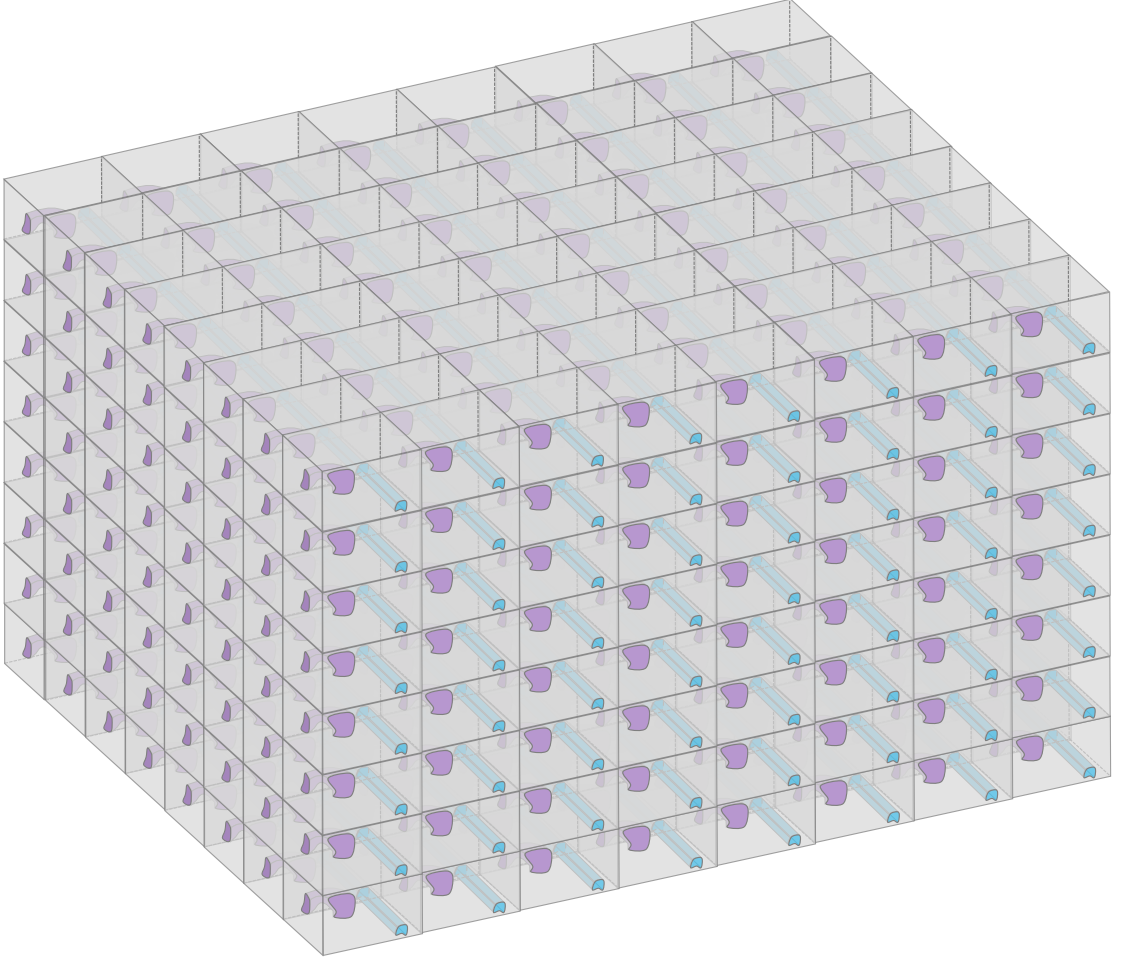


Figure 1.4: A generic composite that features periodicity in three dimensions.

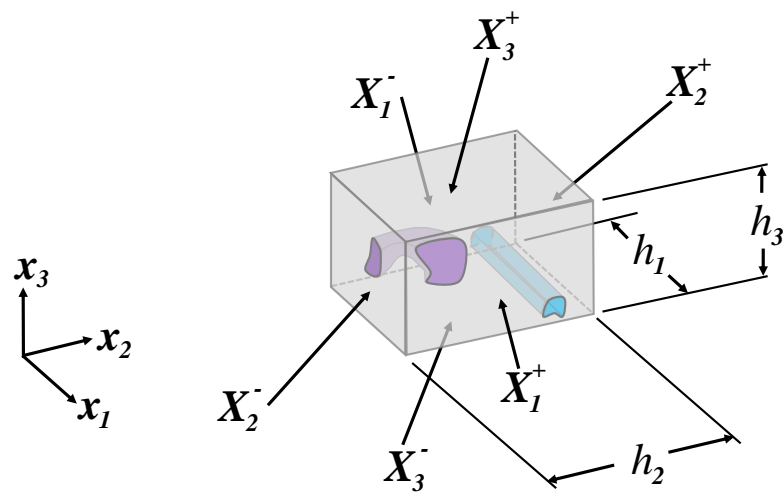


Figure 1.5: Periodic RVE face labels and edge lengths for an arbitrary microstructure.

During homogenization, we seek constitutive relations of the form

$$\begin{aligned}\bar{\sigma}_{ij} &= C_{ijkl}^{E*} \bar{\varepsilon}_{kl} - e_{kij}^* \bar{E}_k \\ \bar{D}_i &= e_{ikl}^* \bar{\varepsilon}_{kl} + k_{ik}^{\varepsilon*} \bar{E}_k\end{aligned}\tag{1.51}$$

where the starred quantities correspond to the homogenized body and an over-bar of any quantity, f , indicates a volume average over the volume of the microstructure, V_m . For example,

$$\bar{f} = \langle f \rangle = \frac{1}{V_m} \iiint_{V_m} f dV_m.\tag{1.52}$$

1.3.1 General Micromechanical Theories

The best three techniques as far as accuracy and microstructural generality are:

- Mechanics of Structure Genome (MSG)
- Mathematical Homogenization Theory (MHT) (a.k.a. Asymptotic Homogenization)
- RVE Analysis

MSG [3] is a multipurpose, and yet, unified micromechanics theory powered by the variational asymptotic method (VAM) [22] (see also [12]). MSG is based on the principle of minimum information loss (PMIL). This principle states that the homogenized model can be constructed by minimizing the information loss between the original heterogeneous body and the homogenized body. There are many brilliant aspects of MSG. One is that it provides constitutive modeling of composite materials, beams [23], and plates without any *ad hoc* assumptions on the field variables. The constitutive properties are guaranteed to be the best possible from the PMIL. MSG's piezoelectric capabilities came from its beam [24], plate [25,26], and 3D [27,28] model precursors. An advantage that MSG has over RVE analysis is that only one analysis (instead of many BVPs) is required for effective properties. This advantage grows in significance when the heterogeneous model requires hundreds of thousands

to millions of FEs. The solution procedure in MHT [29–34] requires the mechanical displacements and the electrical potential to be constructed from an asymptotic series. These functions are substituted into the governing equations and various orders of the solution are obtained. Piezoelectric homogenization with RVE analysis consists of solving (up to) nine BVPs with the FE method and then finding the averages of the local fields followed by post-processing.

Any microstructure may be analyzed numerically with these methods. Analytical solutions for MSG and MHT are possible for simpler microstructures (such as layered composites). RVE analysis requires the use of finite elements so it is limited to numerical solutions in practice. Despite that limitation, RVE analysis is the most popular homogenization scheme (see [35–47, 47–54, 54–59]). One of the reasons for its popularity is that it can be implemented in commercial FE codes. Unfortunately, the popularity does not mean that every use of RVE analysis is equivalent to the accuracy of MSG and MHT. Boundary conditions are critically important. Knowing the best ones to apply can be challenging.

As reported in [1, 60, 61] for purely elastic problems, the PBCs are the most reasonable BCs for RVE analysis; even for microstructures that are not periodic. The PBCs were first reported by Berger *et al* [36] and are

$$u_i^+ - u_i^- = \bar{\varepsilon}_{ij}(y_j^+ - y_j^-) \quad (1.53)$$

and

$$\phi^+ - \phi^- = -\bar{E}_i(y_i^+ - y_i^-). \quad (1.54)$$

It was not until later that Schröder [62] showed that these BCs satisfy a piezoelectric macrohomogeneity condition; the analog to the Hill-Mandel condition. Pettermann and Suresh [35] were the first to call their BCs the PBCs except these are not known to satisfy the macrohomogeneity condition.

A problem with many of the alleged applications of the PBCs for piezoelectric homogenization is that PBCs are not rigorously applied [39, 47, 51–54, 54–58]. A common problem in many works is that uniform displacements and equipotential BCs are

often confused for PBCs. For example, in Berger *et al* [36], periodic equation constraints for mechanical loading were only utilized for the shear behavior. Otherwise, uniform displacement BCs were specified. They described an example and argued that if $u_i^- = 0$ on X_1^- , then (1.53) will be independent of u_i^- . Thus they reasoned that a uniform, nonzero displacement may be applied on X_1^+ . They further argued that except for $\bar{\varepsilon}_{11}$, every other $\bar{\varepsilon}_{ij}$ can be made zero while satisfying the PBC if the displacement is constrained to zero on the other faces (X_2^- , X_2^+ , X_3^- , and X_3^+). Although they show Eq. (1.54) as their electrical BCs, their table of BCs shows that equipotential BCs were utilized instead. Another common issue is that $\bar{\varepsilon}_{ij}$ and \bar{E}_i are not known *a priori* to an analysis. Often, for example, a component of $\bar{\varepsilon}_{ij}$ is *assumed* to be nonzero and all other $\bar{\varepsilon}_{ij}$ are *assumed* to be zero. Only then are Eqs. (1.53) and (1.54) implemented. From articles reviewed in this dissertation, no one checks to see if $\bar{\varepsilon}_{ij}$ and \bar{E}_i equals the true volume average in the RVE. Thus the macrohomogeneity condition is not guaranteed to be satisfied and thus the homogenized material properties are not guaranteed to be energetically equivalent to the heterogeneous body. A final issue with most implementations of RVE analysis is that the symmetry of the obtained constitutive properties is seldom verified. Only Jafari *et al* [58] proposed a symmetry check for the PBCs.

1.3.2 Uniform Field Assumption Methods

It is often convenient to assume that, for an arbitrary loading, various fields are uniform within a microstructure. Such assumptions have led to purely analytical solutions. Hashimoto and Yarnaguchi [63] looked at layered piezocomposites (2-2 connectivity). From the Floquet theorem and assuming periodicity in the stacking direction, they deduced that

$$\begin{aligned} \varepsilon_{11} = \bar{\varepsilon}_{11} \quad \varepsilon_{22} = \bar{\varepsilon}_{22} \quad \sigma_{33} = \bar{\sigma}_{33} \quad \sigma_{23} = \bar{\sigma}_{23} \quad \sigma_{13} = \bar{\sigma}_{13} \quad \varepsilon_{12} = \bar{\varepsilon}_{12} \\ E_1 = \bar{E}_1 \quad E_2 = \bar{E}_2 \quad D_3 = \bar{D}_3. \end{aligned} \quad (1.55)$$

where the x_3 axis is normal to the layer interface. Eq. (1.55) means that certain local fields in each constituent are assumed to be equal to the average value in the microstructure. One may then notice that the in-plane strains, the out-of-plane stresses, in-plane electric field, and out-of-plane electric flux are all considered to be constant within the microstructure. Since all of the field variables are constants, they were able to find the complete set of effective properties for layered composites.

With these assumptions, a Hybrid Rule of Mixtures (HRM) procedure can be described as follows. Rewrite Eq. (1.20) as

$$\varepsilon^H = S^H \sigma^H \quad (1.56)$$

with $\varepsilon^H = [\sigma_{11} \ \sigma_{22} \ \varepsilon_{33} \ 2\varepsilon_{23} \ 2\varepsilon_{13} \ \sigma_{12} \ D_1 \ D_2 \ E_3]^T$ and $\sigma^H = [\varepsilon_{11} \ \varepsilon_{22} \ \sigma_{33} \ \sigma_{23} \ \sigma_{13} \ 2\varepsilon_{12} \ E_1 \ E_2 \ D_3]^T$. Then one can compute the average of ε^H as

$$\bar{\varepsilon}^H = \langle \varepsilon^H \rangle = \langle S^H \sigma^H \rangle = \langle S^H \rangle \bar{\sigma}^H = S^{H*} \bar{\sigma}^H \quad (1.57)$$

Note that $\sigma^H = \bar{\sigma}^H$ due to the assumptions in Eq. (1.55). After rearranging S^{H*} back to the original order of the variables (see Eq. (1.20)), one is able to obtain a complete set of analytical expressions for the effective electromechanical constants. Note that one should be able to perform this kind of procedure beginning from any of the Eqs. (1.15) – (1.18) and find the same results. For example, in Engineering notation, we can write Eq. (1.15) as

$$\sigma^H = C^H \varepsilon^H \quad (1.58)$$

with $\sigma^H = [\sigma_{11} \ \sigma_{22} \ \varepsilon_{33} \ 2\varepsilon_{23} \ 2\varepsilon_{13} \ \sigma_{12} \ D_1 \ D_2 \ E_3]^T$ and $\varepsilon^H = [\varepsilon_{11} \ \varepsilon_{22} \ \sigma_{33} \ \sigma_{23} \ \sigma_{13} \ 2\varepsilon_{12} \ E_1 \ E_2 \ D_3]^T$. Then one can compute the average of σ^H as before

$$\bar{\sigma}^H = \langle \sigma^H \rangle = \langle C^H \varepsilon^H \rangle = \langle C^H \rangle \bar{\varepsilon}^H = C^{H*} \bar{\varepsilon}^H. \quad (1.59)$$

In general, post processing with the appropriate conversions from (1.26) - (1.38) will be required.

Piezoelectric media often consist of miniature piezoelectric rods embedded in a polymeric matrix. This among other possible configurations is classified as 1-3 type

piezocomposites according to Newnham [64] (see also [65]). Popular 1-3 piezocomposites are planar devices that have piezoceramic rods that span one of the in-plane dimensions [66]. This case is referred to as Case A herein and is shown in Figure 1.6. Another highly successful configuration of 1-3 piezocomposites, has been with

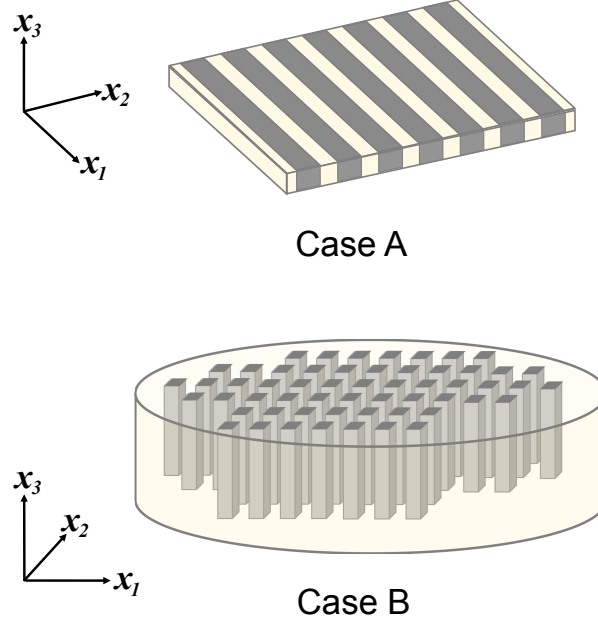


Figure 1.6: Usual rod configurations for piezocomposite transducers.

underwater transducers, medical imaging, and later, structural health monitoring. These smart devices are often thin disk-shaped structures and the piezoelectric rods are placed vertically as illustrated in Case B of Figure 1.6.

Following the same principle that the in-plane strains, out-of-plane stresses, in-plane electric field, and out-of-plane electric flux are constants, many other microstructures have been examined. Deraemaeker *et al* [47, 48] homogenized the so-called active layer of the macro-fiber composite (MFC). This corresponds to Case A. In that work, the layer interfaces are normal to the x_2 axis (layered material stacked horizontally). The assumptions presented in Eq. (1.55) become

$$\begin{aligned} \varepsilon_{11} = \bar{\varepsilon}_{11} \quad \sigma_{22} = \bar{\sigma}_{22} \quad \varepsilon_{33} = \bar{\varepsilon}_{33} \quad \sigma_{23} = \bar{\sigma}_{23} \quad \varepsilon_{13} = \bar{\varepsilon}_{13} \quad \sigma_{12} = \bar{\sigma}_{12} \\ E_1 = \bar{E}_1 \quad D_2 = \bar{D}_2 \quad E_3 = \bar{E}_3. \end{aligned} \quad (1.60)$$

and then one can proceed as before with Eqs. (1.56) – (1.57). Microstructures that are not strictly layered have been approximated with the layered assumptions in a series of successive homogenizations; in particular fiber composites (1-3 connectivity) in [16, 42, 67], particulate composites (0-3 connectivity) in [68], the full MFC in [9, 53–55, 69, 70], and the active fiber composite (AFC) in [71]. It is notable that [16] yields self-conflicting results and [71] is known to violate compatibility and equilibrium [72].

Many [7, 9, 48, 50, 69, 73] have chosen to work with a reduced set of constitutive equations. For example, in [48], instead of starting with Eq. (1.20), Deraemaeker *et al* start with

$$\begin{Bmatrix} \varepsilon_{11} \\ \varepsilon_{22} \\ 2\varepsilon_{23} \\ 2\varepsilon_{13} \\ 2\varepsilon_{12} \\ D_3 \end{Bmatrix} = \begin{bmatrix} S_{11}^E & S_{12}^E & S_{14}^E & S_{15}^E & S_{16}^E & d_{31} \\ & S_{22}^E & S_{24}^E & S_{25}^E & S_{26}^E & d_{32} \\ & & S_{44}^E & S_{45}^E & S_{46}^E & d_{34} \\ & & & S_{55}^E & S_{56}^E & d_{35} \\ & \text{Symm.} & & & S_{66}^E & d_{36} \\ & & & & & k_{33}^\sigma \end{bmatrix} \begin{Bmatrix} \sigma_{11} \\ \sigma_{22} \\ \sigma_{23} \\ \sigma_{13} \\ \sigma_{12} \\ E_3 \end{Bmatrix} \quad (1.61)$$

In search of simpler expressions, they have introduced the following plane-stress-like (PS) assumption: $\sigma_{33} = E_1 = E_2 = 0$. In doing so, they also discarded the equations for ε_{33} , D_1 , and D_2 from Eq. (1.20). They formed $\varepsilon^H = [\sigma_{11} \ \varepsilon_{22} \ 2\varepsilon_{23} \ \sigma_{13} \ 2\varepsilon_{12} \ D_3]^T$ and $\sigma^H = [\varepsilon_{11} \ \sigma_{22} \ \sigma_{23} \ 2\varepsilon_{13} \ \sigma_{12} \ E_3]^T$ to obtain

$$\bar{\varepsilon}^H = S^H \bar{\sigma}^H. \quad (1.62)$$

Finally, it is noted that assumptions similar to Eq. (1.55) have been applied to piezomagnetic homogenization of layered structures [74].

It is well known how the combination of piezoelectric rods in a soft matrix greatly enhances the performance of Case B devices [75, 76]. For example, d_h ($d_h = d_{13} + d_{23} + d_{33}$) is a common hydrostatic figure of merit. It can be greatly enhanced with a soft matrix between the rods. As for medical imaging applications, these composites are superior to monolithic piezoelectric material because the polymer, which is less dense than typical piezoceramics, enables greater acoustic impedance matching to water and living tissues. Therefore Smith and coworkers [77] utilized the uniform field assumptions

to find the effective stiffness, piezoelectric stress coefficient, and permittivity along the fiber axis of 1-3 composites. They did so with reduced constitutive equations and by assuming that the strain and electric field, respectively, are constant in the fiber direction. In the remaining two directions, the electric field was assumed to be zero and the normal stresses were equal in both phases. This approach was reported to yield a good agreement between experimental measures [75, 77].

1.3.3 Mean-Field Theories

Various so-called mean-field theories have been extended to the piezoelectric case. Following the classical Eshelbian solution [78], Dunn and Taya [79] assumed that the microstructure can be considered to be a single ellipsoidal inclusion in an infinite matrix. They provided the expressions for the Eshelby tensors. They extended the Dilute, self-consistent, Mori-Tanaka mean field approach ([80]), and the differential scheme. The Mori-Tanaka method has been used to homogenize bone in [81] (bones are slightly piezoelectric). See [37] for other uses. The Eshelbian approach can be completely analytical for cylindrical and spherical inclusions. However, numerical integration is required for more complicated inclusion geometries such as ellipsoidal inclusions [82].

1.3.4 Other Techniques and Aspects of Homogenization

Analytical Techniques

The so-called *series* and *parallel* models from strength of materials ideas were utilized in some research early on [64, 83, 84]. The effective properties were often calculated through simple formulas such as

$$Y^* = V^f Y^f + (1 - V^f) Y^m \quad \text{or} \quad \frac{1}{Y^*} = \frac{V^f}{Y^f} + \frac{1 - V^f}{Y^m} \quad (1.63)$$

for the elastic modulus. Concentric cylinder models for fiber composites were created in [85–87]. These models are only able to model loading along the fiber axis since

they assume an axisymmetric microstructure and local fields. The General Method of Cells [84, 88] is another homogenization technique. There it is supposed that the microstructure can be subdivided into rectangular parallelepipeds known as subcells. The theory is limited by the linear expansion of the displacement and electrical potential. Other approximate techniques include [89, 90].

Numerical Techniques

There are but a few other piezoelectric homogenization works that are documented here. Lenglet *et al* [72] utilized RVE analysis for the three normal stress cases and the Wave Propagation method for the three shear cases. The Element-free Galerkin method was developed by Eynbeygi and Aghdam [91] but a plane strain condition was assumed as well as $E_1 = E_2 = 0$. The Boundary Element Method was implemented in [92] but they utilized similar assumptions as Eynbeygi and Aghdam did. Multi-Physics Computational Grains was developed by Bishay et al [93]. It appears to be limited to microstructures that have a granular resemblance. The Multiple Scattering technique was utilized in [94], but their first-order theory was limited to low volume fractions. Some [95, 96] have utilized the FE method and Fast Fourier Transforms to find the effective properties of piezocomposites.

Homogenization of Polycrystalline Piezoelectrics

Some researchers [59, 93, 97] are interested in obtaining the overall piezoelectric response of polycrystalline ceramics. Although the microstructures they consider are typically made of the same material, they appear to be a heterogeneous medium because the local material coordinates can vary from crystal to crystal.

Piezoelectric Homogenization with Imperfections

Other researchers have examined the effects of various imperfections on the effective properties. Some have looked at imperfect interfaces are [57, 85, 92, 98] and others have examined the effect of porosity [79, 81, 93]. A hysteresis model was developed from experimental data in [99]. Since most piezoelectric materials are ceramic, studying the effect of cracks is crucial. See [100, 101] for various cracking effects on AFCs and MFCs; however, no homogenization was performed. The effect of cracks on the effective properties is considered in [102]. See also [103] for a crack model for piezoelectrics.

Piezomagneto Micromechanics

Some materials are not only piezoelectric but also magnetic. Barium Titanate is the most common example. Since both piezoelectric and piezomagnetic micromechanics theories are extensions from ordinary composites theories, the piezomagnetic theories are very similar to the methods discussed previously (see [74, 104–106]). An interesting finding from piezomagnetic homogenization is the presence of product properties. These are only present when certain materials are combined, but not present in the individual constituents.

1.4 Piezoelectric Smart Structures

As mentioned at the beginning of this chapter, piezoelectric materials have enabled numerous advances in smart structure technologies such as disturbance sensing, control of flexible structures, and energy harvesting. These applications often consist of piezoelectric material interacting with thin substrates known as host structures. Since piezoelectric material is often limited to small thicknesses due to voltage limitations, many research articles cover the use of various analytical models [107, 108] and plate/shell theories [25, 109–115] to predict macroscopic quantities of interest as

well as the local fields. The vibration of the host, tip deflection, and power generated are commonly sought.

The piezoelectric material in smart structures is often a ceramic material. Thus the brittle nature of monolithic piezoceramic layers hinders its application in various ways. Device handling and placement can be challenging; especially if the host is curved. Flexure of the host can also be very limited during operation. Thus, in practice, piezoelectric transducers come in the form of a patch that is adhered to the host. These patches can be described in terms of protective layers, electrode layers, and an active layer, where the piezoelectric resides. The protective layers are usually polyimide films such as Kapton. The electrode layers can either be uniform or IDEs. If they are uniform, it is possible that they are coated on to be a very thin layer. In which case, the mechanical effects of the electrode can be safely ignored. The IDE case consists of copper fibers that are thick enough that their mechanical effects should be considered. Finally, the active layer can consist of a monolithic piezoceramic layer, such as the Quick Pack [116].

Although the protective layers add some ductility, more damage tolerance and structural flexibility are usually required. Thus active layers are more commonly found to have piezoceramic fibers with epoxy between fibers. In which case, heterogeneity is introduced in the active layer and thus it is often homogenized for the methods mentioned above ([25, 107–115]) to work.

1.5 Multiscale Modeling of Macro Fiber Composites

The MFC has emerged as possibly the most popular piezoelectric patch. This is likely due to its commercialization, elastic flexibility, damage tolerance, and rectangular fibers (see Section 1.2.4). See Figure 1.7 for an illustration of the MFC and a demonstration of its structural compliance. The active layer of this patch is not monolithic but it does consist of fibers and epoxy. This idea was first introduced by Hagood and Bent [7] where they used round fibers surrounded by epoxy. The elec-

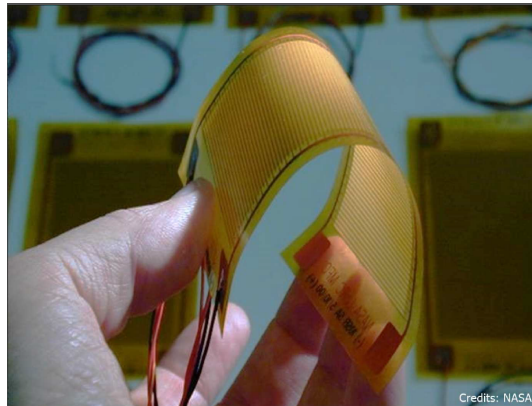


Figure 1.7: A macro-fiber composite and its structural flexibility. Photograph courtesy of NASA.

trodes utilized by Hagood and Bent were uniform; in which case the patch operated in d_{31} -mode. Later, Bent [71] replaced the uniform electrodes with IDEs and thus, the well known, AFC was created [17]. As mentioned in Section 1.2.4, the use of IDEs enabled the use of in-plane electric fields and therefore the more effective d_{33} -mode of the piezoceramic to be utilized in the plane of the actuator. The MFC was introduced by Wilki and his coworkers in the year 2000 [117]. It is similar to the AFC except that the AFC has cylindrical fibers. The use of rectangular fibers in the MFC allows for better electrical contact between the PZT and the electrodes and thus solving the problem of permittivity mismatch between the PZT and epoxy. this reduces the required actuation voltage. The use of rectangular fibers also simplified the handling and manufacturing of the PZT fibers since they may be cut from a PZT wafer. Thus the fiber layers in the MFC are the PZT fiber layer and the two electrodes layers. The electrode layers consist of interdigitated copper fibers that are orthogonal to the PZT fibers and epoxy. It is notable that the MFC has been commercialized [118] and is readily available in both d_{31} - or d_{33} -modes and at a variety of planar dimensions. Here and throughout the dissertation, the d_{33} mode is referred to as P1 (*eg* the P1 MFC) and the d_{31} -mode is called P2. This naming convention is adopted from the manufacturer [118].

Since the piezoelectric fibers do not span the overall length and width of the MFC patches, it is important to distinguish between what will be called the *Active Area* and the *Passive Area*. The Active Area consists of the length and width of the piezoelectric fiber array. It is illustrated in Figure 1.8. The Passive Area spans the remainder of the in-plane patch dimensions. It is important to note that micromechanical treatments of the MFC do not account for effects introduced by the Passive Area. It can be expected that the Passive Area will have negligible effects if it is much smaller than the Active Area. However, for small patches such as the M2503-P1, the effect is not well understood. In M2503-P1, the 25 refers to the active length being 25 mm, and the 03 refers to a 3 mm active width.

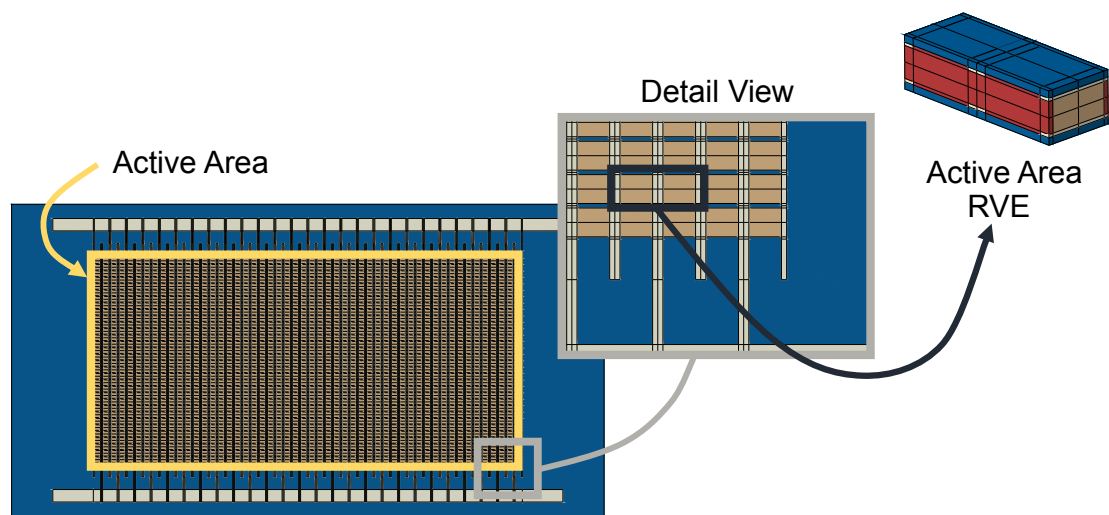


Figure 1.8: A rendering the MFC highlighting the Active Area and the Active Area RVE.

Although the MFC is available in the form of a convenient patch, analysis and design of structures with MFCs have many challenges to overcome. The principal challenge is overcoming the difference in length scale from the fibers and layer thicknesses to that of the host structures they are bonded to. Detailed modeling of the fibers is typically not practical and can be computationally prohibitive in most cases. Therefore, micromechanics should be invoked whereby small scale features are homogenized so that the macroscopic response of the system can be obtained without a cumbersome mesh.

Multiscale modeling of the MFC can be categorized into multilayer models and single layer models. The multilayer model first requires that only the fiber layers (*ie* active and electrode layers) be homogenized. These individual layer properties and thicknesses are usually inputted to a piezoelectric plate/shell analysis [9, 19, 47, 119–125]. The principal problem with this approach is that, from a micromechanics standpoint, homogenization is not applicable to the fiber layers, because doing so violates a fundamental assumption in micromechanics called the scale separation assumption. The violation occurs because the fiber layer thicknesses are of the same order of magnitude as the total MFC thickness. Furthermore, homogenization of the fiber layers introduces an artificial discontinuity that can adversely affect the macroscopic response as well as the local fields. Thus all of the constituents of the MFC must be homogenized simultaneously [2]. Another problem with this approach is that the plate models rely on various plate kinematics assumptions that will not give good results for relatively thick plates. It should be noted that piezoelectric plate models have not been readily accessible by researchers or engineers. Thus, in practice, thermomechanical plate models with a so-called thermal analogy can be used instead of a piezoelectric plate model [124–128]. Another approach that is commonly resorted to is a mechanical plate model with piezoelectric constitutive relations [123, 129, 130]. Both of these options model uncoupled piezoelectricity which can give actuation performance but not the sensing capability.

Plate kinematics assumptions can be avoided with a solid model of the MFC where solid elements discretize each fiber layer. Such an approach is not practical because the microscopic layer thicknesses would require an extraordinary number of elements. Practical solid models use homogenized properties of the full MFC layup like in [131–133]; not the homogenized properties of each layer. This approach is what is referred to as single layer model [123]. Of course, plate and beam models can also utilize homogenized properties of the full MFC layup but *ad hoc* kinematics assumptions are typically introduced [123, 128–130, 134–136].

The properties for this homogenization have been determined experimentally but only the most basic properties can be made available. Refer to the MFC manufacturer [118] and Ref. [137] for experimentally determined effective properties of the full MFC. Thus many have pursued applications of the micromechanical techniques reviewed here. It is also notable that both options have only homogenized the RVE of the Active Area as illustrated in Figure 1.8. Thus the effects of the surrounding Passive Area have been ignored. Thus, the following sections provide a thorough review of the micromechanics of MFCs. Attention is focused on finding the “device-level” properties of the full MFC when modeled as a single layer. Since the operating frequencies tend to be relatively low (*eg* 10-100 Hz for energy harvesting [133]), all of the approaches reviewed here model the electrical behavior with electrostatics. Thus, only real-valued permittivities are obtained.

1.6 Review: Analytical Homogenization of MFCs

Analytical models are highly attractive due to their low cost and ease of use. However, they compromise on accuracy. They require a two-step approach in which, like the aforementioned approaches, the first step violates the separation of scale assumption and introduces an artificial discontinuity. Furthermore, uniform polarization has been a preferred assumption. Thus further approximation is introduced for the P1

MFC since it has nonuniform poling. Note, however, that the nonuniform electric fields from the IDE can be obtained analytically via conformal mapping [138].

Major challenges for analytical methods to overcome are heterogeneity inside the fiber layers, heterogeneity due to the stacking of multiple dissimilar layers, and orthogonal fiber layers. This challenge exists because there is not a way for the analytical methods to homogenize fiber layers with differing fiber angles. Analyzing laminates with differing angles has been possible with Classical Laminated Plate Theory (CLPT) for example. Therefore, analytical homogenization of MFCs is performed in two steps as is illustrated in Figure 1.9. Each step corresponds to a homogenization of the constituent heterogeneities. Fiber and matrix constituents can be homogenized to form the fiber layers. The homogenized electrode layers must be rotated in-plane by 90° . Then these layers along with the protective layers need to be homogenized for the full packaged behavior. Of course, this approach is not unique to the MFC but has also been adapted from ordinary composites to handle more constitutive information and field variables. The extra information and variables have further complicated analytical homogenization and have possibly led some to seek simplifications where possible.

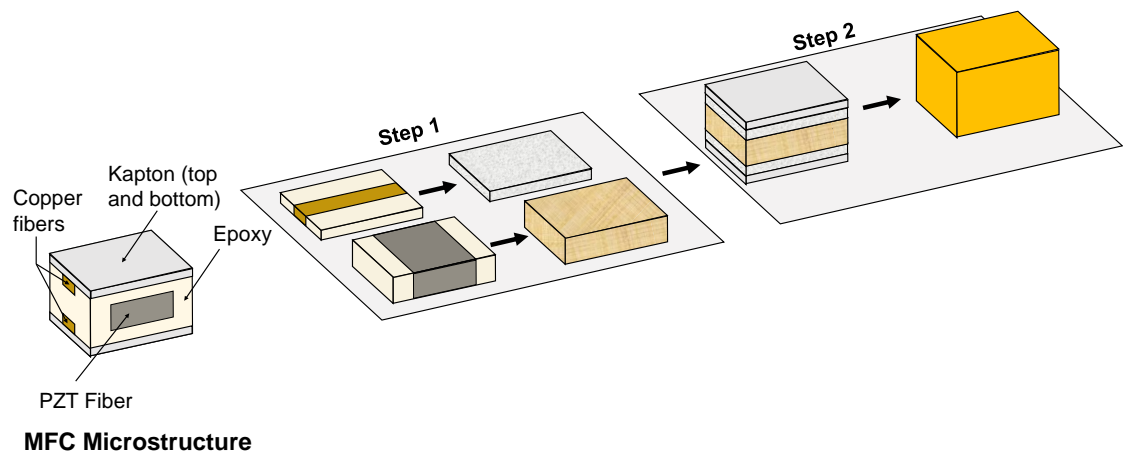
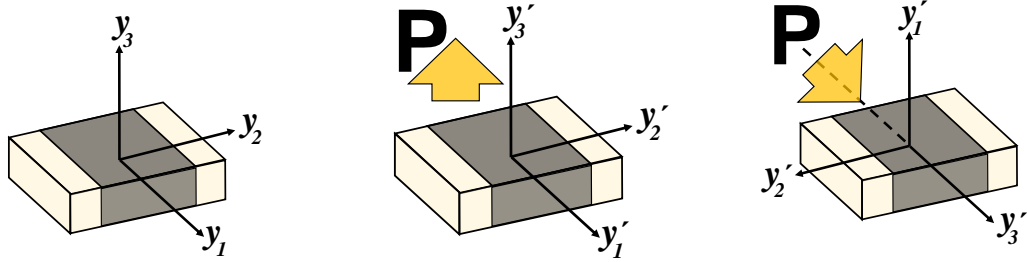


Figure 1.9: Two-Step homogenization for the Macro Fiber Composite.

In what follows is a review of the most popular analytical MFC homogenization approaches. It is separated into the corresponding homogenization steps. The assumptions on the field variables and some of their consequences are also documented.

Here and throughout this dissertation, homogenization at each step occurs in the problem coordinate system, y_i , as shown in Figure 1.10(a). However, the P1 MFC and P2 MFC have different polarization directions and, therefore, have different material coordinates. Note that only the active layer is shown in Figure 1.10 and that the P1 MFC is depicted with the uniform poling approximation. It is also notable that in this dissertation, Case A from Figure 1.6 always has the y_1 axis aligned with the fiber axis. Figure 1.10(b) and (c) show poling differences with the y'_i material coordinate system. Also, note that the y'_3 -direction is the poled direction as is common with piezoelectric materials. Since the problem and material coordinates for the P1 MFC are not identical, we transform the PZT constitutive properties to the problem coordinates before homogenization. Finally, take note that for Step-2 homogenization, the longitudinal axis of the piezoelectric fiber is in the direction of y_1 .



(a) Problem CS for both
P1 and P2 MFCs.

(b) Material CS: P2 MFC.

(c) Material CS: P1 MFC.

Figure 1.10: Relationship between problem coordinate system (CS) and the local PZT material CS for the MFC patch. y_i are the problem coordinates, y'_i are the material coordinates.

1.6.1 Step-1: Fiber Layer Homogenization

One must first homogenize the fibrous components of the MFC. That is, the PZT fiber and the epoxy matrix are homogenized into an equivalent solid to form the so-called *active layer*. Likewise, the copper fiber and the epoxy are homogenized to form the so-called *electrode layer*.

The HRM presented in Section 1.3.2 (a.k.a. Analytical Mixing Rules) are the most popular homogenization technique for the active and electrode layers. Recall that Deraemaeker and coworkers homogenized the active layer with the HRM with the assumptions in (1.60). They were the first to report Mixing Rules for the P2 MFC active layer in 2007 [47]. Also recall that, later [48], a PS assumption was utilized to search for simpler expressions. After performing volume averaging symbolically they report the following formulas for the effective electromechanical properties of the active layers

$$\begin{aligned}
 Y_1^* &= V^f Y_1^f + (1 - V^f) Y_1^m & \frac{1}{Y_2^*} &= \frac{V^f}{Y_2^f} + \frac{1 - V^f}{Y_2^m} \\
 \nu_{12}^* &= V^f \nu_{12}^f + (1 - V^f) \nu_{12}^m & \frac{1}{G_{12}^*} &= \frac{V^f}{G_{12}^f} + \frac{1 - V^f}{G_{12}^m} \\
 G_{13}^* &= V^f G_{13}^f + (1 - V^f) G_{13}^m & \frac{1}{G_{23}^*} &= \frac{V^f}{G_{23}^f} + \frac{1 - V^f}{G_{23}^m}
 \end{aligned} \tag{1.64}$$

$$\begin{aligned}
 d_{31}^* &= \frac{1}{Y_1^*} V^f d_{31}^f Y_1^f & d_{11}^* &= \frac{1}{Y_1^*} V^f d_{11}^f Y_1^f \\
 d_{32}^* &= -d_{31}^* \nu_{12}^* + V^f d_{31}^f (1 + \nu_{12}^f) & d_{12}^* &= -d_{11}^* \nu_{12}^* + V^f (d_{12}^f + d_{11}^f \nu_{12}^f) \\
 k_{33}^{\sigma*} &= V^f k_{33}^{\sigma f} + (1 - V^f) k_{33}^{\sigma m} & k_{11}^{\sigma*} &= V^f k_{11}^{\sigma f} + (1 - V^f) k_{11}^{\sigma m}.
 \end{aligned} \tag{1.65}$$

where Y , G , ν , and V^f denotes Young's modulus, shear modulus, Poisson's ratio, and fiber volume fraction respectively. Also, the superscript f is for the fiber and m is for the matrix. It is important to note that certain terms that they deemed to be minor were omitted from the equations for Y_2^* , $k_{11}^{\sigma*}$, and $k_{33}^{\sigma*}$. Due to the orientation of the PZT relative to the problem coordinate system, the equations d_{33}^* , d_{32}^* , and

$k_{33}^{\sigma*}$ apply to the P2 MFC and d_{11}^* , d_{12}^* and $k_{11}^{\sigma*}$ apply to the P1 MFC. It is also notable that the plane-stress (PS) assumption led to the absence of the transverse (through-the-thickness) properties of the homogenized fiber layers.

1.6.2 Step-2: Stack of Homogeneous Layer Methods

Once the homogenized layer properties are found, a low-order plate theory is often implemented to obtain the effective elastic properties of the MFC patch as in Ref. [9, 48, 139] and more recently in [123]. This approach treats the fiber layers and the isotropic Kapton layers as individual lamina. Ref. [9, 48, 139] utilized the CLPT. In doing so, all three of the Kirchhoff-Love assumptions were invoked and are:

1. The transverse normal is infinitely rigid along its own direction.
2. The transverse normal of the plate remains straight during deformation.
3. The transverse normal remains normal to the reference surface of the plate during deformation.

Furthermore, plane-stress is also assumed for each layer. Since the MFC can be considered as a symmetric stack of layers where the fiber layers were homogenized in Step-1, the overall in-plane MFC properties of the stack can be extracted from S_e^* below

$$S_e^* = hA^{-1} \quad A = \sum_{i=1}^N Q_i t_i \quad (1.66)$$

where h is the total MFC thickness, N is the total number of layers, t_i is the thickness of the i th layer, and Q_i is the plane-stress reduced stiffness matrix of the i th layer:

$$Q_i = \left[\begin{array}{ccc} S_{11}^E & S_{12}^E & S_{16}^E \\ S_{12}^E & S_{22}^E & S_{26}^E \\ S_{16}^E & S_{26}^E & S_{66}^E \end{array} \right]^{-1}_i \quad (1.67)$$

Even if the transverse effective properties were available from Step-1, here we observe that using the plane-stress reduced stiffness matrix in Step-2 leads to the absence of

the traverse effective mechanical properties (*ie*, Y_3^* , G_{23}^* , G_{13}^* , ν_{23}^* , and ν_{13}^*) for the stack of layers.

Li *et al* [123] was able to obtain the transverse shear moduli and the in-plane piezoelectric strain coefficients of the MFC stack of layers. The transverse shear moduli were obtained by using the First-Order-Shear-Deformation-Theory (FSDT) and thereby relaxing the third Kirchhoff-Love assumption. They concluded that

$$G_{23}^* = \langle G_{23} \rangle \quad G_{13}^* = \langle G_{13} \rangle \quad (1.68)$$

Note for composite laminates, the average through the thickness for any quantify f can be computed as

$$\langle f \rangle = \frac{1}{h} \int_{-\frac{h}{2}}^{\frac{h}{2}} f dy_3$$

If f is constant within each layer, we have

$$\langle f \rangle = \frac{1}{h} \sum_{i=1}^N f t_i$$

Also, note that unstarred quantities in Step-2 (*eg* G_{23}) correspond to the starred quantities obtained in Step-1 (*eg* G_{23}^*). The in-plane piezoelectric strain coefficients were found by using piezoelectric constitutive equations in the mechanical plate theory. This uncoupled approach does not allow for finding any permittivities.

Three problems with these analytical approaches have been identified.

1. The plate theories are not able to obtain the complete set of homogenized properties of the MFC. For the mechanical properties, all but Y_3^* , ν_{13}^* , and ν_{23}^* are available. For the electrical properties, only the in-plane piezoelectric strain coefficients are available.
2. Using FSDT questionable due to the large variability in the transverse shear stiffness from layer to layer.
3. Several researchers that have reported homogenized MFC properties from analytical methods [9, 48, 123] seem to have used the PS assumption twice. The

first instance occurs when using the PS assumption when homogenizing the electrode and PZT fiber layers. The second instance occurs when CLPT or FSDT.

A different methodology is given by Biscani *et al* [69]. They sequentially applied the uniform field assumption but they utilized the PS assumption, omitted the electrode layers, and found self-conflicting results.

1.7 Review: Numerical Homogenization of MFCs

To date, only RVE analysis with FEs has made One-Step homogenization of the MFC possible. Trindade and Benjeddou [51, 52] and Prasath and Arockiarajan [53–55, 70] are the few that have performed this type of analyses. The mechanical BCs presented by both groups is shown in Table 1.2 where m is an arbitrary constant.

Table 1.2: Periodic boundary conditions presented in the literature for the MFC.

BVP	X_1^-/X_1^+	X_2^-/X_2^+	X_3^-/X_3^+	Relation
1	$u_1^+ - u_1^- = m$	$u_2^+ - u_2^- = 0$	$u_3^+ - u_3^- = 0$	$C_{ij11}^{E*} = \bar{\sigma}_{ij}/\bar{\epsilon}_{11}$
2	$u_1^+ - u_1^- = 0$	$u_2^+ - u_2^- = m$	$u_3^+ - u_3^- = 0$	$C_{ij22}^{E*} = \bar{\sigma}_{ij}/\bar{\epsilon}_{22}$
3	$u_1^+ - u_1^- = 0$	$u_2^+ - u_2^- = 0$	$u_3^+ - u_3^- = m$	$C_{ij33}^{E*} = \bar{\sigma}_{ij}/\bar{\epsilon}_{33}$
4	$u_1^+ - u_1^- = 0$	$u_3^+ - u_3^- = m$	$u_2^+ - u_2^- = m$	$C_{2323}^{E*} = \bar{\sigma}_{23}/(2\bar{\epsilon}_{23})$
5	$u_3^+ - u_3^- = m$	$u_2^+ - u_2^- = 0$	$u_1^+ - u_1^- = m$	$C_{1313}^{E*} = \bar{\sigma}_{13}/(2\bar{\epsilon}_{13})$
6	$u_2^+ - u_2^- = m$	$u_1^+ - u_1^- = m$	$u_3^+ - u_3^- = 0$	$C_{1212}^{E*} = \bar{\sigma}_{12}/(2\bar{\epsilon}_{12})$
7	$u_1^+ - u_1^- = 0$	$u_2^+ - u_2^- = 0$	$u_3^+ - u_3^- = 0$	

Although, it appears that the mechanical PBCs have been systematically applied, the fact is that these are not PBCs by definition (Eq. (1.53)). The first issue is that only one mechanical degree of freedom (DOF) per boundary node was specified. Leaving the other two unspecified and it leaves a possibly for destroying periodicity. A second issue is that in Eq. (1.53), $\bar{\epsilon}_{ij}(y_j^+ - y_j^-)$ was replaced with arbitrary constants.

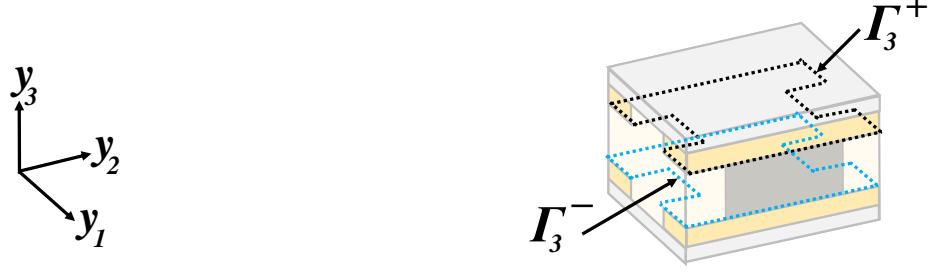


Figure 1.11: Electrode surfaces from [52] for the P2 MFCs.

It appears that only Trindade and Benjeddou have systematically applied the electrical PBCs (Eq. (1.54)) in all three spacial dimensions. Prasath and Arockiarajan used Eq. (1.54) sporadically. This destroys periodicity for the electrical potential for each BVP where it is omitted. The work of Trindade and Benjeddou is distinguished from methods reviewed in Section 1.3.1 in that, instead of applying Eq. (1.54) on X_3 , they accounted for internal electrodes by applying it to Γ_3 faces shown in Figure 1.11. Electrical BCs from Trindade and Benjeddou's work are thus reviewed in Table 1.3. Note that the eighth BVP is for obtaining the free permittivity where all the

Table 1.3: Periodic boundary conditions implemented in Ref. [52] for the P2 MFC.

BVP	X_1^-/X_1^+	X_2^-/X_2^+	X_3^-/X_3^+	Γ_3^+/Γ_3^-	Relation
1	$\phi^+ - \phi^- = 0$	$\phi^+ - \phi^- = 0$	—	$\phi^+ = 0; \phi^- = 0$	$e_{311}^* = \bar{D}_3/\bar{\epsilon}_{11}$
2	$\phi^+ - \phi^- = 0$	$\phi^+ - \phi^- = 0$	—	$\phi^+ = 0; \phi^- = 0$	$e_{322}^* = \bar{D}_3/\bar{\epsilon}_{22}$
3	$\phi^+ - \phi^- = 0$	$\phi^+ - \phi^- = 0$	—	$\phi^+ = 0; \phi^- = 0$	$e_{333}^* = \bar{D}_3/\bar{\epsilon}_{33}$
4	$\phi^+ - \phi^- = 0$	$\phi^+ - \phi^- = 0$	—	$\phi^+ = 0; \phi^- = 0$	
5	$\phi^+ - \phi^- = 0$	$\phi^+ - \phi^- = 0$	—	$\phi^+ = 0; \phi^- = 0$	
6	$\phi^+ - \phi^- = 0$	$\phi^+ - \phi^- = 0$	—	$\phi^+ = 0; \phi^- = 0$	
7	$\phi^+ - \phi^- = 0$	$\phi^+ - \phi^- = 0$	—	$\phi^+ = m; \phi^- = 0$	$k_{33}^{\epsilon*} = \bar{D}_3/\bar{E}_3$
8	$\phi^+ - \phi^- = 0$	$\phi^+ - \phi^- = 0$	—	$\phi^+ = m; \phi^- = 0$	$k_{33}^{\sigma*} = \bar{D}_3/\bar{E}_3$

mechanical PBCs are removed. These BCs are only applicable to the P2 MFC since the predominant electrical behavior is through the thickness. None of the issues with their mechanical BCs apply here since the electrical potential is a scalar and since equipotential conditions were also applied. The issue here is with the post-processing relations of the piezoelectric stress coefficients. They originate from

$$\bar{D}_i = e_{ikl}^* \bar{\varepsilon}_{kl} + k_{ik}^* \bar{E}_k \quad (1.69)$$

in Eq. (1.51). However, no mention was made as to whether utilizing

$$\bar{\sigma}_{ij} = C_{ijkl}^{E*} \bar{\varepsilon}_{kl} - e_{kij}^* \bar{E}_k \quad (1.70)$$

provides equivalent results. It is possible that the definition of Γ breaks the uniqueness of the properties obtained.

Prasath and Arockiarajan modeled both the P1 and P2 MFC full stack of layers. Nonuniform electric fields were able to be considered. However, since there is no mention of the polarization direction, it assumed here that uniform polarization was utilized. Thus, nonuniform polarization *and* nonuniform electric fields RVE analysis for the P1 MFC full stack of layers has not been solved. It has, however, been solved for the active layer alone in [49].

A final issue is that there is disagreement on which volume to utilize in order to compute the volume averages of the electric field and electric displacement. Trindade and Benjeddou utilized the full RVE volume whereas, Prasath and Arockiarajan only utilized the volume of the active layer. It is not clear which one is correct.

Ignoring Protective Films

Numerical techniques have also been applied to the active layer. While assuming three-dimensional periodicity, Biscani *et al* [31] homogenized the active layer of the P2 MFC with MHT. RVE analysis has predominately been used to verify analytical mixing rules [47–49]. Deraemaeker and Nasser [49] performed an RVE analysis that respected the aperiodicity through the thickness and the nonuniform electrical

fields and poling of the P1 MFC. A few shortcomings of their work are discussed here. The properties obtained with their approach are incomplete since they relied on the plane stress assumption. They removed the in-plane mechanical PBCs for the actuator BVP. Instead, they let the displacement DOFs equal zero for the in-plane RVE boundaries. No comment could be found on the uniqueness of the properties they obtained. As with all other uses of the PBCs in Eq. (1.53) - (1.54), it appears that they assumed $\bar{\varepsilon}_{ij}$ *a priori*. Thus there is no guarantee that the piezoelectric macrohomogeneity is satisfied.

1.8 Dissertation Motivation: Towards Improved Micromechanical Analysis of Piezocomposite Patches with the Mechanics of Structure Genome

A new homogenized model of the MFC is needed to improve smart-structure predictions and, therefore, improved device design without explicitly modeling the microscopic details of the MFC. The critical review of current MFC homogenization revealed that all of the constituents of the MFC should be homogenized simultaneously; in a One-Step method. It is noted here that the fully periodic assumption, common to all One-Step methods reviewed here, should be eliminated to account for the reality of 2D periodicity of the Active Area. Furthermore, there is a need for a One-Step method for the P1 MFC that accounts for both nonuniform poling and nonuniform electric fields. Lastly, since the Active Area is 2D periodic, the PBCs need to be rectified so that periodicity of the local fields is guaranteed. This should also guarantee that the effective properties obtained are as realistic as possible. Note that after creating a free account on cdmhub.org, many scripts used to create the results in this work can be downloaded from <https://cdmhub.org/projects/ernestocamarena>.

It is expected that MSG can be utilized to accomplish this and so obtain all of its advantages. However, like almost all of the techniques reviewed in Section 1.3.1, MSG was not formulated to treat the internal electrodes of the MFC. So neither an MSG piezoelectric solid model of the MFC nor an MSG piezoelectric plate model is possible.

In pursuing this solution, it was deemed necessary to first obtain a piezoelectric solid model. As such, no plate models were developed here. Instead, some groundwork is laid with an MSG analytical solution and an RVE analysis for future MSG advances.

1.8.1 MSG Analytical

The research reported here aims to improve analytical homogenization of the MFC 3D solid model by:

- Avoiding any assumptions on the field variables where possible by modifying MSG to homogenize active material embedded among passive material.
- Providing updated fiber layer properties that avoid the PS assumption.
- Obtaining the complete set of effective electromechanical properties of MFCs (stack of layers).

Since the approach proposed here does not make use of assumptions on the field variables, we assess how plate kinematics assumptions from CLPT and FSDT affect the effective properties they provide. We also examine how using the PS assumptions and dropping terms in Step-1 affects homogenization in Step-2. To our knowledge, no one has reported the effect of these assumptions and simplifications. These examinations are extended to volume fractions other than that of the MFC since no restrictions on their use were reported. For the sake of an analytical solution, we accept the uniform poling assumption and violate the separation of scale assumption.

The analytical model was also sought to provide insight on what the electrical behavior of a homogenized solid with internal electrodes should be. This is recognized to clarify the conflicting domains used by others [51–55, 70] for volume averages in MFC RVE analyses. The proposed electrical behavior is verified with a 3D finite element model of the MFC patch.

1.8.2 RVE Analysis for In-plane Periodic Piezocomposite Patches

Of the reviewed literature, the One-Step RVE analyses had periodic boundary conditions for the mechanical displacement on X_3 . It is expected that these conditions best represent the bulk behavior of many MFCs that are stacked together. However, neither the MFC active layer nor the full MFC is periodic in the thickness direction. 2D periodicity is closer to reality and is illustrated in Figure 1.12.

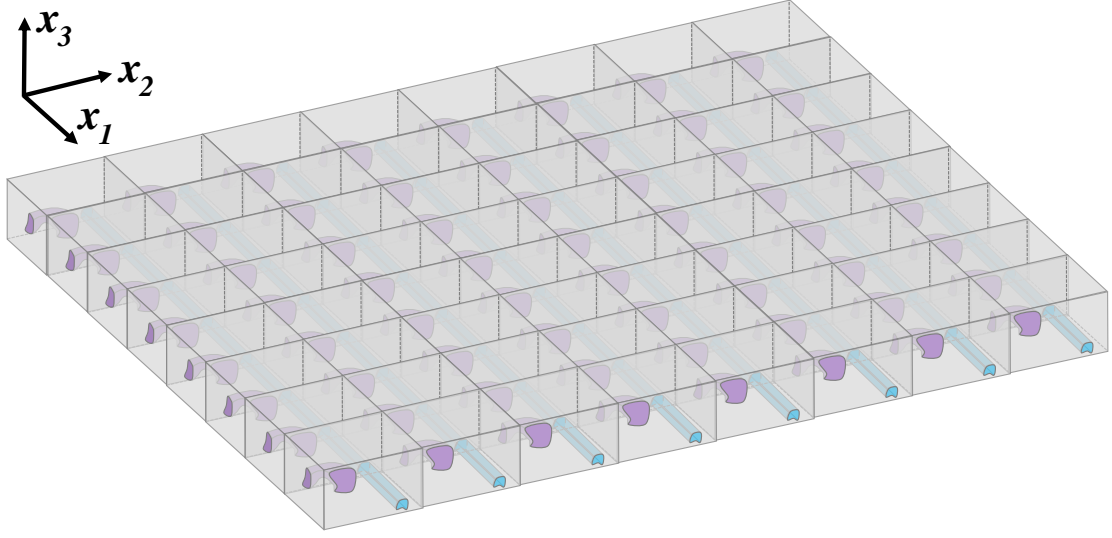


Figure 1.12: A generic composite that features periodicity in two dimensions.

Therefore this dissertation challenges the idea that the MFC can be correctly homogenized assuming full periodicity. This challenge is not new because a few researchers have already studied the effect of device thickness on effective properties. As already mentioned, Deraemaeker and Nasser [49] realized that the MFC is not periodic through-the-thickness. In their RVE analysis, they followed Berger *et al* [36] but relaxed the associated periodicity requirement and utilized the plane-stress assumption; leading to incomplete properties. This may not be an issue when these properties are utilized in plate theories that assume plane stress. However, a failure analysis will not be possible since some of the local fields will not be available. It is

also noteworthy that Liu *et al* [140] has derived the aperiodic capability in MSG, but only for the mechanical properties.

Aperiodicity has also been considered for the effective piezoelectric properties of ultrasonics by Li and Sottos [85]. They obtained a series solution by solving an axisymmetric elasticity problem that considers two concentric cylinders which are subjected to hydrostatic tractions. Rajapakse and Chen [87] observed that Li and Sottos decoupled the electroelastic field by assuming constant electric field in the rod. Rajapakse and Chen improved upon Li and Sottos' model by relaxing the constant electric field assumption. An important issue with these models is the hydrostatic boundary conditions. In applying hydrostatic boundary conditions to the concentric cylinders, one is assuming that the boundary conditions of the microstructure (*ie* the concentric cylinders) are the same as that of the macroscopic body (*ie* the hydrophone underwater.) Another issue arises from assuming axisymmetric fields because it can only correctly describe one of possibly six (three normal and three shear strains) deformation modes of an axisymmetric microstructure. Qi and Cao [40] have taken a different approach by utilizing the FE method. An issue with their approach is that they used “fixed” boundary conditions on the in-plane faces of their unit-cell model. There is no reason for these boundary conditions to resemble reality.

Not only does this work depart from full periodicity it does so without any of the previously stated issues for piezoelectric RVE analyses. The common pitfalls that occur when using the PBCs (Eq. (1.53) and (1.54)) are all circumvented; namely, using uniform BCs, assuming $\bar{\varepsilon}_{ij}$ and \bar{E}_i , sporadic implementation, and overlooking the symmetry of the effective properties. Various proofs are provided for determining the volume averages of the variables needed for the RVE analysis. The significance of the proofs is that they are done at a theoretical level which enables the application to any such RVE.

1.8.3 Local Fields Recovery

Homogenization is a necessary precursor to recovering the local fields after completing a macroscopic analysis. Of the reviewed literature, a dehomogenization procedure of piezoelectric composite patches was not found. Some [28,91,141,142] however, have studied local fields of piezocomposites but their approach is not applicable to the full MFC patch due to its electrodes. Therefore, an objective of this work was to find the local fields of the MFC without having the computational burden of fully discretizing the MFC. This should enable smart-structure designs with improved reliability because the computationally efficient dehomogenization model facilitates failure studies.

1.8.4 Direct Numerical Simulations

As mentioned in Section 1.1, there are two objectives in micromechanics; homogenization and dehomogenization. Here, numerical tests are constructed to verify the theories presented in this dissertation. While physical experiments would be best for validation purposes, numerical tests are best for verification since there will be no differences associated with boundary conditions, uncaptured physics, and microstructural uncertainty in general. The numerical tests consist of constructing macroscopic 3D FEA models that include microscale features. Needless to say, the models can be quite large. Furthermore, some of these models were constructed with and without the Passive Area to evaluate any accuracy loss for different patch sizes. Here these models are referred to as direct numerical simulations (DNSs). The DNSs considered herein are static models of a single MFC that is perfectly bonded to a nonpiezoelectric substrate (unimorph). For the P1 cases, nonuniform poling and electric fields are accounted for in the DNSs. Results from using the effective properties predicted in Chapters 2 and 4, common MFC modeling strategies, as well as the proposed dehomogenization procedure, are all evaluated against the DNSs. Completing these DNSs is a significant undertaking. According to the best knowledge of the author, no such

modeling and simulation have been previously completed. The only other work that is related in by Kim *et al* [143]. They showcase the utility of constructing DNSs with several example cases. One case was the AFC. Although this work recognized the presence of a passive area (similar to by not the same as the Passive Area used herein), the constructed DNS relied on some major approximations. Their formulation is apparently an uncoupled piezoelectric analysis. Also, the electric field was not defined as the negative gradient of the potential. Instead, a uniform field definition was used. Since poling was not mentioned, uniform poling was likely to have been assumed. Finally, the IDEs were omitted from the analysis and E-glass substrates were modeled as isotropic.

2. ANALYTICAL HOMOGENIZATION OF THE MFC

2.1 Piezoelectric Homogenization with Mechanics of Structure Genome

It is proposed that the newly discovered mechanics of structure genome (MSG) [1,3], can provide an improvement in the homogenized properties of the MFC. For the Two-Step approach discussed before, MSG can provide a full set of electromechanical properties analytically and without the assumptions associated with a low-order plate theory.

The scope of this research assumes that the starting point is the full, linear, constitutive relations for each constituent in the MFC microstructure as

$$\begin{aligned}\sigma_{ij} &= C_{ijkl}^E \varepsilon_{kl} - e_{kij} E_k \\ D_i &= e_{ikl} \varepsilon_{kl} + k_{ik}^\varepsilon E_k.\end{aligned}\tag{2.1}$$

Here C_{ijkl}^E , e_{ijk} , and k_{ij}^ε denote the elasticity (at constant electric field), piezoelectric, and dielectric permittivity (at constant strain) tensors. The end point considered herein is the homogenized linear-elastic and piezoelectric properties of the full MFC package. Here and through the rest of this article, index notation is used with Latin indices assuming 1, 2, and 3 and repeated indices are summed over their range (except where explicitly indicated).

First, the homogenized body is described using x_i . Since it is expected that the size of the microstructure is much smaller than the size of the macroscopic structure, local coordinates $y_i = x_i/\epsilon$ are introduced to describe the domain occupied by the microstructure, with ϵ being a small parameter. The mechanical displacement and electric potential fields of the original heterogeneous body can be expressed as

$$\begin{aligned}u_i(x_k, y_l) &= \bar{u}_i(x_k) + \epsilon \chi_i(x_k, y_l) \\ \phi(x_k, y_l) &= \bar{\phi}(x_k) + \epsilon \zeta(x_k, y_l)\end{aligned}\tag{2.2}$$

respectively. Here the over bar is again the average respective field quantity over the microstructure and χ_i and ζ are what one commonly calls fluctuating functions in micromechanics. They are the difference between the corresponding field average and the exact field. Then, from Eqs. (1.6) and (1.5), we can obtain the strain and electric field of the heterogeneous body as

$$\varepsilon_{ij}(x, y) = \bar{\varepsilon}_{ij}(x) + \chi_{(i,j)} \quad E_i = \bar{E}_i - \zeta_{,i} \quad (2.3)$$

respectively. Note that the higher order terms have been neglected according to the variational asymptotic method [22]. The parenthesis in the subscripts indicates a symmetric operation and a comma indicates differentiation: $\chi_{(i,j)} = \frac{1}{2} \left(\frac{\partial \chi_i}{\partial y_j} + \frac{\partial \chi_j}{\partial y_i} \right)$, and $\zeta_{,i} = \frac{\partial \zeta}{\partial y_i}$.

Since we are constructing the homogenized model out of the original heterogeneous model, we need to define the variables of the homogenized model in terms of those of the original model. The natural choice is to define

$$\bar{u}_i = \langle u_i \rangle \quad \bar{\varepsilon}_{ij} = \langle \varepsilon_{ij} \rangle \quad \bar{\phi} = \langle \phi \rangle \quad \bar{E}_i = \langle E_i \rangle. \quad (2.4)$$

Eq. (2.3) and (2.4) imply the following constraints on the fluctuating functions

$$\langle \chi_i \rangle = 0 \quad \langle \chi_{(i,j)} \rangle = 0 \quad \langle \zeta \rangle = 0 \quad \langle \zeta_{,i} \rangle = 0. \quad (2.5)$$

For a linear piezoelectric material, the information loss we want to minimize can be the electric enthalpy (see [144] for piezoelectric enthalpy definition). Thus we seek to minimize the difference between the electric enthalpy of the original model and the homogenized model which is

$$\begin{aligned} \Pi = & \left\langle \frac{1}{2} C_{ijkl}^E \varepsilon_{ij} \varepsilon_{kl} - e_{ijk} E_i \varepsilon_{jk} - \frac{1}{2} k_{ij}^\varepsilon E_i E_j \right\rangle \\ & - \left(\frac{1}{2} C_{ijkl}^{E*} \bar{\varepsilon}_{ij} \bar{\varepsilon}_{kl} - e_{ijk}^* \bar{E}_i \bar{\varepsilon}_{jk} - \frac{1}{2} k_{ij}^{\varepsilon*} \bar{E}_i \bar{E}_j \right). \end{aligned} \quad (2.6)$$

The asterisk denotes the corresponding tensors of the homogenized body. To minimize Π , we consider the homogenized model as given (ie, C_{ijkl}^{E*} , e_{ijk}^* , $k_{ij}^{\varepsilon*}$, $\bar{\varepsilon}_{ij}$, and \bar{E}_i cannot

be varied). Substituting Eq. (2.3) into Eq. (2.6), we obtain the following variational statement to solve for χ_i and ζ .

$$\min_{(\chi_i, \zeta) \in \text{Eq. (2.5)}} \left\langle \frac{1}{2} C_{ijkl}^E (\bar{\varepsilon}_{ij} + \chi_{(i,j)}) (\bar{\varepsilon}_{kl} + \chi_{(k,l)}) - e_{ijk} (\bar{E}_i - \zeta_{,i}) (\bar{\varepsilon}_{jk} + \chi_{(j,k)}) - \frac{1}{2} k_{ij}^\varepsilon (\bar{E}_i - \zeta_{,i}) (\bar{E}_j - \zeta_{,j}) \right\rangle \quad (2.7)$$

Recall that a unique feature of the MFC that makes it a durable and effective transducer is that the electrodes are located *inside* the microstructure. This is not the case for ordinary transducers that have surface mounted electrodes. Thus, the variational statement that is shown in Eq. (2.7) is split into two integrations through the active and passive domains respectively as

$$\min_{(\chi_i, \zeta) \in \text{Eq. (2.5)}} \langle \Pi_{\text{Passive}} \rangle + \langle \Pi_{\text{Active}} \rangle \quad (2.8)$$

with

$$\Pi_{\text{Passive}} = \frac{1}{2} C_{ijkl}^E (\bar{\varepsilon}_{ij} + \chi_{(i,j)}) (\bar{\varepsilon}_{kl} + \chi_{(k,l)}) \quad (2.9)$$

and

$$\Pi_{\text{Active}} = \frac{1}{2} C_{ijkl}^E (\bar{\varepsilon}_{ij} + \chi_{(i,j)}) (\bar{\varepsilon}_{kl} + \chi_{(k,l)}) - e_{ijk} (\bar{E}_i - \zeta_{,i}) (\bar{\varepsilon}_{jk} + \chi_{(j,k)}) - \frac{1}{2} k_{ij}^\varepsilon (\bar{E}_i - \zeta_{,i}) (\bar{E}_j - \zeta_{,j}). \quad (2.10)$$

Here the word *active* denotes electrically active and not necessarily piezoelectric. For example, a non-piezoelectric material can be between the electrodes. Likewise, *passive* means that electrical effects are not accounted for.

Using the calculus of variations, we can conclude that χ_i must satisfy the following three Euler-Lagrange equations in the passive domain

$$(C_{ijkl}^E (\bar{\varepsilon}_{kl} + \chi_{(k,l)}))_{,j} = 0. \quad (2.11)$$

Next, ζ , as well as χ_i , must satisfy the following four Euler-Lagrange equations in the active domain

$$\begin{aligned} (C_{ijkl}^E (\bar{\varepsilon}_{kl} + \chi_{(k,l)}) - e_{kij} (\bar{E}_k - \zeta_{,k}))_{,j} &= 0 \\ (e_{ikl} (\bar{\varepsilon}_{kl} + \chi_{(k,l)}) + k_{ik}^\varepsilon (\bar{E}_k - \zeta_{,k}))_{,i} &= 0 \end{aligned} \quad (2.12)$$

along with the constraints in Eq. (2.5). Additional constraints that must be considered are boundary and interface conditions. For periodic materials that are fully active, χ_i and ζ must be periodic on the domain boundaries. At the interface between adjacent constituents, we require that the displacement and electrical potential be continuous. This implies that the fluctuating functions are also continuous.

2.2 Stack of Homogeneous Layers

Until now, nothing has been mentioned about what the original heterogeneous structure is. In this chapter we specialize the application of MSG to consider that the microstructure is a multi-layer laminate; each layer being homogeneous. Each layer is linearly elastic and possibly anisotropic. One layer is considered to be linear piezoelectric. The governing differential equations in Eq. (2.11) – (2.12) can be solved analytically for this special case. Therefore homogenization of the fiber layers in a prior step is required. Since an analytical solution is a highly desirable model, violation of the separation of scale requirement is accepted and uniform polarization for the P1 MFC is assumed.

Let us use y_1 and y_2 to denote the in-plane coordinates and y_3 to denote the thickness coordinate. Because the composite laminate is uniform in the $y_1 - y_2$ plane and heterogeneous along y_3 direction, χ_i and ζ are functions of y_3 only, that is, the partial derivatives of the fluctuating functions, $\chi_{i,j}$ and $\zeta_{,i}$, will vanish except $\chi_{i,3}$ and $\zeta_{,3}$. As shown in Figure 2.1, let the laminate be defined from $-h_3/2 \leq y_3 \leq h_3/2$ and let the active layer go from $-h_a/2 \leq y_3 \leq h_a/2$ (with $h_a \leq h_3$). The governing differential equation in Eq. (2.11) can then be simplified to the following

$$(C_{i3kl}^E (\bar{\varepsilon}_{kl} + \chi_{k,l}))_{,3} = 0 \quad -\frac{h_3}{2} \leq y_3 < -\frac{h_a}{2} \quad \text{and} \quad \frac{h_a}{2} < y_3 \leq \frac{h_3}{2} \quad (2.13)$$

and Eq. (2.12) becomes

$$\left. \begin{aligned} (C_{i3kl}^E (\bar{\varepsilon}_{kl} + \chi_{k,l}) - e_{ki3} (\bar{E}_k - \zeta_{,k}))_{,3} &= 0 \\ (e_{3kl} (\bar{\varepsilon}_{kl} + \chi_{k,l}) + k_{3k}^\varepsilon (\bar{E}_k - \zeta_{,k}))_{,3} &= 0 \end{aligned} \right\} -\frac{h_a}{2} \leq y_3 \leq \frac{h_a}{2}. \quad (2.14)$$

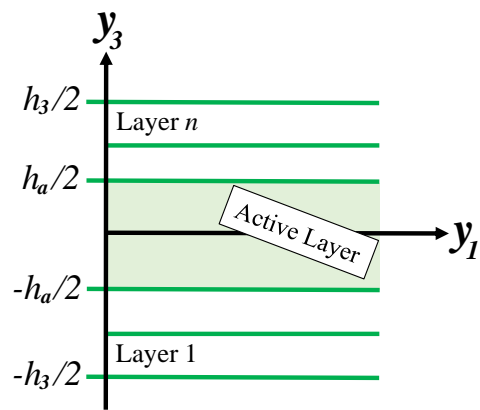


Figure 2.1: The domain of the active region and that of the full laminate.

We assume that the layers within and MFC are perfectly bonded, thus

$$[\chi_i] = 0 \quad \text{at every interface} \quad (2.15)$$

where $[\]$ indicates the jump across an interface. Using the calculus of variations, we can conclude that

$$[\sigma_{i3}] = 0 \quad \text{at every interface.} \quad (2.16)$$

Using Eq. (2.5) along with the interface continuity conditions of Eq. (2.15) and (2.16), we conclude

$$\chi_k \left(y_1, y_2, -\frac{h_3}{2} \right) = \chi_k \left(y_1, y_2, \frac{h_3}{2} \right) \quad (2.17)$$

$$\sigma_{i3} \left(y_1, y_2, -\frac{h_3}{2} \right) = \sigma_{i3} \left(y_1, y_2, \frac{h_3}{2} \right). \quad (2.18)$$

We then integrate Eq. (2.13) – (2.14) through an arbitrary layer in their respective domains and obtain

$$\left. \begin{aligned} C_{i3kl}^E (\bar{\varepsilon}_{kl} + \chi_{k,l}) &= m_i & -\frac{h_3}{2} \leq y_3 < -\frac{h_a}{2} & \text{ and } \frac{h_a}{2} < y_3 \leq \frac{h_3}{2} \\ C_{i3kl}^E (\bar{\varepsilon}_{kl} + \chi_{k,l}) - e_{ki3} (\bar{E}_k - \zeta_{,k}) &= c_i \\ e_{3kl} (\bar{\varepsilon}_{kl} + \chi_{k,l}) + k_{3k}^\varepsilon (\bar{E}_k - \zeta_{,k}) &= c_4 \end{aligned} \right\} -\frac{h_a}{2} \leq y_3 \leq \frac{h_a}{2} \quad (2.19)$$

where m_i are three constants for each layer in the passive region and c_i and c_4 are four constants for each layer in the active layer. Explicitly Eq. (2.19) reads

Passive :

$$\begin{aligned}
& C_{1311}^E \bar{\varepsilon}_{11} + C_{1322}^E \bar{\varepsilon}_{22} + 2C_{1312}^E \bar{\varepsilon}_{12} + C_{1333}^E (\bar{\varepsilon}_{33} + \chi_{3,3}) \\
& + C_{1313}^E (2\bar{\varepsilon}_{13} + \chi_{1,3}) + C_{1323}^E (2\bar{\varepsilon}_{23} + \chi_{2,3}) = m_1 \\
& C_{2311}^E \bar{\varepsilon}_{11} + C_{2322}^E \bar{\varepsilon}_{22} + 2C_{2312}^E \bar{\varepsilon}_{12} + C_{2333}^E (\bar{\varepsilon}_{33} + \chi_{3,3}) \\
& + C_{2313}^E (2\bar{\varepsilon}_{13} + \chi_{1,3}) + C_{2323}^E (2\bar{\varepsilon}_{23} + \chi_{2,3}) = m_2 \\
& C_{3311}^E \bar{\varepsilon}_{11} + C_{3322}^E \bar{\varepsilon}_{22} + 2C_{3312}^E \bar{\varepsilon}_{12} + C_{3333}^E (\bar{\varepsilon}_{33} + \chi_{3,3}) \\
& + C_{3313}^E (2\bar{\varepsilon}_{13} + \chi_{1,3}) + C_{3323}^E (2\bar{\varepsilon}_{23} + \chi_{2,3}) = m_3
\end{aligned}$$

Active :

$$\begin{aligned}
& C_{1311}^E \bar{\varepsilon}_{11} + C_{1322}^E \bar{\varepsilon}_{22} + 2C_{1312}^E \bar{\varepsilon}_{12} + C_{1333}^E (\bar{\varepsilon}_{33} + \chi_{3,3}) \\
& + C_{1313}^E (2\bar{\varepsilon}_{13} + \chi_{1,3}) + C_{1323}^E (2\bar{\varepsilon}_{23} + \chi_{2,3}) \\
& - e_{113} \bar{E}_1 - e_{213} \bar{E}_2 - e_{313} (\bar{E}_3 - \zeta_{,3}) = c_1 \\
& C_{2311}^E \bar{\varepsilon}_{11} + C_{2322}^E \bar{\varepsilon}_{22} + 2C_{2312}^E \bar{\varepsilon}_{12} + C_{2333}^E (\bar{\varepsilon}_{33} + \chi_{3,3}) \\
& + C_{2313}^E (2\bar{\varepsilon}_{13} + \chi_{1,3}) + C_{2323}^E (2\bar{\varepsilon}_{23} + \chi_{2,3}) \\
& - e_{123} \bar{E}_1 - e_{223} \bar{E}_2 - e_{323} (\bar{E}_3 - \zeta_{,3}) = c_2 \\
& C_{3311}^E \bar{\varepsilon}_{11} + C_{3322}^E \bar{\varepsilon}_{22} + 2C_{3312}^E \bar{\varepsilon}_{12} + C_{3333}^E (\bar{\varepsilon}_{33} + \chi_{3,3}) \\
& + C_{3313}^E (2\bar{\varepsilon}_{13} + \chi_{1,3}) + C_{3323}^E (2\bar{\varepsilon}_{23} + \chi_{2,3}) \\
& - e_{133} \bar{E}_1 - e_{233} \bar{E}_2 - e_{333} (\bar{E}_3 - \zeta_{,3}) = c_3 \\
& e_{311} \bar{\varepsilon}_{11} + e_{322} \bar{\varepsilon}_{22} + 2e_{312} \bar{\varepsilon}_{12} + e_{333} (\bar{\varepsilon}_{33} + \chi_{3,3}) \\
& + e_{313} (2\bar{\varepsilon}_{13} + \chi_{1,3}) + e_{323} (2\bar{\varepsilon}_{23} + \chi_{2,3}) \\
& + k_{31}^\varepsilon \bar{E}_1 + k_{32}^\varepsilon \bar{E}_2 + k_{33}^\varepsilon (\bar{E}_3 - \zeta_{,3}) = c_4.
\end{aligned}$$

It is clear that

$$\sigma_{i3} = \begin{cases} C_{i3kl}^E (\bar{\varepsilon}_{kl} + \chi_{k,l}) & -\frac{h_3}{2} \leq y_3 < -\frac{h_a}{2} \quad \text{and} \quad \frac{h_a}{2} < y_3 \leq \frac{h_3}{2} \\ C_{i3kl}^E (\bar{\varepsilon}_{kl} + \chi_{k,l}) - e_{ki3} (\bar{E}_k - \zeta_{,k}) & -\frac{h_a}{2} \leq y_3 \leq \frac{h_a}{2}. \end{cases} \quad (2.20)$$

Thus we can conclude from Eq. (2.16) and (2.18) – (2.20) that the transverse shear and normal stresses are constant through the thickness. That is, $m_i = c_i$ and remain constant for all the layers. It is also clear that

$$D_3 = e_{3kl} (\bar{\varepsilon}_{kl} + \chi_{k,l}) + k_{3k}^{\varepsilon} (\bar{E}_k - \zeta_{,k}) = c_4 \quad -\frac{h_a}{2} \leq y_3 \leq \frac{h_a}{2}. \quad (2.21)$$

Thus the transverse electric displacement is constant in the active layer.

Recall that for a multi-layered laminate the non-vanishing derivatives of the fluctuating functions are $\chi_{i,3}$ and $\zeta_{,3}$. Thus from Eq. (2.3) the local strain is fully described by

$$\begin{aligned} \varepsilon_{11} &= \bar{\varepsilon}_{11} & \varepsilon_{22} &= \bar{\varepsilon}_{22} & \varepsilon_{12} &= \bar{\varepsilon}_{12} \\ \varepsilon_{33} &= \bar{\varepsilon}_{33} + \chi_{3,3} & \varepsilon_{13} &= \bar{\varepsilon}_{13} + \chi_{1,3} & \varepsilon_{23} &= \bar{\varepsilon}_{23} + \chi_{2,3} \end{aligned} \quad (2.22)$$

and the local electric field is

$$E_1 = \bar{E}_1 \quad E_2 = \bar{E}_2 \quad E_3 = \bar{E}_3 - \zeta_{,3}. \quad (2.23)$$

Note, here, that average strains are with respect to a volume occupied by the active and passive domains and the average electric field is with respect to the volume of the active region. Thus the implications are that the in-plane strains are constant and the transverse strains are piecewise constant through the thickness if we would like to approximate a stack of composite laminates as an equivalent homogeneous solid. In the active region alone we have that the in-plane electric fields are constant and the transverse electric field is piecewise constant if the active region has multiple layers. With this conclusion, along with the previous conclusions about the transverse stresses and electric displacement, we can derive a Step-2 hybrid rule of mixtures for MFCs. Note that this is similar to Eq. (1.55) from Hashimoto and Yarnaguchi's [63] conclusion.

It is noted here that Yu [145] and Rique *et al* [146] applied a similar approach for purely mechanical and thermoelastic properties, respectively. Here, however, we have piezoelectricity and internal electrodes.

Lemma 1: For Step-1 Homogenization

We can also derive the same conclusions for a stack of homogeneous layers, with all layers being electrically active; regardless of whether they are piezoelectric or not. If we let $h_a = h_3$, then Π_{Active} is for the full domain.

Thus we conclude from Eq. (2.19) - (2.21) and Eq. (2.27) that transverse shear and normal stresses are constant through the entire thickness of the laminate as well as the transverse electric displacement. When there are no electrodes between each layer, each interface has an absence of free charges. Thus the electric potential must be continuous across the interfaces and therefore we have

$$[\zeta] = 0 \quad \text{at every interface.} \quad (2.24)$$

Then following the calculus of variations, we can conclude that

$$[D_3] = 0 \quad \text{at every interface.} \quad (2.25)$$

Using the constraint in Eq. (2.5) along with the interface continuity conditions in Eq. (2.24) and (2.25), we can conclude

$$\zeta \left(y_1, y_2, -\frac{h_3}{2} \right) = \zeta \left(y_1, y_2, \frac{h_3}{2} \right) \quad (2.26)$$

$$D_3 \left(y_1, y_2, -\frac{h_3}{2} \right) = D_3 \left(y_1, y_2, \frac{h_3}{2} \right). \quad (2.27)$$

In the derivation of Lemma 1, y_3 is the thickness direction of a stack of active layers. If we view y_3 as the stacking direction of multilayered material in general, then the Step-1 assumptions in Eq. (1.60) are proved to be exact by considering the PZT (or copper) fiber and epoxy as being layered material that is stacked in the y_2 direction.

2.3 Hybrid Rule of Mixtures for MFCs

2.3.1 HRM1: Fiber Layers (Step-1)

We retain the use of Eq. (1.60) but the assumptions are now proved as exact by MSG. Much like Eq. (1.56), rewrite Eq. (1.20) as

$$\varepsilon^H = S^H \sigma^H \quad (2.28)$$

except this time with $\varepsilon^H = [\sigma_{11} \ \varepsilon_{22} \ \sigma_{33} \ 2\varepsilon_{23} \ \sigma_{13} \ 2\varepsilon_{12} \ D_1 \ E_2 \ D_3]^T$, $\sigma^H = [\varepsilon_{11} \ \sigma_{22} \ \varepsilon_{33} \ \sigma_{23} \ 2\varepsilon_{13} \ \sigma_{12} \ E_1 \ D_2 \ E_3]^T$. Then one can compute the average as before

$$\bar{\varepsilon}^H = \langle \varepsilon^H \rangle = \langle S^H \sigma^H \rangle = \langle S^H \rangle \bar{\sigma}^H = S^{H*} \bar{\sigma}^H. \quad (2.29)$$

Note that $\sigma^H = \bar{\sigma}^H$ since they are proved to be constant in the microstructure according to MSG. Then, S^{E*} , d^* , and $k^{\sigma*}$ are found by solving for $\bar{\varepsilon}_{ij}$ and \bar{D}_i in terms of $\bar{\sigma}_{ij}$ and \bar{E}_i . This is the same procedure in Ref. [47] but now their assumptions are proved (see *Lemma 1*) by MSG. Also, this Step-1 hybrid rule of mixtures is referred to as HRM1 herein.

Note that Eq. (1.20) is in a compliance form rather than a stiffness form (for example, Eq. (2.1)). Thus all of the entries are on the order of 10^{-12} to 10^{-8} . Therefore no numerical scaling was required. The same rule of mixtures can be implemented in the form of a stiffness-type constitutive relation. In this case, the constitutive inputs can vary from 10^{-12} to 10^{11} . In such a case, it is first necessary to divide all stiffness terms by a scale-factor (such as 10^9) and multiply the permittivities by that same factor. Then a procedure similar to the one presented can be followed and after un-scaling, the exact same results as the compliance-type equations can be obtained. These scaling details are also applicable in the following section.

2.3.2 HRM2: Stack of Homogeneous Layers (Step-2)

Since the active layer is embedded among passive layers, Step-2 proceeds with special treatment. For both MFC types, careful attention is given to the behavior in

the y_3 -direction; namely, D_3 , E_3 . For the P2 MFC, this direction is the main direction of electrical activity whereas for the P1 MFC it is a direction of secondary effects.

With the fiber layers homogenized, Step-2 proceeds as in Step-1 but with three modifications. First, $\varepsilon^H = [\sigma_{11} \ \sigma_{22} \ \varepsilon_{33} \ 2\varepsilon_{23} \ 2\varepsilon_{13} \ \sigma_{12} \ D_1 \ D_2 \ E_3]^T$, $\sigma^H = [\varepsilon_{11} \ \varepsilon_{22} \ \sigma_{33} \ \sigma_{23} \ \sigma_{13} \ 2\varepsilon_{12} \ E_1 \ E_2 \ D_3]^T$. Second, the electrical energy contribution for material located outside of the active region (*ie*, for $|y_3| > h_a/2$) is ignored. This requires setting d_{kij} and k_{ij}^σ to null values for the passive layers. Performing averaging through the whole laminate gives

$$\bar{\varepsilon}^H = \langle \varepsilon^H \rangle = \langle S^H \sigma^H \rangle = \langle S^H \rangle \bar{\sigma}^H = S^{H*} \bar{\sigma}^H. \quad (2.30)$$

It is important to note that E_α ($\alpha = 1$ or 2), and D_3 were proved to be constant *in the active region*. Therefore note the last three terms in $\bar{\sigma}^H = [\bar{\varepsilon}_{11} \ \bar{\varepsilon}_{22} \ \bar{\sigma}_{33} \ \bar{\sigma}_{23} \ \bar{\sigma}_{13} \ 2\bar{\varepsilon}_{12} \ E_1 \ E_2 \ D_3]^T$. They are not averaged quantities through the entire laminate; they are active layer variables. This is the third difference and concludes what will be called HRM2. Refer to Appendix A for a sample Mathematica [147] code.

Figure 2.2 illustrates the electrical behavior obtained with the HRM2. Since the electrode configurations between the heterogeneous model and the homogeneous model are different, we are free to redefine \bar{E}_α , and \bar{D}_3 . For the in-plane electrical behavior, note that $\bar{E}_\alpha = E_\alpha$ since the electrode spacing between the heterogeneous model and the homogenized model is considered to be equal. Since the electrode spacing for the out-of-plane electrical fields differ, \bar{D}_3 is redefined from $\bar{D}_3 = V_a D_3$ to $\bar{D}_3 = D_3$, where $V^a = h_a/h_3$. Therefore $\bar{\sigma}^H$ will hold all variables from the homogenized model. We then find S^{E*} , d^* , and $k^{\sigma*}$ by solving Eq. (2.30) for $\bar{\varepsilon}_{ij}$ and \bar{D}_i in terms of $\bar{\sigma}_{ij}$ and \bar{E}_i . In this way, it is expected that voltages predicted by the homogeneous model will be equal to that of the heterogeneous model of both P1 and P2 MFCs. It has been verified that the HRM1 and HRM2 provide the exact same results when formulated from Eq. (1.15) rather than from Eq. (1.16) (similar to Eqs. (1.58) – (1.59)).

It should be noted that in-plane electric fluxes and the transverse electric field that are obtained are averaged over all the layers, whereas, the in-plane electric fields and the through-the-thickness flux will be of the actual active layer. Thus, if all electrical field quantities in the active layer are required after a macroscopic analysis they may be recovered by

$$\begin{aligned} E_\alpha &= \bar{E}_\alpha & D_\alpha &= \bar{D}_\alpha/V^a \\ E_3 &= \bar{E}_3/V^a & D_3 &= \bar{D}_3 \end{aligned} \quad (2.31)$$

see Figure 2.2.

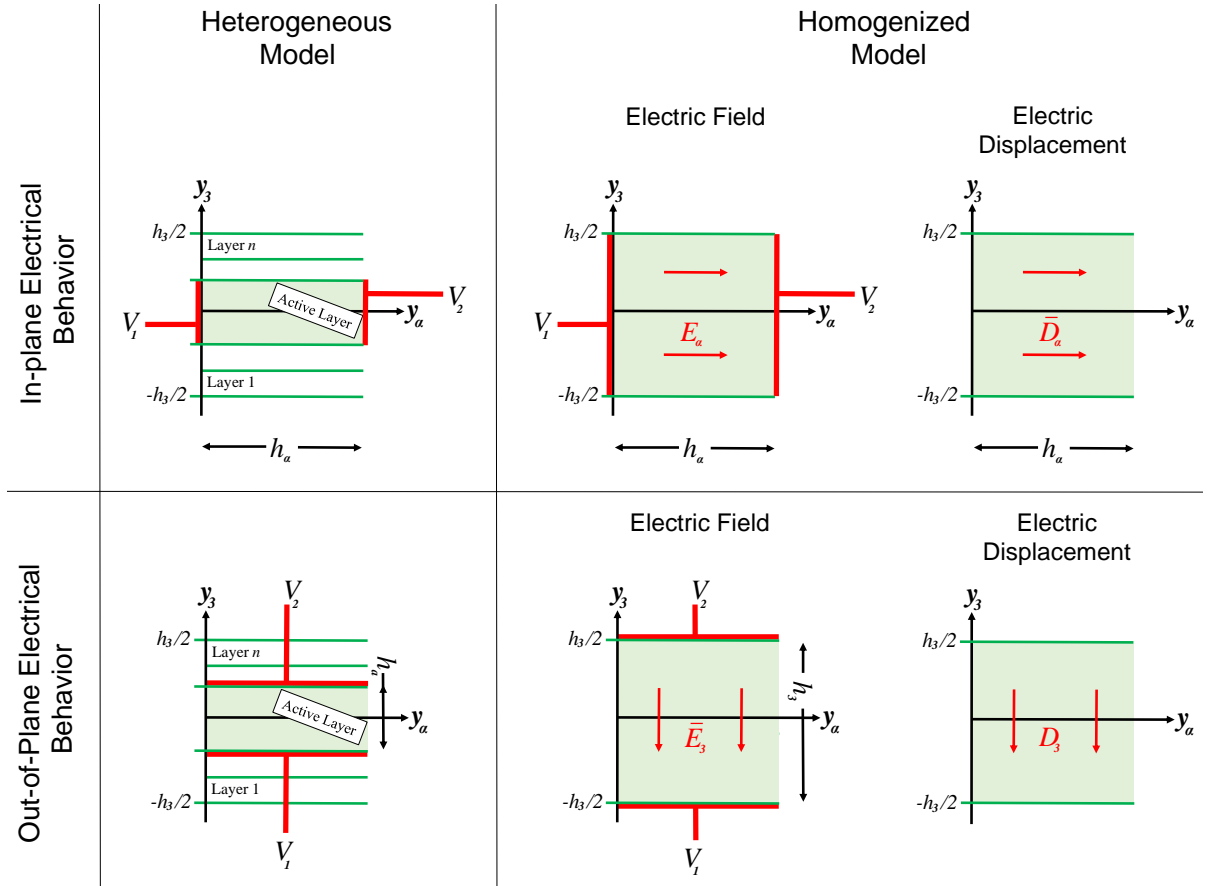


Figure 2.2: Illustration of the electrical behavior of the HRM (Step-2); applicable to both MFC types.

2.4 Analysis and Results

2.4.1 Assumed Microstructural Details of the MFC

The microstructural details of the MFC were obtained from references [47, 48]. A fiber volume fraction is defined for each of the fiber layers. The volume fraction of the PZT in the active layer, V_{PZT}^f , was set to 0.8654 [47]. Similarly, the volume fraction of the copper in the electrode layer, V_{Cu}^f , was set to 0.2400 [48]. The layer thicknesses were 40 μm , 18 μm , 180 μm , for the Kapton, electrode, and active layers respectively [48]. The piezoceramic is SONOX P502. Finally, Tables 2.1 - 2.2 show the elastic, piezoelectric and dielectric properties of each constituent considered in the microstructure. Note that the primed notation for the SONOX P502 properties (eg d'_{31}) indicate that the values are reported in the material coordinate system. In what follows, unprimed variables indicate that they are in the problem coordinate system. Also note that the SONOX P502 is transversely isotropic and thus we have $Y_1^{E'} = Y_2^{E'}$, $G_{13}^{E'} = G_{23}^{E'}$, $\nu_{13}^{E'} = \nu_{23}^{E'}$, $d'_{31} = d'_{32}$, $d'_{24} = d'_{15}$, $\kappa_{11}^{\sigma'}/\epsilon_0 = \kappa_{22}^{\sigma'}/\epsilon_0$. Since the material coordinate system is the same as the problem coordinate system for the P2 MFC, the piezoelectric strain coefficients in the problem coordinates for the P2 MFC are arranged as

$$\begin{bmatrix} 0 & 0 & 0 & 0 & d'_{15} & 0 \\ 0 & 0 & 0 & d'_{24} & 0 & 0 \\ d'_{31} & d'_{32} & d'_{33} & 0 & 0 & 0 \end{bmatrix}^T = \begin{bmatrix} 0 & 0 & 0 & 0 & d_{15} & 0 \\ 0 & 0 & 0 & d_{24} & 0 & 0 \\ d_{31} & d_{32} & d_{33} & 0 & 0 & 0 \end{bmatrix}^T. \quad (2.32)$$

A coordinate transformation of the P2 MFC piezoelectric strain matrix to the coordinate system shown in Figure 1.10(c) reveals that the P1 piezoelectric strain matrix is

$$\begin{bmatrix} d'_{33} & d'_{32} & d'_{31} & 0 & 0 & 0 \\ 0 & 0 & 0 & 0 & 0 & d'_{24} \\ 0 & 0 & 0 & 0 & d'_{15} & 0 \end{bmatrix}^T = \begin{bmatrix} d_{11} & d_{12} & d_{13} & 0 & 0 & 0 \\ 0 & 0 & 0 & 0 & 0 & d_{26} \\ 0 & 0 & 0 & 0 & d_{35} & 0 \end{bmatrix}^T. \quad (2.33)$$

Finally, it is notable that there are uncertainties in some of the microstructural details of the MFC. Some research articles report and model the presence of an acrylic layer

in the MFC. Moreover, Ref. [47] introduced the use of the SONOX P502 piezoelectric fiber when the real material is PZT-5A1. In addition, there may be small uncertainties on the fiber volume fractions to use. It is also noted here that the SONOX P502 material properties reported in Ref. [47] are not quite transversely isotropic. Thus, their reported value for $G_{12}^{E'}$ was discarded herein and instead, it was computed from

$$G_{12}^{E'} = \frac{Y_1^{E'}}{2(1 + \nu_{12}^{E'})}. \quad (2.34)$$

Table 2.1: Mechanical and piezoelectric properties for SONOX P502 in the material coordinate system (y'_i) . The 3-direction corresponds to the polarization direction.

$$\epsilon_0 = 8.854 \text{ pF/m.}$$

$Y_1^{E'}$ (GPa)	$Y_3^{E'}$	$G_{13}^{E'}$	$\nu_{12}^{E'}$	$\nu_{13}^{E'}$	d'_{31}	d'_{33}	d'_{24}	$\kappa_{11}^{\sigma'}/\epsilon_0$	$\kappa_{33}^{\sigma'}/\epsilon_0$
54.05	48.30	19.48	0.41	0.44	-185	440	560	1950	1850

Table 2.2: Isotropic MFC constituent material properties. $\epsilon_0 = 8.854 \text{ pF/m.}$

Property	Copper	Kapton	Epoxy
Y (GPa)	117.2	2.8	2.9
ν	0.31	0.3	0.3
κ/ϵ_0	5	3.4	4.25

2.4.2 Comparison of Homogenized Fiber Layer Methods (Step-1 Homogenization)

Before the properties of the full MFC are presented, we examine the effects that the PS assumption and neglected terms have on the fiber layer properties. Tables 2.3 and

2.4 show the homogenized properties of the MFC fiber layers (Step-1 homogenization). The properties of each layer are given in the coordinate system of the respective fiber layer (Figure 1.10(a)). Here and throughout this article, we categorize Step-1 homogenization into three types: Step-1 Hybrid Rule of Mixtures (HRM1) from Eq. (2.29), Plane-Stress-like Rule of Mixtures (PSRM) without dropping terms [48], and the Plane-Stress-like Rule of Mixtures with dropped terms (PSRM**)—Eqs. (1.64) and (1.65). We show our independent calculations if they were different than those reported from Deraemaeker *et al* [48] and Li *et al* [123] (Note: PSRM** has not been previously reported for the active layers). For the P1 MFC, we have transformed the results of Deraemaeker *et al* to the problem coordinate system (see Figure 1.10(a)) by performing a coordinate transformation of the compliance matrix. In general, we find the relations shown below. Note, that they report in terms of Y'_L , Y'_T , G'_{LT} , G'_{Tz} ,

$$\begin{aligned} Y_1 &= Y'_3 & Y_2 &= Y'_2 & Y_3 &= Y'_1 \\ G_{12} &= G'_{23} & G_{13} &= G'_{13} & G_{23} &= G'_{12} \\ \nu_{12} &= \nu'_{32} & \nu_{13} &= \nu'_{31} & \nu_{23} &= \nu'_{21} \end{aligned}$$

G'_{Lz} , and ν'_{LT} with $L = 3$, $T = 2$, $z = 1$ (in the material coordinate system: see Figure 1.10(c)).

It can be seen in Table 2.3 that for each fiber layer, the PS assumption will underpredict Y_2^* and is exacerbated by dropping terms. Moreover, the in-plane Poisson's ratio ν_{12}^* , is slightly over predicted. For the P2 MFC, Table 2.4 shows excellent agreement for the piezoelectric strain coefficient along the fiber axis (namely d_{31}^* and d_{11}^* in the respective cases). However, there are some appreciable differences for the 2-direction piezoelectric strain properties (that is, d_{32}^* and d_{12}^* in the respective cases).

Our PSRM calculations for the shear moduli in the P1 MFC active layer are not in agreement with those in Deraemaeker *et al* [48]. Deraemaeker *et al* worked in the material coordinates (see Figure 1.10(c)) so we will show how to compute $G'^*_{LT} = \left(\frac{V^f}{G^f_{LT}} + \frac{1-V^f}{G^m_{LT}} \right)^{-1}$ to give one example of the disagreement. For the P1 MFC, $L = 3$ and $T = 2$ so $G'^*_{LT} = G'^*_{32}$ and $G^f_{LT} = G^f_{32} = G^f_{23}$. From Table 2.1, we

Table 2.3: Effective elastic properties for each MFC fiber layer. All moduli are in GPa.

	Y_1^{E*}	Y_2^{E*}	Y_3^{E*}	G_{12}^{E*}	G_{13}^{E*}	G_{23}^{E*}	ν_{12}^{E*}	ν_{13}^{E*}	ν_{23}^{E*}
P2 MFC									
PSRM**	47.17	16.02	-	6.03	17.00	6.06	0.395	-	-
PSRM [48, 123]	47.17	16.98	-	6.03	17.00	6.06	0.395	-	-
HRM1 [47]	47.17	19.12	42.19	6.03	17.01	6.68	0.388	0.439	0.170
P1 MFC									
PSRM**	42.19	16.02	-	6.06	17.00	6.03	0.381	-	-
PSRM [48, 123]	42.18	16.97	-	6.03	6.06	17.00	0.38	-	-
PSRM	42.19	16.97	-	6.06	17.01	6.03	0.381	-	-
HRM1	42.19	19.12	47.17	6.68	17.01	6.03	0.376	0.392	0.157
Electrode layer									
PSRM** [123]	30.33	3.79	-	1.46	11.58	1.46	0.302	-	-
PSRM	30.33	4.11	-	1.46	11.58	1.46	0.302	-	-
HRM1	30.33	4.88	30.33	1.46	11.58	1.46	0.299	0.309	0.048

Table 2.4: Effective piezoelectric and dielectric properties for each MFC fiber layer.

Piezoelectric stain constants are in pC/N.

	d_{31}^*	d_{32}^*	d_{33}^*	d_{24}^*	d_{15}^*	$\kappa_{11}^{\sigma^*}/\epsilon_0$	$\kappa_{22}^{\sigma^*}/\epsilon_0$	$\kappa_{33}^{\sigma^*}/\epsilon_0$
P2 MFC								
PSRM**	-183.5	-153.2	-	-	-	-	-	1601.5
PSRM [48, 123]	-183	-153	-	-	-	-	-	1600
HRM1	-183.0	-173.5	435.9	7.739	555.1	1682.8	31.1	1593.0
	d_{11}^*	d_{12}^*	d_{13}^*	d_{26}^*	d_{35}^*	$\kappa_{11}^{\sigma^*}/\epsilon_0$	$\kappa_{22}^{\sigma^*}/\epsilon_0$	$\kappa_{33}^{\sigma^*}/\epsilon_0$
P1 MFC								
PSRM**	435.9	-176.3	-	-	-	1601.5	-	-
PSRM [48, 123]	436	-176	-	-	-	1593	-	-
HRM1	435.9	-173.5	-183.0	7.739	555.1	1593.0	31.1	1682.8
						$\kappa_{11}^{\sigma^*}/\epsilon_0$	$\kappa_{22}^{\sigma^*}/\epsilon_0$	$\kappa_{33}^{\sigma^*}/\epsilon_0$
Electrode layer								
PSRM**	-	-	-	-	-	-	-	4.43
PSRM	-	-	-	-	-	-	-	4.43
HRM1	-	-	-	-	-	4.43	4.41	4.43

use $G_{32}^f = 19.48$ GPa in $\left(\frac{V^f}{G_{32}^f} + \frac{1-V^f}{G_{32}^m}\right)^{-1}$ to find that $G_{32}'^* = 6.06$ GPa. Table 2.3 reports properties in the problem coordinates so we recall that $G_{23}' = G_{12}$ which gives $G_{12}'^* = 6.06$ GPa. Contrary to this exposition, note that Ref. [48] reports $G_{LT}'^* = 6.03$ GPa. If $L = 3$ and $T = 2$, then $G_{32}'^* = 6.03$ GPa according to [48]. When transformed to the problem coordinates as in Table 2.3, the result is $G_{12}'^* = 6.03$ GPa. Note, Li *et al* [123] repeats Deraemaeker's properties and reports them in the problem coordinate system as we have shown here. They also include elastic properties for the electrode layer.

An investigation of the effects that the PS assumption had on the lamina properties was extended to all fiber volume fractions. Our main findings are that the PS assumption underpredicts the lateral elastic modulus for most volume fractions as shown in Figure 2.3(a). There the error on the vertical axes is defined as $((M_i^*|^{PSRM} - M_i^*|^{HRM1})/M_i^*|^{HRM1}) \times 100$. M_i^* represents any of the homogenized electromechanical properties. The dashed curves correspond to the dropped terms (PSRM**). Note that the P2 MFC active layer was omitted for brevity but had nearly identical curves as the P1 MFC active layer. Another major finding is shown in Figure 2.3(b). It shows that the approximation for the d_{32}^* is unacceptable for the P2 MFC for most volume fractions.

Other plane-stress errors are reported in Figure 2.4. Each of the properties was grouped together with similar error magnitudes. It can be observed in Figure 2.4(a) that large overpredictions are possible for the active layers at low volume fractions; however, at the volume fractions relevant to MFCs, the error is acceptable. Figure 2.4(b) reveals that the effective properties along the fiber axis, (*ie*, Y_1^{E*} , d_{11}^* , and $k_{11}^{\sigma*}$ for the P1 MFC) have the smallest error (less than about 0.5%). Again, poorer results are obtained at lower volume fractions. Figure 2.4(c) shows the error for the shear behavior (including the shear coupling terms): note that all four curves plot identically. G_{12}^{E*} and G_{13}^{E*} for the P2 MFC are not plotted in Figures 2.3 and 2.4 because there was no error for those terms. Similarly, G_{13}^{E*} and G_{23}^{E*} for the P1 MFC were not plotted.

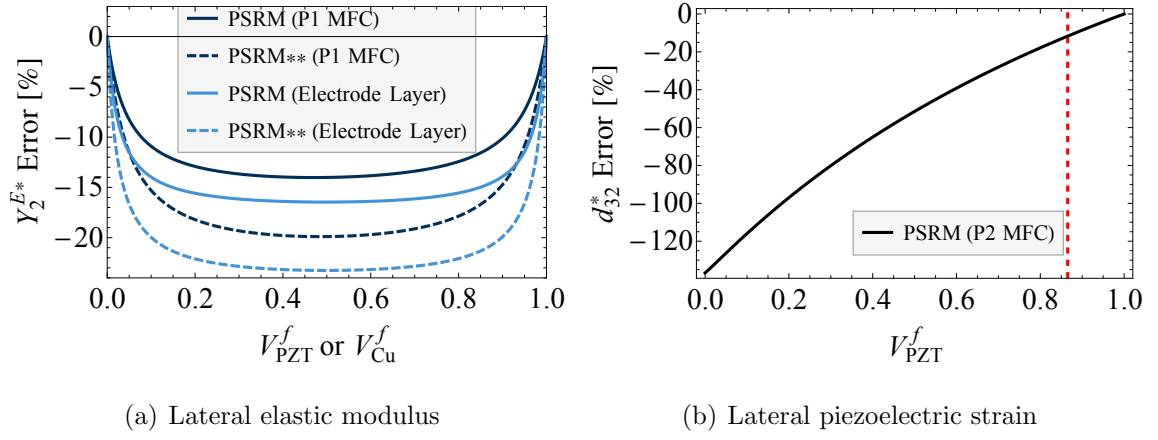
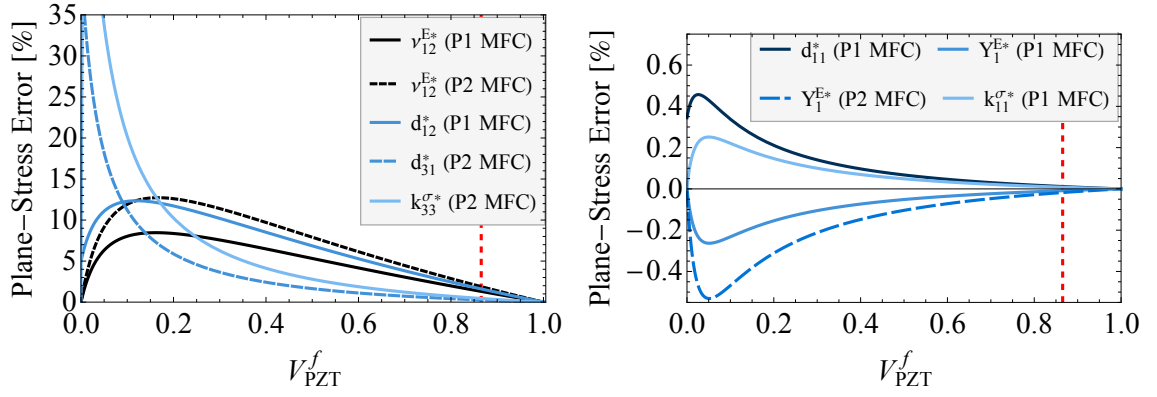
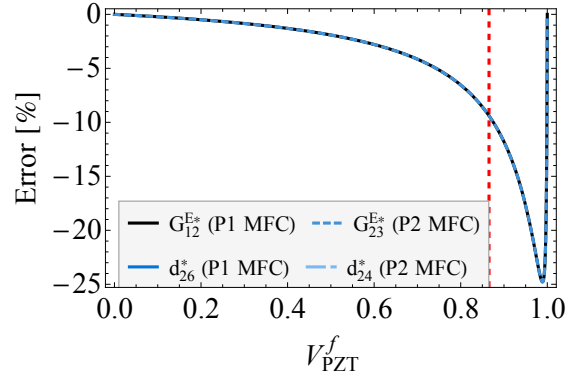


Figure 2.3: Major errors found for fiber layers due to the plane-stress-like assumption. The vertical dashed line for fiber volume fractions relevant to MFC active layer.



(a) Effective constants with moderate error. (b) Effective constants with moderate error.



(c) Effective constants with low error.

Figure 2.4: Other active layer plane-stress errors.

2.4.3 HRM2 Device Properties and Verification

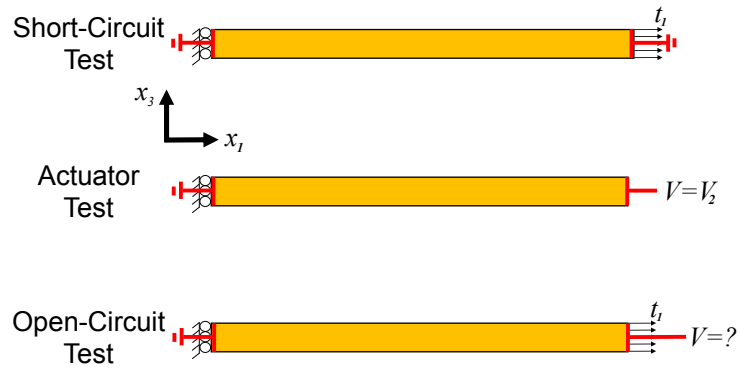
It is distinguished here that the proposed model gives *device properties* rather than *material properties*. This is because the proposed properties are only applicable to the MFC with the assumed layer thicknesses and thus the total thickness. If any of the layer thicknesses change, then the proposed HRM2 homogenization procedure needs to be repeated to obtain new properties. The traditional definition of material properties is not applicable, because material properties do not allow for such a dependence on layer thicknesses. The piezoelectric device properties that are obtained after implementing HRM1 followed by HRM2 are tabulated in Table 2.5. Only nonzero coefficients are reported. The mechanical properties are in Table 2.8.

The HRM2 properties are verified with a DNS in the present section. Since the purpose of this DNS is to verify the analytical model, the DNS only models the Active Area (see Figure 1.8 for the Active Area definition) since that is what the HRM2 would model. Furthermore, nonuniform poling and electric fields in the P1 case are ignored in this DNS (but not ignored elsewhere in this dissertation).

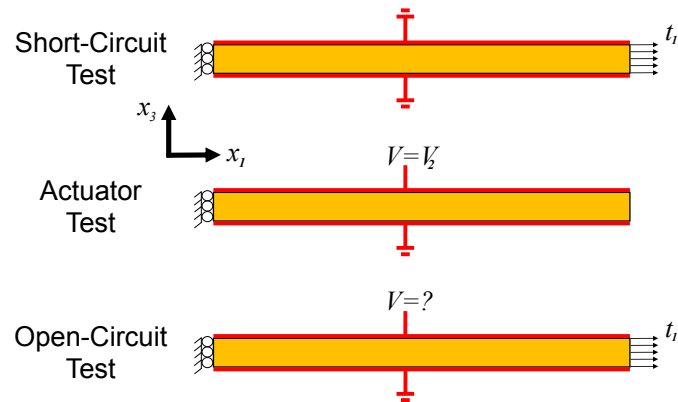
The omission of a host structure and consideration of elementary load types simplifies the use of device properties. Three load cases can be constructed to test the elastic, piezoelectric, and dielectric properties respectively. Here they will be referred to as the Short-Circuit Test, Actuator Test, and the Open-Circuit Test. These tests are illustrated in Figure 2.5(a) for the P1 MFC and 2.5(b) for the P2 MFC. The mechanical and electrical boundary conditions are illustrated as well. It should be noted that Figure 2.5 also represents the BCs applied in the DNS. Since uniform electric fields are being considered, Figure 2.5(a) shows the electrical BCs applied to the DNS. As for the P2 DNS, Figure 2.5(b) does show a resemblance of the electrical BCs except, internal electrodes were properly accounted for. Refer to Figures 4.3 and 4.4 for details of the P2 electrode surface definition.

Table 2.5: The HRM2 effective piezoelectric and dielectric device properties for the full homogenized MFC in problem coordinates.

	HRM1 ↓ HRM2
P1 MFC	
d_{11}^* (pC/N)	409.1
d_{12}^* (pC/N)	-129.8
d_{13}^* (pC/N)	-140.1
d_{26}^* (pC/N)	6.94
d_{35}^* (pC/N)	555.1
$\kappa_{11}^{\sigma*}/\epsilon_0$	934.37
$\kappa_{22}^{\sigma*}/\epsilon_0$	18.9
$\kappa_{33}^{\sigma*}/\epsilon_0$	2767.3
P2 MFC	
d_{31}^* (pC/N)	-297.2
d_{32}^* (pC/N)	-201.9
d_{33}^* (pC/N)	489.9
d_{24}^* (pC/N)	4.706
d_{15}^* (pC/N)	337.5
$\kappa_{11}^{\sigma*}/\epsilon_0$	1023.3
$\kappa_{22}^{\sigma*}/\epsilon_0$	18.9
$\kappa_{33}^{\sigma*}/\epsilon_0$	2568.2



(a) P1 MFC.



(b) P2 MFC.

Figure 2.5: Illustration of the numerical tests performed to verify the HRM2 device properties.

The Short-Circuit test results in

$$\begin{aligned}
\bar{\varepsilon}_{11} &= S_{11}^{E*} \bar{\sigma}_{11} = \bar{\sigma}_{11} / Y_1^{E*} \\
\bar{\varepsilon}_{22} &= S_{12}^{E*} \bar{\sigma}_{11} = -\nu_{12}^{E*} \bar{\sigma}_{11} / Y_1^{E*} \\
\bar{\varepsilon}_{33} &= S_{13}^{E*} \bar{\sigma}_{11} = -\nu_{13}^{E*} \bar{\sigma}_{11} / Y_1^{E*} \\
\bar{D}_t &= d_{t1}^* \bar{\sigma}_{11}
\end{aligned} \tag{2.35}$$

where $t = 1$ for the P1 MFC and $t = 3$ for the P2 MFC. No summation over t is implied in Eqs. (2.35) - (2.39). l_t is the distance between the electrodes. For the P1 case, the electrodes are supposed to be at the end of the DNS, thus, $l_1 = 5.2917$ mm. For the P2 case, the electrodes are the top and bottom surfaces of the homogenized model (see Figure 2.2) thus, $l_3 = h_3 = 0.296$ mm. The Actuator Test yields

$$\begin{aligned}
\bar{E}_t &= -\Delta V / l_t & \bar{D}_t &= k_{tt}^* \bar{E}_t \\
\bar{\varepsilon}_{11} &= d_{t1}^* \bar{E}_t & \bar{\varepsilon}_{22} &= d_{t2}^* \bar{E}_t & \bar{\varepsilon}_{33} &= d_{t3}^* \bar{E}_t.
\end{aligned} \tag{2.36}$$

Finally, the Open-Circuit Tests gives

$$\begin{aligned}
\bar{\varepsilon}_{11} &= S_{11}^{D*} \bar{\sigma}_{11} & \bar{\varepsilon}_{22} &= S_{12}^{D*} \bar{\sigma}_{11} & \bar{\varepsilon}_{33} &= S_{13}^{D*} \bar{\sigma}_{11} \\
\bar{E}_t &= -g_{t1}^* \bar{\sigma}_{11} & V_2 &= -\bar{E}_t l_t.
\end{aligned} \tag{2.37}$$

Note that with the help of Eq. (1.32) ($[S^D] = [S^E] - [g][d]^T$), the open-circuit elastic compliance components can be calculated from

$$S_{11}^{D*} = \frac{1}{Y_1^{E*}} - \frac{d_{t1}^* d_{t1}^*}{k_{tt}^{\sigma*}} \quad S_{12}^{D*} = -\frac{\nu_{12}^{E*}}{Y_1^{E*}} - \frac{d_{t1}^* d_{t2}^*}{k_{tt}^{\sigma*}} \quad S_{13}^{D*} = -\frac{\nu_{13}^{E*}}{Y_1^{E*}} - \frac{d_{t1}^* d_{t3}^*}{k_{tt}^{\sigma*}}. \tag{2.38}$$

Again, no summation on t is implied. Likewise, the piezoelectric voltage coefficient can be computed with the help of Eq. (1.31) ($[g] = [d][\beta^\sigma]$)

$$g_{t1}^* = \frac{d_{t1}^*}{k_{tt}^{\sigma*}}. \tag{2.39}$$

The patch geometry considered is shown in Figure 2.6. It consisted of the repetition of RVEs that are defined in Chapter 4. There were 5 RVEs along x_1 and 11 RVEs along x_2 . A total of six analyses were tested. Each test was solved on a mesh

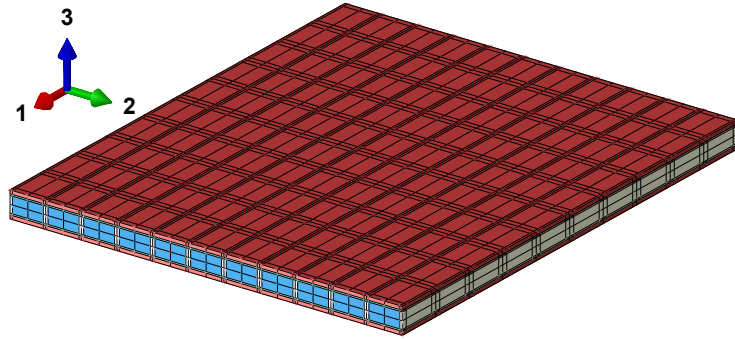


Figure 2.6: Perspective view of the MFC patch for numerical tests without a Passive Area and host substrates.

of 31,680 C3D20E elements (141,893 nodes). 20 CPUs solved the problem for each test in about 6 minutes of wallclock time per test. For each load case, the averages of the local fields in a centrally located RVE were computed from

$$\begin{aligned}\bar{\sigma}_{ij} &= \frac{\sum_{p=1}^N \sigma_{ij}^{(p)} V^{(p)}}{V_m} & \bar{\varepsilon}_{ij} &= \frac{\sum_{p=1}^N \varepsilon_{ij}^{(p)} V^{(p)}}{V_m} \\ \bar{D}_i &= \frac{\sum_{p=1}^N D_i^{(p)} V^{(p)}}{V_m} & \bar{E}_i &= \frac{\sum_{p=1}^N E_i^{(p)} V^{(p)}}{V_m}\end{aligned}\quad (2.40)$$

where the superscript (p) on the field variable data corresponds to the integration point, p , $V^{(p)}$ is the associated integration point volume, and N is the total number of integration points in the RVE. Note that for the Open Circuit cases, V_2 was computed as the arithmetic mean of the nodal potential for all nodes on the top electrode of the whole patch. In keeping with the electrical behavior represented in Figure 2.2, note that \bar{D}_3 is not to be compared to the analytical model results. Instead the volume average of D_3 in the active layer alone is computed by

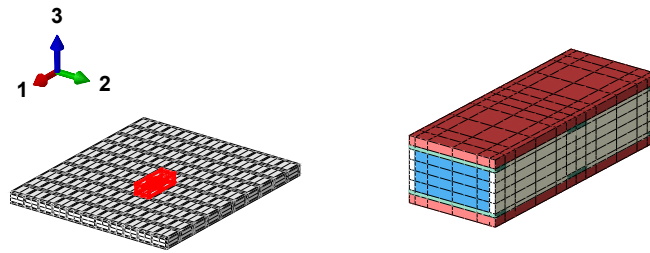
$$\bar{D}_3^a = \frac{\sum_{p=1}^{N_a} D_3^{(p)} V^{(p)}}{V_a} \quad (2.41)$$

where N_a is the total number of integration points in the active layer and V_a is the active layer volume. Figure 2.7 shows both volumes used for volume averaging and their relative locations.

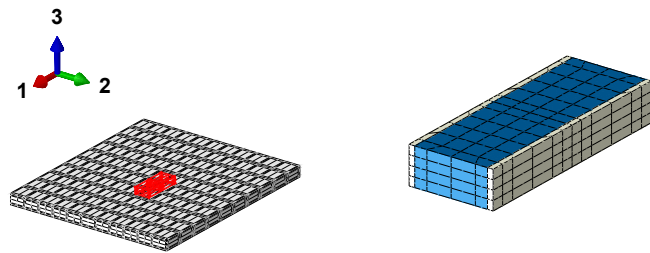
Tables 2.6 - 2.7 show the comparisons of some macroscopic quantities as computed from the DNS and that of Eqs. (2.35) – (2.39) used in conjunction with results from HRM2. The comparison between the DNS and the analytical results for the device response yields good agreement for both MFCs.

For the P1 actuator case, note that V_2 is artificially high due to the in-plane loading being prescribed on x_1^+ and x_1^- rather than on X_1^+ and X_1^- . Furthermore, V_2 was computed as the arithmetic mean over the entire x_1^+ face for the Open Circuit Test. Since there is good agreement between the DNS and the analytical model, the analytical model is verified along with the electrical behavior in Figure 2.2.

It is notable from Table 2.5 that properties associated to \bar{E}_3 (namely d_{31}^* , d_{32}^* , d_{33}^* , and $\kappa_{33}^{\sigma*}/\epsilon_0$ for the P2 MFC and d_{35}^* , and $\kappa_{33}^{\sigma*}/\epsilon_0$ for the P1 MFC) appear to be equal



(a) Full RVE and volume averaging location.



(b) Active layer volume and its volume averaging location.

Figure 2.7: Center volumes utilized to compute volume averaged quantities.

Table 2.6: Macroscopic variable comparison between a DNS of the P1 MFC patch and the HRM2 effective behavior.

	$\bar{\varepsilon}_{11}$ ($\mu\varepsilon$)	$\bar{\varepsilon}_{22}$ ($\mu\varepsilon$)	$\bar{\varepsilon}_{33}$ ($\mu\varepsilon$)	$\bar{D}_1 \times 10^{-3}$ ($\mu\text{C}/\text{mm}^2$)	\bar{E}_1 (V/mm)	V_1 (V)	V_2 (V)
Short Circuit Test							
HRM1 \rightarrow HRM2	366.1	-109.8	-119.6	4.091	0.0	c	c
DNS	347.4	-115.5	-124.1	3.879	-1.0	0.0	0.0
Difference (%)	5.38	-4.93	-3.66	5.46	-100	N/A	N/A
Actuator Test							
HRM1 \rightarrow HRM2	818.1	-259.6	-280.2	16.55	2000	0.0	-10583.3
DNS	779.9	-275.2	-291.4	16.15	2002	0.0	-10583.3
Difference (%)	4.91	-5.68	-3.82	2.42	-0.11	0.0	0.0
Open Circuit Test							
HRM1 \rightarrow HRM2	163.8	-45.6	-50.3	0.0	-494.5	0.0	2553.7
DNS	160.0	-49.4	-54.1	0.0	-481.8	0.0	2546.8
Difference (%)	2.40	-7.68	-7.02	0.0	2.62	0	0.27

Table 2.7: Macroscopic variable comparison between a DNS of the P2 MFC patch and the HRM2 effective behavior.

	$\bar{\varepsilon}_{11}$ ($\mu\varepsilon$)	$\bar{\varepsilon}_{22}$ ($\mu\varepsilon$)	$\bar{\varepsilon}_{33}$ ($\mu\varepsilon$)	$\bar{D}_3^a \times 10^{-3}$ ($\mu\text{C}/\text{mm}^2$)	\bar{E}_3 (V/mm)	V_1 (V)	V_2 (V)
Short Circuit Test							
HRM1 \rightarrow HRM2	329.3	-101.6	-116.8	-2.97	0.0	c	c
DNS	317.2	-106.6	-122.6	-2.83	0.0	0.0	0.0
Difference (%)	3.82	-4.72	-4.76	4.99	0	N/A	N/A
Actuator Test							
HRM1 \rightarrow HRM2	361.5	245.5	-595.9	-27.66	-1216	0.0	360
DNS	344.5	251.7	-589.9	-27.44	-1207	0.0	360
Difference (%)	4.93	-2.45	1.01	0.78	0.77	0	0
Open Circuit Test							
HRM1 \rightarrow HRM2	290.4	-128.0	-52.8	0.0	130.7	0.0	-38.69
DNS	281.6	-132.5	-61.8	0.0	124.1	0.0	-35.8
Difference (%)	3.15	-3.39	-14.61	0	5.3	0	8.10

to or higher than known active layer properties [47]. Values being higher than the active layer may be explained by revisiting Figure 2.2 (see Out-of-Plane Electrical Behavior). Let the electrical potential difference be $\Delta V = V_2 - V_1$. For a given ΔV , the electrical field in the heterogeneous model will be $E_3 = -\Delta V/h_a$; this is considered to be the true electric field. However, the electrodes of the present model are considered to be on the outer surfaces of the full stack of MFC layers. For the same ΔV , the electric field in the homogenized model will be $\bar{E}_3 = -\Delta V/h_3$. Since $h_a < h_3$ for the MFC, then $\bar{E}_3 < E_3$. Therefore, the through-the-thickness electrical field in the new model will be smaller than the true electrical field and the associated *properties may be larger to preserve the same voltage difference*. Nonetheless the predicted device response will be correct as shown in Table 2.7.

2.4.4 Comparison of Analytical Homogenization Methods for the Full MFC (Step-2 Homogenization)

Mechanical Properties

Since the definition of the mechanical variables (*ie* $\bar{\varepsilon}_{ij}$ and $\bar{\sigma}_{ij}$) in the present model agree with those of previous models, the effective mechanical properties can be compared directly. Table 2.8 compares our HRM2 to the common techniques found in the literature. We also performed homogenization with the “PSRM** + CLPT” since it is anticipated that it is the simplest and the most commonly used. Since our HRM2 does not use plate kinematics assumptions, we can assess their effects by comparing “HRM1 + CLPT” and “PSRM + Eq. (1.68)” to our HRM2. Finally, note that results in Table 2.8 required an in-plane 90° rotation of the electrode layer properties.

It is clear from Table 2.8 that our HRM2 provides the complete set of elastic properties for both MFCs. Since the property set is now complete and since various assumptions were avoided, it is expected that greater energy equivalence between reality and the homogenized model has been achieved. It is interesting that the HRM1

with CLPT gives identical results for the in-plane properties as the HRM2. This was verified for numerous PZT and copper volume fractions. Thus, the Kirchhoff-Love assumptions are exact for determining the in-plane mechanical properties. This also means that the PS assumption in Step-2 does not affect the final in-plane mechanical properties. Another noteworthy observation is that the lateral Young's Modulus, Y_2^{E*} , is the most adversely affected by the PS assumption. It is underpredicted by about 8% in both MFCs. This effect is exacerbated by neglecting terms (PSRM**). Finally, comparing the results from Eq. (1.68) to the HRM2 suggests that FSDT overestimates G_{13}^* and G_{23}^* by about 300% and 100% respectively. Recall in Section 2.4.2 that there was a mistake in the transverse shear moduli from Ref. [48] for the P1 MFC. It is noted that the Step-2 transverse shear moduli reported in Ref. [123] seem to have been incorrectly computed for the P1 MFC due to the Step-1 error.

To further characterize the error in Step-2 from using the PSRM in Step-1, we plot the error for the in-plane mechanical properties at a variety of PZT and copper volume fractions in Figure 2.8. The error on the vertical axes is defined as $((M_i^*|^{PSRM+CLPT} - M_i^*|^{HRM1+HRM2})/M_i^*|^{HRM1+HRM2}) \times 100$. M_i^* represents the homogenized elastic property after Step-2 homogenization for the P1 MFC configuration. The trends in Figure 2.8 were nearly identical for the P2 MFC configuration so they are omitted for brevity. The dashed curves show how using the PSRM** exacerbates the error. Each shade in 2.8(a) - (d) corresponds to a single copper fiber volume fraction as indicated in Figure 2.8(a). By comparing Figure 2.8(a) to 2.8(b), it can be seen that the PSRM has a greater impact on the overall Y_2^{E*} of the transducer than it does for Y_1^{E*} . The Y_2^{E*} underprediction is expected since Y_2^{E*} of each fiber layer is underpredicted as was shown in Figures 2.3(a). What was somewhat surprising was that the PSRM also has an adverse effect for Y_1^{E*} of the transducer as shown in Figure 2.8(a). The error becomes larger at low PZT volume fractions which is in accord with the Y_1^{E*} active layer trends in Figure 2.4(b). One can also observe that the error is almost zero when the copper volume fraction is zero. This error increases with increasing copper amounts. Since the electrode layers were rotated 90° , this suggests,

Table 2.8: Effective elastic properties for the full MFC in the problem coordinate system.

	HRM1 ↓ HRM2	HRM1 ↓ CLPT	HRM1 ↓ Eq. (1.68)	PSRM ↓ FSDT [123]	PSRM ↓ CLPT	PSRM** ↓ CLPT
P1 MFC						
Y_1^{E*} (GPa)	27.32	27.32	-	27.14	27.23	27.20
Y_2^{E*} (GPa)	16.09	16.09	-	14.79	14.80	14.22
Y_3^{E*} (GPa)	10.70	-	-	-	-	-
G_{12}^{E*} (GPa)	4.53	4.53	-	4.13	4.15	4.15
G_{13}^{E*} (GPa)	2.70	-	10.81	5.39	-	-
G_{23}^{E*} (GPa)	2.76	-	5.37	10.50	-	-
ν_{12}^{E*}	0.300	0.300	-	0.292	0.295	0.290
ν_{13}^{E*}	0.327	-	-	-	-	-
ν_{23}^{E*}	0.228	-	-	-	-	-
P2 MFC						
Y_1^{E*} (GPa)	30.37	30.37	-	30.20	30.29	30.25
Y_2^{E*} (GPa)	16.10	16.10	-	14.80	14.81	14.22
Y_3^{E*} (GPa)	10.52	-	-	-	-	-
G_{12}^{E*} (GPa)	4.13	4.13	-	4.13	4.13	4.13
G_{13}^{E*} (GPa)	2.70	-	10.81	10.50	-	-
G_{23}^{E*} (GPa)	2.84	-	5.76	5.39	-	-
ν_{12}^{E*}	0.309	0.309	-	0.303	0.305	0.300
ν_{13}^{E*}	0.355	-	-	-	-	-
ν_{23}^{E*}	0.237	-	-	-	-	-

that underpredicting Y_2^{E*} at the electrode layer will cause underpredictions of Y_1^{E*} of the full-stack of layers; especially at higher copper volume fractions. The effect on the in-plane Poisson's ratio is smaller but is documented in Figure 2.8(c). Figure 2.8(d) shows that the error in the in-plane shear modulus is largest at higher volume fractions and that electrode layer is not as influential. Thus, it is recommended to use fiber layer properties from the HRM1 rather than the PSRM.

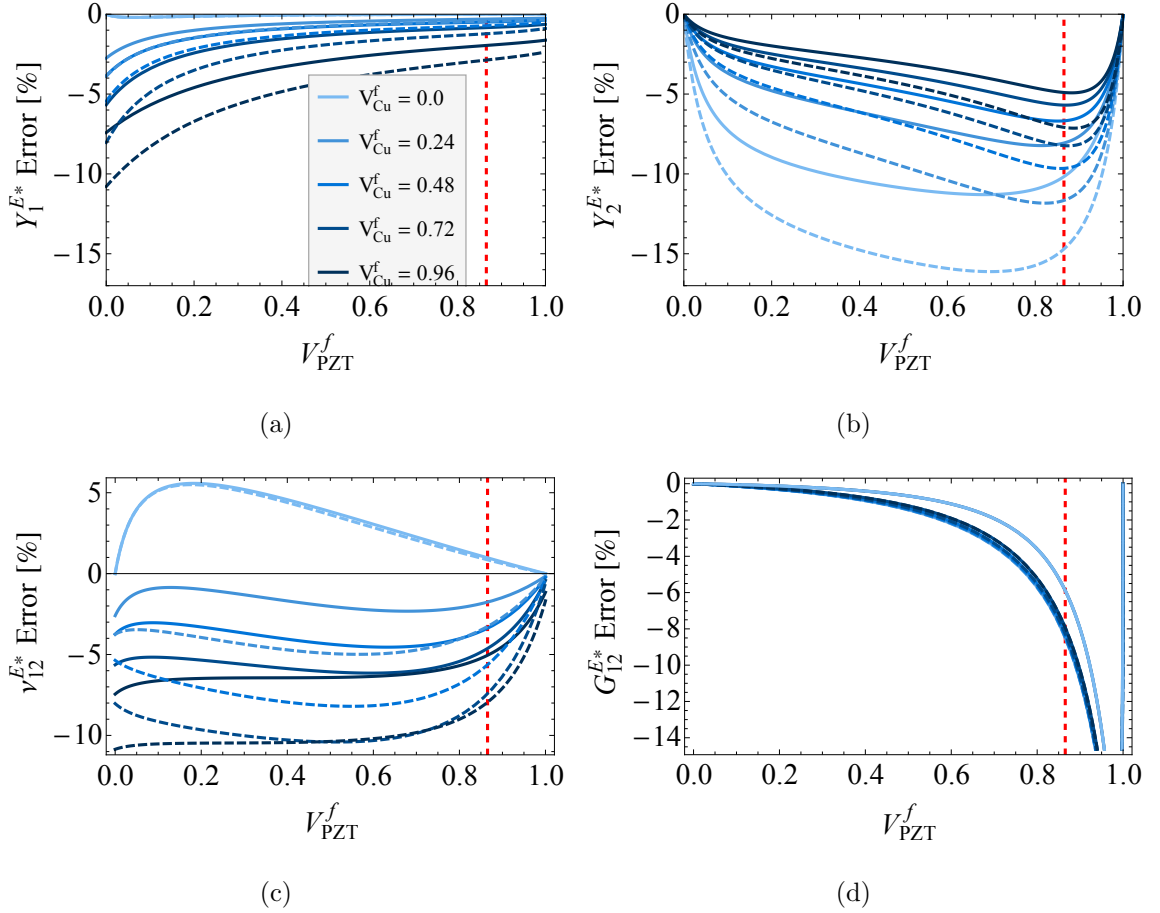


Figure 2.8: The effect of assuming $\varepsilon_{33} = E_1 = E_2 = 0$ in Step-1 on the in-plane Young's moduli in Step-2 at a variety of PZT and electrode volume fractions. The dashed curves are when the plane-stress assumption is used with dropped terms (Eq. (1.64)). The vertical dashed lines are at $V_{PZT}^f = 0.8654$ [47].

Next, we evaluate the effect of using Eq. (1.68) presented by Li *et al* [123] for the P1 MFC. Again, the trends in Figure 2.9 were nearly identical for the P2 MFC configuration and thus they are omitted. Figure 2.9 is a plot of the effective transverse shear moduli of the full MFC stack of layers for a variety of PZT and copper fiber volume fractions. The dashed curves are Eq. (1.68) and the solid curves are for the HRM2 presented here. Each fiber layer was homogenized by HRM1. It is apparent that, for G_{23}^{E*} , both methods are in agreement for low piezoelectric fiber volume fractions and zero copper fiber volume fraction for the electrode layer. Otherwise, FSDT will overshoot G_{23}^{E*} . There is little agreement between FSDT and HRM2 for G_{13}^{E*} . These results suggest that FSDT will vastly overpredict the transverse shear stiffness for almost all volume fraction combinations.

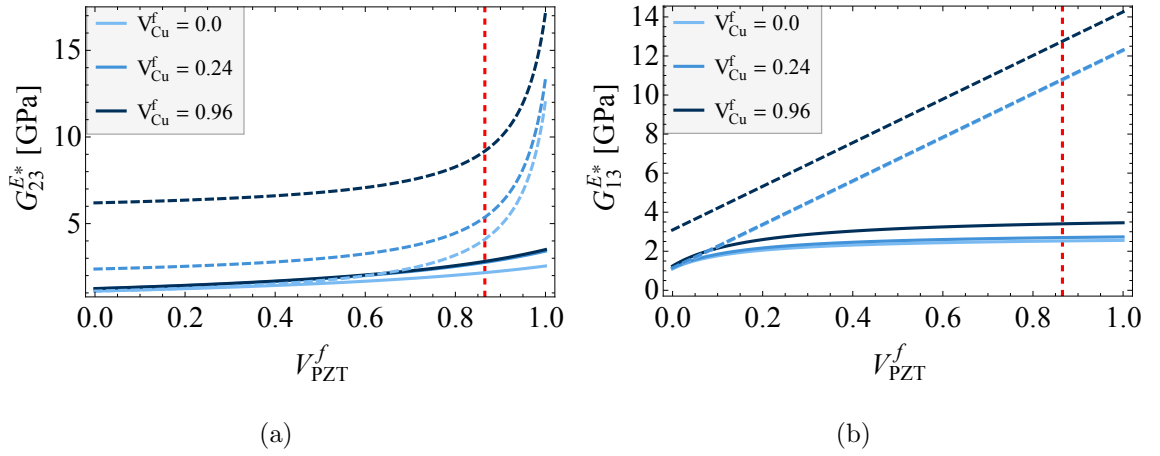


Figure 2.9: Overall transverse shear moduli comparison between HRM2 and FSDT (Eq. (1.68)) at a variety of PZT and electrode volume fractions. The solid curves are from HRM2 and the dashed curves are Eq. (1.68). The vertical dashed lines are at $V_{PZT}^f = 0.8654$ [47].

Piezoelectric and Dielectric Properties

Note that the permittivities and the piezoelectric coupling coefficients of the present model cannot be compared to any other work, because the device properties here have different definitions of the transverse macroscopic electric field in the active layer (E_3). This difference, which is allowable, comes from differing locations of the electrodes in the homogenized models.

Recall from Section 2.3.2 that the different electrode spacings allowed for a redefinition of some variables. Recall from Eq. (2.31) that, in the active layer, the transverse electric field is $E_3 = \bar{E}_3/V^a$ and the transverse electric displacement is $D_3 = \bar{D}_3$. Prior works let $E_3 = \bar{E}_3$ which will result in $D_3 = \bar{D}_3/V^a$ for the Short-Circuit Test (Eq. (2.35)) and $D_3 = \bar{D}_3$ in the Actuator Test (Eq. (2.36)). This dual definition of D_3 is an artifact of the fact that only part of the domain is electrically active and yet the induced strain from the actuator test is present in the active and passive layers. A constitutive relation that is comparable to prior works can be obtained from the HRM2 if the recommended definition of $E_3 = \bar{E}_3/V^a$ and $D_3 = \bar{D}_3$ is replaced with $E_3 = \bar{E}_3$ and $D_3 = \bar{D}_3/V^a$. The resulting properties obtained with this transformation appear in Table 2.9. Note that our approach is able to obtain the full set of piezoelectric and dielectric coefficients of the full MFC stack of layers.

The definition adopted throughout this dissertation (*eg*, Chapter 4) is $E_3 = \bar{E}_3/V^a$ and $D_3 = \bar{D}_3$. This is because the transverse electric displacement in the active layer can be known without post-processing and voltage at the electrodes of the homogenized model need not be scaled. For RVE analysis, this would mean that the transverse electric displacement should be averaged in the active layer and the transverse electric field should be averaged throughout the full RVE domain (this was also done with the DNS results in Tables 2.6 - 2.7). This clarifies the disagreement between Trindade and Benjeddou [51, 52] and Prasath and Arockiarajan [53–55, 70] with regard to which volume to consider when averaging the electrical fields in an RVE analysis.

Table 2.9: Comparison of the modified HRM2 (with $E_3 = \bar{E}_3$ and $D_3 = \bar{D}_3/V^a$) effective piezoelectric and dielectric properties to the literature and the active layer in problem coordinates.

	HRM1	PSRM	HRM1	PSRM
	↓	↓	↓	↓
	HRM2	FSDT [123]	N/A	N/A
P1 MFC				
d_{11}^* (pC/N)	409.1	410.9	435.9	435.9
d_{12}^* (pC/N)	-129.8	-127.9	-173.5	-176.3
d_{13}^* (pC/N)	-140.1	-	-183	-
d_{26}^* (pC/N)	6.94	-	7.739	-
d_{35}^* (pC/N)	337.5	-	555.1	-
$\kappa_{11}^{\sigma*}/\epsilon_0$	934.37	-	1593	1593.1
$\kappa_{22}^{\sigma*}/\epsilon_0$	18.9	-	31.1	-
$\kappa_{33}^{\sigma*}/\epsilon_0$	1023.3	-	1682.8	-
P2 MFC				
d_{31}^* (pC/N)	-180.7	-180.9	-183	-183.5
d_{32}^* (pC/N)	-122.8	-142.5	-173.5	-153.2
d_{33}^* (pC/N)	297.9	-	435.9	-
d_{24}^* (pC/N)	4.706	-	7.739	-
d_{15}^* (pC/N)	337.5	-	555.1	-
$\kappa_{11}^{\sigma*}/\epsilon_0$	1023.3	-	1682.8	-
$\kappa_{22}^{\sigma*}/\epsilon_0$	18.9	-	31.1	-
$\kappa_{33}^{\sigma*}/\epsilon_0$	949.7	-	1593	1600.1

It was also interesting to consider the constraining effects that other copper volume fractions have on the P1 device properties in Figure 2.10. These effects are also plotted for transducers that operate as the P2 MFC in Figure 2.11. These plots have the recommended HRM2 with $D_3 = \bar{D}_3$ and $E_3 = \bar{E}_3/V^a$.

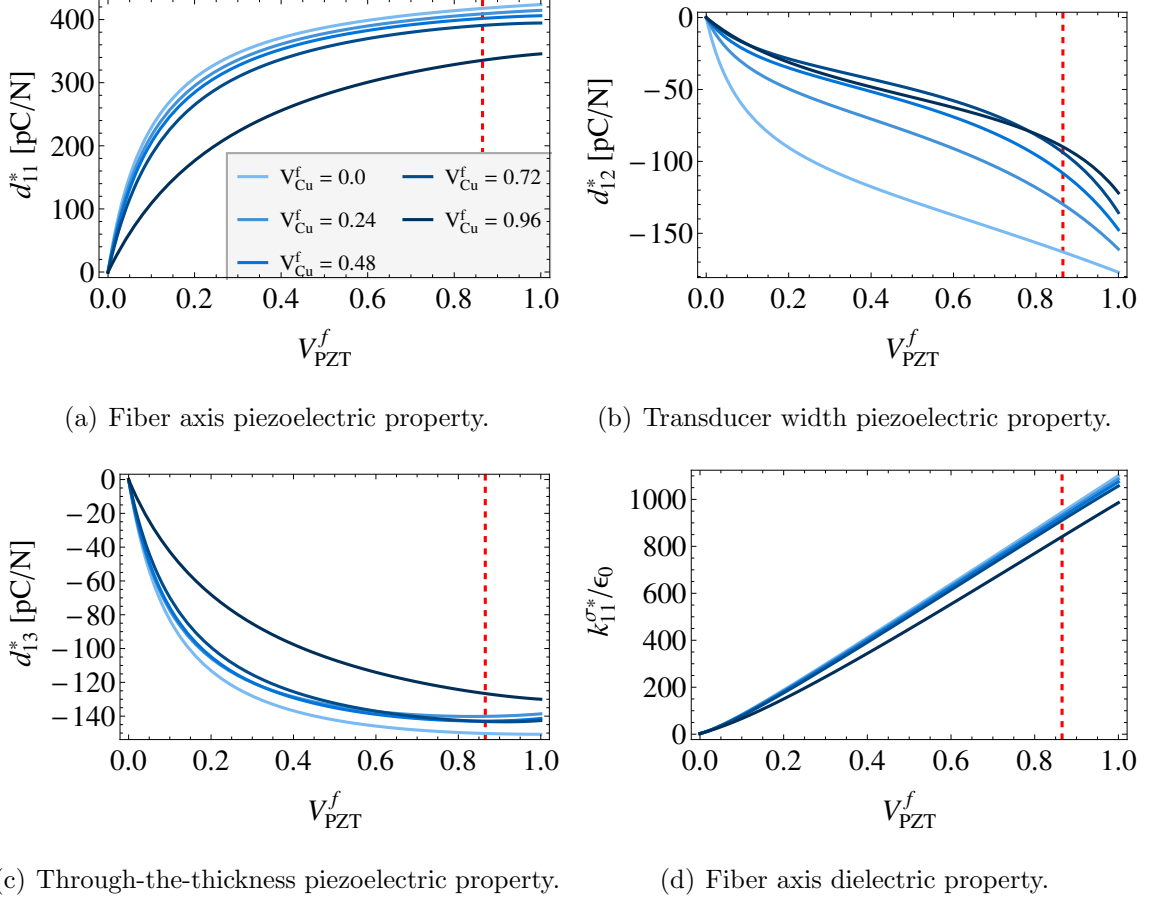


Figure 2.10: PZT and copper fiber volume fraction study with the HRM2 of the P1 MFC. Results with the recommended $D_3 = \bar{D}_3$ and $E_3 = \bar{E}_3/V^a$ are shown. The vertical dashed lines are at $V_{PZT}^f = 0.8654$.

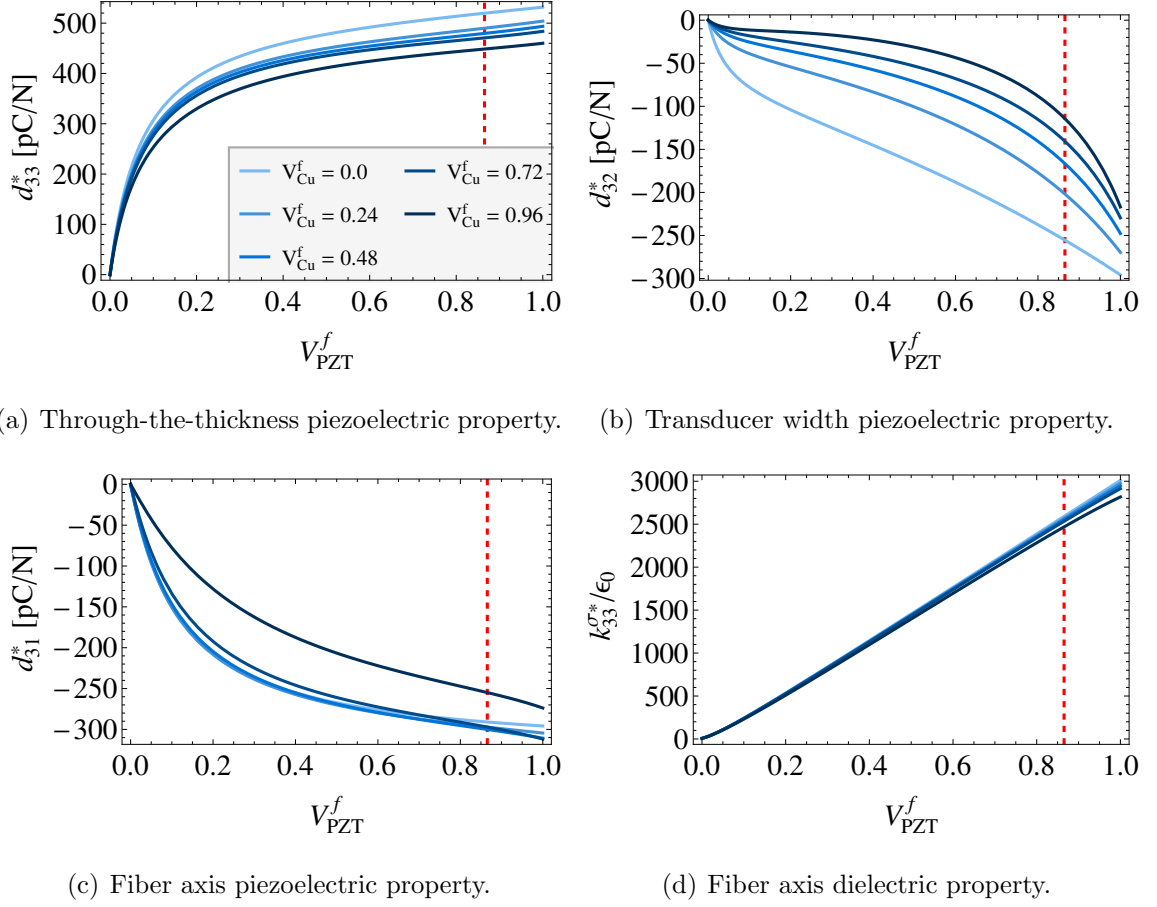


Figure 2.11: PZT and copper fiber volume fraction study with the HRM2 of the P2 MFC. Results with the recommended $D_3 = \bar{D}_3$ and $E_3 = \bar{E}_3/V^a$ are shown. The vertical dashed lines are at $V_{PZT}^f = 0.8654$.

2.4.5 Discussion

Using the PS assumption in Step-1 led to large underpredictions for both the elastic modulus and piezoelectric strain coefficients along the lateral direction (y_2 direction) of the MFC (see Tables 2.8 and 2.9). Although this is not the principal direction that such transducers are intended to operate, this may lead to significant errors when analyzing orientation angles of orthotropic host substrates as in Ref. [121]. Moreover, errors will compound for systems that use distributed transducers such as in Ref. [122]. Finally, the increases in the elastic modulus along the transducer width should give better performance for smart-structures that actuate/sense along the fiber direction but are load bearing along its width (for example morphing compliant aircraft wings as in Ref. [125]).

2.4.6 Limitations

1. The micromechanics model idealizes the MFC microstructure to be a stack of homogeneous layers. Thus geometrical considerations of the fibers are not considered. Furthermore, an artificial discontinuity at the interface is introduced by modeling the MFC as a stack of homogeneous layers.
2. The method assumes perfect bonding between all constituents of the MFC.
3. Although our approach is general for any layup of piezoelectric layers, it does not capture any bending behavior of unsymmetric layups. Luckily the MFC has a symmetric layup.
4. The piezoelectric properties of the PZT are known to be dependent on the electric field [52]. No consideration about this is given here. The hysteretic behavior of the MFC is not captured [148].

5. Uniformly and fully polarized PZT was assumed for both the P1 and P2 MFC. It is known, however, that the P1 MFC is nonuniformly poled [11] and has small regions of unpoled and partially poled material.

3. MIXED BOUNDARY CONDITIONS FOR FINITE THICKNESS EFFECTS

3.1 Theory Development for Active Layers

This chapter presents new boundary conditions that are a mixture of the Periodic Boundary Conditions (PBCs) for the in-plane faces and homogeneous stress boundary conditions (HSBCs) on the out-of-plane faces. This mixture of BCs has been proposed by Espadas-Escalante *et al* [149] to determine the effective properties of woven composites for the purely mechanical case. The proposed boundary conditions are shown to satisfy a previous piezoelectric extension to the well-known Hill-Mandel macrohomogeneity condition. In order to carefully examine the symmetry of the properties that are obtained, a post-processing procedure that provides all 81 effective properties is presented.

3.2 RVE Analysis for In-plane Periodic Piezocomposites

In multiscale modeling, real boundary conditions are imposed on the boundaries of macroscopic structures. The boundary conditions we impose on an RVE to obtain the effective properties are fictitious. The Hill-Mandel condition can provide guidelines as to which boundary conditions to apply. The Hill-Mandel condition was extended for the non-dissipative piezoelectric case by Schroder [62]. We wish to find under which conditions we will have

$$\langle \sigma_{kl} \varepsilon_{kl} + E_i D_i \rangle = \bar{\sigma}_{kl} \bar{\varepsilon}_{kl} + \bar{E}_i \bar{D}_i. \quad (3.1)$$

Taking the difference between these two quantities gives

$$\Pi = \langle \sigma_{kl} \varepsilon_{kl} + E_i D_i \rangle - (\bar{\sigma}_{kl} \bar{\varepsilon}_{kl} + \bar{E}_i \bar{D}_i). \quad (3.2)$$

Thus the needed conditions are met when Π vanishes. Using the following identity

$$\begin{aligned} \iiint_{V_m} \varepsilon_{ij} \bar{\sigma}_{ij} dV_m &= \bar{\sigma}_{ij} \iiint_{V_m} \varepsilon_{ij} dV_m = \bar{\sigma}_{kl} \bar{\varepsilon}_{kl} \\ \iiint_{V_m} E_i \bar{D}_i dV_m &= \bar{D}_i \iiint_{V_m} E_i dV_m = \bar{D}_i \bar{E}_i \end{aligned}$$

we have

$$\begin{aligned} \langle \sigma_{kl} \varepsilon_{kl} + E_i D_i \rangle - \\ (\bar{\sigma}_{kl} \bar{\varepsilon}_{kl} + \bar{E}_i \bar{D}_i) &= \frac{1}{V_m} \iiint_{V_m} (\sigma_{ij} u_{i,j} - u_{i,j} \bar{\sigma}_{ij}) dV_m \\ &\quad + \frac{1}{V_m} \iiint_{V_m} (E_i D_i - \bar{E}_i \bar{D}_i) dV_m \\ &= \frac{1}{V_m} \iiint_{V_m} (\sigma_{ij} u_{i,j} - u_{i,j} \bar{\sigma}_{ij}) dV_m \\ &\quad + \frac{1}{V_m} \iiint_{V_m} (-D_i \phi_{,i} + \phi_{,i} \bar{D}_i) dV_m \\ &= \frac{1}{V_m} \iiint_{V_m} (\sigma_{ij} u_{i,j} - \bar{\sigma}_{ij} u_{i,j} - \sigma_{ij} \bar{\varepsilon}_{ij} + \bar{\sigma}_{ij} \bar{\varepsilon}_{ij}) dV_m \\ &\quad + \frac{1}{V_m} \iiint_{V_m} (\bar{D}_i \phi_{,i} - D_i \phi_{,i} - D_i \bar{E}_i + \bar{D}_i \bar{E}_i) dV_m \\ &= \frac{1}{V_m} \iiint_{V_m} (\sigma_{ij} - \bar{\sigma}_{ij}) (u_{i,j} - \bar{\varepsilon}_{ij}) dV_m \\ &\quad + \frac{1}{V_m} \iiint_{V_m} (\bar{D}_i - D_i) (\phi_{,i} + \bar{E}_i) dV_m \\ &= \frac{1}{V_m} \iiint_{V_m} (\sigma_{ik} - \bar{\sigma}_{ik}) (u_{i,k} - \delta_{jk} \bar{\varepsilon}_{ij}) dV_m \\ &\quad + \frac{1}{V_m} \iiint_{V_m} (\bar{D}_k - D_k) (\phi_{,k} + \delta_{ik} \bar{E}_i) dV_m \\ &= \frac{1}{V_m} \iiint_{V_m} (\sigma_{ik} - \bar{\sigma}_{ik}) (u_{i,k} - y_{j,k} \bar{\varepsilon}_{ij}) dV_m \\ &\quad + \frac{1}{V_m} \iiint_{V_m} (\bar{D}_k - D_k) (\phi_{,k} + y_{i,k} \bar{E}_i) dV_m. \end{aligned} \tag{3.3}$$

Note that

$$(\sigma_{ik} - \bar{\sigma}_{ik}) (u_{i,k} - y_{j,k} \bar{\varepsilon}_{ij}) = \sigma_{ik} u_{i,k} - \bar{\sigma}_{ik} u_{i,k} - \sigma_{ik} y_{j,k} \bar{\varepsilon}_{ij} + \bar{\sigma}_{ik} y_{j,k} \bar{\varepsilon}_{ij}. \tag{3.4}$$

From the definition of the chain rule we have

$$\begin{aligned}
(\sigma_{ik} u_i)_{,k} &= \cancel{\sigma_{ik,k} u_i}^0 + u_{i,k} \sigma_{ik} = u_{i,k} \sigma_{ik} \\
(\sigma_{ik} y_j)_{,k} &= \cancel{\sigma_{ik,k} y_j}^0 + \sigma_{ik} y_{j,k} = \sigma_{ik} y_{j,k} \\
(\bar{\sigma}_{ik} u_i)_{,k} &= \cancel{\bar{\sigma}_{ik,k} u_i}^0 + u_{i,k} \bar{\sigma}_{ik} = u_{i,k} \bar{\sigma}_{ik} \\
(\bar{\sigma}_{ik} y_j)_{,k} &= \cancel{\bar{\sigma}_{ik,k} y_j}^0 + \bar{\sigma}_{ik} y_{j,k} = \bar{\sigma}_{ik} y_{j,k}
\end{aligned} \tag{3.5}$$

where $\sigma_{ik,k} = 0$ was used from the equilibrium of linear momentum in the absence of body forces (*cf* Eq. (1.4)).

$$\begin{aligned}
(\sigma_{ik} - \bar{\sigma}_{ik})(u_{i,k} - y_{j,k} \bar{\varepsilon}_{ij}) &= (\sigma_{ik} u_i)_{,k} - (\bar{\sigma}_{ik} u_i)_{,k} - \bar{\varepsilon}_{ij} (\sigma_{ik} y_j)_{,k} + \bar{\varepsilon}_{ij} (\bar{\sigma}_{ik} y_j)_{,k} \\
&= (\sigma_{ik} u_i)_{,k} - (\bar{\sigma}_{ik} u_i)_{,k} - (\bar{\varepsilon}_{ij} \sigma_{ik} y_j)_{,k} + (\bar{\varepsilon}_{ij} \bar{\sigma}_{ik} y_j)_{,k} \\
&= [(\sigma_{ik} - \bar{\sigma}_{ik})(u_i - y_j \bar{\varepsilon}_{ij})]_{,k}
\end{aligned} \tag{3.6}$$

In like manner from Eq. (3.3)

$$(\bar{D}_k - D_k)(\phi_{,k} + y_{i,k} \bar{E}_i) = \bar{D}_k \phi_{,k} - D_k \phi_{,k} + \bar{D}_k y_{i,k} \bar{E}_i - D_k y_{i,k} \bar{E}_i \tag{3.7}$$

From the definition of the chain rule we have

$$\begin{aligned}
(D_k \phi)_{,k} &= \cancel{D_{k,k} \phi}^0 + \phi_{,k} D_k = \phi_{,k} D_k \\
(D_k y_i)_{,k} &= \cancel{D_{k,k} y_i}^0 + D_k y_{i,k} = D_k y_{i,k} \\
(\bar{D}_k \phi)_{,k} &= \cancel{\bar{D}_{k,k} \phi}^0 + \phi_{,k} \bar{D}_k = \phi_{,k} \bar{D}_k \\
(\bar{D}_k y_i)_{,k} &= \cancel{\bar{D}_{k,k} y_i}^0 + \bar{D}_k y_{i,k} = \bar{D}_k y_{i,k}
\end{aligned} \tag{3.8}$$

where $D_{k,k} = 0$ was used from Gauss' Law (*cf* Eq. (1.2)) when there are zero charges in V_m .

$$\begin{aligned}
(\bar{D}_k - D_k)(\phi_{,k} + y_{i,k} \bar{E}_i) &= (\bar{D}_k \phi)_{,k} - (D_k \phi)_{,k} + \bar{E}_i (\bar{D}_k y_i)_{,k} - \bar{E}_i (D_k y_i)_{,k} \\
&= (\bar{D}_k \phi)_{,k} - (D_k \phi)_{,k} + (\bar{E}_i \bar{D}_k y_i)_{,k} - (\bar{E}_i D_k y_i)_{,k} \\
&= [(\bar{D}_k - D_k)(\phi + y_i \bar{E}_i)]_{,k}
\end{aligned} \tag{3.9}$$

Eq. (3.3) now reads

$$\begin{aligned}
\Pi &= \frac{1}{V_m} \iiint_{V_m} [(\sigma_{ik} - \bar{\sigma}_{ik})(u_i - y_j \bar{\varepsilon}_{ij})]_{,k} dV_m \\
&\quad + \frac{1}{V_m} \iiint_{V_m} [(\bar{D}_k - D_k)(\phi + y_i \bar{E}_i)]_{,k} dV_m \\
&= \frac{1}{V_m} \iint_{S_m} n_k (\sigma_{ik} - \bar{\sigma}_{ik})(u_i - y_j \bar{\varepsilon}_{ij}) dS_m \\
&\quad + \frac{1}{V_m} \iint_{S_m} n_k (\bar{D}_k - D_k)(\phi + y_i \bar{E}_i) dS_m \\
&= \Pi_m + \Pi_e
\end{aligned} \tag{3.10}$$

where we have let

$$\begin{aligned}
\Pi_m &= \frac{1}{V_m} \iint_{S_m} n_k (\sigma_{ik} - \bar{\sigma}_{ik})(u_i - y_j \bar{\varepsilon}_{ij}) dS_m \\
\Pi_e &= \frac{1}{V_m} \iint_{S_m} n_k (\bar{D}_k - D_k)(\phi + y_i \bar{E}_i) dS_m.
\end{aligned} \tag{3.11}$$

S_m is the exterior boundary surfaces of the RVE and n_k is the outward pointing unit normal on S_m . Thus the piezoelectric macrohomogeneity condition is satisfied when both surface integrals vanish and therefore $\Pi = 0$ in Eq. (3.2).

It is noted here that there are infinitely many ways to satisfy the piezoelectric macrohomogeneity condition. One way to set $\Pi = 0$ is by letting $(u_i - y_j \bar{\varepsilon}_{ij})^+ = (u_i - y_j \bar{\varepsilon}_{ij})^-$ and $(\phi + y_i \bar{E}_i)^+ = (\phi + y_i \bar{E}_i)^-$ at every point on the boundary of the RVE. These are the periodic boundary conditions for a piezoelectric homogenization problem. In practice, these can be implemented with Eq. (1.53) and (1.54) respectively.

3.2.1 Proposed Boundary Conditions

Here we account for the reality that the RVE is not periodic along the x_3 direction. As mentioned, our approach retains the PBCs only for the in-plane faces of an RVE. The out-of-plane faces have the HSBCs for the mechanical BCs and equipotential conditions for the representation of electrodes. To give an overview of the RVE analysis, nine boundary value problems (BVPs) are created to obtain the complete set

of piezoelectric properties. Each BVP must satisfy $\Pi = 0$ to ensure that piezoelectric macrohomogeneity condition is satisfied.

The problems can be categorized into sensor and actuator problems. In this paper, the sensor behavior is for the first six of the nine BVPs. The predominant behaviors are three in-plane (Problems 1, 2, and 6) deformations and three out-of-plane deformations (Problems 3, 4, and 5). For these cases, the electrodes on X_3 need to be grounded in order to obtain the short-circuit stiffness of the composite. Problems 7-9 are the actuator BVPs. The three BVPs need to respectively correspond to three components of the electrical field (E_i) loading.

It is important to note that many of the boundary conditions presented here (and in prior works [36, 47, 52]) depend on a volume averaged quantity over the RVE domain. Since the volume average of a field variable is not generally known before solving a BVP, we distinguish between an *applied* quantity and the *resulting volume average* of that quantity after the BVP has been solved. Thus, here and throughout this article, a zero superscript indicates that the quantity is an applied quantity (and an overbar indicates volume average as already mentioned). Since finite elements are used here to solve the BVPs, the resulting volume average fields are found from Eq. (2.40) and is repeated here

$$\begin{aligned}\bar{\sigma}_{ij} &= \frac{\sum_{p=1}^N \sigma_{ij}^{(p)} V^{(p)}}{V_m} & \bar{\varepsilon}_{ij} &= \frac{\sum_{p=1}^N \varepsilon_{ij}^{(p)} V^{(p)}}{V_m} \\ \bar{D}_i &= \frac{\sum_{p=1}^N D_i^{(p)} V^{(p)}}{V_m} & \bar{E}_i &= \frac{\sum_{p=1}^N E_i^{(p)} V^{(p)}}{V_m}.\end{aligned}\tag{3.12}$$

3.2.2 Mechanical BCs

To satisfy $\Pi_m = 0$, from Eq. (3.11), Π_m is split as

$$\begin{aligned}\Pi_m &= \frac{1}{V_m} \iint_{S_1} n_k (\sigma_{ik} - \bar{\sigma}_{ik}) (u_i - y_j \bar{\varepsilon}_{ij}) dS_1 \\ &\quad + \frac{1}{V_m} \iint_{S_2} n_k (\sigma_{ik} - \bar{\sigma}_{ik}) (u_i - y_j \bar{\varepsilon}_{ij}) dS_2 \\ &\quad + \frac{1}{V_m} \iint_{S_3} n_k (\sigma_{ik} - \bar{\sigma}_{ik}) (u_i - y_j \bar{\varepsilon}_{ij}) dS_3.\end{aligned}\tag{3.13}$$

Each BC will be shown to vanish each surface integral individually.

Since PBCs will be used in-plane, the notation in Eq. (1.53) is then slightly modified by substituting the volume average strain by the applied strain, ε_{ij}^0 . Later we verify if $\varepsilon_{ij}^0 = \bar{\varepsilon}_{ij}$. It will be useful to expand Eq. (1.53) and in the *applied* notation as

$$\begin{aligned} u_i^+ - u_i^- = & \varepsilon_{i1}^0(y_1^+ - y_1^-) + \varepsilon_{i2}^0(y_2^+ - y_2^-) \\ & + \varepsilon_{i3}^0(y_3^+ - y_3^-). \end{aligned} \quad (3.14)$$

In-plane Faces

Since the X_α surfaces are respectively normal to n_α , then, for a periodic mesh, on X_1 we have

$$\begin{aligned} \text{For the } X_1 \text{ faces :} \quad & y_1^+ - y_1^- = h_1 \\ & y_2^+ = y_2^- \\ & y_3^+ = y_3^- \\ \text{For the } X_2 \text{ faces :} \quad & y_1^+ = y_1^- \\ & y_2^+ - y_2^- = h_2 \\ & y_3^+ = y_3^-. \end{aligned} \quad (3.15)$$

Thus from Eq. (3.14) we are left with

$$\begin{aligned} \text{For the } X_1 \text{ faces :} \quad & u_1^+ - u_1^- = \varepsilon_{11}^0(y_1^+ - y_1^-) = \varepsilon_{11}^0 h_1 \\ & u_2^+ - u_2^- = \varepsilon_{21}^0(y_1^+ - y_1^-) = \varepsilon_{21}^0 h_1 \\ & u_3^+ - u_3^- = \varepsilon_{31}^0(y_1^+ - y_1^-) = \varepsilon_{31}^0 h_1 \\ \text{For the } X_2 \text{ faces :} \quad & u_1^+ - u_1^- = \varepsilon_{12}^0(y_2^+ - y_2^-) = \varepsilon_{12}^0 h_2 \\ & u_2^+ - u_2^- = \varepsilon_{22}^0(y_2^+ - y_2^-) = \varepsilon_{22}^0 h_2 \\ & u_3^+ - u_3^- = \varepsilon_{32}^0(y_2^+ - y_2^-) = \varepsilon_{32}^0 h_2. \end{aligned} \quad (3.16)$$

Note that, in general, ε_{ij}^0 need not equal $\bar{\varepsilon}_{ij}$.

Here we show that $\bar{\varepsilon}_{\alpha\beta}$ can be computed theoretically prior to solving any BVP on any RVE as follows. First notice that

$$\begin{aligned}\langle \varepsilon_{ij} \rangle &= \bar{\varepsilon}_{ij} = \frac{1}{V_m} \iiint_{V_m} \varepsilon_{ij} dV_m = \frac{1}{2V_m} \iiint_{V_m} (u_{i,j} + u_{j,i}) dV_m \\ &= \frac{1}{2V_m} \iint_{S_m} (u_i n_j + u_j n_i) dS_m.\end{aligned}\quad (3.17)$$

Then $\bar{\varepsilon}_{11}$ can be found by

$$\bar{\varepsilon}_{11} = \frac{1}{2V_m} \iint_{S_m} (u_1^0 n_1 + u_1^0 n_1) dS_m = \frac{1}{V_m} \iint_{S_m} u_1^0 n_1 dS_m. \quad (3.18)$$

Since n_1 is nonzero only on the X_1 faces, we have

$$\begin{aligned}\bar{\varepsilon}_{11} &= \frac{1}{V_m} \iint_{X_1} u_1^0 n_1 dX_1 = \frac{1}{V_m} \iint_{X_1} (u_1^+ - u_1^-) dX_1 \\ &= \frac{1}{V_m} \iint_{X_1} \varepsilon_{11}^0 h_1 dX_1 = \varepsilon_{11}^0\end{aligned}\quad (3.19)$$

since $\iint_{X_1} dX_1 = h_2 h_3$ and $V_m = h_1 h_2 h_3$. Likewise for $\bar{\varepsilon}_{22}$, we have

$$\begin{aligned}\bar{\varepsilon}_{22} &= \frac{1}{V_m} \iint_{S_m} u_2^0 n_2 dS_m = \frac{1}{V_m} \iint_{X_2} u_2^0 n_2 dX_2 \\ &= \frac{1}{V_m} \iint_{X_2} (u_2^+ - u_2^-) dX_2 = \frac{1}{V_m} \iint_{X_2} \varepsilon_{22}^0 h_2 dX_2 = \varepsilon_{22}^0\end{aligned}\quad (3.20)$$

since $\iint_{X_2} dX_2 = h_1 h_3$. Finally for $\bar{\varepsilon}_{12}$ we have

$$\begin{aligned}2\bar{\varepsilon}_{12} &= \frac{1}{V_m} \iint_{S_m} (u_1^0 n_2 + u_2^0 n_1) dS_m = \frac{1}{V_m} \left(\iint_{X_2} u_1^0 n_2 dX_2 + \iint_{X_1} u_2^0 n_1 dX_1 \right) \\ &= \frac{1}{V_m} \left(\iint_{X_2} (u_1^+ - u_1^-) dX_2 + \iint_{X_1} (u_2^+ - u_2^-) dX_1 \right) \\ &= \frac{1}{V_m} \left(\iint_{X_2} \varepsilon_{12}^0 h_2 dX_2 + \iint_{X_1} \varepsilon_{21}^0 h_1 dX_1 \right) = 2\varepsilon_{12}^0\end{aligned}\quad (3.21)$$

since $\varepsilon_{12}^0 = \varepsilon_{21}^0$. Therefore, $\bar{\varepsilon}_{\alpha\beta} = \varepsilon_{\alpha\beta}^0$ for any RVE with in-plane PBCs. Notice that there are transverse shear strains in Eq. (3.16). Since a theoretical proof on how to know $\bar{\varepsilon}_{3\alpha}$ is not given here, this boundary condition is obtained iteratively until $\bar{\varepsilon}_{3\alpha} = \varepsilon_{3\alpha}^0$. That is, for a given BVP, $\varepsilon_{3\alpha}^0$ is initially applied. $\bar{\varepsilon}_{3\alpha}$ is then computed and the u_3 BCs on the in-plane faces are updated according to (3.16) but with $\varepsilon_{3\alpha}^0 = \bar{\varepsilon}_{3\alpha}$. This process is repeated until $|\bar{\varepsilon}_{32} - \varepsilon_{32}^0| < 10^{-9}$ and $|\bar{\varepsilon}_{31} - \varepsilon_{31}^0| < 10^{-9}$.

The PBCs imply that $t_i^+ = -t_i^-$. Since PBCs are on the in-plane faces for all nine BVPs, the integrals over S_α vanish in Eq. (3.13).

Out-of-plane Faces

If left as is, the out-of-plane properties would be unobtainable. Note that the mechanical PBCs are not enforced on the X_3 faces. Instead we apply the HSBCs

$$t_i^0 = \sigma_{ij}^0 n_j. \quad (3.22)$$

Here t_i^0 are the applied tractions and σ_{ij}^0 is a constant stress tensor. We apply this condition to X_3^+ and X_3^- thus

$$t_i^0 = \sigma_{i3}^0 n_3. \quad (3.23)$$

$\bar{\sigma}_{i3}$ can also be found prior to solving any BVP. Thus we seek to know what $\bar{\sigma}_{i3}$ is when the out-of-plane RVE loading is determined by Eq. (3.23) and when the in-plane faces are constrained by the PBCs. First note that

$$\sigma_{ij} = \sigma_{ik} \delta_{jk} = \sigma_{ik} \frac{\partial y_j}{\partial y_k} = (\sigma_{ik} y_j)_{,k} - \sigma_{ik,k} y_j = (\sigma_{ik} y_j)_{,k} \quad (3.24)$$

where $\sigma_{ik,k} = 0$ due to static equilibrium. An integration through the volume and an application of the divergence theorem gives

$$\begin{aligned} \langle \sigma_{i3} \rangle = \bar{\sigma}_{i3} &= \frac{1}{V_m} \iiint_{V_m} (\sigma_{ik} y_3)_{,k} dV_m = \frac{1}{V_m} \iint_{S_m} \sigma_{ik} y_3 n_k dS_m \\ &= \frac{1}{V_m} \iint_{S_m} t_i y_3 dS_m. \end{aligned} \quad (3.25)$$

Splitting the surface integral over X_i gives

$$\begin{aligned} \bar{\sigma}_{i3} &= \frac{1}{V_m} \left(\iint_{X_1} t_i y_3 dX_1 + \iint_{X_2} t_i y_3 dX_2 \right. \\ &\quad \left. + \iint_{X_3} t_i y_3 dX_3 \right). \end{aligned} \quad (3.26)$$

PBCs on the X_α faces imply that $t_i^+ = -t_i^-$ for every y_3 . Thus the surface integrals over the in-plane faces vanish. Also note that $t_i = t_i^0 = \sigma_{ij}^0 n_j$ on the X_3 faces. Eq. (3.26) simplifies to

$$\begin{aligned} \bar{\sigma}_{i3} &= \frac{1}{V_m} \iint_{X_3} \sigma_{ij}^0 n_j y_3 dX_3 = \frac{1}{V_m} \iint_{X_3} \sigma_{i3}^0 n_3 y_3 dX_3. \\ &= \frac{\sigma_{i3}^0}{V_m} \left(\iint_{X_3^+} y_3 n_3 dX_3^+ + \iint_{X_3^-} y_3 n_3 dX_3^- \right). \end{aligned} \quad (3.27)$$

Note that on X_3^+ we have $n_3 = 1$ and $y_3 = h_3/2$. On X_3^- we have $n_3 = -1$ and $y_3 = -h_3/2$. Thus

$$\bar{\sigma}_{i3} = \frac{\sigma_{i3}^0}{V_m} \left(\frac{h_3}{2} \iint_{X_3^+} dX_3^+ + \frac{h_3}{2} \iint_{X_3^-} dX_3^- \right) = \sigma_{i3}^0 \quad (3.28)$$

since $\iint_{X_3} dX_3 = h_1 h_2$.

The integral over S_3 in Eq. (3.13) has $n_\alpha = 0$ leaving $n_3 = \pm 1$. Thus the integral will vanish since $\sigma_{i3} = \sigma_{i3}^0$ on the boundary and $\bar{\sigma}_{i3} = \sigma_{i3}^0$ from Eq. (3.28); which completes the proof of $\Pi_m = 0$ for each of the nine BVPs.

3.2.3 Electrical BCs

First, we substitute $q = -D_k n_k$ in the second part of Eq. (3.11)

$$\Pi_e = \frac{1}{V_m} \iint_{S_m} (n_k \bar{D}_k + q) (\phi + y_i \bar{E}_i) dS_m. \quad (3.29)$$

Then the equation is split as before to yield

$$\begin{aligned} \Pi_e = \frac{1}{V_m} & \left(\iint_{S_1} (n_k \bar{D}_k + q) (\phi + y_i \bar{E}_i) dS_1 \right. \\ & + \iint_{S_2} (n_k \bar{D}_k + q) (\phi + y_i \bar{E}_i) dS_2 \\ & \left. + \iint_{S_3} (n_k \bar{D}_k + q) (\phi + y_i \bar{E}_i) dS_3 \right). \end{aligned} \quad (3.30)$$

Like the mechanical BCs, each of the integrals is shown to vanish under the selected BCs. It will also be useful to expand Eq. (1.54) and in the *applied* notation as

$$\begin{aligned} \phi^+ - \phi^- = & -E_1^0(y_1^+ - y_1^-) - E_2^0(y_2^+ - y_2^-) \\ & - E_3^0(y_3^+ - y_3^-). \end{aligned} \quad (3.31)$$

In-plane Faces

For the in-plane faces, the continuity of the electrical potential is enforced with the electrical PBCs. Eq. (3.15) also applies here so Eq. (3.31) becomes

$$\begin{aligned} \text{For the } X_1 \text{ faces :} \quad & \phi^+ - \phi^- = -E_1^0 h_1 \\ \text{For the } X_2 \text{ faces :} \quad & \phi^+ - \phi^- = -E_2^0 h_2. \end{aligned} \quad (3.32)$$

Take note that \bar{E}_α can also be known *a priori* to any FE analyses. Recall that the electric field is defined as the negative gradient of the electric potential (*cf* Eq. (1.5)). Thus, an integration over the volume followed by a utilization of the divergence theorem yields

$$\langle E_i \rangle = \bar{E}_i = -\frac{1}{V_m} \iiint_{V_m} \phi_{,i} dV_m = -\frac{1}{V_m} \iint_{S_m} \phi n_i dS_m. \quad (3.33)$$

For the in-plane electric fields we have

$$\begin{aligned} \bar{E}_1 &= -\frac{1}{V_m} \iint_{X_1} \phi n_1 dX_1 = -\frac{1}{V_m} \iint_{X_1} (\phi^+ - \phi^-) dX_1 \\ &= \frac{1}{V_m} \iint_{X_1} E_1^0 h_1 dX_1 = E_1^0. \end{aligned} \quad (3.34)$$

Likewise

$$\begin{aligned} \bar{E}_2 &= -\frac{1}{V_m} \iint_{X_2} \phi n_2 dX_2 = -\frac{1}{V_m} \iint_{X_2} (\phi^+ - \phi^-) dX_2 \\ &= \frac{1}{V_m} \iint_{X_2} E_2^0 h_2 dX_2 = E_2^0. \end{aligned} \quad (3.35)$$

Since $\bar{E}_\alpha = E_\alpha^0$, Eq. (3.32) will vanish the integrals over S_α in Eq. (3.30) for all nine BVPs. Thus only the out-of-plane surface integral remains.

Out-of-plane Faces

In general, the presence of electrodes is represented best by the equipotential condition. Thus, for Problems 1-6, $\phi^+ = \phi^- = 0$ on X_3 so as to represent the short-circuit condition. The question to answer next is what should the electrical BCs on X_3 be for the actuator problems; Problems 7 to 9.

It supposed that real piezoelectric devices do not have electrodes on every exterior surface so as to capture electrical behavior in all three directions. As mentioned earlier, only two opposing surfaces are typically coated with electrodes. The load case for E_3^0 (Problem 9) is straightforward since an electrode is actually present on X_3 . For this case, the electric potential is set to be $\phi^+ = c_1$ and $\phi^- = c_2$ on X_3 , where $c_1 - c_2 \neq 0$. The load cases for E_α^0 (Problems 7 and 8) are not as straightforward because the

actuating electrodes would be on in-plane boundaries of *the device* (x_α^+ and x_α^-) and not on in-plane boundaries of *the RVE* (X_α^+ and X_α^-). Nonetheless, we still seek to obtain a complete set of effective properties. Thus we seek boundary conditions that will produce a uniform in-plane electric field if the RVE were a homogeneous material. The electrical BCs options for X_3 are

$$\phi^+ = \phi^- = 0 \quad \phi^+ - \phi^- = 0 \quad q^+ = q^- = 0. \quad (3.36)$$

The selected BC on X_3 is $q^+ = q^- = 0$. This is because if in-plane electric fields were being applied, the electrodes on X_3 are expected to be absent. Thus it could not be short-circuited nor would the potential need to be periodic on X_3 .

Next, for every BVP, we need to examine whether the electrical BCs for X_3^+ and X_3^- satisfy the remaining surface integral in Eq. (3.30) which is written here

$$\Pi_e = \frac{1}{V_m} \iint_{S_3} (n_k \bar{D}_k + q) (\phi + y_i \bar{E}_i) dS_3. \quad (3.37)$$

Problems 1-6 and 9 have electrodes so $\phi^- = V_1$ on X_3^- and $\phi^+ = V_2$ on X_3^+ where V_1 and V_2 are constants. Substituting these constants into Eq. (3.31) and noting that, for a periodic mesh, we have $y_1^+ = y_1^-$, $y_2^+ = y_2^-$, $y_3^+ - y_3^- = h_3$, then we are left with

$$V_2 - V_1 = -E_3^0 h_3. \quad (3.38)$$

To complete the proof for $\Pi_e = 0$, we just need to show that $E_3^0 = \bar{E}_3$ under the equipotential difference. In like manner from Eq. (3.34) - (3.35) we have

$$\begin{aligned} \bar{E}_3 &= -\frac{1}{V_m} \iint_{X_3} \phi n_3 dX_3 = -\frac{1}{V_m} \iint_{X_3} (\phi^+ - \phi^-) dX_3 \\ &= \frac{1}{V_m} \iint_{X_3} E_3^0 h_3 dX_3 = E_3^0. \end{aligned} \quad (3.39)$$

and thus, the equipotential BCs satisfy the piezoelectric macrohomogeneity condition.

Finally, we address Problems 7 and 8 which are charge free on the out-of-plane faces. Among the many ways to have Π_e equal to zero in Eq. (3.37), we can choose to let $(n_k \bar{D}_k + q) = 0$. Thus, we need to show if $n_k \bar{D}_k = 0$ when q^+ and q^- are

zero. Since $n_\alpha = 0$ and $n_3 = \pm 1$ on X_3^+ and X_3^- , it is sufficient to show that $\bar{D}_3 = 0$ when $q^+ = q^- = 0$. Proceeding in a similar way to Eq. (3.24), it can first be shown that $D_j = (D_k y_j)_{,k}$. An integration through the volume and an application of the divergence theorem gives

$$\begin{aligned} \langle D_3 \rangle = \bar{D}_3 &= \frac{1}{V_m} \iiint_{V_m} (D_k y_3)_{,k} dV_m = \frac{1}{V_m} \iint_{S_m} D_k y_3 n_k dS_m \\ &= \frac{1}{V_m} \iint_{S_m} q y_3 dS_m = 0. \end{aligned} \quad (3.40)$$

This is because $q^+ = -q^-$ on X_α from the PBCs and $q = 0$ on X_3 from the absence of electrodes. This concludes the derivations for the boundary conditions and how each BVP rigorously satisfies the piezoelectric macrohomogeneity condition. In summary the boundary conditions we have arrived at are shown in Table 3.1.

Table 3.1. In-plane periodic boundary conditions for RVE analysis of thin piezocomposites.

Problem	X_1^-/X_1^+	X_2^-/X_2^+	X_3^-/X_3^+
1	$u_1^+ - u_1^- = h_1$	$u_1^+ - u_1^- = 0$	$t_i^+ = 0; t_i^- = 0$
	$u_2^+ - u_2^- = 0$	$u_2^+ - u_2^- = 0$	
	$u_3^+ - u_3^- = \bar{\varepsilon}_{31} h_1$	$u_3^+ - u_3^- = \bar{\varepsilon}_{32} h_2$	
	$\phi^+ - \phi^- = 0$	$\phi^+ - \phi^- = 0$	$\phi^+ = 0; \phi^- = 0$
2	$u_1^+ - u_1^- = 0$	$u_1^+ - u_1^- = 0$	$t_i^+ = 0; t_i^- = 0$
	$u_2^+ - u_2^- = 0$	$u_2^+ - u_2^- = h_2$	
	$u_3^+ - u_3^- = \bar{\varepsilon}_{31} h_1$	$u_3^+ - u_3^- = \bar{\varepsilon}_{32} h_2$	
	$\phi^+ - \phi^- = 0$	$\phi^+ - \phi^- = 0$	$\phi^+ = 0; \phi^- = 0$
3	$u_\alpha^+ - u_\alpha^- = 0$	$u_\alpha^+ - u_\alpha^- = 0$	$t_\alpha^+ = 0; t_\alpha^- = 0$
	$u_3^+ - u_3^- = \bar{\varepsilon}_{31} h_1$	$u_3^+ - u_3^- = \bar{\varepsilon}_{32} h_2$	$t_3^+ = 1; t_3^- = -1$
	$\phi^+ - \phi^- = 0$	$\phi^+ - \phi^- = 0$	$\phi^+ = 0; \phi^- = 0$
4	$u_\alpha^+ - u_\alpha^- = 0$	$u_\alpha^+ - u_\alpha^- = 0$	$t_1^+ = 0; t_1^- = 0$
Continued on next page			

Table 3.1 – continued from previous page

Problem	X_1^-/X_1^+	X_2^-/X_2^+	X_3^-/X_3^+
5	$t_2^+ = 1; t_2^- = -1$		
	$u_3^+ - u_3^- = \bar{\varepsilon}_{31}h_1$	$u_3^+ - u_3^- = \bar{\varepsilon}_{32}h_2$	$t_3^+ = 0; t_3^- = 0$
	$\phi^+ - \phi^- = 0$	$\phi^+ - \phi^- = 0$	$\phi^+ = 0; \phi^- = 0$
	$u_\alpha^+ - u_\alpha^- = 0$	$u_\alpha^+ - u_\alpha^- = 0$	$t_1^+ = 1; t_1^- = -1$
	$t_2^+ = 0; t_2^- = 0$		
	$u_3^+ - u_3^- = \bar{\varepsilon}_{31}h_1$	$u_3^+ - u_3^- = \bar{\varepsilon}_{32}h_2$	$t_3^+ = 0; t_3^- = 0$
6	$u_1^+ - u_1^- = 0$	$u_1^+ - u_1^- = h_2/2$	$t_i^+ = 0; t_i^- = 0$
	$u_2^+ - u_2^- = h_1/2$	$u_2^+ - u_2^- = 0$	
	$u_3^+ - u_3^- = \bar{\varepsilon}_{31}h_1$	$u_3^+ - u_3^- = \bar{\varepsilon}_{32}h_2$	
	$\phi^+ - \phi^- = 0$	$\phi^+ - \phi^- = 0$	$\phi^+ = 0; \phi^- = 0$
	$u_\alpha^+ - u_\alpha^- = 0$	$u_\alpha^+ - u_\alpha^- = 0$	$t_i^+ = 0; t_i^- = 0$
	$u_3^+ - u_3^- = \bar{\varepsilon}_{31}h_1$	$u_3^+ - u_3^- = \bar{\varepsilon}_{32}h_2$	
7	$\phi^+ - \phi^- = -h_1$	$\phi^+ - \phi^- = 0$	$q^+ = 0; q^- = 0$
	$u_\alpha^+ - u_\alpha^- = 0$	$u_\alpha^+ - u_\alpha^- = 0$	$t_i^+ = 0; t_i^- = 0$
	$u_3^+ - u_3^- = \bar{\varepsilon}_{31}h_1$	$u_3^+ - u_3^- = \bar{\varepsilon}_{32}h_2$	
	$\phi^+ - \phi^- = -h_1$	$\phi^+ - \phi^- = 0$	$q^+ = 0; q^- = 0$
	$u_\alpha^+ - u_\alpha^- = 0$	$u_\alpha^+ - u_\alpha^- = 0$	$t_i^+ = 0; t_i^- = 0$
	$u_3^+ - u_3^- = \bar{\varepsilon}_{31}h_1$	$u_3^+ - u_3^- = \bar{\varepsilon}_{32}h_2$	
8	$\phi^+ - \phi^- = 0$	$\phi^+ - \phi^- = -h_2$	$q^+ = 0; q^- = 0$
	$u_\alpha^+ - u_\alpha^- = 0$	$u_\alpha^+ - u_\alpha^- = 0$	$t_i^+ = 0; t_i^- = 0$
	$u_3^+ - u_3^- = \bar{\varepsilon}_{31}h_1$	$u_3^+ - u_3^- = \bar{\varepsilon}_{32}h_2$	
	$\phi^+ - \phi^- = 0$	$\phi^+ - \phi^- = -h_2$	$q^+ = 0; q^- = 0$
	$u_\alpha^+ - u_\alpha^- = 0$	$u_\alpha^+ - u_\alpha^- = 0$	$t_i^+ = 0; t_i^- = 0$
	$u_3^+ - u_3^- = \bar{\varepsilon}_{31}h_1$	$u_3^+ - u_3^- = \bar{\varepsilon}_{32}h_2$	
9	$\phi^+ - \phi^- = 0$	$\phi^+ - \phi^- = 0$	$\phi^+ = -h_3; \phi^- = 0$
	$u_\alpha^+ - u_\alpha^- = 0$	$u_\alpha^+ - u_\alpha^- = 0$	$t_i^+ = 0; t_i^- = 0$
	$u_3^+ - u_3^- = \bar{\varepsilon}_{31}h_1$	$u_3^+ - u_3^- = \bar{\varepsilon}_{32}h_2$	
	$\phi^+ - \phi^- = 0$	$\phi^+ - \phi^- = 0$	$\phi^+ = -h_3; \phi^- = 0$
	$u_\alpha^+ - u_\alpha^- = 0$	$u_\alpha^+ - u_\alpha^- = 0$	$t_i^+ = 0; t_i^- = 0$
	$u_3^+ - u_3^- = \bar{\varepsilon}_{31}h_1$	$u_3^+ - u_3^- = \bar{\varepsilon}_{32}h_2$	

For an example, Problem 1 considers $\varepsilon_{11}^0 = 1$ and all other $\varepsilon_{\alpha\beta}^0$, σ_{i3}^0 , and E_i^0 to be equal to zero. Note that letting $\sigma_{i3}^0 = 0$ leads to the X_3 faces being traction free. Then the required mechanical equation constrains for the in-plane faces are:

$$\begin{aligned}
\text{For the } X_1 \text{ faces : } \quad & u_1^+ - u_1^- = \varepsilon_{11}^0(y_1^+ - y_1^-) = h_1 \\
& u_2^+ - u_2^- = \varepsilon_{21}^0(y_1^+ - y_1^-) = 0 \\
& u_3^+ - u_3^- = \varepsilon_{31}^0(y_1^+ - y_1^-) = \varepsilon_{31}^0 h_1 \\
\text{For the } X_2 \text{ faces : } \quad & u_1^+ - u_1^- = \varepsilon_{12}^0(y_2^+ - y_2^-) = 0 \\
& u_2^+ - u_2^- = \varepsilon_{22}^0(y_2^+ - y_2^-) = 0 \\
& u_3^+ - u_3^- = \varepsilon_{32}^0(y_2^+ - y_2^-) = \varepsilon_{32}^0 h_2. \tag{3.41}
\end{aligned}$$

Then one needs to compare whether $\varepsilon_{3\alpha}^0 = \bar{\varepsilon}_{3\alpha}$. If not, the BVP needs to be solved again after updating the u_3 BCs on the in-plane faces with $u_3^+ - u_3^- = \bar{\varepsilon}_{3\alpha}(y_\alpha^+ - y_\alpha^-)$.

3.3 Rectification of the PBCs

As mentioned in Chapter 1, there have been many issues with the application of the PBCs. The issue with [58] is that they assumed that $\varepsilon_{ij}^0 = \bar{\varepsilon}_{ij}$. In the previous section it was shown that $\bar{\varepsilon}_{\alpha\beta} = \varepsilon_{\alpha\beta}^0$, $\bar{E}_\alpha = E_\alpha^0$ for any RVE with in-plane PBCs. All that is left is to show that $\bar{\varepsilon}_{i3} = \varepsilon_{i3}^0$ and $\bar{E}_3 = E_3^0$ with the PBCs are utilized on the out-of-plane faces.

Following Eq. (3.17), $\bar{\varepsilon}_{33}$ can be found with

$$\begin{aligned}
\bar{\varepsilon}_{33} &= \frac{1}{V_m} \iint_{S_m} u_3^0 n_3 dS_m = \frac{1}{V_m} \iint_{X_3} u_3^0 n_3 dX_3 \\
&= \frac{1}{V_m} \iint_{X_3} (u_3^+ - u_3^-) dX_3 = \frac{1}{V_m} \iint_{X_3} \varepsilon_{33}^0 h_3 dX_3 = \varepsilon_{33}^0 \tag{3.42}
\end{aligned}$$

since $\iint_{X_3} dX_3 = h_1 h_2$. For $\bar{\varepsilon}_{13}$ we have

$$\begin{aligned} 2\bar{\varepsilon}_{13} &= \frac{1}{V_m} \iint_{S_m} (u_1^0 n_3 + u_3^0 n_1) dS_m = \frac{1}{V_m} \left(\iint_{X_3} u_1^0 n_3 dX_3 + \iint_{X_1} u_3^0 n_1 dX_1 \right) \\ &= \frac{1}{V_m} \left(\iint_{X_3} (u_1^+ - u_1^-) dX_3 + \iint_{X_1} (u_3^+ - u_3^-) dX_1 \right) \\ &= \frac{1}{V_m} \left(\iint_{X_3} \varepsilon_{13}^0 h_3 dX_3 + \iint_{X_1} \varepsilon_{31}^0 h_1 dX_1 \right) = 2\varepsilon_{13}^0. \end{aligned} \quad (3.43)$$

For $\bar{\varepsilon}_{23}$ we have

$$\begin{aligned} 2\bar{\varepsilon}_{23} &= \frac{1}{V_m} \iint_{S_m} (u_2^0 n_3 + u_3^0 n_2) dS_m = \frac{1}{V_m} \left(\iint_{X_3} u_2^0 n_3 dX_3 + \iint_{X_2} u_3^0 n_2 dX_2 \right) \\ &= \frac{1}{V_m} \left(\iint_{X_3} (u_2^+ - u_2^-) dX_3 + \iint_{X_2} (u_3^+ - u_3^-) dX_2 \right) \\ &= \frac{1}{V_m} \left(\iint_{X_3} \varepsilon_{23}^0 h_3 dX_3 + \iint_{X_2} \varepsilon_{32}^0 h_2 dX_2 \right) = 2\varepsilon_{23}^0. \end{aligned} \quad (3.44)$$

Then, following Eq. (3.33)

$$\begin{aligned} \bar{E}_3 &= -\frac{1}{V_m} \iint_{X_3} \phi n_3 dX_3 = -\frac{1}{V_m} \iint_{X_3} (\phi^+ - \phi^-) dX_3 \\ &= \frac{1}{V_m} \iint_{X_3} E_3^0 h_3 dX_3 = E_3^0. \end{aligned} \quad (3.45)$$

Therefore $\bar{\varepsilon}_{ij} = \varepsilon_{ij}^0$ and $\bar{E}_i = E_i^0$ for any RVE with PBCs on every boundary face.

3.4 Post-Processing for Mixed BCs and PBCs

The effective properties can be found after solving every BVP. A new post-processing scheme was developed to enable crosschecking the symmetry of the obtained constitutive relations. It was also found to be a unified procedure for the effective properties. The same procedure is applicable to any piezoelectric homogenization; regardless of BCs and the material poling direction. First we numerically compute components of $\bar{\sigma}_{ij}$, $\bar{\varepsilon}_{ij}$, \bar{D}_i , and \bar{E}_i with Eq. (2.40) (note that it is not necessary to compute some of the field averages because of Eqs. (3.19), (3.20), (3.21), (3.28), (3.34), (3.35), (3.39) and (3.40)). Then, for each of the nine BVPs, nine

equations are formulated from Eq. (1.51) and the numerically computed field averages; yielding a total of 81 equations. There are 81 unknowns and they are effective properties in Eq. (1.51). They can be obtained by solving the linear system.

3.5 Results

The following sections show results obtained from Abaqus[®]. Python scripts were implemented to facilitate the modeling. All element types were C3D20E. The dielectric and mechanical stiffness coefficients are scaled with a scale factor in an effort to avoid numerical errors. The chosen scale factor, s , was 10^{10} . The scaling is performed with

$$\frac{1}{s}C_{ijkl}^E \quad \frac{s}{s}e_{kij} \quad \frac{s}{1}k_{ij}^\varepsilon. \quad (3.46)$$

After performing the volume averaging and post-processing, the effective properties are obtained by performing the inverse operation of each property type.

3.5.1 Case A Example

As mentioned earlier, composites that have unidirectional, continuous, and prismatic fibers that span an in-plane dimension is an important case (see Figure 1.6, Case A). Here we present a comparison between boundary conditions for rectangular SONOX P502 piezoceramic fibers and epoxy. The thickness is fixed and the fiber width is varied. The constituent information as well as the thickness ($0.18 \mu\text{m}$) was obtained from Deraemaeker *et al* [48]. The relevant properties of SONOX P502 can be found in Table 2.1. For the epoxy we take $Y = 2.9 \text{ GPa}$, $\nu = 0.3$, and $\kappa/\epsilon_0 = 4.25$.

Here it is important to disclose that the MIX-sensor (Problem 4) and MIX-actuator (Problem 8) BVPs produced differing properties for e_{24}^* and therefore d_{24}^* . This would lead to an asymmetric constitutive relation that is due to the modelling choices and is not expected to be a physical property of MFCs. Figure 3.1 shows d_{24}^* and the other secondary properties d_{15}^* , and $k_{\alpha\alpha}^{\sigma*}$ (no summation on α implied).

These are considered secondary because electrodes are only expected on X_3 . Two curves for each BC case are plotted to examine the symmetry of the effective constitutive relations. Note that since $[k^{\sigma*}]$ is obtained from $[k^{\varepsilon*}]$ after post-processing

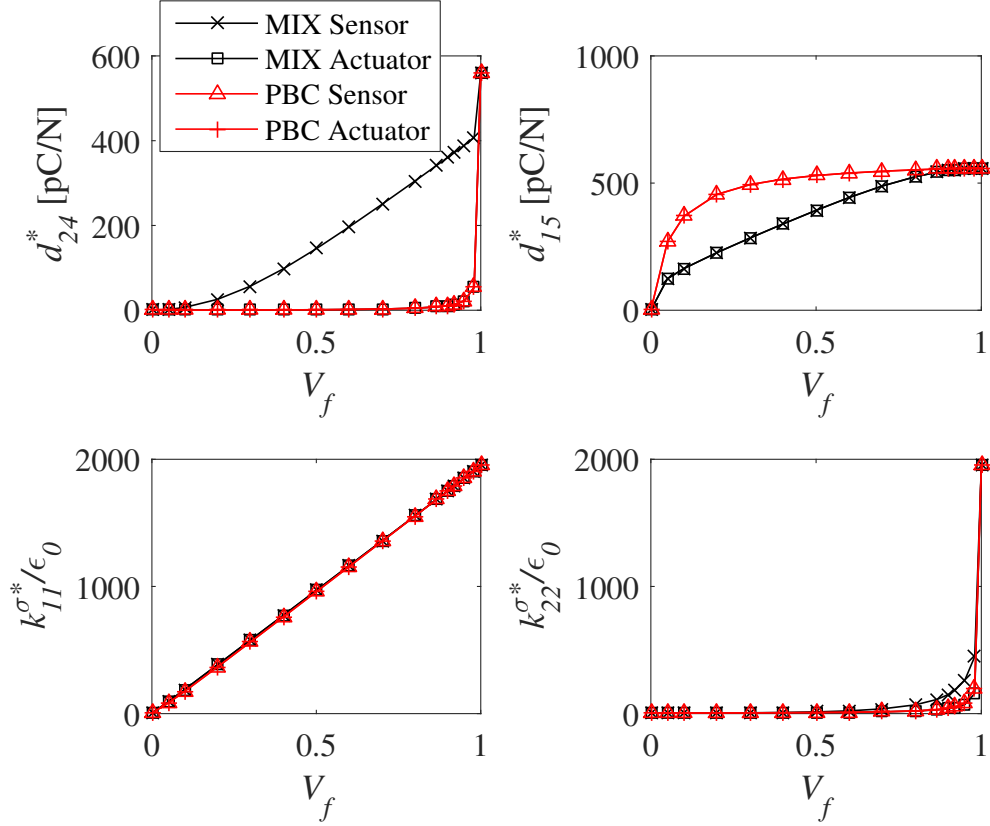


Figure 3.1: Symmetry examination of the piezoelectric strain coefficients for Case A composites.

($[k^{\sigma*}] = [k^{\varepsilon*}] + [d^*]^T[e^*]$) and since d^*_{24} and e^*_{24} each have two values for each fiber volume fraction, then two curves for $k^{\sigma*}_{22}$ have also been plotted. Let $[d^*]$, $[e^*]$, and $[k^{\sigma*}]$ be the properties obtained from the sensor problems (Problems 1 to 6) and $[d^*]$, $[e^*]$, and $[k^{\sigma*}]$ be the properties obtained from the actuator problems (Problems 7 to 9). Then

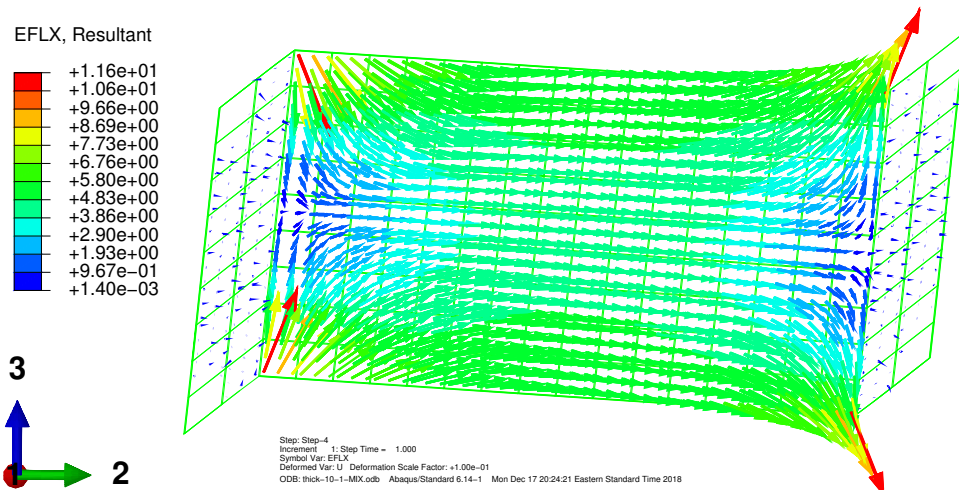
$$[k^{\sigma*}] = [k^{\varepsilon*}] + [d^*]^T[e^*] \quad [k^{\sigma*'}] = [k^{\varepsilon*}] + [d^{*'}]^T[e^{*'}]. \quad (3.47)$$

Note that $k^{\varepsilon*}$ and $k^{\sigma*}$ (as well as C^{E*}) were verified to be symmetric.

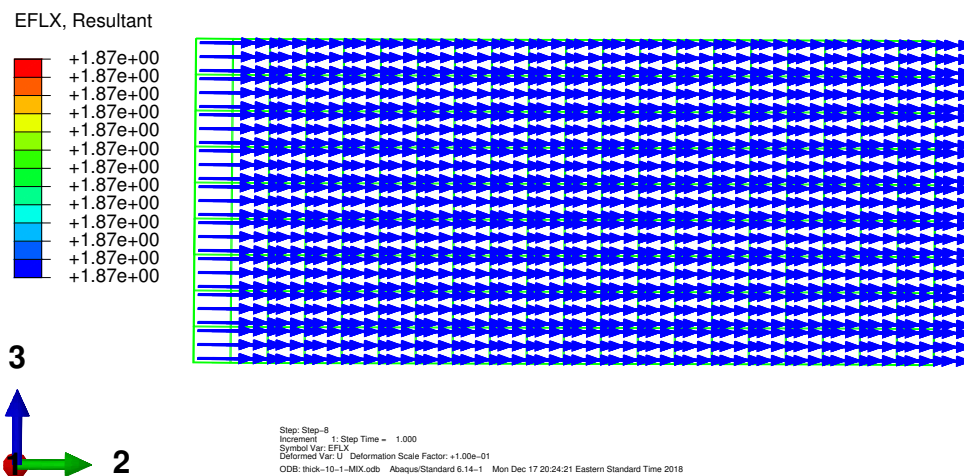
It is clear from Figure 3.1 that MIX results for d_{24}^* (sensor) is much larger than $d_{24}^{*'} (actuator)$ for most volume fractions. However, the reason for the disparity is uncertain. One reason for the difference may be that the fourth BVP in Table 3.1 produces nonuniform electric displacements *in the PZT fiber* whereas the eighth BVP produces uniform electric displacements throughout *the whole RVE*. These effects are illustrated in Figure 3.2. This disparity also affects the $k_{22}^{\sigma*}$ due to the post-processing. The other properties were found to be symmetric for both MIX and PBC cases. Thus they each have $d_{15}^* = d_{15}^{*'}$ and $k_{11}^{\sigma*} = k_{11}^{\sigma*'}$.

Verification of the Asymmetric Shear Coupling

The great difference between d_{24}^* and $d_{24}^{*'}$ warranted further investigation. The asymmetric result was verified to be correct by performing two direct numerical simulations (DNS) of the MFC active layer ($V_f = 0.8654$) that included 11 fibers. The DNS is represented in Figure 3.3. One case was the sensor case whereby transverse shear tractions were applied (to produce $\bar{\sigma}_{23}$). The other case was the actuator case where a potential difference between x_2^+ and x_2^- was specified while the remaining faces were charge free. Note that x_i^+ and x_i^- are used here to denote boundaries of the macroscopic structure. X_i^+ and X_i^- are reserved for RVE boundaries. See Table 3.2 for BCs applied to both problems. The width, as well as the length, was 4.525 mm and the height was 0.180 mm (actually all geometric lengths were normalized by 0.41137 mm; the supposed width of the RVE along x_2). The aforementioned DNS dimensions were deemed sufficiently large such that St. Venant effects do not influence the local fields of an RVE near the centroid of the structure. Therefore the DNSs did not have any of the in-plane PBC constraints as in the MIX RVE analysis. The model consisted of 98,670 C3D20E elements in Abaqus® (which results in 458,670 nodes). 20 Central processing units (CPUs) solved the BPVs in 1.8 minutes of wallclock time. Refer to Chapter 5 for more details of the CPUs.



(a) BVP 4.



(b) BVP 8.

Figure 3.2: Resultant of the scaled electric displacement ($\mu\text{C}/\text{mm}^2/\text{s}$) from BVPs in Table 3.1 plotted on the deformed shape. $V_f = 0.8$.

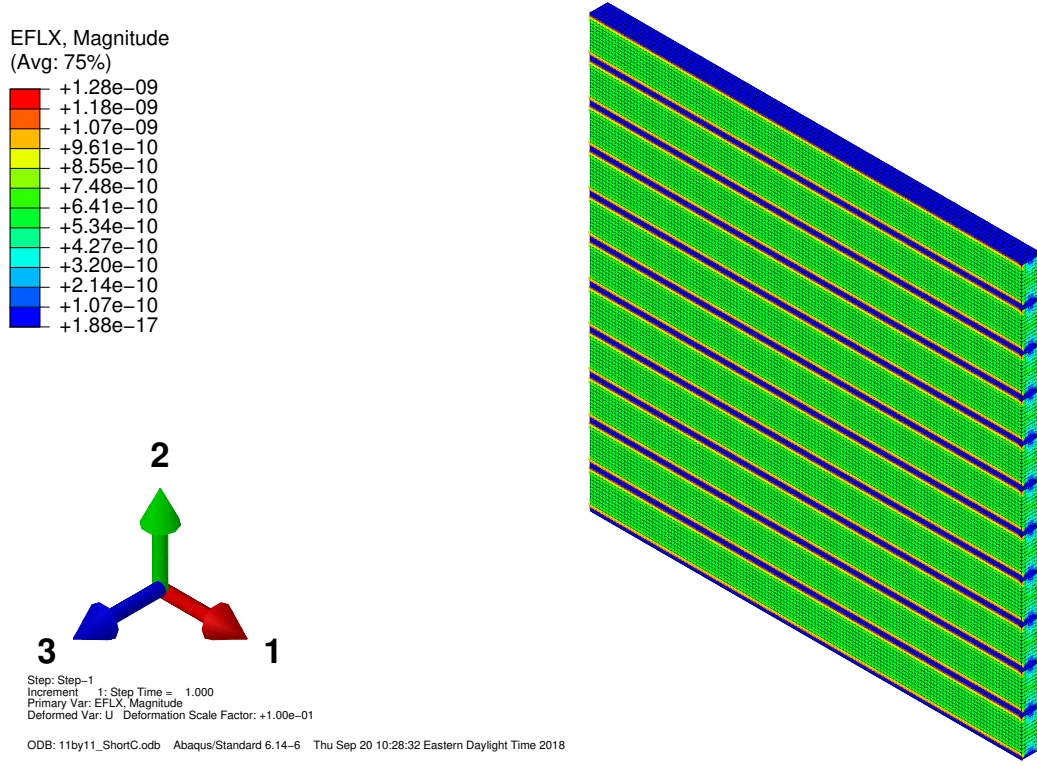


Figure 3.3: The DNS of the active layer.

Table 3.2: Boundary Conditions for two DNSs that verify asymmetric piezoelectric shear coupling results from the proposed RVE analysis.

Problem	x_1^-/x_1^+	x_2^-/x_2^+	x_3^-/x_3^+
4 (Sensor)	$t_i^+ = 0; t_i^- = 0$	$t_1^+ = 0; t_1^- = 0$	$t_1^+ = 0; t_1^- = 0$
		$t_2^+ = 0; t_2^- = 0$	$t_2^+ = 1; t_2^- = -1$
		$t_3^+ = 1; t_3^- = -1$	$t_3^+ = 0; t_3^- = 0$
		$q^+ = 0; q^- = 0$	$\phi^+ = 0; \phi^- = 0$
8 (Actuator)	$t_i^+ = 0; t_i^- = 0$	$t_i^+ = 0; t_i^- = 0$	$t_i^+ = 0; t_i^- = 0$
		$\phi^+ = 1500; \phi^- = 0$	$q^+ = 0; q^- = 0$

d_{24}^* was computed from the sensor problem by computing $\bar{D}_2/\bar{\sigma}_{23} = 341.72$ pC/N (cf. Table 3.4). $d_{24}^{*'}$ was computed from the other problem by computing $2\bar{\varepsilon}_{23}/\bar{E}_2 = 7.739$ pC/N. These are in agreement to the proposed RVE analysis. The procedure was verified by changing the epoxy regions to PZT and redoing the computations; thus converting the problem to an analysis of a homogeneous PZT. The procedure correctly recovered the SONOX P502 properties with $d_{24}^* = d_{24}^{*'} = 560$ pC/N. This is consistent with our MIX RVE analysis since the plot for d_{24}^* in Figure 3.1 shows that MIX produces equal properties for the sensor and actuator cases at $V_f = 1.0$.

Since an asymmetric constitutive relation cannot be utilized, it is recommended that engineers and designers use d_{24}^* (or e_{24}^*) resulting from the sensor problem (Problem 4 in Case A) rather than $d_{24}^{*'} (e_{24}^{*'})$ obtained from the actuator problem (Problem 8). Reason being that in-plane electric field actuation is not expected to be a real mode of operation.

Figure 3.4 shows the short-circuit elastic properties as the BCs and fiber volume fraction are varied. We note perfect agreement between the MIX and PBCs for Y_1^{E*} and G_{12}^{E*} . Also note that Y_2^{E*} and G_{23}^{E*} for MIX are similar but not identical to the PBCs in their respective cases. Significant differences are noted for the out-of-plane properties Y_3^{E*} , G_{13}^{E*} , ν_{13}^{E*} , and ν_{23}^{E*} .

Figure 3.5 shows the piezoelectric coefficients for the constitutive form of Eq. (1.15) while Figure 3.6 shows the form of Eq. (1.16). Note that the results in Figure 3.6 are that of Figure 3.5 but post-processed with $[d^*] = [C^{E*}]^{-1}[e^*]$ and $[k^{\sigma*}] = [k^{\varepsilon*}] + [d^*]^T[e^*]$. As recommended earlier, e_{24}^* and d_{24}^* from the Sensor behavior is plotted. Like the last chapter, the permittivity was normalized by the permittivity of free-space ($\epsilon_0 = 8.854$ pF/m). With the exception of e_{32}^* and d_{32}^* , the out-of-plane properties are again the most affected. e_{32}^* and d_{32}^* feature significant differences for most volume fractions. The piezoelectric coefficients related to deformation along x_1 , namely, d_{31}^* and e_{31}^* , are affected by a small amount.

Many of the differences between the MIX and PBC cases are from the added flexibility of the X_3 faces for the MIX case. Figures 3.7 and 3.8 illustrate the occurrence

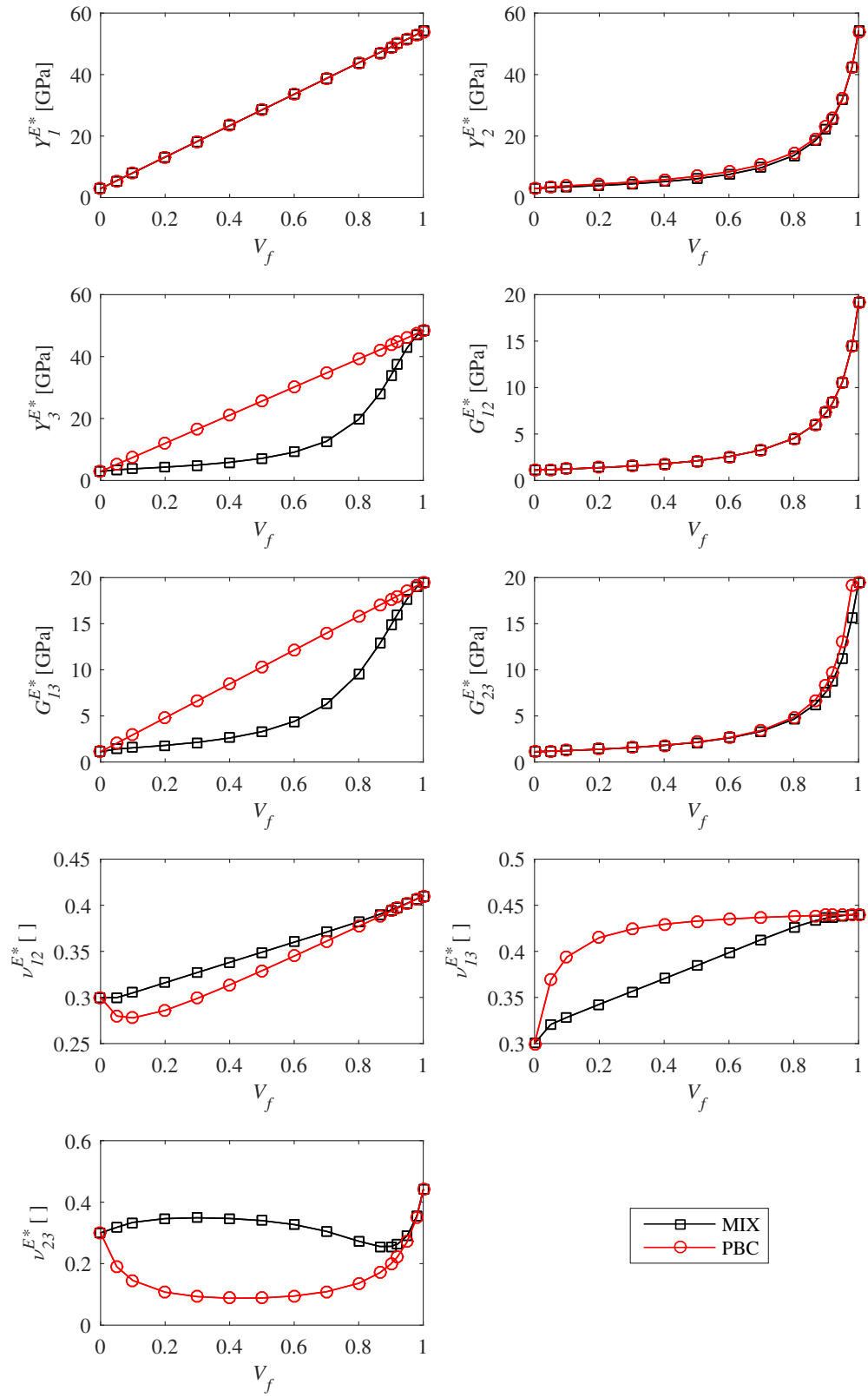


Figure 3.4: Boundary condition effects on the effective elastic moduli for Case A composites.

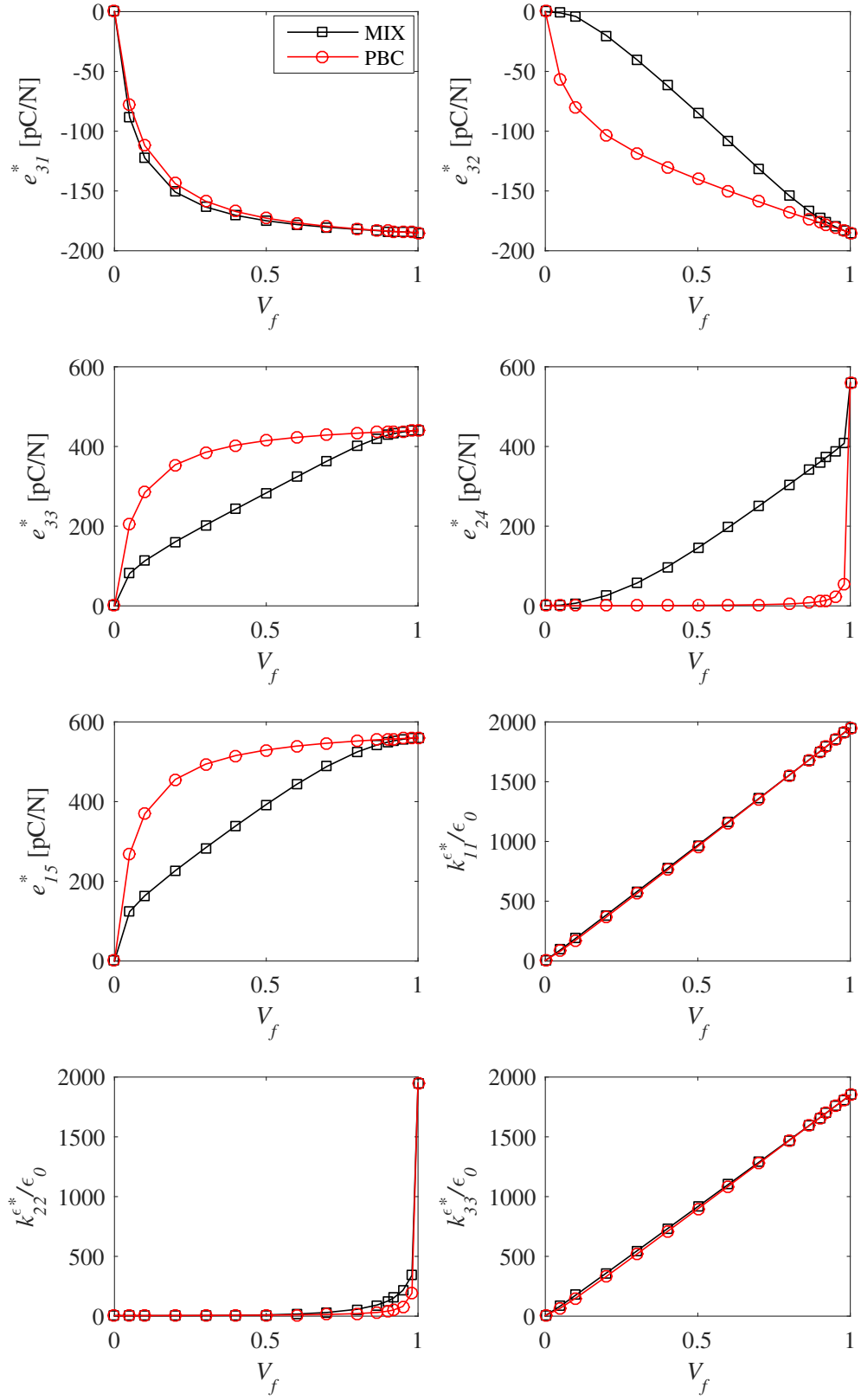


Figure 3.5: Boundary condition effects on the effective piezoelectric e-form coefficients for Case A composites.

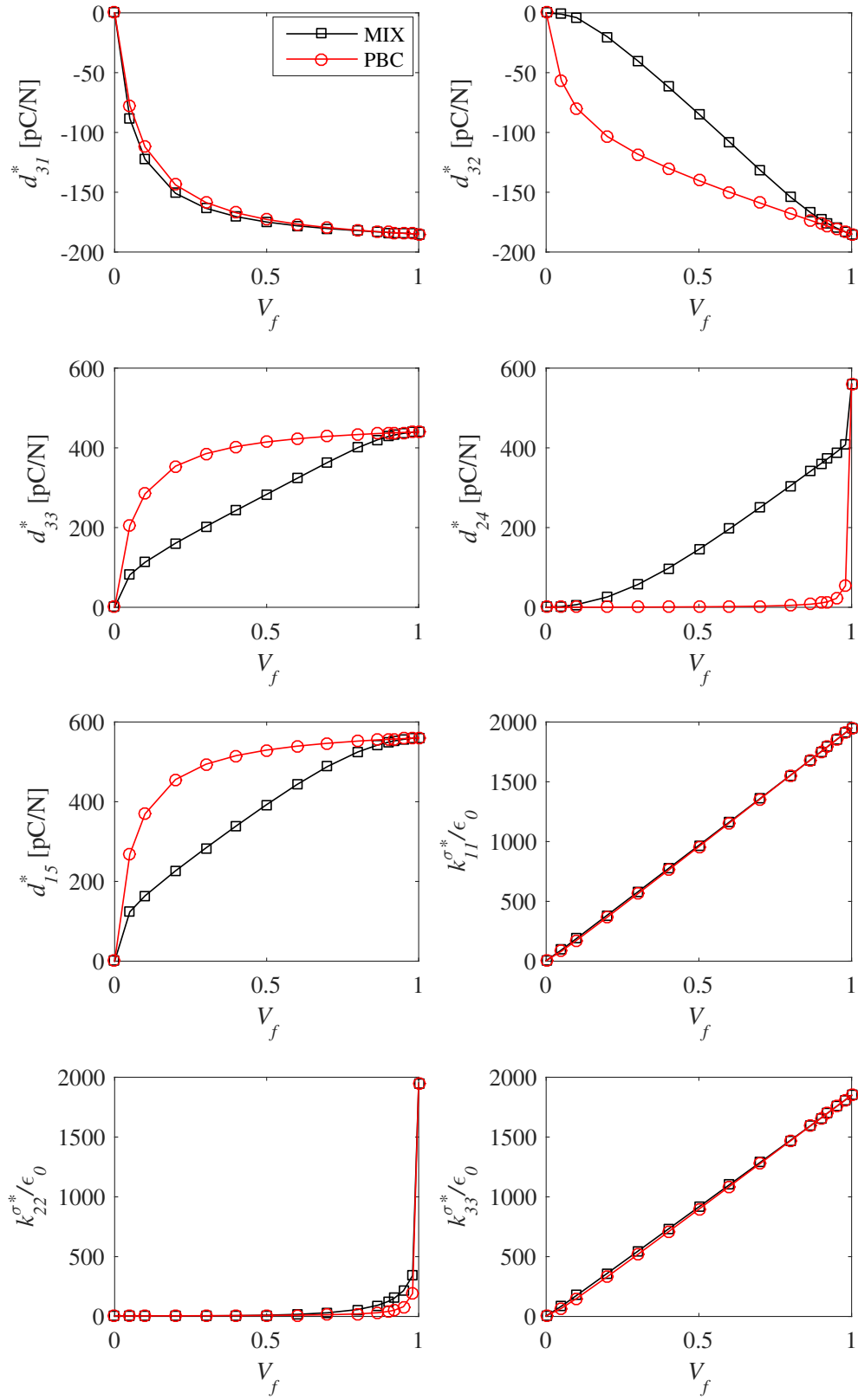


Figure 3.6: Boundary condition effects on the effective piezoelectric d-form coefficients for Case A composites.

of nonuniform strains in the MIX case whereas the PBC case predicts uniform results. Figure 3.7 shows the response when the RVE is subjected to purely out-of-plane loading whereas Figure 3.8 shows a transverse shear deformation case (ε_{13}). In both figures, it is notable that the MIX BCs allow for most of the deformation to be concentrated in the epoxy. This is not the case for the PBCs. Thus the MIX BCs are better able to account for the added flexibility of the epoxy. Refer to [87] for studies of nonuniform displacement profiles of the top surface for a Case B composite.

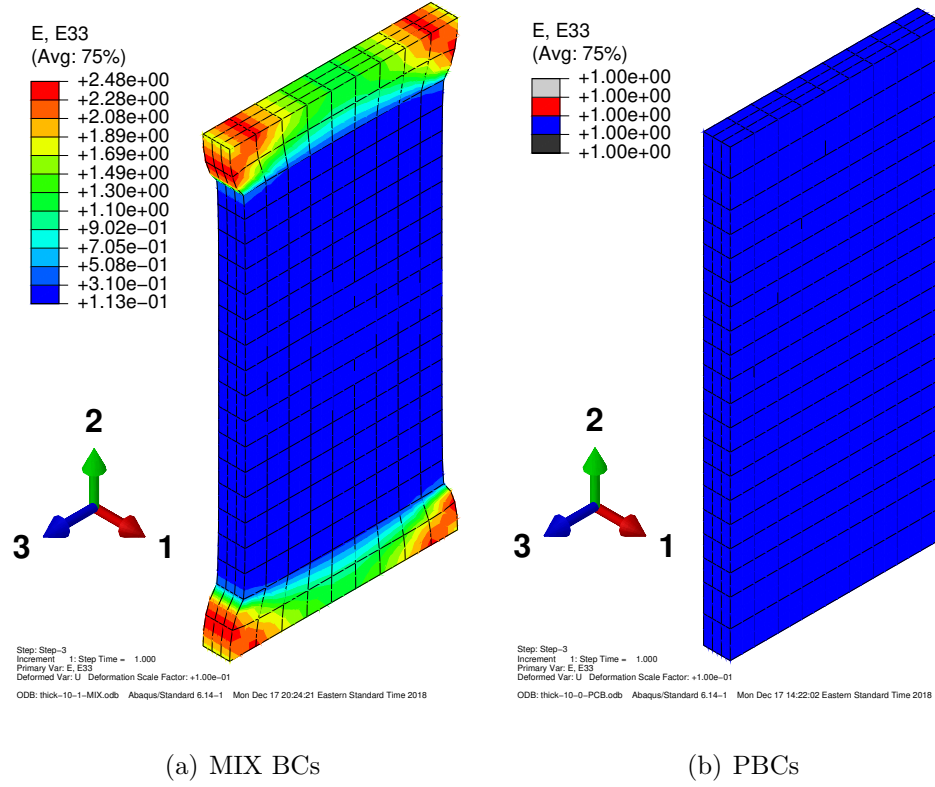


Figure 3.7: Deformed shapes that contrast the nonuniform transverse normal strain of the MIX BCs to the uniform result of the PBCs. $V_f = 0.8$.

The previous results on the MFC active layer have been presented to study boundary condition effects for many volume fractions. Now we present tabular data at the volume fraction that is relevant to commercially available MFCs. Simply by performing material transformations, one can simulate different axes of poling. Here we can

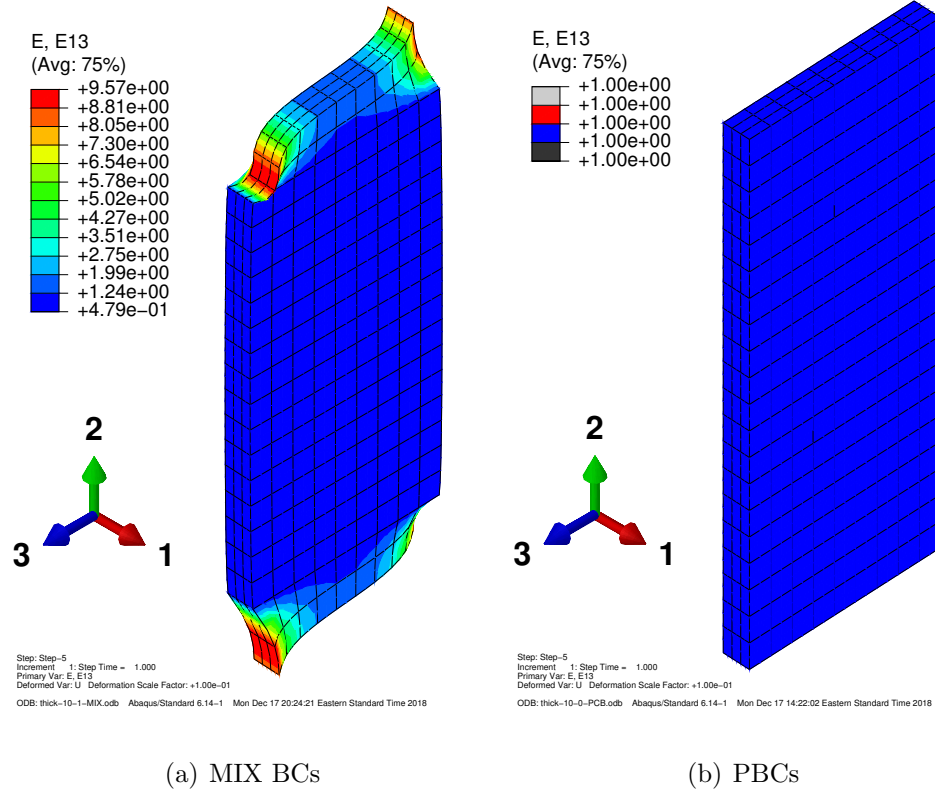


Figure 3.8: Deformed shapes that contrast a nonuniform transverse shear strain of the MIX BCs to the uniform result of the PBCs. $V_f = 0.8$.

consider uniform poling along x_1 or x_3 (see x_i in Case A of Figure 1.6). (Recall that the subscript, 3, in Table 2.1 corresponds to the poling direction.) The P2 MFC can be simulated when the poling axis is along x_3 (as in the preceding plots). The nonuniform poling of the P1 MFC can be approximated with PZT material that is uniformly and fully poled along x_1 [49]. The effective properties of each of the two cases are at a volume fraction of $V_f = 0.8654$ [47] and are tabulated in Tables 3.3 and 3.4. Note that all of the properties are reported in the x_i coordinate system of Figure 1.6; regardless of the poling axis. As it was recommended above, the sensor properties ($[d^*]$, $[e^*]$, and $[k^{\sigma*}]$) rather than the actuator ($[d'^*]$, $[e'^*]$, and $[k^{\sigma'*}]$) are documented.

Table 3.3: Effective elastic properties for uniformly poled MFC fiber layers. All moduli are in GPa.

	Y_1^{E*}	Y_2^{E*}	Y_3^{E*}	G_{12}^{E*}	G_{13}^{E*}	G_{23}^{E*}	ν_{12}^{E*}	ν_{13}^{E*}	ν_{23}^{E*}
P2 MFC (MIX)	47.17	18.38	28.06	6.031	12.83	6.233	0.3902	0.4331	0.2558
P2 MFC (PBC)	47.17	19.12	42.19	6.031	17.01	6.685	0.3879	0.4388	0.1702
P1 MFC (MIX)	42.19	18.37	29.93	6.219	12.85	6.031	0.3773	0.3886	0.2449
P1 MFC (PBC)	42.19	19.12	47.17	6.685	17.01	6.031	0.3758	0.3925	0.1572

Table 3.4: Effective piezoelectric and dielectric properties for uniformly poled MFC fiber layers. Piezoelectric stain constants are in pC/N.

	d_{31}^*	d_{32}^*	d_{33}^*	d_{24}^*	d_{15}^*	$\kappa_{11}^{\sigma*}/\epsilon_0$	$\kappa_{22}^{\sigma*}/\epsilon_0$	$\kappa_{33}^{\sigma*}/\epsilon_0$
P2 MFC (MIX)	-183.1	-167.0	420.4	341.3	542.4	1684	111.3	1595
P2 MFC (PBC)	-183.0	-173.5	435.9	7.739	555.1	1683	31.14	1593
	d_{11}^*	d_{12}^*	d_{13}^*	d_{26}^*	d_{35}^*	$\kappa_{11}^{\sigma*}/\epsilon_0$	$\kappa_{22}^{\sigma*}/\epsilon_0$	$\kappa_{33}^{\sigma*}/\epsilon_0$
P1 MFC (MIX)	435.9	-174.4	-180.8	352.4	542.5	1593	118.3	1684
P1 MFC (PBC)	435.9	-173.5	-183.0	7.739	555.1	1593	31.14	1683

3.5.2 Case B Example

The MIX boundary conditions are now compared to results found in Berger *et al* [36] which is Case B. Recall that they do not actually utilize the full PBCs. Therefore results from the full PBCs according to Eq. (1.53) and (1.54) along with the post-processing described in Section 3.4 are also included. Following [36], we consider a cylindrical piezoceramic rod in an epoxy matrix. The rod is made of PZT-7A and is fully polarized along the x_3 -axis (see Figure 1.6, Case B). This axis is also the axis of symmetry for the rod geometry and its material properties. The material properties of the PZT-7A and the epoxy were identical to Table 3 of Berger *et al* [36]. The comparisons are facilitated by converting, $[C^{E*}]$, $[e^*]$, and $[k^\varepsilon]$ to $[C^{D*}]$, $[h^*]$, and $[\beta^{\varepsilon*}]$ with

$$\begin{aligned} [S^{E*}] &= [C^{E*}]^{-1} & [d^*] &= [S^{E*}] [e^*] \\ [k^{\sigma*}] &= [k^{\varepsilon*}] + [d^*]^T [e^*] & [\beta^{\sigma*}] &= [k^{\sigma*}]^{-1} \\ [g^*] &= [d^*] [\beta^{\sigma*}] & [S^{D*}] &= [S^{E*}] - [g^*] [d^*]^T \\ [C^{D*}] &= [S^{D*}]^{-1} & [h^*] &= [C^{D*}] [g^*] \end{aligned} \quad (3.48)$$

from Section 1.2.3. We are interested in knowing what effects do our proposed boundary conditions (and post-processing) have on the effective properties for a variety of rod volume fractions, V_f , and rod aspect ratio h_3/d (d is the rod diameter).

At a given aspect ratio and V_f , the rod diameter is found from $d = 2\sqrt{V_f/\pi}$. Then h_3 is determined from

$$h_3 = (h_3/d)d. \quad (3.49)$$

Note that h_α is fixed to 1.0 m for all cases. Figure ?? illustrates the RVE height differences for each considered aspect ratio.

Table 3.5 compares the MIX BCs to full PBCs and to [36] for $V_f = 0.6$. It numerically shows the convergent behavior of the MIX BCs to the PBCs as the aspect ratio increases. As in Case A, the sensor properties are reported for piezoelectric coupling terms (note that the MIX BCs will produce two asymmetric shear coupling

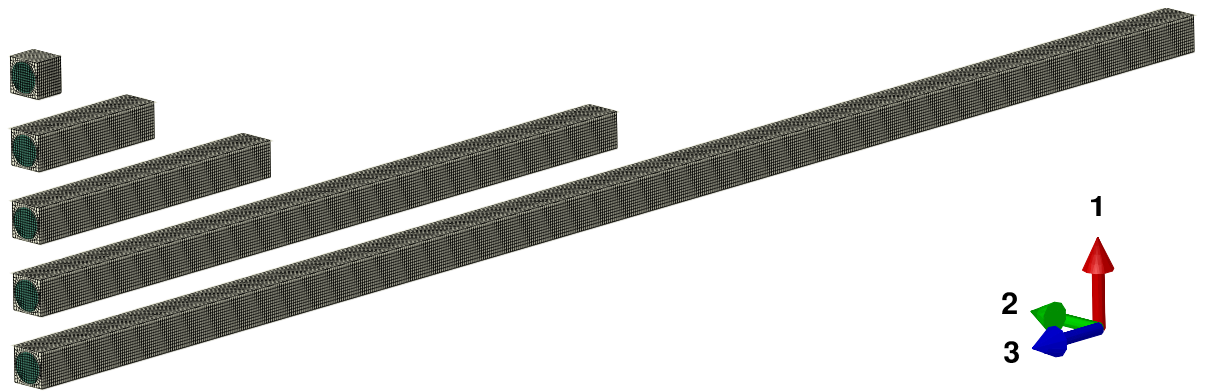


Figure 3.9: Case B meshes used with fiber aspect ratios of 1, 5, 10, 25, and 50 ($V_f = 0.6$).

terms for Case B since the composite is transversely isotropic; namely e_{24}^* and e_{15}^*). Note that only the shear coupling term, $h_{15}^{*'}$, from the actuator problem is appended to the table for reference. It is notable that $h_{15}^{*'}$ from the MIX BCs also appears to converge to the fully PBC case.

Table 3.5: Comparison of Case B effective properties obtained from the periodic BCs and a mixture of periodic and homogeneous stress BCs at $V_f = 0.6$.

MIX						Fully PBC	Berger et al [36]
h_3/d	1	5	10	25	50	1	
C_{11}^{D*} (GPa)	24.65	24.91	24.94	24.96	24.97	24.97	25.17
C_{12}^{D*} (GPa)	8.984	8.775	8.75	8.735	8.732	8.726	8.71
C_{13}^{D*} (GPa)	9.921	10.41	10.56	10.68	10.71	10.77	10.82
C_{33}^{D*} (GPa)	32.83	64.57	74.10	81.3	84.03	86.74	86.97
C_{44}^{D*} (GPa)	7.807	6.623	6.609	6.619	6.625	6.632	6.66
C_{66}^{D*} (GPa)	4.604	4.608	4.610	4.612	4.604	4.610	4.64
$\beta_{11}^{\varepsilon*}$ ($\frac{\text{GVm}}{\text{C}}$)	6.564	6.447	6.432	6.416	6.383	6.413	6.364
$\beta_{33}^{\varepsilon*}$ ($\frac{\text{GVm}}{\text{C}}$)	0.5368	0.682	0.7253	0.759	0.7737	0.783	0.781
h_{31}^* ($\frac{\text{GV}}{\text{m}}$)	-0.2122	-0.1797	-0.1697	-0.1624	-0.1601	-0.1563	-0.157
h_{33}^* ($\frac{\text{GV}}{\text{m}}$)	1.392	3.538	4.181	4.671	4.866	5.034	5.034
h_{15}^* ($\frac{\text{GV}}{\text{m}}$)	3.539	1.027	0.6805	0.4687	0.3956	0.3258	0.328
$h_{15}^{*'}$ ($\frac{\text{GV}}{\text{m}}$)	0.2858	0.3174	0.3216	0.3242	0.3251	0.3258	N/A

A comparison of these values reveals that, like Case A, the out-of-plane effective properties are the most affected by the finite-thickness effects captured by the MIX BCs. It is notable that h_{33}^* and C_{33}^{D*} about doubled when the aspect ratio was increased from one to five; indicating a large sensitivity to aspect ratio at low ratios. See Gururaja *et al* [150] for experimental evidence of finite thickness effects. The aspect ratio had little to no effect on the in-plane properties. It was also verified, as

expected, that the PBCs are insensitive to the fiber aspect ratio and therefore the device thickness. The reason for the differences between the MIX and PBC results is again due to the flexibility added from the MIX BCs.

3.6 Discussion

Recall that the most accurate piezoelectric homogenization methods are based on the assumption of a fully (3D) periodic RVE; that is, FE with PBCs [36], Asymptotic Homogenization [29], and VAMUCH [28]. However, from our results, it is clear that finite thicknesses can have a strong influence on many of the effective properties at relevant rod aspect ratios and thickness. Therefore, the fully periodic RVE assumption may be invalid for most piezoelectric fiber composites of technological importance.

Our results showed that using the equipotential BCs to resemble electrodes destroyed the symmetry in some of the piezoelectric shear coupling coefficients. Physical experiments should be performed to validate these theoretical findings.

4. RVE ANALYSIS OF MACRO FIBER COMPOSITES

This chapter presents a micromechanical treatment for the MFC Active Area. Homogenization, as well as a dehomogenization procedure, is proposed. They are based on the theory developed in Chapter 3 but extended here for the full stack of MFC layers. Future modifications to MSG that enable micromechanical analysis of the full MFC can be verified with the procedure presented here.

Overview

Consider the analysis overview presented in Figure 4.1. It shows how one can efficiently obtain the macroscopic host response as well as the local fields. This chapter presents the homogenization analysis and its results. It is an RVE analysis

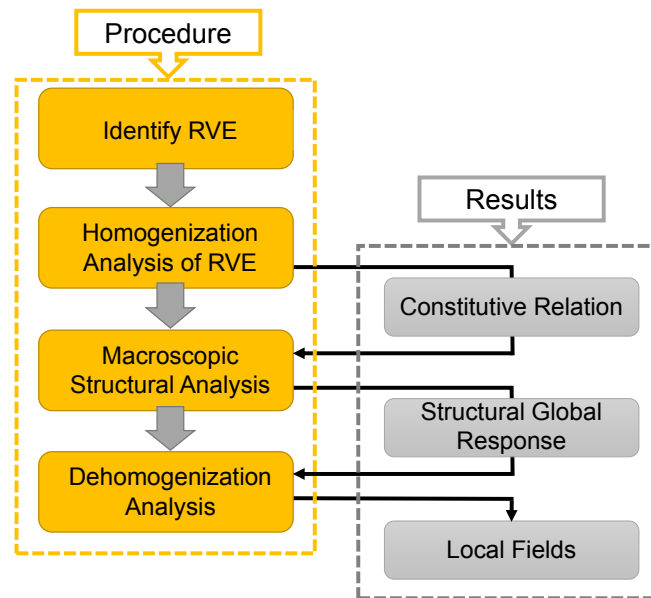


Figure 4.1: Micromechanical analysis overview.

based on the previously developed BCs in Table 3.1 but with modifications to account for passive MFC layers as well as realistic electrode loading. The next chapter details the macroscopic analysis as well as the results thereafter in the workflow of Figure 4.1. This chapter does, however, present the dehomogenization procedure (with its results left to the next chapter). Refer to [32, 43–45, 62, 151] for other multiscale piezoelectric algorithms; none of which are applicable to MFCs (and AFCs) due to the internal electrodes.

Microstructural Considerations

The P1 and P2 MFCs were considered to have the same RVE. The only differences came from the BCs and material specification of the PZT. The microstructural details were the same as that of Chapter 2 (details obtained from references [47, 48]). A summary of the geometric dimensions of the RVE can be found in Table 4.1. The fiber volume fractions of the PZT and copper were the most important parameter to keep consistent among various methodologies. The fiber widths for the copper and the PZT were obtained from [9] and [139] respectively. The kerf width (the in-plane gap between adjacent fibers) was then obtained by considering the volume fractions of 0.8654 [47] for the PZT and 0.2400 [48] for the copper (same as Chapter 2). Material

Table 4.1: Geometric parameters for the MFC RVEs.

Property	SONOX		
(μm)	Kapton	Copper	P502
Thickness	40	18	180
Fiber width	N/A	127	356
Kerf width	N/A	402.17	55.37

properties were kept the same as before (*cf* Tables 2.1 - 2.2). The mesh utilized for both MFCs is shown in Figure 4.2. Note that this is the RVE of P1 MFC due to the

nonuniform poling and that it is actually two unit cells for the P2 MFC. Although an RVE with one unit cell was sufficient for the P2 MFC, it was kept at two unit cells to simplify analysis procedures. This fact, along with the values from Table 4.1, gives $h_1 = 2 \times 0.529167$ mm and $h_2 = 0.411370$ mm. $h_3 = 0.296$ mm as in Chapter 2. The mesh consisted of 1,728 cubic piezoelectric brick elements (C3D20E) with full integration. With 20 nodes per element, the model had 8,509 nodes. This mesh was the coarsest mesh that was found to provide converged device properties for the P1 MFC. The same mesh was used for the P2 case.

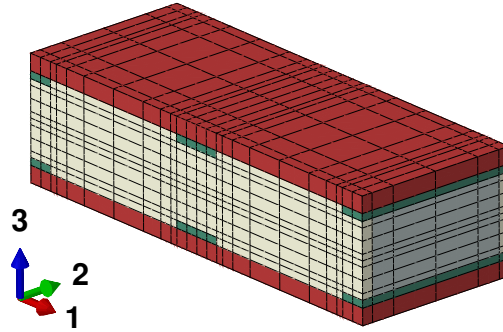


Figure 4.2: RVE mesh utilized throughout the work presented in this dissertation.

Internal electrodes were accounted for by specifying equipotential BCs on surfaces within the RVE; denoted by Γ^+ and Γ^- . The P1 and P2 MFC have different Γ faces and are illustrated in Figure 4.3. Note that, in both cases, the BCs span the perimeter of the copper electrodes (copper is green in Figure 4.3(a)). Trindade and Benjeddou [52] were the first to introduce the Γ BC (*cf* Figure 1.11) faces but they did not consider the P1 MFC and their Γ surface did not encompass the perimeter of the copper fibers. Top and side views of the electrodes are shown in Figure 4.4. Note that, for the P2 case, Γ includes the surfaces immediately above and below the PZT. In practice there would be a very thin layer of nickel there (about $2 \mu\text{m}$ thick according to [152]) which is not accounted for here and other places [52, 53].

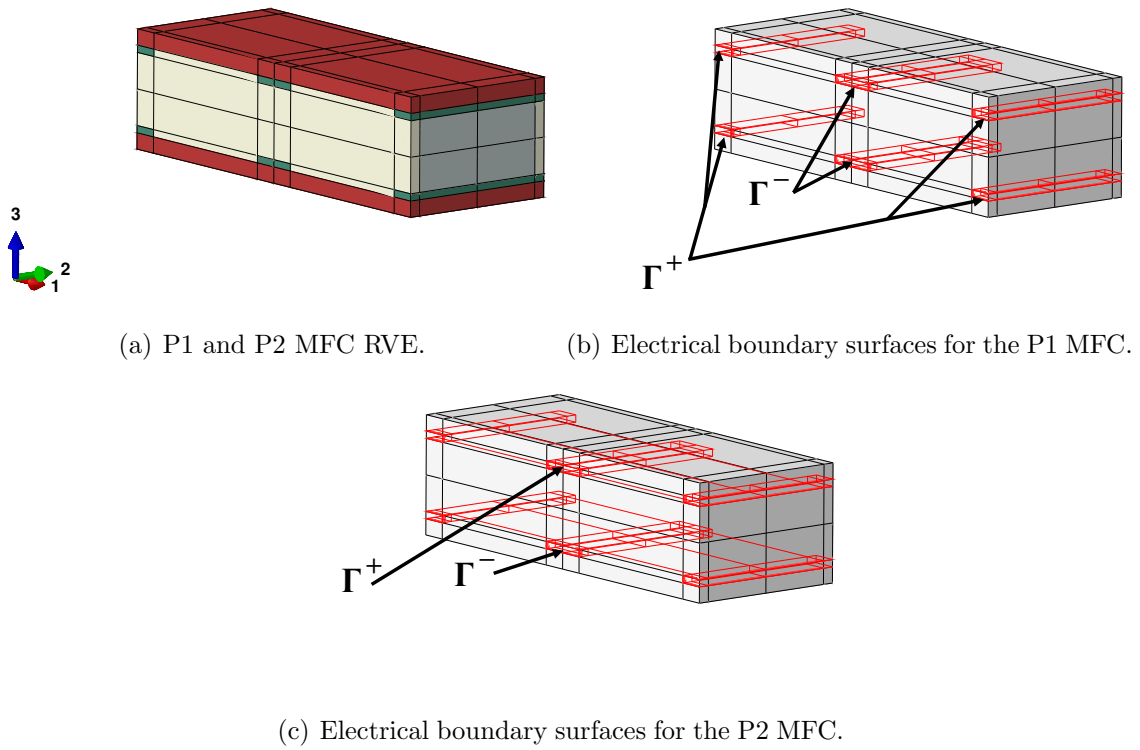


Figure 4.3: Specification of the internal electrode faces (Γ) for both MFCs.

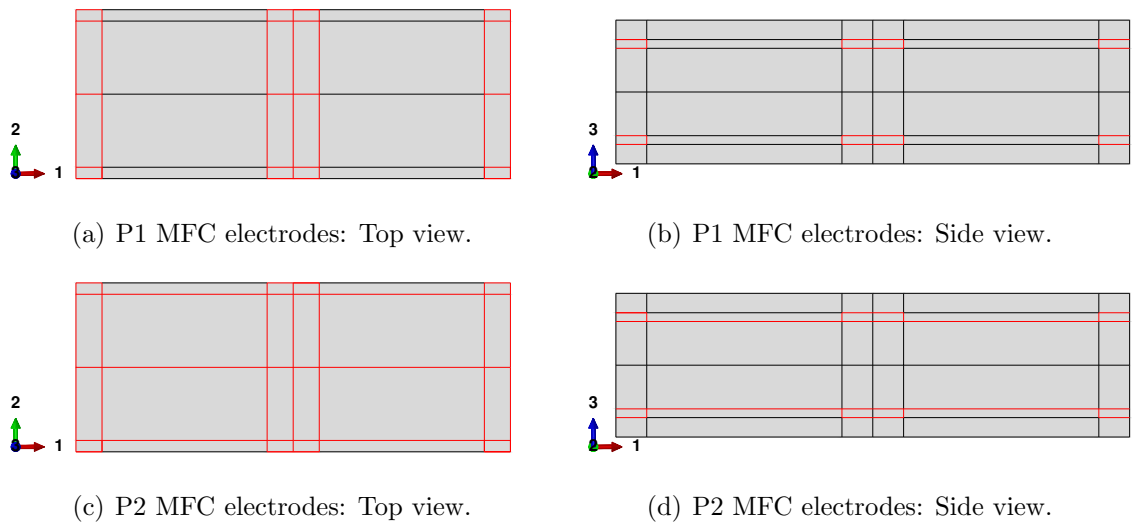


Figure 4.4: Top and side views of the internal electrode faces (Γ) for both MFCs.

4.1 Homogenization

Much like Chapter 3, in general, two classes of boundary conditions were considered here; namely, PBC and MIX.

4.1.1 PBCs

In this chapter, PBC refers to applying

$$u_i^+ - u_i^- = \bar{\varepsilon}_{ij}(y_j^+ - y_j^-)$$

on all X_i faces and

$$\phi^+ - \phi^- = -\bar{E}_i(y_i^+ - y_i^-)$$

on all X_α faces. Equipotential conditions are specified on the Γ faces of each respective MFC. These are essentially the BCs proposed by Trindade and Benjeddou [51,52] (*cf* Tables 1.2 and 1.3) for the P2 MFC except here, the issues raised in Chapter 1 are rectified. Two more BVPs are also created here in order to obtain the complete set of properties. The required BVPs are written explicitly in Table 4.2.

Table 4.2. Periodic boundary conditions for the full MFC
(P1 and P2 MFC cases).

Problem	X_1^-/X_1^+	X_2^-/X_2^+	X_3^-/X_3^+	Γ^-/Γ^+
1	$u_1^+ - u_1^- = h_1$	$u_1^+ - u_1^- = 0$	$u_1^+ - u_1^- = 0$	
	$u_2^+ - u_2^- = 0$	$u_2^+ - u_2^- = 0$	$u_2^+ - u_2^- = 0$	
	$u_3^+ - u_3^- = 0$	$u_3^+ - u_3^- = 0$	$u_3^+ - u_3^- = 0$	
	$\phi^+ - \phi^- = 0$	$\phi^+ - \phi^- = 0$	$q^+ = 0; q^- = 0$	$\phi^+ = 0; \phi^- = 0$
2	$u_1^+ - u_1^- = 0$	$u_1^+ - u_1^- = 0$	$u_1^+ - u_1^- = 0$	
	$u_2^+ - u_2^- = 0$	$u_2^+ - u_2^- = h_2$	$u_2^+ - u_2^- = 0$	

Continued on next page

Table 4.2 – continued from previous page

Problem	X_1^-/X_1^+	X_2^-/X_2^+	X_3^-/X_3^+	Γ^-/Γ^+
	$u_3^+ - u_3^- = 0$	$u_3^+ - u_3^- = 0$	$u_3^+ - u_3^- = 0$	
	$\phi^+ - \phi^- = 0$	$\phi^+ - \phi^- = 0$	$q^+ = 0; q^- = 0$	$\phi^+ = 0; \phi^- = 0$
3	$u_1^+ - u_1^- = 0$	$u_1^+ - u_1^- = 0$	$u_1^+ - u_1^- = 0$	
	$u_2^+ - u_2^- = 0$	$u_2^+ - u_2^- = 0$	$u_2^+ - u_2^- = 0$	
	$u_3^+ - u_3^- = 0$	$u_3^+ - u_3^- = 0$	$u_3^+ - u_3^- = h_3$	
	$\phi^+ - \phi^- = 0$	$\phi^+ - \phi^- = 0$	$q^+ = 0; q^- = 0$	$\phi^+ = 0; \phi^- = 0$
4	$u_1^+ - u_1^- = 0$	$u_1^+ - u_1^- = 0$	$u_1^+ - u_1^- = 0$	
	$u_2^+ - u_2^- = 0$	$u_2^+ - u_2^- = 0$	$u_2^+ - u_2^- = h_3/2$	
	$u_3^+ - u_3^- = 0$	$u_3^+ - u_3^- = h_2/2$	$u_3^+ - u_3^- = 0$	
	$\phi^+ - \phi^- = 0$	$\phi^+ - \phi^- = 0$	$q^+ = 0; q^- = 0$	$\phi^+ = 0; \phi^- = 0$
5	$u_1^+ - u_1^- = 0$	$u_1^+ - u_1^- = 0$	$u_1^+ - u_1^- = h_3/2$	
	$u_2^+ - u_2^- = 0$	$u_2^+ - u_2^- = 0$	$u_2^+ - u_2^- = 0$	
	$u_3^+ - u_3^- = h_1/2$	$u_3^+ - u_3^- = 0$	$u_3^+ - u_3^- = 0$	
	$\phi^+ - \phi^- = 0$	$\phi^+ - \phi^- = 0$	$q^+ = 0; q^- = 0$	$\phi^+ = 0; \phi^- = 0$
6	$u_1^+ - u_1^- = 0$	$u_1^+ - u_1^- = h_2/2$	$u_1^+ - u_1^- = 0$	
	$u_2^+ - u_2^- = h_1/2$	$u_2^+ - u_2^- = 0$	$u_2^+ - u_2^- = 0$	
	$u_3^+ - u_3^- = 0$	$u_3^+ - u_3^- = 0$	$u_3^+ - u_3^- = 0$	
	$\phi^+ - \phi^- = 0$	$\phi^+ - \phi^- = 0$	$q^+ = 0; q^- = 0$	$\phi^+ = 0; \phi^- = 0$
7	$u_1^+ - u_1^- = 0$	$u_1^+ - u_1^- = 0$	$u_1^+ - u_1^- = 0$	
	$u_2^+ - u_2^- = 0$	$u_2^+ - u_2^- = 0$	$u_2^+ - u_2^- = 0$	
	$u_3^+ - u_3^- = 0$	$u_3^+ - u_3^- = 0$	$u_3^+ - u_3^- = 0$	
	$\phi^+ - \phi^- = 0$	$\phi^+ - \phi^- = 0$	$q^+ = 0; q^- = 0$	$\phi^+ = 0; \phi^- = -h_1/2$
8	$u_1^+ - u_1^- = 0$	$u_1^+ - u_1^- = 0$	$u_1^+ - u_1^- = 0$	
	$u_2^+ - u_2^- = 0$	$u_2^+ - u_2^- = 0$	$u_2^+ - u_2^- = 0$	
	$u_3^+ - u_3^- = 0$	$u_3^+ - u_3^- = 0$	$u_3^+ - u_3^- = 0$	

Continued on next page

Table 4.2 – continued from previous page

Problem	X_1^-/X_1^+	X_2^-/X_2^+	X_3^-/X_3^+	Γ^-/Γ^+
	$\phi^+ - \phi^- = 0$	$\phi^+ - \phi^- = -h_2$	$q^+ = 0; q^- = 0$	
9	$u_1^+ - u_1^- = 0$	$u_1^+ - u_1^- = 0$	$u_1^+ - u_1^- = 0$	
	$u_2^+ - u_2^- = 0$	$u_2^+ - u_2^- = 0$	$u_2^+ - u_2^- = 0$	
	$u_3^+ - u_3^- = 0$	$u_3^+ - u_3^- = 0$	$u_3^+ - u_3^- = 0$	
	$\phi^+ - \phi^- = 0$	$\phi^+ - \phi^- = 0$	$q^+ = 0; q^- = 0$	$\phi^+ = -h_a; \phi^- = 0$

It is important to emphasize that these BCs are applicable to both MFCs but with nuances for the definition of Γ . Each MFC will have different Γ surfaces for different BVPs. The sensor problems (BVPs 1-6), the P1 MFC has Γ defined from Figure 4.3(b) while for the P2 MFC, that would be Figure 4.3(c). Then follows the actuator problems (BVPs 7-9). Since Problem 7 is for \bar{E}_1 dominated action, both MFCs had Γ defined from Figure 4.3(b). For the P1 MFC, this corresponds to actual usage. However for the P2 MFC, it is an artificial load condition created to obtain properties related to \bar{E}_1 . Similarly, Problem 9 is for \bar{E}_3 dominated action. Both MFCs had Γ defined from Figure 4.3(c). This time the actual use condition is for the P2 MFC and the artificial load corresponds to the P1 MFC. The artificial loads are rather arbitrary. For example, consider a P2 MFC placed between a parallel plate capacitor such that the voltage difference generated E_1 (predominantly) in the MFC. To get this effective behavior, BVP 7 should be modified to remove the Γ BCs altogether and, instead, let $\phi^+ - \phi^- = -\bar{E}_1 h_1$ on the X_1 faces.

4.1.2 MIX BCs

Table 4.3 presents the MIX BCs for the full MFC. They were developed following Chapter 3 but modified with provisions for the internal electrodes presented in this chapter.

Table 4.3. Mixed boundary conditions for the full MFC
(P1 and P2 MFC cases).

Problem	X_1^-/X_1^+	X_2^-/X_2^+	X_3^-/X_3^+	Γ^-/Γ^+
1	$u_1^+ - u_1^- = h_1$	$u_1^+ - u_1^- = 0$	$t_i^+ = 0; t_i^- = 0$	
	$u_2^+ - u_2^- = 0$	$u_2^+ - u_2^- = 0$		
	$u_3^+ - u_3^- = \bar{\varepsilon}_{31}h_1$	$u_3^+ - u_3^- = \bar{\varepsilon}_{32}h_2$		
	$\phi^+ - \phi^- = 0$	$\phi^+ - \phi^- = 0$	$q^+ = 0; q^- = 0$	$\phi^+ = 0; \phi^- = 0$
2	$u_1^+ - u_1^- = 0$	$u_1^+ - u_1^- = 0$	$t_i^+ = 0; t_i^- = 0$	
	$u_2^+ - u_2^- = 0$	$u_2^+ - u_2^- = h_2$		
	$u_3^+ - u_3^- = \bar{\varepsilon}_{31}h_1$	$u_3^+ - u_3^- = \bar{\varepsilon}_{32}h_2$		
	$\phi^+ - \phi^- = 0$	$\phi^+ - \phi^- = 0$	$q^+ = 0; q^- = 0$	$\phi^+ = 0; \phi^- = 0$
3	$u_\alpha^+ - u_\alpha^- = 0$	$u_\alpha^+ - u_\alpha^- = 0$	$t_\alpha^+ = 0; t_\alpha^- = 0$	
	$u_3^+ - u_3^- = \bar{\varepsilon}_{31}h_1$	$u_3^+ - u_3^- = \bar{\varepsilon}_{32}h_2$	$t_3^+ = 1; t_3^- = -1$	
	$\phi^+ - \phi^- = 0$	$\phi^+ - \phi^- = 0$	$q^+ = 0; q^- = 0$	$\phi^+ = 0; \phi^- = 0$
4	$u_\alpha^+ - u_\alpha^- = 0$	$u_\alpha^+ - u_\alpha^- = 0$	$t_1^+ = 0; t_1^- = 0$	
			$t_2^+ = 1; t_2^- = -1$	
	$u_3^+ - u_3^- = \bar{\varepsilon}_{31}h_1$	$u_3^+ - u_3^- = \bar{\varepsilon}_{32}h_2$	$t_3^+ = 0; t_3^- = 0$	
	$\phi^+ - \phi^- = 0$	$\phi^+ - \phi^- = 0$	$q^+ = 0; q^- = 0$	$\phi^+ = 0; \phi^- = 0$
5	$u_\alpha^+ - u_\alpha^- = 0$	$u_\alpha^+ - u_\alpha^- = 0$	$t_1^+ = 1; t_1^- = -1$	
			$t_2^+ = 0; t_2^- = 0$	
	$u_3^+ - u_3^- = \bar{\varepsilon}_{31}h_1$	$u_3^+ - u_3^- = \bar{\varepsilon}_{32}h_2$	$t_3^+ = 0; t_3^- = 0$	
	$\phi^+ - \phi^- = 0$	$\phi^+ - \phi^- = 0$	$q^+ = 0; q^- = 0$	$\phi^+ = 0; \phi^- = 0$

Continued on next page

Table 4.3 – continued from previous page

Problem	X_1^-/X_1^+	X_2^-/X_2^+	X_3^-/X_3^+	Γ^-/Γ^+
6	$u_1^+ - u_1^- = 0$	$u_1^+ - u_1^- = h_2/2$	$t_i^+ = 0; t_i^- = 0$	
	$u_2^+ - u_2^- = h_1/2$	$u_2^+ - u_2^- = 0$		
	$u_3^+ - u_3^- = \bar{\varepsilon}_{31}h_1$	$u_3^+ - u_3^- = \bar{\varepsilon}_{32}h_2$		
	$\phi^+ - \phi^- = 0$	$\phi^+ - \phi^- = 0$	$q^+ = 0; q^- = 0$	$\phi^+ = 0; \phi^- = 0$
7	$u_\alpha^+ - u_\alpha^- = 0$	$u_\alpha^+ - u_\alpha^- = 0$	$t_i^+ = 0; t_i^- = 0$	
	$u_3^+ - u_3^- = \bar{\varepsilon}_{31}h_1$	$u_3^+ - u_3^- = \bar{\varepsilon}_{32}h_2$		
	$\phi^+ - \phi^- = 0$	$\phi^+ - \phi^- = 0$	$q^+ = 0; q^- = 0$	$\phi^+ = 0; \phi^- = -h_1/2$
8	$u_\alpha^+ - u_\alpha^- = 0$	$u_\alpha^+ - u_\alpha^- = 0$	$t_i^+ = 0; t_i^- = 0$	
	$u_3^+ - u_3^- = \bar{\varepsilon}_{31}h_1$	$u_3^+ - u_3^- = \bar{\varepsilon}_{32}h_2$		
	$\phi^+ - \phi^- = 0$	$\phi^+ - \phi^- = -h_2$	$q^+ = 0; q^- = 0$	
9	$u_\alpha^+ - u_\alpha^- = 0$	$u_\alpha^+ - u_\alpha^- = 0$	$t_i^+ = 0; t_i^- = 0$	
	$u_3^+ - u_3^- = \bar{\varepsilon}_{31}h_1$	$u_3^+ - u_3^- = \bar{\varepsilon}_{32}h_2$		
	$\phi^+ - \phi^- = 0$	$\phi^+ - \phi^- = 0$	$q^+ = 0; q^- = 0$	$\phi^+ = -h_a; \phi^- = 0$

4.1.3 Nonuniform Polarization from IDEs

Referring back to Section 1.2.1 we know that the bulk orientation of piezoceramics is aligned with the poling electric field. We also know that the P1 MFC is polarized by IDEs and from Section 1.2.4, we recall that IDEs produce nonuniform electrical field variables (see Figure 1.3). Therefore the PZT fibers in P1 MFCs are polarized nonuniformly. The nonuniformity is in both degree and direction. In the following analysis, the piezoelectric material is allowed to be polarized with a nonuniform orientation but is approximated to be fully polarized. Unpolarized and partially polarized material was not accounted for.

The procedure is iterative and sequential. First, the PZT material orientation is set to coincidence with the problem coordinates (see Figure 1.10(a)). A voltage difference of 1500V is specified at the IDE and no other equation constraints are applied for the first estimate. For each element, the poling direction is determined from

$$n_i^p = \frac{E_i}{\sqrt{E_k E_k}} \quad (4.1)$$

For each PZT element, the element coordinates are then modified to become n_i^p . A new BVP is then defined with this time with spatially varying element coordinates. The PBCs are also applied by first computing the required $\bar{\varepsilon}_{ij}$ and \bar{E}_i from the initial run. This is repeated until the difference between the poling direction of the current step, $n_i^{p(k)}$, and the previous step, $n_i^{p(k-1)}$, has converged. The convergence was defined by

$$\sqrt{a_i a_i} < 0.05 \quad (4.2)$$

where

$$a_i = n_i^{p(k)} - n_i^{p(k-1)} \quad (4.3)$$

and k is the iteration count. The poling BCs for the MIX and PBC cases are shown in Table 4.4. Note the poling voltage is 1500V and it is scaled by s due to the scaling of the constitutive property inputs. Care was taken to allow the MFC RVE to deform as needed since it is expected that the MFC is poled under free conditions (not blocked). Therefore $\bar{\varepsilon}_{ij}$ is allowed to be nonzero and the PBCs are updated after each step. Refer to [11, 103, 153] for poling schemes that account for remnant polarization. Figure 4.5 shows the poling electric field from the IDE as well as the resulting element coordinate systems in the PZT fiber.

4.1.4 Volume Averaging Nuances for MFCs

Recall in Chapter 2, Section 2.4.3, that the MSG analytical model was verified with a DNS. Thus the electrical behavior presented in Figure 2.2 is correct. From this fact, the volume averaging for the RVE homogenization proceeds as was it did

Table 4.4: Boundary Conditions for poling the P1 MFC.

Problem	X_1^-/X_1^+	X_2^-/X_2^+	X_3^-/X_3^+	Γ^-/Γ^+
MIX	$u_1^+ - u_1^- = \bar{\varepsilon}_{11}h_1$	$u_1^+ - u_1^- = \bar{\varepsilon}_{12}h_2$	$t_i^+ = 0; t_i^- = 0$	
	$u_2^+ - u_2^- = \bar{\varepsilon}_{21}h_1$	$u_2^+ - u_2^- = \bar{\varepsilon}_{22}h_2$		
	$u_3^+ - u_3^- = \bar{\varepsilon}_{31}h_1$	$u_3^+ - u_3^- = \bar{\varepsilon}_{32}h_2$		$\phi^+ = 0$
	$\phi^+ - \phi^- = -\bar{E}_1h_1$	$\phi^+ - \phi^- = -\bar{E}_2h_2$	$q^+ = 0; q^- = 0$	$\phi^- = -1500/s$
PBC	$u_1^+ - u_1^- = \bar{\varepsilon}_{11}h_1$	$u_1^+ - u_1^- = \bar{\varepsilon}_{12}h_2$	$u_1^+ - u_1^- = \bar{\varepsilon}_{13}h_3$	
	$u_2^+ - u_2^- = \bar{\varepsilon}_{21}h_1$	$u_2^+ - u_2^- = \bar{\varepsilon}_{22}h_2$	$u_2^+ - u_2^- = \bar{\varepsilon}_{23}h_3$	
	$u_3^+ - u_3^- = \bar{\varepsilon}_{31}h_1$	$u_3^+ - u_3^- = \bar{\varepsilon}_{32}h_2$	$u_3^+ - u_3^- = \bar{\varepsilon}_{33}h_3$	$\phi^+ = 0$
	$\phi^+ - \phi^- = -\bar{E}_1h_1$	$\phi^+ - \phi^- = -\bar{E}_2h_2$	$q^+ = 0; q^- = 0$	$\phi^- = -1500/s$

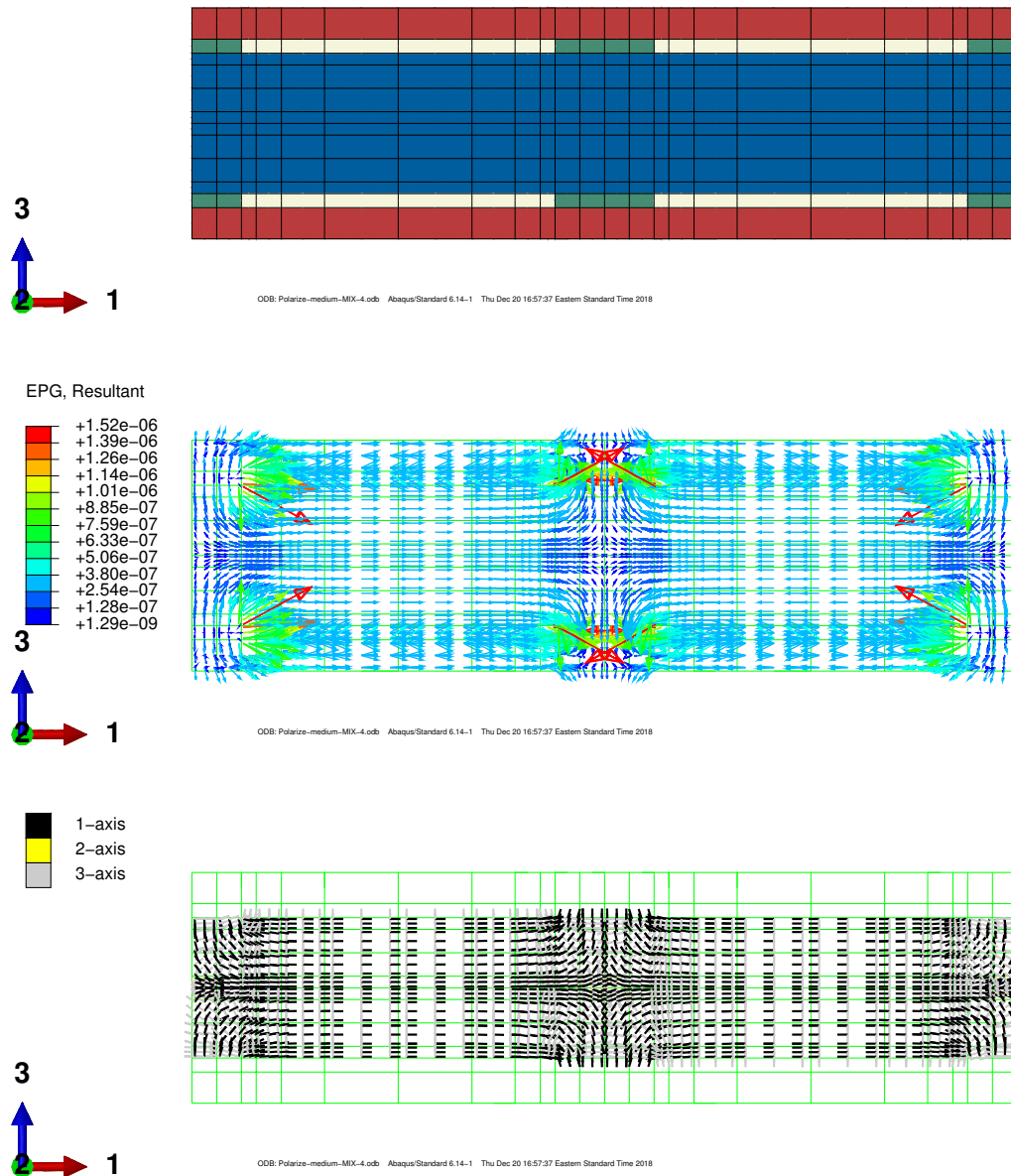


Figure 4.5: Illustration of the poling process after convergence of the electric field. Figures from top to bottom: A central cross section of the RVE; scaled electric field resultant (V/mm/s); resulting element coordinate systems in the PZT.

in Section 2.4.3. Namely, all but D_3 is averaged in the unit-cell while D_3 is averaged in active layer of a unit cell (Eq. (2.41)).

Coordinate Transforms

It is was important to consider that the local fields that were output by Abaqus[®] were in the element coordinate system. For the P2 case, volume averaging can be performed directly since the element coordinate system (CS) was equivalent to the problem CS. For the P1 case, it is necessary to transform the stress and strain for each element back to the problem coordinates. This was made conveniently available with the Abaqus[®] scripting command “getTransformedField”. As for the electric field and electric displacement, it was not well understood which CS to perform volume averaging. The uncertainty comes from the symmetry of the electrical fields within the RVE. Note in Figure 4.5 that there are two planes of symmetry. The first is a y_1 - y_2 plane that passes through the geometric centroid of the RVE. If volume averaging is performed in the problem CS, this symmetry should cause $\bar{E}_3 = 0$. The second plane of symmetry also passes through the centroid but is a y_2 - y_3 . Here volume averaging in the problem CS should give $\bar{E}_1 = 0$. Having $\bar{E}_1 = 0$ and $\bar{E}_3 = 0$ is not desirable since those values are to be used to find device properties that are nonzero in value.

Therefore, two volume averaging procedures are explored here. The first is referred to as *Full Transform*. This scheme transforms the stress, strain, and both electrical fields to the problem coordinate system. The second approach is referred to as *Mechanical Transform* where only the stress and strain are transformed to the problem CS. This leaves the electrical field outputs in the element CSs. Both procedures were performed within a single geometric unit-cell (note that the RVE in Figure 4.3 consists of two unit-cells).

4.2 Dehomogenization

Local fields at select material points in a macroscopic structural analysis can be examined with a dehomogenization analysis. Unlike the RVE homogenization, the dehomogenization consists of solving one BVP per material point of interest. The BCs are the mixed BCs proposed for the homogenization. Except now, the BCs are updated to include the stress and strain obtained from a macroscopic analysis of the homogenized model. The BCs on Γ are equal to what was applied in the macroscopic analysis. Table 4.5 shows the BCs. Note that since the material properties of the constituents of the RVE were scaled by s , the macroscopic stresses and the potential needs to be scaled as well. Finally, all of the fields are reported in the problem CS.

Table 4.5: Boundary conditions P1 and P2 dehomogenization analyses.

Problem	X_1^-/X_1^+	X_2^-/X_2^+	X_3^-/X_3^+	Γ^-/Γ^+
1	$u_1^+ - u_1^- = \bar{\varepsilon}_{11}$	$u_1^+ - u_1^- = \bar{\varepsilon}_{12}$	$t_i^+ = \bar{\sigma}_{13}/s$	
			$t_i^- = -\bar{\sigma}_{13}/s$	
	$u_2^+ - u_2^- = \bar{\varepsilon}_{21}$	$u_2^+ - u_2^- = \bar{\varepsilon}_{22}$	$t_i^+ = \bar{\sigma}_{23}/s$	
			$t_i^- = -\bar{\sigma}_{23}/s$	
	$u_3^+ - u_3^- = \bar{\varepsilon}_{31}$	$u_3^+ - u_3^- = \bar{\varepsilon}_{32}$	$t_i^+ = \bar{\sigma}_{33}/s$	
			$t_i^- = -\bar{\sigma}_{33}/s$	
	$\phi^+ - \phi^- = -\bar{E}_1$	$\phi^+ - \phi^- = -\bar{E}_2$	$q^+ = 0$	$\phi^+ = V_2/s$
			$q^- = 0$	$\phi^- = V_1/s$

Note that since the constituent properties and loading were scaled, the local fields obtained are

$$\frac{\sigma_{ij}}{s} \quad \frac{\varepsilon_{ij}}{1} \quad \frac{D_i}{1} \quad \frac{E_i}{s} \quad \frac{\phi}{s} \quad (4.4)$$

Therefore, the local fields can be obtained by performing the inverse operation for each field.

4.3 Homogenization Results

4.3.1 P2 MFC

The device properties of the P2 MFC are shown first since the poling is not as complicated as the P1 case. The Python script utilized to create each BVP (for P1 and P2 cases) in Abaqus® can be found in Appendix B. Table 4.6 shows a comparison of the mechanical properties as computed by the HRM from Chapter 2, the MIX and PBCs from the present chapter. Comparing the MSG analytical model (HRM2) to the others reveals that the homogeneous layer assumption in the analytical model results in a slightly more compliant response. It is also notable that the PBC result in a slightly stiffer response for Y_1^{E*} , Y_2^{E*} , and Y_3^{E*} . In like manner, the piezoelectric

Table 4.6: Effective elastic properties for the full P2 MFC in the problem coordinate system.

	HRM1		
	↓	MIX	PBC
Property	HRM2		
Y_1^{E*} (GPa)	30.37	31.36	31.38
Y_2^{E*} (GPa)	16.1	17.64	17.94
Y_3^{E*} (GPa)	10.52	8.35	8.529
G_{12}^{E*} (GPa)	4.13	5.971	5.974
G_{13}^{E*} (GPa)	2.70	2.752	2.769
G_{23}^{E*} (GPa)	2.84	2.462	2.513
ν_{12}^{E*}	0.309	0.3343	0.3354
ν_{13}^{E*}	0.355	0.3881	0.3828
ν_{23}^{E*}	0.237	0.3004	0.2925

and dielectric properties are shown in Table 4.7. Like the last chapter, the Sensor designation means that the RVE analysis properties came from the sensor BVPs

(Problems 1-6). The Actuator designation indicates that the properties originated from the actuator BVPs (Problems 7-9). Comparing the respective Sensor and Actuator data reveals that the properties obtained are not unique; for either case. Again, it is recalled that this check is omitted in the literature [51–55, 70]. Refer back to Eq. (3.47) for why the Sensor and Actuator cases have different permittivities at constant stress; even though they are diagonal terms. Except for d_{24}^* and $k_{22}^{\sigma*}$, the properties are relatively close between the Sensor and Actuator designations.

Table 4.7: Effective piezoelectric and dielectric properties for the full P2 MFC in problem coordinates.

	HRM1				
	↓	MIX	MIX	PBC	PBC
Property	HRM2	(Sensor)	(Actuator)	(Sensor)	(Actuator)
d_{31}^* (pC/N)	-297.2	-284.9	-287.4	-284.9	-287.3
d_{32}^* (pC/N)	-201.9	-205.7	-207.8	-208.9	-211.1
d_{33}^* (pC/N)	489.9	485.8	489.5	486.6	490.5
d_{24}^* (pC/N)	4.706	217.3	6.432	221.1	6.630
d_{15}^* (pC/N)	337.5	334.4	320.3	334.6	355.2
$\kappa_{11}^{\sigma*}/\epsilon_0$	1023.3	976.1	973.2	970.6	975.0
$\kappa_{22}^{\sigma*}/\epsilon_0$	18.9	37.9	24.7	39.0	25.1
$\kappa_{33}^{\sigma*}/\epsilon_0$	2568.2	2567.4	2577.0	2565.8	2575.8

4.3.2 P2 MFC Verification

The MIX properties shown in the previous tables (Tables 4.6 - 4.7) are utilized in Eqs. (2.35) - (2.39) and the results are compared to the P2 DNS results reported in Section 2.4.3. Table 4.8 shows the results for each of the three cases: Short Circuit Test, Actuator Test, and Open Circuit Test. V_1 and V_2 are defined in the “Out-of-

Plane Electrical Behavior” portion of Figure 2.2. The comparisons are all excellent.

Table 4.8: Macroscopic variable comparison between a DNS of the P2 MFC Active Area and the MIX effective behavior.

	$\bar{\varepsilon}_{11}$ ($\mu\varepsilon$)	$\bar{\varepsilon}_{22}$ ($\mu\varepsilon$)	$\bar{\varepsilon}_{33}$ ($\mu\varepsilon$)	$\bar{D}_3^a \times 10^{-3}$ ($\mu\text{C}/\text{mm}^2$)	\bar{E}_3 (V/mm)	V_1 (V)	V_2 (V)
Short Circuit Test							
DNS	317.2	-106.6	-122.6	-2.83	0.0	0.0	0.0
MIX (Sensor)	318.9	-106.6	-123.8	-2.85	0	m	m
Difference (%)	0.54	-0.05	0.92	0.64	N/A	N/A	N/A
MIX (Actuator)	318.9	-106.6	-123.8	-2.87	0	m	m
Difference (%)	0.54	-0.05	0.92	1.5	N/A	N/A	N/A
Actuator Test							
DNS	344.5	251.7	-589.9	-27.44	-1207.0	0.0	360
MIX (Sensor)	346.5	250.2	-590.8	-27.65	-1216.2	0.0	360.0
Difference (%)	0.58	-0.60	0.16	0.75	0.77	0.0	0.0
MIX (Actuator)	349.5	252.7	-595.4	-27.65	-1216.2	0.0	360.0
Difference (%)	1.44	0.41	0.93	0.75	0.77	0.0	0.0
Open Circuit Test							
DNS	281.6	-132.5	-61.8	0.00	124.1	0.0	-35.8
MIX (Sensor)	283.1	-132.4	-62.9	0.00	125.3	0.0	-37.10
Difference (%)	0.56	-0.08	1.78	0.00	0.97	0.0	3.65
MIX (Actuator)	282.7	-132.8	-62.1	0.00	125.9	0.0	-37.28
Difference (%)	0.39	0.21	0.54	0.00	1.45	0.0	4.15

4.3.3 P1 MFC

Like the P2 case, Table 4.9 shows a comparison of the mechanical properties as computed by the HRM2 from Chapter 2, to the MIX and PBCs from the present chapter. This time, more device properties are shown due to the different element CS transformations. Note that a sample Python script to polarize FE models is presented in Appendix C. It is apparent that the MIX and PBCs of the present chapter results in a stiffer Y_1^{E*} , Y_2^{E*} , G_{12}^{E*} and a more compliant Y_3^{E*} when compared to the HRM2. The transverse shear moduli of the HRM2 is much closer to the numerical results than the FSDT result of [123]. Furthermore, the Mechanical Transform results in a stiffer Y_1^{E*} . Comparing the MIX to the PBCs reveals that the PBCs result in a slightly stiffer Y_1^{E*} , Y_2^{E*} , and Y_3^{E*} . This was also observed for the P2 case (*cf* Table 4.6).

Table 4.9: Effective piezoelectric and dielectric properties for the full homogenized P1 MFC in problem coordinates.

Property	HRM1	MIX		PBC	
	↓	Full	Mechanical	Full	Mechanical
	HRM2	Transform	Transform	Transform	Transform
Y_1^{E*} (GPa)	27.32	30.90	32.43	31.09	32.70
Y_2^{E*} (GPa)	16.09	17.67	17.66	17.96	17.95
Y_3^{E*} (GPa)	10.70	8.62	8.65	8.87	8.90
G_{12}^{E*} (GPa)	4.53	6.34	6.34	6.34	6.34
G_{13}^{E*} (GPa)	2.70	2.75	2.74	2.76	2.75
G_{23}^{E*} (GPa)	2.76	2.44	2.44	2.49	2.49
ν_{12}^{E*}	0.300	0.352	0.372	0.356	0.377
ν_{13}^{E*}	0.327	0.329	0.305	0.314	0.284
ν_{23}^{E*}	0.228	0.278	0.287	0.268	0.279

Tables 4.10 and 4.11 contain the effective electrical properties for the MIX and PBC cases respectively. The HRM2 results are included in Table 4.10 for comparison. The HRM2 results in a much larger d_{11}^* , and to a lesser extent d_{13}^* , than the other cases. This is not the case for d_{12}^* . Both of these observations suggest that the uniform poling assumption of the analytical model may not be valid for the P1 case. It is interesting that the HRM2 results for d_{26}^* and $k_{22}^{\sigma*}$ seem to be of similar magnitude as the Actuator properties from the other cases. However, there are large differences for d_{26}^* between the Sensor and Actuator properties; same being true for $k_{22}^{\sigma*}$. This is attributed to the asymmetries discovered in Chapter 3 when homogenizing the active layer alone. Finally, greater differences seem to exist between the Sensor and Actuator properties of the P1 MFC than that of the P2 MFC (*cf* Table 4.7). This suggests that the nonuniform poling of the P1 case exacerbates the asymmetry of the obtained constitutive relations.

Table 4.10: MIX effective piezoelectric and dielectric properties for the full homogenized MFC in problem coordinates.

Property	HRM1	Full		Mechanical	
	↓	Transform		Transform	
	HRM2	Sensor	Actuator	Sensor	Actuator
d_{11}^* (pC/N)	409.1	328.9	359.9	322.4	341.7
d_{12}^* (pC/N)	-129.8	-124.8	-143.4	-134.7	-136.1
d_{13}^* (pC/N)	-140.1	-104.1	-104.0	-88.67	-98.69
d_{26}^* (pC/N)	6.94	202.9	9.67	202.6	9.672
d_{35}^* (pC/N)	555.1	471.2	510.1	367.4	564.1
$\kappa_{11}^{\sigma*}/\epsilon_0$	934.37	862.1	936.9	914.9	961.5
$\kappa_{22}^{\sigma*}/\epsilon_0$	18.9	53.16	23.77	53.24	23.77
$\kappa_{33}^{\sigma*}/\epsilon_0$	2767.3	2702	2714	2696	2753

Table 4.11: PBC effective piezoelectric and dielectric properties for the full homogenized MFC in problem coordinates.

Property	Full Transform		Mechanical Transform	
	Sensor	Actuator	Sensor	Actuator
d_{11}^* (pC/N)	323.3	354.9	314.6	335.8
d_{12}^* (pC/N)	-124.3	-143.7	-134.1	-135.9
d_{13}^* (pC/N)	-88.7	-83.9	-69.6	-79.3
d_{26}^* (pC/N)	201.2	9.638	200.8	9.636
d_{35}^* (pC/N)	467.3	569.2	361.2	633.6
$k_{11}^{\sigma*}/\epsilon_0$	852.1	927.8	900.0	950.4
$k_{22}^{\sigma*}/\epsilon_0$	52.7	23.8	52.7	23.8
$k_{33}^{\sigma*}/\epsilon_0$	2685.7	2718.6	2682.4	2766.5

4.3.4 P1 MFC Verification

Finally, the P1 MFC is also verified with a test case like that in Section 2.4.3. This time the DNS modeled the IDE poling with a procedure like the one in Section 4.1.3. Unlike the poling the RVE, the DNS poling did not have any PBCs. V_1 and V_2 for the homogenized model are defined in the “In-plane Electrical Behavior” portion of Figure 2.2. Note that the heterogeneous model in this chapter is the DNS and it is not defined in that figure. Instead, from Figure 4.3(b), V_1 corresponds to Γ^+ and V_2 corresponds to Γ^- . A finer mesh was utilized for the nonuniformly poled case. The resulting mesh consisted of 95,040 C3D20E elements (411,013 nodes). The DNS was solved a total of eight times with 20 CPUs. Each time took about four minutes of wallclock time. The poling process took five iterations to complete. The other three were for each of the three tests.

The comparisons are all excellent. In general, the best results are obtained from the Mechanical Transform case (Table 4.12). Particularly the Actuator case provides slightly better average strain predictions. However, the prediction of \bar{D}_1 is worse with an error of 10%. Therefore properties from this case are recommended and they are the ones that are utilized in the next chapter for the P1 MFC.

Table 4.12: Macroscopic variable comparison between a DNS of the P1 MFC patch and the MIX effective behavior considering the Mechanical Transform.

	$\bar{\varepsilon}_{11}$ ($\mu\varepsilon$)	$\bar{\varepsilon}_{22}$ ($\mu\varepsilon$)	$\bar{\varepsilon}_{33}$ ($\mu\varepsilon$)	$\bar{D}_1 \times 10^{-3}$ ($\mu\text{C}/\text{mm}^2$)	\bar{E}_1 (V/mm)	V_1 (V)	V_2 (V)
Short Circuit Test							
DNS	303.2	-114.4	-91.2	3.11	-12.79	0.0	0.0
MIX (Sensor)	308.4	-114.7	-94.1	3.22	0	m	m
Difference (%)	1.69	0.23	3.21	3.78	-100	N/A	N/A
MIX (Actuator)	308.4	-114.7	-94.1	3.42	0	m	m
Difference (%)	1.69	0.23	3.21	9.98	-100	N/A	N/A
Actuator Test							
DNS	670.1	-267.3	-193.2	16.29	1962.0	1058.3	0.0
MIX (Sensor)	644.9	-269.5	-177.3	16.20	2000.0	1058.3	0.0
Difference (%)	-3.76	0.82	-8.21	-0.56	1.94	0.0	0.0
MIX (Actuator)	677.8	-272.3	-197.4	16.60	1983.5	1058.3	0.0
Difference (%)	1.15	1.86	2.17	1.86	1.09	0.0	0.0
Open Circuit Test							
DNS	175.9	-63.5	-54.6	0.02	-385.5	0.0	198.9
MIX (Sensor)	180.0	-61.1	-58.8	0.00	-398.0	0.0	210.62
Difference (%)	2.32	-3.87	7.80	-100	3.26	0.0	5.87
MIX (Actuator)	171.2	-60.1	-54.5	0.00	-401.4	0.0	212.40
Difference (%)	-2.70	-5.46	-0.12	-100	4.14	0.0	6.76

Table 4.13: Macroscopic variable comparison between a DNS of the P1 MFC patch and the MIX effective behavior considering the Full Transform.

	$\bar{\varepsilon}_{11}$ ($\mu\varepsilon$)	$\bar{\varepsilon}_{22}$ ($\mu\varepsilon$)	$\bar{\varepsilon}_{33}$ ($\mu\varepsilon$)	$\bar{D}_1 \times 10^{-3}$ ($\mu\text{C}/\text{mm}^2$)	\bar{E}_1 (V/mm)	V_1 (V)	V_2 (V)
Short Circuit Test							
DNS	303.2	-114.4	-91.2	-55033.58	-55.03	0.0	0.0
MIX (Sensor)	323.6	-114.0	-106.4	3.29	0	m	m
Difference (%)	6.73	-0.41	16.73	-100	0.00	N/A	N/A
MIX (Actuator)	323.6	-114.0	-106.4	3.29	0	m	m
Difference (%)	6.73	-0.41	16.73	-100	-100	N/A	N/A
Actuator Test							
DNS	670.1	-267.3	-193.2	14.81	1862.6	1058.3	0.0
MIX (Sensor)	657.9	-249.6	-208.1	15.27	2000.0	1058.3	0.0
Difference (%)	-1.83	-6.63	7.72	3.09	7.38	0.0	0.0
MIX (Actuator)	713.9	-286.8	-207.9	14.82	1983.5	1058.3	0.0
Difference (%)	6.54	7.29	7.61	0.04	6.49	0.0	0.0
Open Circuit Test							
DNS	175.9	-63.5	-54.6	0.02	-409.2	0.0	198.9
MIX (Sensor)	181.9	-60.2	-61.6	0.00	-430.9	0.0	228.03
Difference (%)	3.38	-5.25	12.91	-100	5.31	0.0	14.62
MIX (Actuator)	167.5	-51.8	-61.3	0.00	-433.9	0.0	229.60
Difference (%)	-4.82	-18.53	12.43	-100	6.04	0.0	15.41

5. UNIMORPH DIRECT NUMERICAL SIMULATIONS

Since micromechanical theories generally assume that numerous RVEs are present in the macroscopic structure, the most critical case to test is the smallest MFC that is available off the shelf. For the P1 MFC, that would be the M2503-P1. Thus, here two MFC sizes are tested, namely, the M2503-P1 and M2814-P1. Both patch sizes can be contrasted in Figure 5.1 (note that only the PZT fibers, the electrodes and a single layer of Kapton are displayed). Three examples cases are devised to simulate

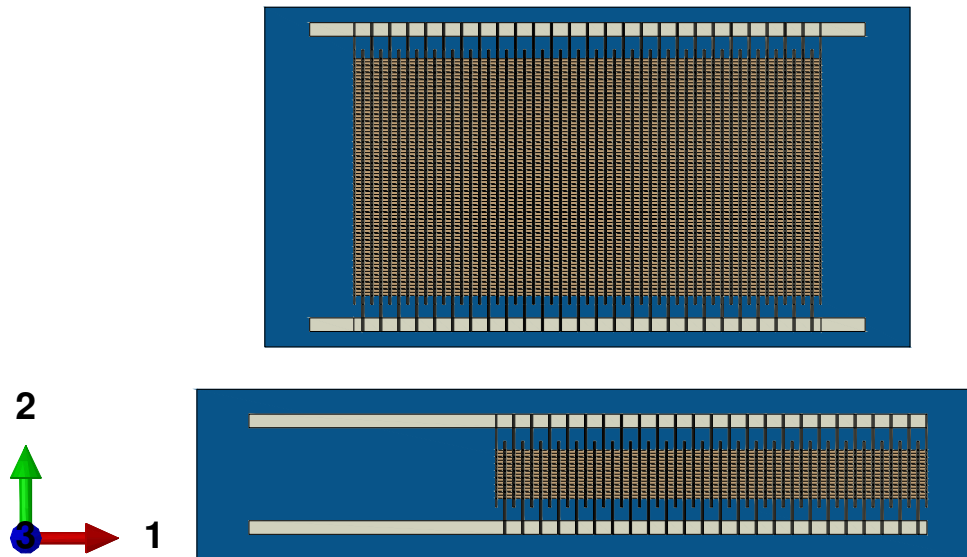


Figure 5.1: In-plane size comparison of both MFC patches considered.

possible device behavior. The cases are diversified by sensing vs. actuating responses, P1 and P2 configurations and anisotropy of the host structure. The first case is a model of the smaller patch being actuated on an isotropic host. The second case is the same as the first except the larger patch is considered. The third case is a sensor case of the P2 MFC where the larger patch is modeled and the substrate made of two orthotropic layers. The cases considered are all shown in Table 5.1. Note that the

designation “a” (*eg* 2a) refers to a complete representation of the MFC that includes both the Active Area and the Passive Area. The “b” indicates that only the Active Area was modeled.

Table 5.1: Test matrix considered for the DNS studies.

Case	MFC	Patch	MFC	Transducer	Host
	Type	Name	Geometry	Response	
1a	P1	M2503-P1	Full Patch	Actuator	Isotropic
1b	P1	M2503-P1	Active Area	Actuator	Isotropic
2a	P1	M2814-P1	Full Patch	Actuator	Isotropic
2b	P1	M2814-P1	Active Area	Actuator	Isotropic
3a	P2	M2814-P2	Full Patch	Sensor	Anisotropic
3b	P2	M2814-P2	Active Area	Sensor	Anisotropic

5.1 DNS Details

5.1.1 Geometry

The Active Area was constructed from merging numerous RVE geometry instances. The number of RVEs along, say x_α , is referred to as N_α . Thus the length of the DNS Active Area in the x_α direction is $H_\alpha = N_\alpha h_\alpha$ (no summation over α). For each patch size, N_α were selected such that H_α most closely matched the Active Area dimensions given by the MFC manufacturer [118]. The Passive Area was created from the overall patch dimensions given by the supplier and from estimates for the parameters in Figure 5.2. It should be noted that the manufacturer listed the overall in-plane dimension of the M2814-P1 MFC to be 38 by 20 mm while that of the M2814-P2 was listed as 37 by 18 mm. This artifact was deemed to be negligible and both were modeled as 38 by 20 mm. The geometric details are summarized in Table 5.2. Note that L_α are the overall patch lengths. Parameters associated to x_3

are omitted since there is only one RVE through the thickness which was considered to be 0.296 mm thick. It should be noted that the width of the electrode bus was estimated to be 0.8 mm and the in-plane dimensions of the host were the same as the overall in-plane MFC patch dimensions. The host thickness used was 0.438 mm. This made the total thickness to be $h = 0.734$ mm. Figure 5.2 also shows the problem coordinate system. The origin of x_3 is located at the middle of the host thickness.

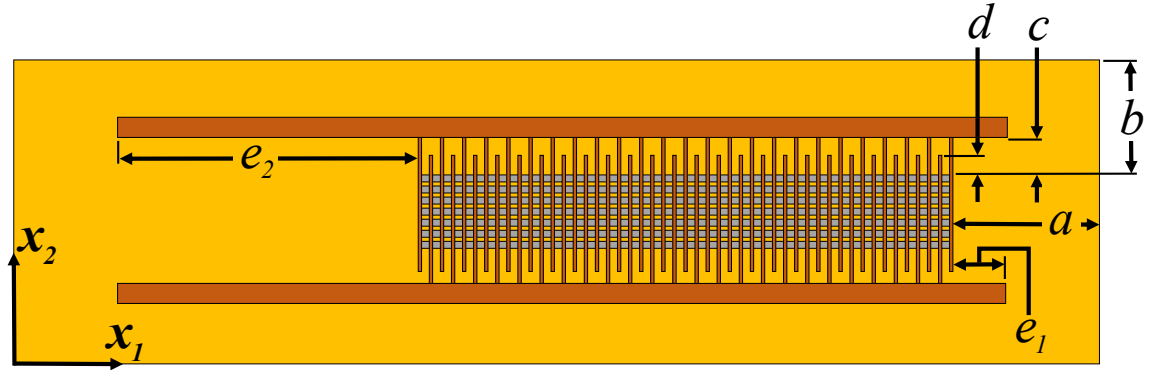


Figure 5.2: In-plane geometrical parameters for the Passive Area and the problem coordinate system location.

Each MFC was discretized entirely with piezoelectric brick elements that had 20 nodes per element (C3D20E). The host had elements of the same order but were not piezoelectric and reduced integration was appropriate since localized fields were not to be extracted there (C3D20R). It is finally noted that, after performing a mesh sensitivity study, it was determined the two elements through the thickness of the host are required as well as a mesh seed of 1 mm throughout.

5.1.2 Material Models

A linear elastic material model was sufficient for the behavior that was sought. The host was considered to be aluminum with $Y = 70.7$ GPa and $\nu = 0.32$ for the isotropic cases. For the anisotropic host case, the layup considered was $[40^\circ/30^\circ]$. The

Table 5.2: Geometric parameters for the MFCs tested.

	M2814-P1 and	
	M2503-P1	M2814-P2
L_1 (mm)	46	38
L_2 (mm)	10	20
H_1 (mm)	25.4	27.517
H_2 (mm)	2.88	13.99
N_1	24	26
N_2	7	34
a (mm)	3	5.242
b (mm)	3.56	3.007
c (mm)	1.3	1.3
d (mm)	0.5	0.5
e_1 (mm)	0	2.6
e_2 (mm)	14.6	2.6

MFC was at 0° and it was in contact with the 40° layer. Each layer had $Y_1 = 140$ GPa, $Y_2 = 10$ GPa, $G_{12} = 7$ GPa, $\nu_{12} = 0.3$, and $\nu_{23} = 0.46$ in its own material coordinate system. The thickness of each layer was 0.219 mm.

5.1.3 Boundary Conditions

In all three cases, the host was clamped at one end and free at all the other ends. Case 1 and 2 were actuator cases for the P1 MFC. They had $\phi = 1058.33$ V on Γ^+ and $\phi = 0$ V on Γ^- . The Γ surfaces are based on the Γ surfaces defined in Figures 4.3 and 4.4 except that they are appropriately extended to include the rest of the IDE when the Passive Area is being accounted for (*eg* see the IDE in Figure 1.3). With Case 3 being a sensor problem with an anisotropic host, in-plane tractions were applied on the tip of the host and the MFC had short-circuit conditions on the electrodes. Namely $(t_1, t_2, t_3) = (-4.380, 2.190, 0)$ MPa on the surface of the host located at $x_1 = L_1$ and $\phi = 0$ V on Γ^+ and Γ^- .

To obtain cantilevered action, the host was clamped at $x_1 = 0$ and the MFC was tied to the host with *Tie* constraints. To provide a fair comparison to the plate models, the clamped BC for the host was carefully constructed to resemble the BCs that may be applied to a plate model. For the host, $u_1 = 0$ at $x_1 = 0$ and $u_3 = 0$ along the line $(0, x_2, 0)$. For Case 3, $u_2 = 0$ along this line as well so that translation along x_2 would be prevented.

5.2 Details for Homogenized Models

Two homogenized models were considered. A solid model and a plate model. Neither of which considered the Passive Area. The geometry of the solid MFC model was also created by repeating RVEs by the number of times required for each case. The RVE consisted of the exact same dimensions as the heterogeneous RVE but without any heterogeneity. C3D20E elements were used as in the heterogeneous cases. This geometry was then tied to a host with the exact same geometry, mesh

size, and mechanical BCs for each respective case. Only the Γ faces from Figure 4.3 were modified for the solid model and are shown in Figure 5.3. Note the uniform poling directions as indicated by the red arrows. Then the exact same electrical potential value as the heterogeneous cases was applied to the new Γ faces.

Piezoelectric actuation is often simplified with a mechanical plate model. A so-called thermal analogy is adopted where the piezoelectric actuation strain is approximated with uniform temperature change and with coefficients of thermal expansion, α [124–128]. The coefficients of thermal expansion were

$$\alpha_{11}^* = d_{11}^* \quad \alpha_{22}^* = d_{12}^* \quad \alpha_{33}^* = d_{13}^* \quad (5.1)$$

and the artificial temperature difference was

$$\Delta T = -\frac{V_2 - V_1}{h_1/2} = -\frac{0 - 1058.33 \text{ V}}{0.529167 \text{ mm}} = 2000 \text{ V/mm} \quad (5.2)$$

Note that only Cases 1 and 2 had a plate model for comparisons since they are the actuator cases. Finally, a few notable details for the plate models are given here. They consisted of S8R elements in Abaqus®. A mesh seed of 1 mm was found to have converged results on the displacement. The shell section was defined with Composite Layups. The P1 MFC was modeled with the HRM2 device properties given in Chapter 2.

5.3 Computing Resources

The DNS models in the present chapter, as well as those in Chapters 2 and 3, were ran in a high performance computing cluster named Halstead at Purdue University (main campus). Each compute node had two Intel® Xeon®-E5 processors (Haswell) with a clock speed of 2.60 GHz. 20 cores and 128 GB of memory accompanied each node. The homogenized models (such as HRM-Plate and HRM-Solid) were run on a PC that had two Xenon®-E5 -2697 v2 processors with a clock speed of 2.70 GHz. It had 128 GB of random access memory.

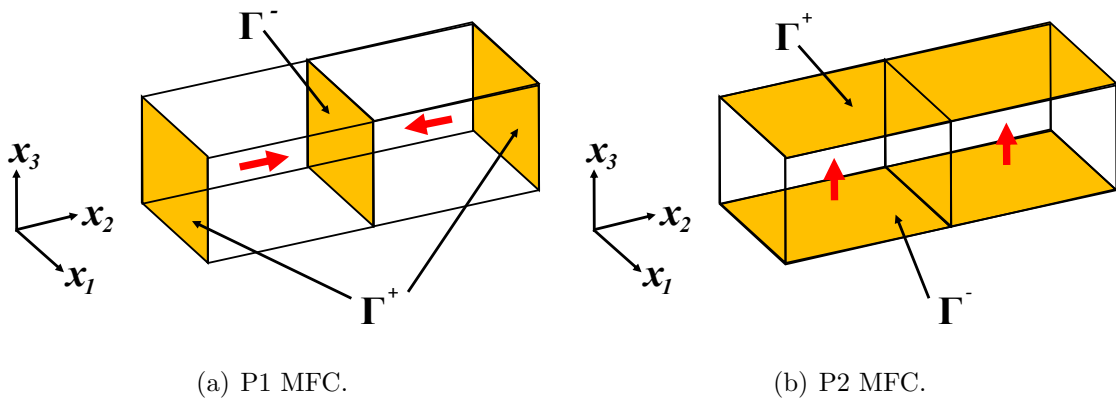


Figure 5.3: Specification of the internal electrode faces (Γ) and poling for the homogenized MFCs.

5.4 Results

Mesh statistics and computing resources utilized are recorded in Table 5.3. The number of CPUs for each analysis was determined by the CPUs that were available on the Halstead Cluster. A peculiar mesh artifact was noted for the M2814 cases. The mesh size of the full patch had a smaller mesh than that of the Active Area model. A closer investigation revealed that the Abaqus[®] meshing strategy placed three elements through the thicknesses of the electrode and Kapton layers for the Active Area models while the Full Patch models had one element through these thicknesses.

5.4.1 Macroscopic Response

The static macroscopic response was the displacement of the host. For each of the three cases, the displacements along the two paths shown in Figure 5.5 were examined. One path was the centerline of the host which was along the line $(x_1, L_2/2, 0)$. It will be referred to as “Centerline”. The second path will be referred to as “Tip Line” and was a path on the free tip of the host and along $(L_1, x_2, 0)$. Figures 5.6 - 5.9 respectively show the displacements of the host for each of the three cases. The first three figures, namely Figures 5.6, 5.7, and 5.8, show the transverse displacement. Part (a) of those figures is the displacement along Centerline and part (b) is along Tip Line. The values of the transverse tip deflection at Centerline $(L_1, L_2/2, 0)$ are shown in Table 5.4. The values in parentheses are computed from

$$\frac{u_3 - u_3^{\text{DNS}}}{u_3^{\text{DNS}}} \times 100 \quad (5.3)$$

and are the percent errors relative to the DNS in each respective case.

Comparing the DNS curves to the DNS without the Passive Area in Figures 5.6 and 5.7 reveals the effect of the Passive Area. The DNS without the Passive Area curves are closer to the DNS curves for Case 2 than for Case 1. This means that, as expected, accounting for the Active Area is non-negligible for the smaller patch. It also means that for patches as wide or wider than the one in Case 2, ignoring the

Table 5.3: Total element and node count as well as resources used for each MFC patch.

Case	MFC Name	Model Type	Number of		Number of Nodes	Number of CPUs	Wallclock	
			Elements	Elements			Time (hrs.)	Time (sec.)
1a	M2503-P1	DNS	918,528	3,935,689	220		0.22	802
1b	M2503-P1	DNS w/o Passive Area	290,304	1,257,301	80		0.08	302
		MIX-Solid	1,592	9,654	1		1×10^{-3}	5
		HRM-Solid	1,592	9,654	1		3×10^{-3}	12
		HRM-Plate	460	1,493	1		3×10^{-4}	1
2a	M2814-P1	DNS	2,874,240	12,262,589	200		3.10	11,186
2b	M2814-P1	DNS w/o Passive Area	3,435,960	14,315,137	240		8.04	28,954
		MIX-Solid	5,056	28,970	1		1×10^{-2}	36
		HRM-Solid	5,056	28,970	1		3×10^{-3}	10
		HRM-Plate	760	2,397	1		1×10^{-3}	5
3a	M2814-P2	DNS	2,874,240	12,262,589	240		12.18	43,876
3b	M2814-P2	DNS w/o Passive Area	3,435,960	14,315,137	160		3.69	13,269
		MIX-Solid	5,056	28,970	1		9×10^{-3}	33
		HRM-Solid	5,056	28,970	1		1×10^{-2}	36

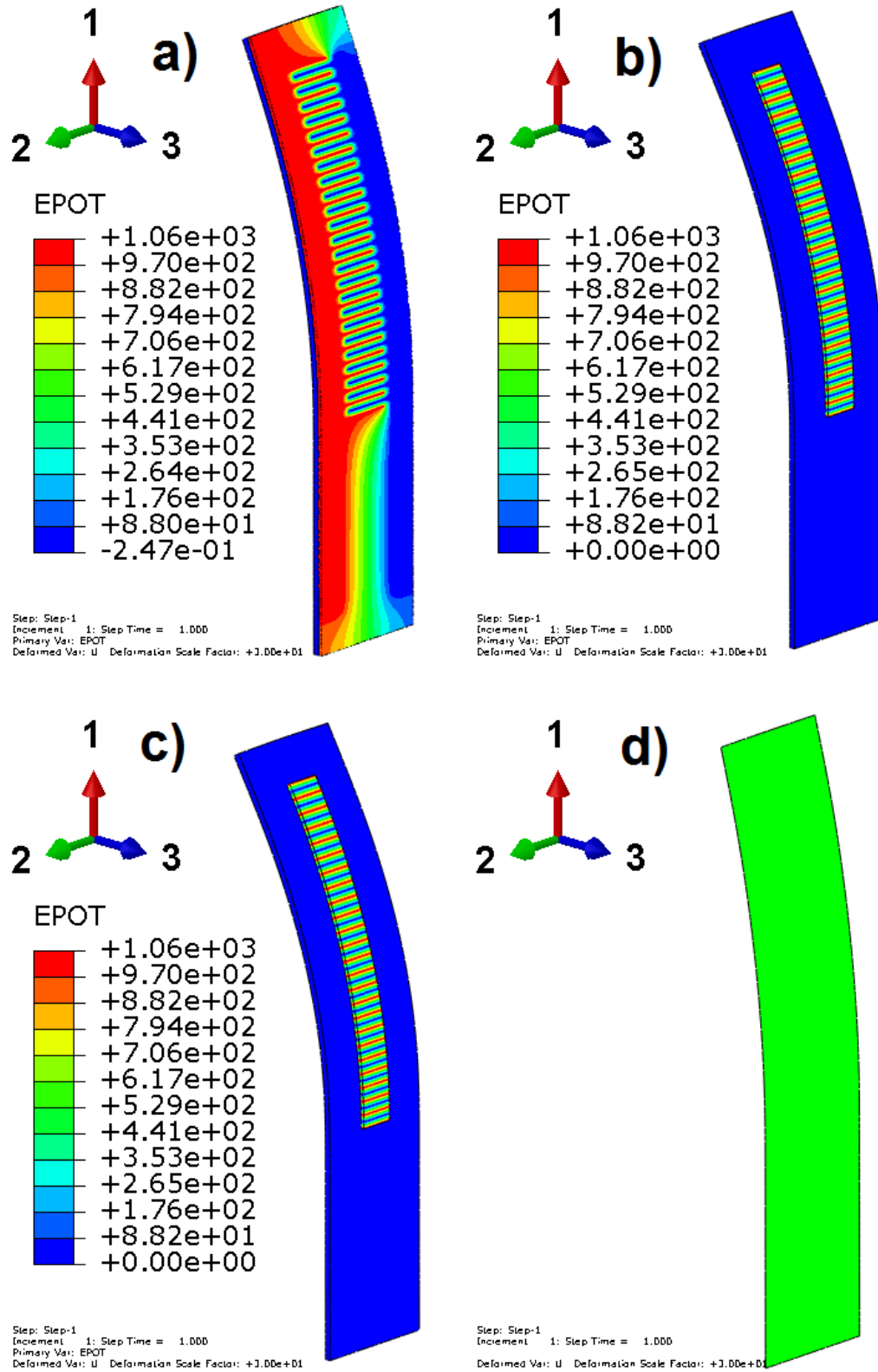


Figure 5.4: Macroscopic model illustration with the M2503-P1 case. Electrical potential [V/mm] shown for all but the plate model. a) DNS b) DNS w/o Passive Area c) HRM-Solid d) HRM-Plate.

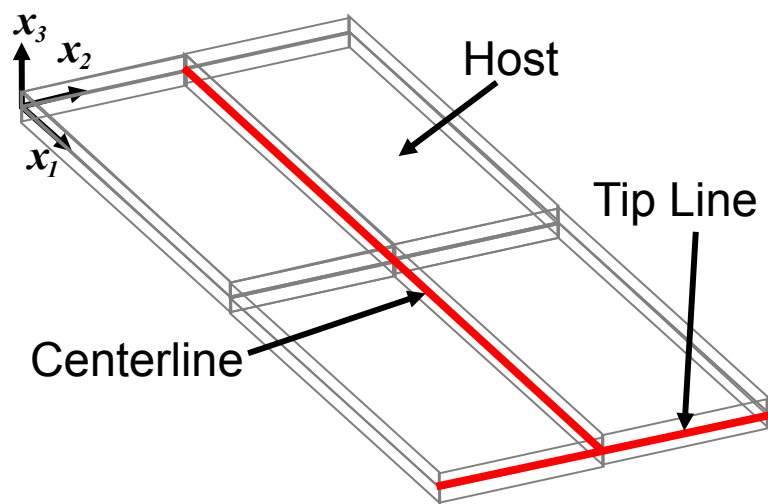


Figure 5.5: Relative locations for macroscopic quantities of interest and definitions of “Centerline” and “Tip Line”.

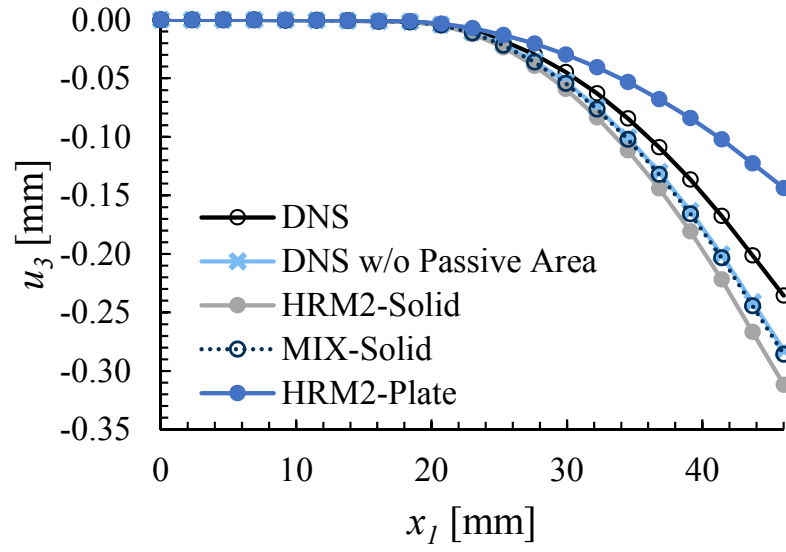
Passive Area is reasonable. Doing so should provide an error of about 4.3% (or less) as indicated in Table 5.4.

In comparing the solid models, the DNS shows the strengths and weaknesses of the solid model modeling strategy. It is apparent that neither the HRM2-Solid or the MIX-Solid models capture the actuator behavior in Cases 1 very well. They are better, however, for than the Plate estimate. For Case 2, the HRM2-Solid gives a 19% error while the MIX-Solid gives a better result at 5.2%. Both solid models provide satisfactory results for Case 3; with the MIX-Solid model being the best. This suggests that the uniform polarization assumption for the HRM2-Solid model of the P1 MFC is unacceptable. The P2 (Case 3) case seems to affirm that ignoring the separation of scale assumption (and supposing that the MFC is a stack of homogeneous layers) can be acceptable (for uniform poling and electrical fields).

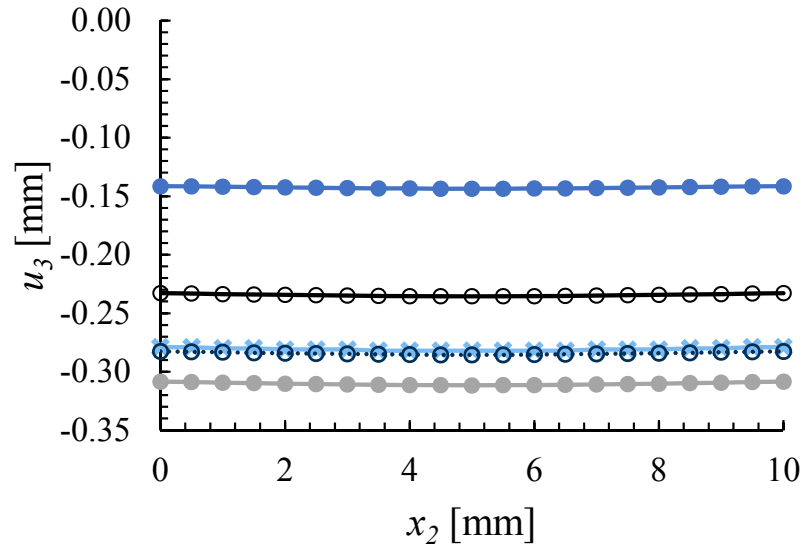
Finally, one can compare the HRM2-Solid to the HRM2-Plate to find the combined effects of the plate kinematics and the thermal analogy. This is because the HRM2-Solid model is the elasticity solution of the homogenized solid and HRM2-Plate models that model. For both cases considered by the plate mode (Case 1 and 2), the plate model seems to provide overly stiff behavior when compared to the DNS. This extra stiffness, which is likely from the assumptions in the plate kinematics, seems to compensate for neglecting to account for the Passive Area. It is overcompensated in Case 1 and about right for Case 2.

Table 5.4: Transverse tip deflection, u_3 , in [mm] at Centerline ($L_1, L_2/2, 0$). Values in parentheses are the percent errors relative to the DNS in each respective case.

	DNS	DNS w/o Passive Area	HRM2- Solid	MIX- Solid	HRM2- Plate
Case 1	-0.236	-0.282 (19.7)	-0.312 (32.2)	-0.286 (21.2)	-0.144 (-39.0)
Case 2	-0.517	-0.539 (4.3)	-0.616 (19.0)	-0.544 (5.2)	-0.492 (-4.8)
Case 3	-0.305	0.301 (-1.2)	-0.290 (-5.0)	-0.293 (-3.8)	N/A

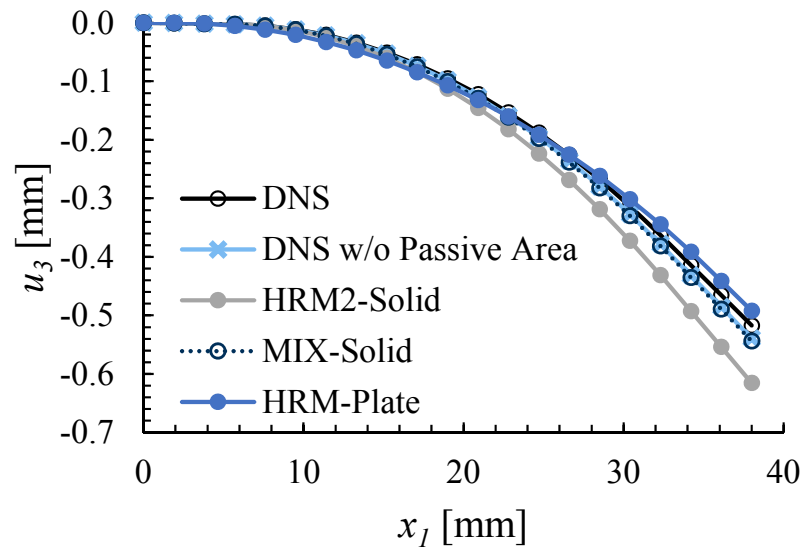


(a) Displacement along Centerline.

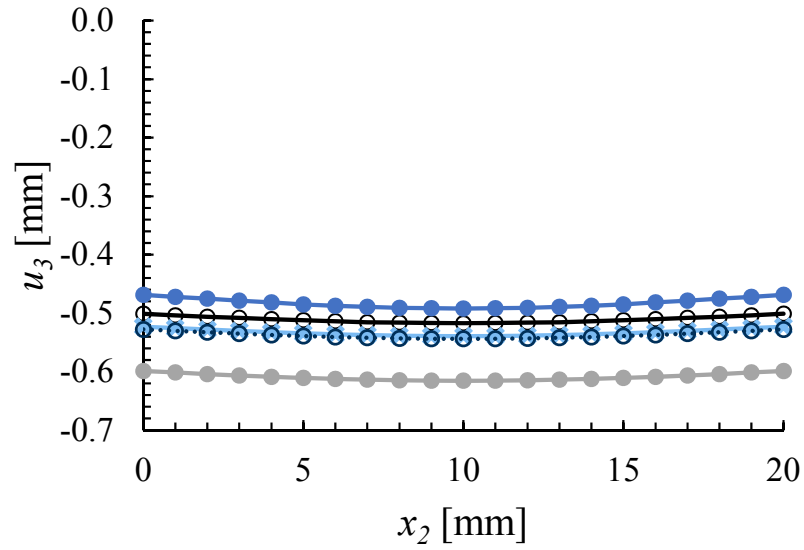


(b) Displacement along Tip Line.

Figure 5.6: Static displacement of the host for Case 1.

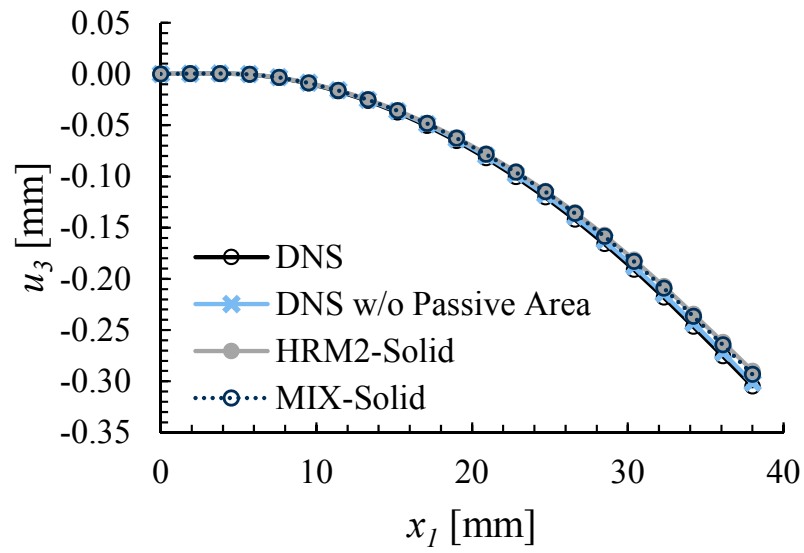


(a) Displacement along Centerline.

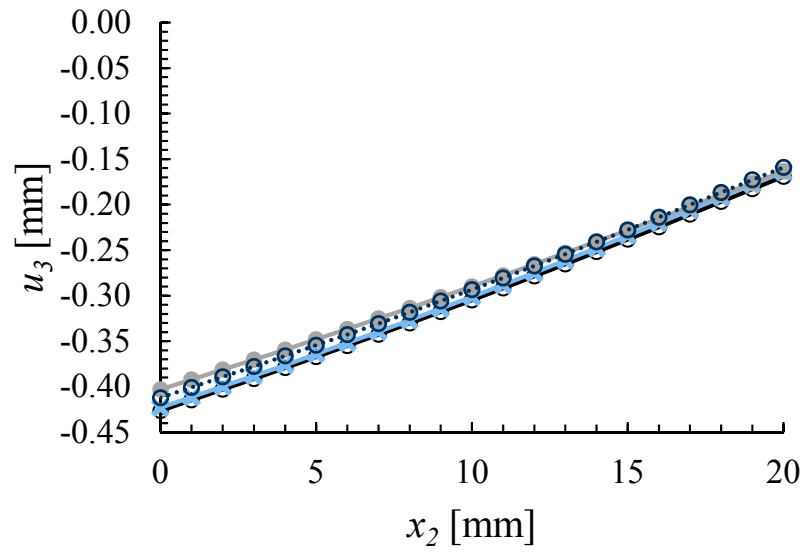


(b) Displacement along Tip Line.

Figure 5.7: Static displacement of the host for Case 2.



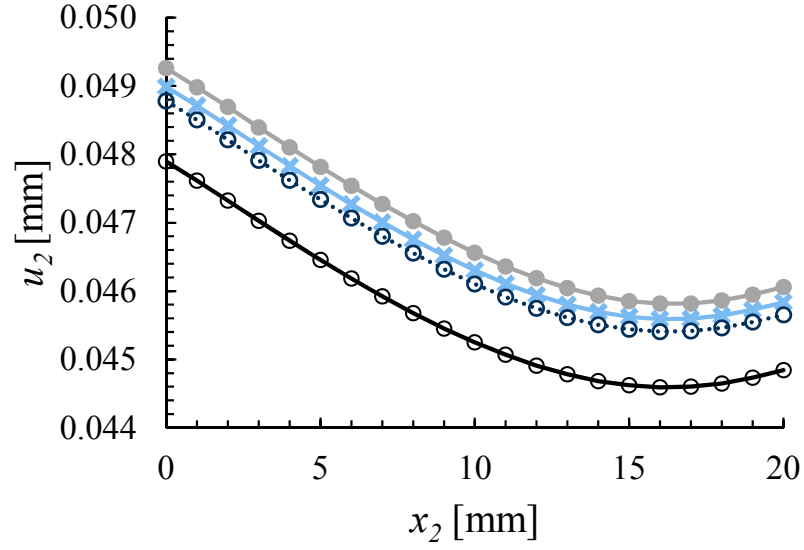
(a) Displacement along Centerline.



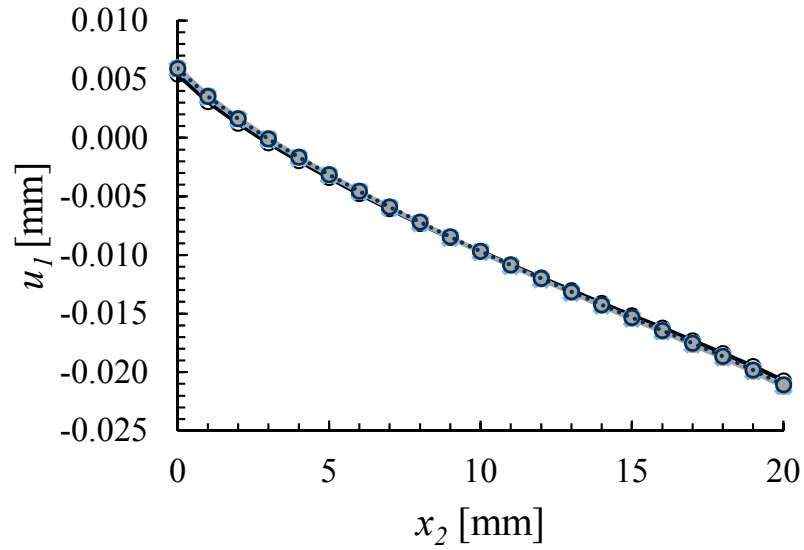
(b) Displacement along Tip Line.

Figure 5.8: Transverse displacement of the host for Case 3.

Since Case 3 has an anisotropic host, nontrivial results are obtained for the lateral and longitudinal displacement along Tip Line. Therefore, Figure 5.9 documents those results.



(a) Lateral displacement.



(b) Longitudinal displacement.

Figure 5.9: Other static displacements of the host for Case 3 along Tip Line.

5.4.2 Comparison of Local Fields

The dehomogenization procedure described in Section 4.2 is demonstrated for an RVE from Case 3. Recall from Table 5.2 that $(N_1, N_2)=(26, 34)$. If counted from the corner of the Active Area closest to the origin, then the RVE where local fields are to be compared was located at $(13, 17)$. At this location, the fields were averaged in the MIX-Solid model and then transferred to complete the BCs specified in Table 4.5. After solving the BVP in Table 4.5, the fields were extracted along selected lines in the RVE. Figure 5.10 helps to define these lines. Line A is along $(y_1, 0, 0)$ and Line B is along $(0, 0, y_3)$. The origin of y_i is at the geometric centroid of the RVE. Line C is included and it is part of the material interface at the top of the PZT fiber. This was an interesting location to interrogate the transverse electric displacement to see what charge may develop at the electrode (*cf* Eq. (1.1)). Line C corresponds to a line along $(y_1, 0, 0.09 \text{ mm})$.

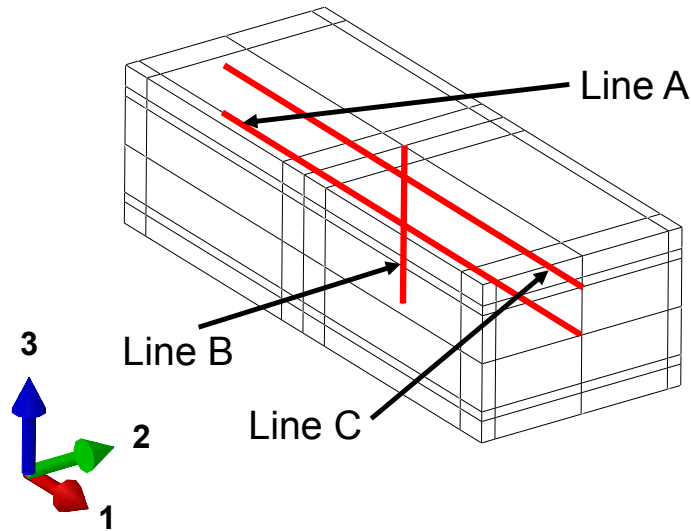
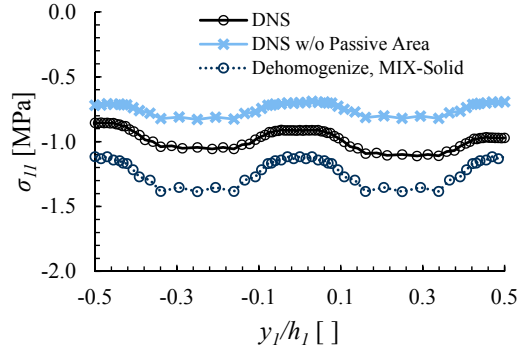
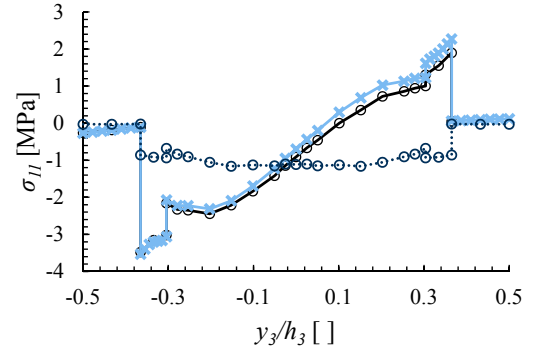


Figure 5.10: Relative locations for microscopic quantities of interest and definitions of “Line A,” “Line B,” and “Line C”.

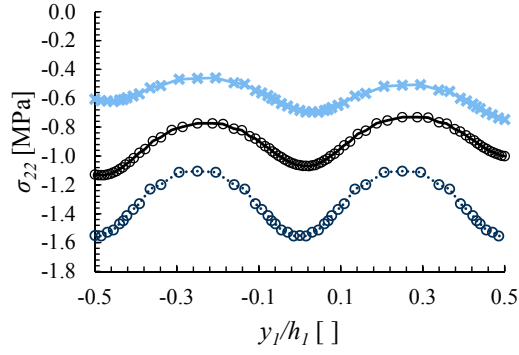
Figure 5.11 - 5.12 shows some of the local fields obtained. The figures compare the DNS (Case 3a), the DNS without the Passive Area (Case 3b), as well as the dehomogenization results. Figure 5.11 compares the normal stresses along Line A and Line B. Parts (a), (c), and (e) of that Figure show Line A results while parts (b), (d), and (f) show Line B results. Examining the results on Line B reveals that the dehomogenization is unable to account for the flexural stresses. The results along Line A show that the trends are captured by the dehomogenization but the magnitude stress values are overpredicted. Figure 5.12 shows the transverse electric displacement along Line C. Again the overall trends are captured but the magnitude is overpredicted. Finally, it is notable to observe the effects of neglecting the Passive Area. Neglecting the Passive Area tends to underestimate the normal stress values.



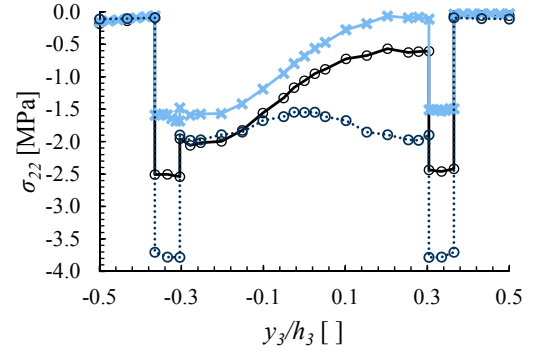
(a) Longitudinal normal stress along Line A.



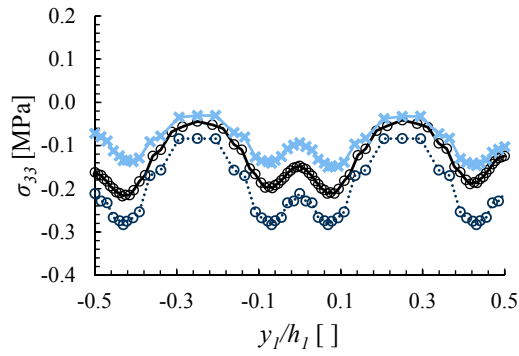
(b) Longitudinal normal stress along Line B.



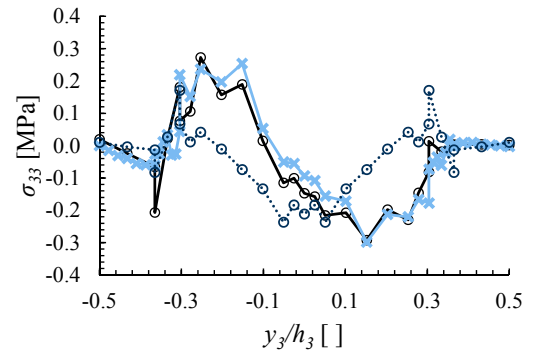
(c) Lateral normal stress along Line A.



(d) Lateral normal stress along Line B.



(e) Transverse normal stress along Line A.



(f) Transverse normal stress along Line B.

Figure 5.11: Contrasting the local fields obtained from Line A and Line B for Case

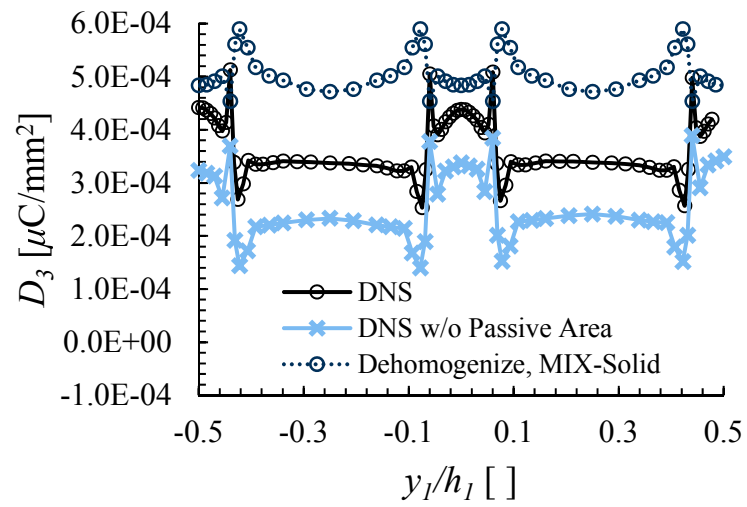


Figure 5.12: Transverse electric displacement along Line C.

6. SUMMARY AND RECOMMENDATIONS

6.1 Summary

A major reason for the MFC's success and popularity stems from its various material heterogeneities. These small-scale heterogeneities pose a formidable challenge for designs and analyses with host structures at the macroscale. Previous homogenizations of the MFC were found to be inadequate and dehomogenization was nonexistent. To a certain extent, the inadequacy of the homogenization treatments of the MFC emanated from an inability of established micromechanical theories to account for internal electrodes. Of all of the piezoelectric homogenization methods reviewed, only RVE analysis has been modified to account for the internal electrodes [51–55, 70]. Their approach assumed full periodicity and it was shown that their approach lacked rigor.

Analytical homogenization is attractive due to its ease of use and low cost; however, prior analytical efforts have been typically limited by plane-stress-like assumptions and plate-kinematics. Thus a new analytical approach that is founded upon the rigorous mechanics of structure genome has been presented as a homogenization tool that is able to homogenize a general stack of piezoelectric layers. For Step-2 homogenization, our approach minimizes the difference of the electric enthalpy between a stack of piezoelectric layers and that of a general anisotropic and piezoelectric solid model. As a result, it was proved that the in-plane strains and the transverse stresses are equal in each layer and the in-plane electric fields and transverse electric displacement are constant between the electrodes. This proof was also applied to Step-1 homogenization by recognizing that the active layer can be viewed as a lateral stack of layers. This knowledge was then applied to MFCs by homogenizing the fiber layers and the full stack of MFC layers by the Hybrid Rules of Mixtures. Special treatment

was given to account for the active layer being embedded among passive layers. Thus, improvements in accuracy and completeness were obtained on the effective properties of MFCs via analytical methods. The derivation clarified what the electrical behavior of the homogenized solid should be. This behavior was also verified by DNSs. Last but not least, the prolific use of plane-stress-like assumptions to homogenize the fiber layers has been examined. The error of using these assumptions and neglecting terms have been traced from the homogenization of the fiber layers to homogenization of the MFC stack of layers. Our results showed that the lateral Young's modulus and piezoelectric strain coefficient are the most adversely affected. Indeed, the plane-stress assumption serves as a useful estimate of the fiber layer properties of the MFC. However, if accuracy is a concern, then the plane-stress-like assumption should be avoided in Step-1 homogenization. As for Step-2, the plane-stress assumption and plate kinematics did not affect the in-plane mechanical properties but FSDT greatly overpredicted the transverse shear stiffnesses.

The fact that piezoelectric fiber composites of technological importance are relatively thin raised the question of whether full periodicity can be used. New RVE analysis BCs have been proposed as a mixture of boundary condition types (MIX). The conditions were first derived for microstructures without internal electrodes. The periodic boundary conditions remained for the in-plane faces but periodicity through the thickness was relaxed. Instead, homogeneous stress BCs were applied on the out-of-plane faces and equipotential BCs were applied when simulating the electrodes. The new boundary conditions were shown to satisfy a previous extension of a piezoelectric macrohomogeneity condition. A series of proofs have been provided to enable rigorous use of the PBCs. Additionally, a new post-processing scheme was devised that enabled crosschecking the material symmetry. It was also found to be a unified procedure for the effective properties. Two typical examples were presented to showcase the difference between the PBCs and the present boundary conditions. For both examples, sizable differences were found for most of the out-of-plane properties. Full PBCs were shown to be insensitive to thickness effects. Sensor and actuator type

loadings were found to provide differing shear coupling coefficients when the equipotential BCs were used for the electrodes. This artifact was also verified with a DNS of the active layer. This suggests that the MFC cannot be homogenized as rigorously as expected.

For the full MFC, the fully periodic BCs were rectified and the MIX BCs from Chapter 3 were implemented. Asymmetric constitutive relations were found; even for the case of 3D periodicity of the mechanical fields proposed in the literature. The IDE case posed difficulty in averaging of the local fields. The difficulty came from the symmetry of the electrical fields within the RVE. Thus two volume averaging schemes were explored and were named *Full Transform* and *Mechanical Transform*. When compared to a DNS of the Active Area, the Mechanical Transform effective properties were found to outperform the Full Transform. Sensor and actuator type loadings continued to yield differing shear coupling coefficients. The P1 case exacerbated the asymmetry.

Large scale 3D FEA models that included microscale features were constructed to test the multiscale methodology. MFCs acting in a unimorph configuration were considered. The most critical case to test was the smallest MFC that is available off the shelf. Some of the test models were constructed with and without the Passive Area. The results revealed that accounting for the Passive Area in the smaller patch was non-negligible. The uniform polarization assumption for the P1 MFC was found to be inadequate. Analytical homogenization, which includes ignoring the separation of scale assumption and supposing that the MFC is a stack of homogeneous layers, was found to be acceptable for the P2 MFC. A mechanical plate model with a thermal analogy was found to provide overly stiff behavior when compared to the DNS of the smaller patch. This extra stiffness, which is likely from the assumptions in the plate kinematics, seems to compensate for neglecting to account for the Passive Area. Methodology for extraction of the local MFC fields was presented and also tested from the unimorph test models. The prediction of the local fields was found to need improvement.

Many files used to create the results in this work can be obtained from <https://cdmhub.org/projects/ernestocamarena>.

6.2 Recommendations

- Recall that Chapter 3 showed that the newly developed MIX BCs satisfy a piezoelectric macrohomogeneity condition for the active layer. These BCs were applied to the full MFC with modifications for internal electrodes and nonuniform poling. The macrohomogeneity condition should be verified for the full MFC as it was for the active layer.
- The proposed RVE analysis for the full MFC was for an RVE of the Active Area. It is recommended that a micromechanical approach should be developed such that both the Active and Passive Areas could be homogenized and then dehomogenized. At the very least, this should be performed for the smaller MFCs such as the M2503-P1 MFC. This may require using the ideas developed here about handling electrodes that are internal to the RVE. With the M2503-P1 MFC being the smallest patch, it would be reasonable to perform an RVE analysis where the RVE is the complete geometry of the patch. Homogeneous stress boundary conditions could be used for all of the mechanical BCs since it would not necessarily be periodic in any direction.
- In this work, it was instructive to first obtain a solid model with an MSG analytical solution. The versatility of MSG allows for a plate model to be constructed directly from information about the host and the MFC. This approach is expected to provide faster results than the solid models but without any of the drawbacks associated with other plate models.
- Here, linear piezoelectricity was utilized. However, real piezoelectric materials have been shown to have nonlinear behavior for high electric fields and hysteresis

[8, 11, 97, 99, 148]. Thus efforts should be made to extend the developments in this dissertation to account for these realities.

A. MATHEMATICA CODE FOR HRM2

The Mathematica [147] code for obtaining results from the HRM2 are presented here. Note that only the code for the Step 2 of the P2 case is provided for brevity. This and many other files can be downloaded from <https://cdmhub.org/projects/ernestocamarena>.

```
In[1]:= SetOptions[Plot, BaseStyle → {FontFamily → "Times", FontSize → 19}];
```

```
In[2]:= legendSize = 14; ρf = 0.8654; angles = {0, 90, 0};
      tKapton = 40 * 10-6; tElect = 18 * 10-6; tActive = 180 * 10-6;
```

```
In[3]:= ti = {2 tKapton, 2 tElect, tActive}; ε0 = 8.854 × 10-12;
```

```
In[4]:= nLam = Length[ti]
```

```
Out[4]= 3
```

```
In[5]:= z = Accumulate[ti]; h = N[z[[nLam]]]
```

```
Out[5]= 0.000296
```

```
In[6]:= VfLam = N[ti / h]
```

```
Out[6]= {0.27027027027, 0.121621621622, 0.608108108108}
```

d31_PZT STEP 1 Inputs

```
In[7]:= epoxyMat = {Ee → 2.9 * 109, ve → 0.3, ke → 4.25 * ε0};
```

```
In[8]:= mat = Join[fiberMat, epoxyMat];
```

```
In[9]:= DD[3] = {{(3.18681318681 * 109 + 5.52173567387 * 1010 Vf) /
      (9.24175824176 * 1018 + 3.26783843354 * 1020 Vf + 2.82071978288 * 1021 Vf2),
      (-9.56043956044 * 108 - 1.37105981328 * 1010 Vf - 9.27906758063 * 109 Vf2) /
      (9.24175824176 * 1018 + 3.26783843354 * 1020 Vf + 2.82071978288 * 1021 Vf2),
      (-9.56043956044 * 108 - 2.47417908112 * 1010 Vf) /
      (9.24175824176 * 1018 + 3.26783843354 * 1020 Vf + 2.82071978288 * 1021 Vf2),
      0, 0, 0, 0, 0, ((-2.25216136856 * 1010 - 5.61476282442 * 1011 Vf) Vf) /
      (9.24175824176 * 1018 + 3.26783843354 * 1020 Vf + 2.82071978288 * 1021 Vf2)},
      {(-1.95613538122 * 10-14 - 6.19464965843 * 10-13 Vf -
      5.05053004571 * 10-12 Vf2 - 3.28960984957 * 10-12 Vf3) /
      (0.000189093086852 + 0.00996261777485 Vf + 0.173565201131 Vf2 + 1. Vf3),
      (6.52045127075 * 10-14 + 3.07099806637 * 10-12 Vf + 4.70702577203 * 10-11 Vf2 +
      2.18543330384 * 10-10 Vf3 - 2.46849385281 * 10-10 Vf4) /
      (0.000189093086852 + 0.00996261777485 Vf + 0.173565201131 Vf2 + 1. Vf3),
      (-1.95613538122 * 10-14 - 6.77502037491 * 10-13 Vf -
      6.03394095293 * 10-12 Vf2 - 2.90517403277 * 10-12 Vf3) /
      (0.000189093086852 + 0.00996261777485 Vf + 0.173565201131 Vf2 + 1. Vf3),
      0, 0, 0, 0, 0, (Vf (-3.98218985963 * 10-13 - 1.39075177003 * 10-11 Vf -
      1.25963429097 * 10-10 Vf2 - 7.87184629356 * 10-11 Vf3)) /
      (0.000189093086852 + 0.00996261777485 Vf + 0.173565201131 Vf2 + 1. Vf3)},
      {(-1.95613538122 * 10-14 - 8.45171181116 * 10-13 Vf -
      8.77144584207 * 10-12 Vf2) /
      (0.000189093086852 + 0.00996261777485 Vf + 0.173565201131 Vf2 + 1. Vf3),
      (-1.95613538122 * 10-14 - 6.77502037491 * 10-13 Vf -
      6.03394095293 * 10-12 Vf2 - 2.90517403277 * 10-12 Vf3) /
      (0.000189093086852 + 0.00996261777485 Vf + 0.173565201131 Vf2 + 1. Vf3),
      (6.52045127075 * 10-14 + 2.40183537928 * 10-12 Vf +
      2.20405566296 * 10-11 Vf2) /
```

```

(0.000189093086852 + 0.00996261777485 Vf + 0.173565201131 Vf^2 + 1. Vf^3),
0, 0, 0, 0, 0, (Vf (1.38096228442 * 10^-12 +
5.0966024162 * 10^-11 Vf + 4.68488454831 * 10^-10 Vf^2)) /
(0.000189093086852 + 0.00996261777485 Vf + 0.173565201131 Vf^2 + 1. Vf^3)},
{0, 0, 0, (8.98510015197 * 10^-10 - 1.76181818299 * 10^-9 Vf +
8.63420295502 * 10^-10 Vf^2) / (1.00218424772 - 1. Vf), 0,
0, 0, - ((1.22317872286 * 10^-12 Vf) / (-1.00218424772 + 1. Vf)), 0},
{0, 0, 0, 0, 5.44525425149 * 10^-11 / (0.0607355281897 + 1. Vf), 0,
(5.94011895786 * 10^-10 Vf) / (0.0607355281897 + 1. Vf), 0, 0},
{0, 0, 0, 0, 0, 8.96551724138 * 10^-10 - 8.44377811094 * 10^-10 Vf, 0, 0, 0},
{0, 0, 0, 0, (5.94011895786 * 10^-10 Vf) / (0.0607355281897 + 1. Vf), 0,
(2.28544755801 * 10^-12 + 7.12932198542 * 10^-10 Vf + 1.75986994688 * 10^-8 Vf^2) /
(0.0607355281897 + 1. Vf), 0, 0},
{0, 0, 0, - ((1.22317872286 * 10^-12 Vf) / (-1.00218424772 + 1. Vf)), 0,
0, 0, - (3.77116921496 * 10^-11 / (-1.00218424772 + 1. Vf)), 0},
{(Vf (-4.60808575737 * 10^-13 - 1.9472562485 * 10^-11 Vf -
1.99054257658 * 10^-10 Vf^2)) /
(0.000189093086852 + 0.00996261777485 Vf + 0.173565201131 Vf^2 + 1. Vf^3),
(Vf (-3.98218985963 * 10^-13 - 1.39075177003 * 10^-11 Vf -
1.25963429097 * 10^-10 Vf^2 - 7.87184629356 * 10^-11 Vf^3)) /
(0.000189093086852 + 0.00996261777485 Vf + 0.173565201131 Vf^2 + 1. Vf^3),
(Vf (1.38096228442 * 10^-12 + 5.0966024162 * 10^-11 Vf +
4.68488454831 * 10^-10 Vf^2)) /
(0.000189093086852 + 0.00996261777485 Vf + 0.173565201131 Vf^2 + 1. Vf^3),
0, 0, 0, 0, 0, (7.11547831168 * 10^-15 + 1.69513356504 * 10^-12 Vf + 1.0537381265 *
10^-10 Vf^2 + 2.33214479829 * 10^-9 Vf^3 + 1.69499437868 * 10^-8 Vf^4) /
(0.000189093086852 + 0.00996261777485 Vf + 0.173565201131 Vf^2 + 1. Vf^3)}};

```

Copper

```
ln[10]:= CufiberMat = {Ec -> 117.2 * 10^9, νc -> 0.31, κσc -> 5 * ε0};
```

```
ln[11]:= Cumat = Join[CufiberMat, epoxyMat];
```

```

In[12]:= DD[2] = Simplify[
  {{ (-Ee (-1 + Vfc) (-1 + vc^2) + Ec Vfc (-1 + ve^2)) / (Ee^2 (-1 + Vfc)^2 (-1 + vc^2) -
    2 Ec Ee (-1 + Vfc) Vfc (-1 + vc ve) + Ec^2 Vfc^2 (-1 + ve^2)),
    (Vfc (vc - ve) + ve - vc ve) / (Ee (-1 + Vfc + vc - Vfc vc) + Ec Vfc (-1 + ve)),
    (Ee (-1 + Vfc) (-1 + vc^2) ve - Ec Vfc vc (-1 + ve^2)) /
    (Ee^2 (-1 + Vfc)^2 (-1 + vc^2) - 2 Ec Ee (-1 + Vfc) Vfc (-1 + vc ve) +
    Ec^2 Vfc^2 (-1 + ve^2)), 0, 0, 0, 0, 0, 0},
  {(Vfc (vc - ve) + ve - vc ve) / (Ee (-1 + Vfc + vc - Vfc vc) + Ec Vfc (-1 + ve)),
    (-Ee^2 (-1 + Vfc) Vfc (-1 + vc + 2 vc^2) - Ec^2 (-1 + Vfc) Vfc (-1 + ve + 2 ve^2) +
    Ec Ee (-1 + vc - 2 Vfc (-1 + vc + 2 vc ve) + Vfc^2 (-2 + vc + ve + 4 vc ve))) /
    (Ec Ee (Ee (-1 + Vfc + vc - Vfc vc) + Ec Vfc (-1 + ve))), (Vfc (vc - ve) + ve - vc ve) /
    (Ee (-1 + Vfc + vc - Vfc vc) + Ec Vfc (-1 + ve)), 0, 0, 0, 0, 0, 0},
  {(Ee (-1 + Vfc) (-1 + vc^2) ve - Ec Vfc vc (-1 + ve^2)) / (Ee^2 (-1 + Vfc)^2
    (-1 + vc^2) - 2 Ec Ee (-1 + Vfc) Vfc (-1 + vc ve) + Ec^2 Vfc^2 (-1 + ve^2)),
    (Vfc (vc - ve) + ve - vc ve) / (Ee (-1 + Vfc + vc - Vfc vc) + Ec Vfc (-1 + ve)),
    (-Ee (-1 + Vfc) (-1 + vc^2) + Ec Vfc (-1 + ve^2)) / (Ee^2 (-1 + Vfc)^2 (-1 + vc^2) -
    2 Ec Ee (-1 + Vfc) Vfc (-1 + vc ve) + Ec^2 Vfc^2 (-1 + ve^2)), 0, 0, 0, 0, 0, 0},
  {0, 0, 0, (2 Vfc (1 + vc)) / Ec - (2 (-1 + Vfc) (1 + ve)) / Ee, 0, 0, 0, 0, 0},
  {0, 0, 0, 0, -((2 (1 + vc) (1 + ve)) / (Ee (-1 + Vfc) (1 + vc) - Ec Vfc (1 + ve))), 0, 0,
    0, 0}, {0, 0, 0, 0, 0, (2 Vfc (1 + vc)) / Ec - (2 (-1 + Vfc) (1 + ve)) / Ee, 0, 0, 0},
  {0, 0, 0, 0, 0, 0, ke - ke Vfc + ksc Vfc, 0, 0},
  {0, 0, 0, 0, 0, 0, 0, (ke ksc) / (ksc + ke Vfc - ksc Vfc), 0},
  {0, 0, 0, 0, 0, 0, 0, 0, ke - ke Vfc + ksc Vfc} /. Cumat];

```

Kapton Layer

```

In[13]:= KaptonMat = {Ek → 2.8 * 10^9, vk → 0.3, kk → 3.4 e0};

```

```

In[14]:= DD[1] = 
$$\begin{pmatrix} \frac{1}{Ek} & \frac{-vk}{Ek} & \frac{-vk}{Ek} & 0 & 0 & 0 & 0 & 0 & 0 \\ \frac{-vk}{Ek} & \frac{1}{Ek} & \frac{-vk}{Ek} & 0 & 0 & 0 & 0 & 0 & 0 \\ \frac{-vk}{Ek} & \frac{-vk}{Ek} & \frac{1}{Ek} & 0 & 0 & 0 & 0 & 0 & 0 \\ 0 & 0 & 0 & \frac{2(1+vk)}{Ek} & 0 & 0 & 0 & 0 & 0 \\ 0 & 0 & 0 & 0 & \frac{2(1+vk)}{Ek} & 0 & 0 & 0 & 0 \\ 0 & 0 & 0 & 0 & 0 & \frac{2(1+vk)}{Ek} & 0 & 0 & 0 \\ 0 & 0 & 0 & 0 & 0 & 0 & kk & 0 & 0 \\ 0 & 0 & 0 & 0 & 0 & 0 & 0 & kk & 0 \\ 0 & 0 & 0 & 0 & 0 & 0 & 0 & 0 & kk \end{pmatrix} /. KaptonMat;$$


```

```

In[15]:=

```

Partition S, d, k for individual transformations to Global CS

Transform with Clockwise rotations

```

In[16]:= β = 
$$\begin{pmatrix} \text{Cos}[\theta \text{ Degree}] & -\text{Sin}[\theta \text{ Degree}] & 0 \\ \text{Sin}[\theta \text{ Degree}] & \text{Cos}[\theta \text{ Degree}] & 0 \\ 0 & 0 & 1 \end{pmatrix};$$


```

```
In[17]:= Rσ = {{β112, β122, β132, 2 β12 β13, 2 β11 β13, 2 β11 β12}, {β212, β222, β232, 2 β22 β23,
  2 β21 β23, 2 β21 β22}, {β312, β322, β332, 2 β32 β33, 2 β31 β33, 2 β31 β32},
  {β21 β31, β22 β32, β23 β33, β23 β32 + β22 β33, β23 β31 + β21 β33, β22 β31 + β21 β32},
  {β11 β31, β12 β32, β13 β33, β13 β32 + β12 β33, β13 β31 + β11 β33, β12 β31 + β11 β32},
  {β11 β21, β12 β22, β13 β23, β13 β22 + β12 β23, β13 β21 + β11 β23, β12 β21 + β11 β22}} /.
  {β11 → β[[1, 1]], β12 → β[[1, 2]], β13 → β[[1, 3]], β21 → β[[2, 1]],
    β22 → β[[2, 2]], β23 → β[[2, 3]], β31 → β[[3, 1]], β32 → β[[3, 2]], β33 → β[[3, 3]]};
```

```
In[18]:= Rε = {{β112, β122, β132, β12 β13, β11 β13, β11 β12},
  {β212, β222, β232, β22 β23, β21 β23, β21 β22},
  {β312, β322, β332, β32 β33, β31 β33, β31 β32}, {2 β21 β31, 2 β22 β32, 2 β23 β33,
  β23 β32 + β22 β33, β23 β31 + β21 β33, β22 β31 + β21 β32}, {2 β11 β31, 2 β12 β32,
  2 β13 β33, β13 β32 + β12 β33, β13 β31 + β11 β33, β12 β31 + β11 β32}, {2 β11 β21,
  2 β12 β22, 2 β13 β23, β13 β22 + β12 β23, β13 β21 + β11 β23, β12 β21 + β11 β22}} /.
  {β11 → β[[1, 1]], β12 → β[[1, 2]], β13 → β[[1, 3]], β21 → β[[2, 1]], β22 → β[[2, 2]],
    β23 → β[[2, 3]], β31 → β[[3, 1]], β32 → β[[3, 2]], β33 → β[[3, 3]]}; ;
```

Partition S, d, k for individual transformations to Global

```
In[19]:= listSE = Array[f, {nLam, 6, 6}];
```

```
In[20]:= listd0 = Array[f, {nLam, 6, 3}];
```

```
In[21]:= listkσ = Array[f, {nLam, 3, 3}];
```

```
In[22]:= d0 =  $\begin{pmatrix} d011 & d021 & d031 \\ d012 & d022 & d032 \\ d013 & d023 & d033 \\ d014 & d024 & d034 \\ d015 & d025 & d035 \\ d016 & d026 & d036 \end{pmatrix}$ ; SE0 =  $\begin{pmatrix} SE011 & SE012 & SE013 & 0 & 0 & SE016 \\ SE012 & SE022 & SE023 & 0 & 0 & SE026 \\ SE013 & SE023 & SE033 & 0 & 0 & SE036 \\ 0 & 0 & 0 & SE044 & SE045 & 0 \\ 0 & 0 & 0 & SE045 & SE055 & 0 \\ SE016 & SE026 & SE036 & 0 & 0 & SE066 \end{pmatrix}$ ;
```

$$k\sigma = \begin{pmatrix} k\sigma011 & k\sigma012 & k\sigma013 \\ k\sigma012 & k\sigma022 & k\sigma023 \\ k\sigma013 & k\sigma023 & k\sigma033 \end{pmatrix};$$

```
In[23]:= Do[Do[listSE[[k, i, j]] = SE0[[i, j]] → ((DD[k])[[1 ;; 6, 1 ;; 6]])[[i, j]],
  {j, 6}, {i, 6}], {k, nLam}];
```

```
In[24]:= Do[Do[listd0[[k, i, j]] = d0[[i, j]] → Transpose[((DD[k])[[7 ;; 9, 1 ;; 6]])[[i, j]],
  {j, 3}, {i, 6}], {k, nLam}];
```

```
In[25]:= Do[Do[listkσ[[k, i, j]] = kσ[[i, j]] → ((DD[k])[[7 ;; 9, 7 ;; 9]])[[i, j]],
  {j, 3}, {i, 3}], {k, nLam}];
```

```
In[26]:= Do[a[k] = Join[Flatten[listSE[[k]]], Flatten[listd0[[k]]], Flatten[listkσ[[k]]]],
  {k, 1, nLam}]
```

```
In[27]:= kσθe = Simplify[β.kσ.Transpose[β]];
```

```
In[28]:= Clear[listSEθ, listdθ, listkσθ]
```

```
In[29]:= SEθe = Re.SE0.Transpose[Re];
```

```
In[30]:= dθe = Re.d0.Transpose[β];
```

```
In[31]:= listSE0 = Array[f, {nLam, 6, 6}];
```

```
In[32]:= listd0 = Array[f, {nLam, 6, 3}];
```

```
In[33]:= listk0 = Array[f, {nLam, 3, 3}];
```

```
In[34]:=
```

$$\text{In[35]:= } \mathbf{d\theta} = \begin{pmatrix} d_{11} & d_{21} & d_{31} \\ d_{12} & d_{22} & d_{32} \\ d_{13} & d_{23} & d_{33} \\ d_{14} & d_{24} & d_{34} \\ d_{15} & d_{25} & d_{35} \\ d_{16} & d_{26} & d_{36} \end{pmatrix}; \quad \mathbf{SE\theta} = \begin{pmatrix} SE_{11} & SE_{12} & SE_{13} & 0 & 0 & SE_{16} \\ SE_{12} & SE_{22} & SE_{23} & 0 & 0 & SE_{26} \\ SE_{13} & SE_{23} & SE_{33} & 0 & 0 & SE_{36} \\ 0 & 0 & 0 & SE_{44} & SE_{45} & 0 \\ 0 & 0 & 0 & SE_{45} & SE_{55} & 0 \\ SE_{16} & SE_{26} & SE_{36} & 0 & 0 & SE_{66} \end{pmatrix};$$

$$\mathbf{k\sigma\theta} = \begin{pmatrix} k\sigma_{11} & k\sigma_{12} & k\sigma_{13} \\ k\sigma_{12} & k\sigma_{22} & k\sigma_{23} \\ k\sigma_{13} & k\sigma_{23} & k\sigma_{33} \end{pmatrix};$$

```
In[36]:= Do[Do[listSE0[[k, i, j]] = SE0[[i, j]] → SE0e[[i, j]] /. a[k] /. θ → angles[[k]],
  {j, 6}, {i, 6}], {k, nLam}];
```

```
In[37]:= Do[Do[listd0[[k, i, j]] = d0[[i, j]] → d0e[[i, j]] /. a[k] /. θ → angles[[k]],
  {j, 3}, {i, 6}], {k, nLam}];
```

```
In[38]:= Do[Do[listk0[[k, i, j]] = k0[[i, j]] → k0e[[i, j]] /. a[k] /. θ → angles[[k]],
  {j, 3}, {i, 3}], {k, nLam}];
```

```
In[39]:= Do[b[k] = Join[Flatten[listSE0[[k]]], Flatten[listd0[[k]]], Flatten[listk0[[k]]]],
  {k, 1, nLam}]
```

Passive Layers First

$$\text{In[40]:= } \mathbf{S} = \begin{pmatrix} SE_{11} & SE_{12} & SE_{13} & 0 & 0 & SE_{16} \\ SE_{12} & SE_{22} & SE_{23} & 0 & 0 & SE_{26} \\ SE_{13} & SE_{23} & SE_{33} & 0 & 0 & SE_{36} \\ 0 & 0 & 0 & SE_{44} & SE_{45} & 0 \\ 0 & 0 & 0 & SE_{45} & SE_{55} & 0 \\ SE_{16} & SE_{26} & SE_{36} & 0 & 0 & SE_{66} \end{pmatrix}; \quad \boldsymbol{\sigma} = \begin{pmatrix} \sigma_{11} \\ \sigma_{22} \\ \sigma_{33} \\ \sigma_{23} \\ \sigma_{13} \\ \sigma_{12} \end{pmatrix};$$

$$\boldsymbol{\Gamma} = \begin{pmatrix} \epsilon_{11} \\ \epsilon_{22} \\ \epsilon_{33} \\ \epsilon_{23} \\ \epsilon_{13} \\ \epsilon_{12} \end{pmatrix}; \quad \boldsymbol{\epsilon\text{avg}} = \begin{pmatrix} \epsilon_{11\text{avg}} \\ \epsilon_{22\text{avg}} \\ \epsilon_{33\text{avg}} \\ \epsilon_{23\text{avg}} \\ \epsilon_{13\text{avg}} \\ \epsilon_{12\text{avg}} \end{pmatrix}; \quad \boldsymbol{\sigma\text{avg}} = \begin{pmatrix} \sigma_{11\text{avg}} \\ \sigma_{22\text{avg}} \\ \sigma_{33\text{avg}} \\ \sigma_{23\text{avg}} \\ \sigma_{13\text{avg}} \\ \sigma_{12\text{avg}} \end{pmatrix};$$

```
In[41]:= n = Length[σ];
```

```
In[42]:= σH = σ; εH = Γ;
```

```
In[43]:= pointer = {1, 2, 6};
```

```
In[44]:= Nswitch = Length[pointer];
```

Switching prescribed strain and/or stress values

```
In[45]:= Do[σH[[pointer[[i]]]] = Γ[[pointer[[i]]]], {i, 1, Nswitch}]
```



```
In[46]:= Do[eH[[pointer[[i]]]] = σ[[pointer[[i]]]], {i, 1, Nswitch}]
```

```
In[47]:= MatrixForm[σH]
```

```
Out[47]//MatrixForm=
```

$$\begin{pmatrix} \epsilon_{11} \\ \epsilon_{22} \\ \sigma_{33} \\ \sigma_{23} \\ \sigma_{13} \\ \epsilon_{12} \end{pmatrix}$$

```
In[48]:= MatrixForm[eH]
```

```
Out[48]//MatrixForm=
```

$$\begin{pmatrix} \sigma_{11} \\ \sigma_{22} \\ \epsilon_{33} \\ \epsilon_{23} \\ \epsilon_{13} \\ \sigma_{12} \end{pmatrix}$$

```
In[49]:= SHp = ConstantArray[0, {n + 3, n + 3}];
```

```
In[50]:= e = S.σ; MatrixForm[e]
```

```
Out[50]//MatrixForm=
```

$$\begin{pmatrix} SE_{11} \sigma_{11} + SE_{16} \sigma_{12} + SE_{12} \sigma_{22} + SE_{13} \sigma_{33} \\ SE_{12} \sigma_{11} + SE_{26} \sigma_{12} + SE_{22} \sigma_{22} + SE_{23} \sigma_{33} \\ SE_{13} \sigma_{11} + SE_{36} \sigma_{12} + SE_{23} \sigma_{22} + SE_{33} \sigma_{33} \\ SE_{45} \sigma_{13} + SE_{44} \sigma_{23} \\ SE_{55} \sigma_{13} + SE_{45} \sigma_{23} \\ SE_{16} \sigma_{11} + SE_{66} \sigma_{12} + SE_{26} \sigma_{22} + SE_{36} \sigma_{33} \end{pmatrix}$$

```
In[51]:= Do[eqn[i] = Γ[[i]][[1]] == ε[[i, 1]], {i, 1, n}]
```

```
In[52]:= eqnList = ConstantArray[0, n]; vars = ConstantArray[0, n];
```

```
In[53]:= Do[eqnList[[i]] = eqn[i], {i, 1, n}];
```

```
In[54]:= Do[vars[[i]] = eH[[i]][[1]], {i, 1, n}]
```

```
In[55]:= eqnList
```

```
Out[55]= {ε11 == SE11 σ11 + SE16 σ12 + SE12 σ22 + SE13 σ33,
          ε22 == SE12 σ11 + SE26 σ12 + SE22 σ22 + SE23 σ33,
          ε33 == SE13 σ11 + SE36 σ12 + SE23 σ22 + SE33 σ33, ε23 == SE45 σ13 + SE44 σ23,
          ε13 == SE55 σ13 + SE45 σ23, ε12 == SE16 σ11 + SE66 σ12 + SE26 σ22 + SE36 σ33}
```

```
In[56]:= vars
```

```
Out[56]= {σ11, σ22, ε33, ε23, ε13, σ12}
```

```
In[57]:= sol = Simplify[Solve[eqnList, vars]][[1]];]
```

```
In[58]:= Do[temp[i] = eH[[i]][[1]] /. sol[[i]], {i, 1, n}]
```

```
In[59]:= Do[Do[SHp[[i, j]] = Simplify[(Coefficient[temp[i], σH[[j]])][[1]]], {j, 1, n}],
          {i, 1, n}]
```

```
In[60]:= ClearAll[S, σ, Γ, eavg, σavg, n]
```

Active Layer

$$\text{In[61]:= } S = \begin{pmatrix} SE11 & SE12 & SE13 & 0 & 0 & SE16 & 0 & 0 & d31 \\ SE12 & SE22 & SE23 & 0 & 0 & SE26 & 0 & 0 & d32 \\ SE13 & SE23 & SE33 & 0 & 0 & SE36 & 0 & 0 & d33 \\ 0 & 0 & 0 & SE44 & SE45 & 0 & 0 & d24 & 0 \\ 0 & 0 & 0 & SE45 & SE55 & 0 & d15 & 0 & 0 \\ SE16 & SE26 & SE36 & 0 & 0 & SE66 & 0 & 0 & 0 \\ 0 & 0 & 0 & 0 & d15 & 0 & k\sigma11 & 0 & 0 \\ 0 & 0 & 0 & d24 & 0 & 0 & 0 & k\sigma22 & 0 \\ d31 & d32 & d33 & 0 & 0 & 0 & 0 & 0 & k\sigma33 \end{pmatrix};$$

$$\sigma = \begin{pmatrix} \sigma11 \\ \sigma22 \\ \sigma33 \\ \sigma23 \\ \sigma13 \\ \sigma12 \\ E1 \\ E2 \\ E3 \end{pmatrix}; \Gamma = \begin{pmatrix} \epsilon11 \\ \epsilon22 \\ \epsilon33 \\ \epsilon23 \\ \epsilon13 \\ \epsilon12 \\ D1 \\ D2 \\ D3 \end{pmatrix}; eavg = \begin{pmatrix} \epsilon11avg \\ \epsilon22avg \\ \epsilon33avg \\ \epsilon23avg \\ \epsilon13avg \\ \epsilon12avg \\ D1avg \\ D2avg \\ D3avg \end{pmatrix}; \sigmaavg = \begin{pmatrix} \sigma11avg \\ \sigma22avg \\ \sigma33avg \\ \sigma23avg \\ \sigma13avg \\ \sigma12avg \\ E1avg \\ E2avg \\ E3avg \end{pmatrix};$$

```
In[62]:= n = Length[σ];
```

```
In[63]:= σH = σ; εH = Γ;
```

```
In[64]:= pointer = {1, 2, 6, 9};
```

```
In[65]:= Nswitch = Length[pointer];
```

Switching prescribed strain and/or stress values

```
In[66]:= Do[σH[[pointer[[i]]]] = Γ[[pointer[[i]]]], {i, 1, Nswitch}]
```

```
In[67]:= Do[εH[[pointer[[i]]]] = σ[[pointer[[i]]]], {i, 1, Nswitch}]
```

```
In[68]:= MatrixForm[σH]
```

```
Out[68]//MatrixForm=
```

$$\begin{pmatrix} \epsilon11 \\ \epsilon22 \\ \sigma33 \\ \sigma23 \\ \sigma13 \\ \epsilon12 \\ E1 \\ E2 \\ D3 \end{pmatrix}$$

```

In[69]:= MatrixForm[eH]
Out[69]//MatrixForm=

$$\begin{pmatrix} \sigma_{11} \\ \sigma_{22} \\ \epsilon_{33} \\ \epsilon_{23} \\ \epsilon_{13} \\ \sigma_{12} \\ D_1 \\ D_2 \\ E_3 \end{pmatrix}$$


In[70]:= SHa = ConstantArray[0, {n, n}];

In[71]:= e = S. $\sigma$ ; MatrixForm[e]
Out[71]//MatrixForm=

$$\begin{pmatrix} d_{31} E_3 + SE_{11} \sigma_{11} + SE_{16} \sigma_{12} + SE_{12} \sigma_{22} + SE_{13} \sigma_{33} \\ d_{32} E_3 + SE_{12} \sigma_{11} + SE_{26} \sigma_{12} + SE_{22} \sigma_{22} + SE_{23} \sigma_{33} \\ d_{33} E_3 + SE_{13} \sigma_{11} + SE_{36} \sigma_{12} + SE_{23} \sigma_{22} + SE_{33} \sigma_{33} \\ d_{24} E_2 + SE_{45} \sigma_{13} + SE_{44} \sigma_{23} \\ d_{15} E_1 + SE_{55} \sigma_{13} + SE_{45} \sigma_{23} \\ SE_{16} \sigma_{11} + SE_{66} \sigma_{12} + SE_{26} \sigma_{22} + SE_{36} \sigma_{33} \\ E_1 k \sigma_{11} + d_{15} \sigma_{13} \\ E_2 k \sigma_{22} + d_{24} \sigma_{23} \\ E_3 k \sigma_{33} + d_{31} \sigma_{11} + d_{32} \sigma_{22} + d_{33} \sigma_{33} \end{pmatrix}$$


In[72]:= Do[eqn[i] = F[[i]][[1]] == e[[i, 1]], {i, 1, n}]

In[73]:= eqnList = ConstantArray[0, n]; vars = ConstantArray[0, n];

In[74]:= Do[eqnList[[i]] = eqn[i], {i, 1, n}];

In[75]:= Do[vars[[i]] = eH[[i]][[1]], {i, 1, n}]

In[76]:= eqnList
Out[76]= {e11 == d31 E3 + SE11  $\sigma_{11}$  + SE16  $\sigma_{12}$  + SE12  $\sigma_{22}$  + SE13  $\sigma_{33}$ ,
e22 == d32 E3 + SE12  $\sigma_{11}$  + SE26  $\sigma_{12}$  + SE22  $\sigma_{22}$  + SE23  $\sigma_{33}$ ,
e33 == d33 E3 + SE13  $\sigma_{11}$  + SE36  $\sigma_{12}$  + SE23  $\sigma_{22}$  + SE33  $\sigma_{33}$ , e23 == d24 E2 + SE45  $\sigma_{13}$  + SE44  $\sigma_{23}$ ,
e13 == d15 E1 + SE55  $\sigma_{13}$  + SE45  $\sigma_{23}$ , e12 == SE16  $\sigma_{11}$  + SE66  $\sigma_{12}$  + SE26  $\sigma_{22}$  + SE36  $\sigma_{33}$ ,
D1 == E1 k  $\sigma_{11}$  + d15  $\sigma_{13}$ , D2 == E2 k  $\sigma_{22}$  + d24  $\sigma_{23}$ , D3 == E3 k  $\sigma_{33}$  + d31  $\sigma_{11}$  + d32  $\sigma_{22}$  + d33  $\sigma_{33}$ }

In[77]:= vars
Out[77]= { $\sigma_{11}$ ,  $\sigma_{22}$ ,  $\epsilon_{33}$ ,  $\epsilon_{23}$ ,  $\epsilon_{13}$ ,  $\sigma_{12}$ , D1, D2, E3}

In[78]:= sol = Simplify[Solve[eqnList, vars]][[1]];

In[79]:= Do[temp[i] = eH[[i]][[1]] /. sol[[i]], {i, 1, n}]

In[80]:= Do[Do[SHA[[i, j]] = Simplify[(Coefficient[temp[i],  $\sigma$ H[[j]]])[1]], {j, 1, n}],
{i, 1, n}]

```

```
In[81]:= Print[ MatrixForm[eH[[;;]]], "=", MatrixForm[SHa], MatrixForm[σH[[;;]]]]
```

$$\begin{pmatrix} \sigma_{11} \\ \sigma_{22} \\ \epsilon_{33} \\ \epsilon_{23} \\ \epsilon_{13} \\ \sigma_{12} \\ D_1 \\ D_2 \\ E_3 \end{pmatrix} = \begin{pmatrix} -\frac{k\sigma_{33} SE_{66} (-k\sigma_{33} SE_{26}^2 - d_{32}^2 SE_{66} + k\sigma_{33} SE_{22} SE_{66})}{(k\sigma_{33} SE_{16} SE_{26} + d_{31} d_{32} SE_{66} - k\sigma_{33} SE_{12} SE_{66})^2 + (-k\sigma_{33} SE_{26}^2 - d_{32}^2 SE_{66} + k\sigma_{33} SE_{22} SE_{66})} \\ \frac{-k\sigma_{33} SE_{16} SE_{26} - d_{31} d_{32} SE_{66} + k\sigma_{33} SE_{12} SE_{66}}{d_{32}^2 (-SE_{16}^2 + SE_{11} SE_{66}) + 2 d_{31} d_{32} (SE_{16} SE_{26} - SE_{12} SE_{66}) + d_{31}^2 (-SE_{26}^2 + SE_{22} SE_{66}) + k\sigma_{33} (SE_{16}^2 SE_{22} - SE_{12} SE_{26})} \\ \frac{d_{32}^2 (SE_{16} SE_{36} - SE_{13} SE_{66}) + d_{31} d_{33} (SE_{26}^2 - SE_{22} SE_{66}) + d_{32} (-d_{33} SE_{16} SE_{26} - d_{31} SE_{26} SE_{36} + d_{33} SE_{12} SE_{66} + d_{31} SE_{23} SE_{66}) + k\sigma_{33} (SE_{16} SE_{26} - SE_{12} SE_{66})}{d_{32}^2 (SE_{16}^2 - SE_{11} SE_{66}) + d_{31} d_{32} (-2 SE_{16} SE_{26} + 2 SE_{12} SE_{66}) + d_{31}^2 (SE_{26}^2 - SE_{22} SE_{66}) - k\sigma_{33} (SE_{16}^2 SE_{22} - SE_{12} SE_{26})} \\ 0 \\ 0 \\ \frac{-d_{32}^2 SE_{16} + k\sigma_{33} SE_{16} SE_{22} + d_{31} d_{32} SE_{26} - k\sigma_{33} SE_{12}}{d_{32}^2 (-SE_{16}^2 + SE_{11} SE_{66}) + 2 d_{31} d_{32} (SE_{16} SE_{26} - SE_{12} SE_{66}) + d_{31}^2 (-SE_{26}^2 + SE_{22} SE_{66}) + k\sigma_{33} (SE_{16}^2 SE_{22} - SE_{12} SE_{26})} \\ 0 \\ 0 \\ \frac{d_{32} SE_{16} SE_{26} - d_{31} SE_{26}^2 - d_{32} SE_{12} SE_{66} + d_{31} SE_{22}}{d_{32}^2 (-SE_{16}^2 + SE_{11} SE_{66}) + 2 d_{31} d_{32} (SE_{16} SE_{26} - SE_{12} SE_{66}) + d_{31}^2 (-SE_{26}^2 + SE_{22} SE_{66}) + k\sigma_{33} (SE_{16}^2 SE_{22} - SE_{12} SE_{26})} \end{pmatrix}$$

```
In[82]:= SHstar =
```

```
Sum[VfLam[[i]] * SHp /. b[i], {i, 1, 2}] + Sum[VfLam[[i]] * SHa /. b[i], {i, 3, nLam}];
```

$$\text{In[83]:= } \Gamma\text{Havg} = \begin{pmatrix} \sigma_{11\text{avg}} \\ \sigma_{22\text{avg}} \\ \epsilon_{33\text{avg}} \\ \epsilon_{23\text{avg}} \\ \epsilon_{13\text{avg}} \\ \sigma_{12\text{avg}} \\ D_{1\text{avg}} \\ D_{2\text{avg}} \\ E_{3\text{avg}} \end{pmatrix}; \quad \sigma\text{Havg} = \begin{pmatrix} \epsilon_{11\text{avg}} \\ \epsilon_{22\text{avg}} \\ \sigma_{33\text{avg}} \\ \sigma_{23\text{avg}} \\ \sigma_{13\text{avg}} \\ \epsilon_{12\text{avg}} \\ E_{1\text{avg}} \\ E_{2\text{avg}} \\ D_{3\text{avg}} \end{pmatrix};$$

```
In[84]:= eHavg = SHstar.σHavg;
```

```
In[85]:= Do[EQN[i] = ΓHavg[[i]][[1]] == eHavg[[i, 1]], {i, 1, n}]
```

```
In[86]:= EQNlist = ConstantArray[0, n]; VARS = ConstantArray[0, n];
```

```
In[87]:= Do[EQNlist[[i]] = EQN[i], {i, 1, n}];
```

```
In[88]:= Do[VARS[[i]] = eavg[[i]][[1]], {i, 1, n}]
```

```
In[89]:= SOL = Solve[EQNlist, VARS][[1]];
```

```
In[90]:= Do[TEMP[i] = eavg[[i]][[1]] /. SOL[[i]], {i, 1, n}]
```

```
In[91]:= SHstarNew = ConstantArray[0, {n, n}];
```

```
In[92]:= Do[
  Do[SHstarNew[[i, j]] = (Coefficient[TEMP[i], σavg[[j]]])[1], {j, 1, n}], {i, 1, n}]
```

```
In[93]:= listS = Array[f, {6, 6}]; listd = Array[f, {6, 3}];
listd2 = Array[f, {6, 3}]; listk = Array[f, {3, 3}];
```

```
In[94]:= Do[listS[[i, j]] = SE0[[i, j]] → (SHstarNew[[1 ;; 6, 1 ;; 6]])[[i, j]], {j, 6}, {i, 6}]
```

```
In[95]:= Do[listd[[i, j]] = d0[[i, j]] → (SHstarNew[[1 ;; 6, 7 ;; 9]])[[i, j]], {j, 3}, {i, 6}]
```

```
In[96]:= Do[listd2[[i, j]] = d0[[i, j]] → (SHstarNew[[7 ;; 9, 1 ;; 6]])[[j, i]], {j, 3}, {i, 6}]
```

```
In[97]:= Do[listk[[i, j]] = kσ[[i, j]] → (SHstarNew[[7 ;; 9, 7 ;; 9]])[[i, j]], {j, 3}, {i, 3}]
```

```

In[98]:= c = Join[Flatten[listS], Flatten[listd], Flatten[listk]];

In[99]:= c2 = Join[Flatten[listS], Flatten[listd2], Flatten[listk]];

In[100]:= kσStar = kσ /. c;

In[101]:= CE0 = Inverse[SE0] /. c;

In[102]:= e = Inverse[SE0].d0 /. c;

In[103]:= dθ =  $\begin{pmatrix} d_{11} & d_{21} & d_{31} \\ d_{12} & d_{22} & d_{32} \\ d_{13} & d_{23} & d_{33} \\ d_{14} & d_{24} & d_{34} \\ d_{15} & d_{25} & d_{35} \\ d_{16} & d_{26} & d_{36} \end{pmatrix}$ ; SEθ =  $\begin{pmatrix} SE_{11} & SE_{12} & SE_{13} & 0 & 0 & SE_{16} \\ SE_{12} & SE_{22} & SE_{23} & 0 & 0 & SE_{26} \\ SE_{13} & SE_{23} & SE_{33} & 0 & 0 & SE_{36} \\ 0 & 0 & 0 & SE_{44} & SE_{45} & 0 \\ 0 & 0 & 0 & SE_{45} & SE_{55} & 0 \\ SE_{16} & SE_{26} & SE_{36} & 0 & 0 & SE_{66} \end{pmatrix}$ ;

kσθ =  $\begin{pmatrix} k_{\sigma 11} & k_{\sigma 12} & k_{\sigma 13} \\ k_{\sigma 12} & k_{\sigma 22} & k_{\sigma 23} \\ k_{\sigma 13} & k_{\sigma 23} & k_{\sigma 33} \end{pmatrix}$ ;

In[104]:= keStar = (kσ - Transpose[d0].e) /. c; MatrixForm[keStar / ε0 /. {Vf → ρf, Vfc → 0.24}]

Out[104]/MatrixForm=

$$\begin{pmatrix} 988.588975803 & 0. & 0. \\ 0. & 18.9285961597 & 0. \\ 0. & 0. & 1986.15350555 \end{pmatrix}$$


In[105]:= keStar = (kσ - Transpose[d0].e) /. c2; MatrixForm[keStar / ε0 /. {Vf → ρf, Vfc → 0.24}]

Out[105]/MatrixForm=

$$\begin{pmatrix} 988.588975803 & 0. & 0. \\ 0. & 18.9285961597 & 0. \\ 0. & 0. & 1986.15350555 \end{pmatrix}$$


In[106]:= Sstar = SHstarNew[[1 ;; 6, 1 ;; 6]];

In[107]:= dStar = SHstarNew[[1 ;; 6, 7 ;; 9]];
MatrixForm[dStar / 10-12 /. {Vf → 0.8654, Vfc → 0.24}]

Out[107]/MatrixForm=

$$\begin{pmatrix} 0 & 0 & -297.232788432 \\ 0 & 0 & -201.862649728 \\ 0 & 0 & 489.934494328 \\ 0 & 4.70599559785 & 0 \\ 337.534587797 & 0 & 0 \\ 0 & 0 & 0 \end{pmatrix}$$


In[108]:= dStar = Transpose[SHstarNew[[7 ;; 9, 1 ;; 6]]];
MatrixForm[dStar / 10-12 /. {Vf → 0.8654, Vfc → 0.24}]

Out[108]/MatrixForm=

$$\begin{pmatrix} 0 & 0 & -297.232788432 \\ 0 & 0 & -201.862649728 \\ 0 & 0 & 489.934494328 \\ 0 & 4.70599559785 & 0 \\ 337.534587797 & 0 & 0 \\ 0 & 0 & 0 \end{pmatrix}$$


```

In[109]:=

```

In[110]:= E1star =  $\frac{1}{Sstar[[1, 1]]}$  ; E2star =  $\frac{1}{Sstar[[2, 2]]}$  ; E3star =  $\frac{1}{Sstar[[3, 3]]}$  ;

G12star =  $\frac{1}{Sstar[[6, 6]]}$  ; G13star =  $\frac{1}{Sstar[[5, 5]]}$  ; G23star =  $\frac{1}{Sstar[[4, 4]]}$  ;
v12star = -Sstar[[1, 2]] * E1star;
v13star = -Sstar[[1, 3]] * E1star; v23star = -Sstar[[2, 3]] * E2star;

```

In[113]:= Cstar = CE0 /. c;

In[114]:= eStar = CE0.d0 /. c; MatrixForm[eStar /. {Vf → 0.8654, Vfc → 0.24}]

Out[114]/MatrixForm=

$$\begin{pmatrix} 0. & 0. & -9.01199929273 \\ 0. & 0. & -3.90827063237 \\ 0. & 0. & 3.44157649913 \\ 0. & 0.0133527162396 & 0. \\ 0.911658846091 & 0. & 0. \\ 0. & 0. & 0. \end{pmatrix}$$

In[115]:= eStar2 = CE0.d0 /. c2; MatrixForm[eStar2 /. {Vf → 0.8654, Vfc → 0.24}]

Out[115]/MatrixForm=

$$\begin{pmatrix} 0. & 0. & -9.01199929273 \\ 0. & 0. & -3.90827063237 \\ 0. & 0. & 3.44157649913 \\ 0. & 0.0133527162396 & 0. \\ 0.911658846091 & 0. & 0. \\ 0. & 0. & 0. \end{pmatrix}$$

In[116]:= nsigFig = 5;

In[117]:= varNames3D = {"E1", "E2", "E3", "G12", "G13", "G23", "v12", "v13", "v23", "d31",
"d32", "d33", "d24", "d15", "k^σ₁₁", "k^σ₂₂", "k^σ₃₃", "k^ε₁₁", "k^ε₂₂", "k^ε₃₃"};

```

In[118]:= threeDResults = {E1star/10^9, E2star/10^9, E3star/10^9, G12star/10^9,
  G13star/10^9, G23star/10^9, v12star, v13star, v23star, dStar[[1, 3]]/10^-12,
  dStar[[2, 3]]/10^-12, dStar[[3, 3]]/10^-12, dStar[[4, 2]]/10^-12, dStar[[5, 1]]/10^-12,
  koStar[[1, 1]]/ε0, koStar[[2, 2]]/ε0, koStar[[3, 3]]/ε0, keStar[[1, 1]]/ε0,
  keStar[[2, 2]]/ε0, keStar[[3, 3]]/ε0}; Print[MatrixForm[varNames3D],
  "=", MatrixForm[threeDResults /. {Vf → 0.8654, Vfc → 0.24}]]

```

$$\begin{pmatrix} E_1 \\ E_2 \\ E_3 \\ G_{12} \\ G_{13} \\ G_{23} \\ v_{12} \\ v_{13} \\ v_{23} \\ d_{31} \\ d_{32} \\ d_{33} \\ d_{24} \\ d_{15} \\ k_{11}^\sigma \\ k_{22}^\sigma \\ k_{33}^\sigma \\ k_{11}^\epsilon \\ k_{22}^\epsilon \\ k_{33}^\epsilon \end{pmatrix} = \begin{pmatrix} 30.3690843274 \\ 16.0987614385 \\ 10.5199568464 \\ 4.1352790212 \\ 2.70093459767 \\ 2.83738392057 \\ 0.308575243133 \\ 0.354687418679 \\ 0.236990950935 \\ -297.232788432 \\ -201.862649728 \\ 489.934494328 \\ 4.70599559785 \\ 337.534587797 \\ 1023.34348143 \\ 18.9356932711 \\ 2568.23421333 \\ 988.588975803 \\ 18.9285961597 \\ 1986.15350555 \end{pmatrix}$$

B. RVE ANALYSIS SCRIPTS FOR THE FULL MFC

Once the RVE geometry has been created and the P1 case was poled, the following Python code is for homogenizing the full MFC (P1 or P2). This and many other files can be downloaded from <https://cdmhub.org/projects/ernestocamarena>.


```

# -*- coding: mbcs -*-
# Do not delete the following import lines
from abaqus import *
from abaqusConstants import *
import __main__
import section
import regionToolset
import displayGroupMdbToolset as dgm
import part
import mesh
import material
import assembly
import step
import interaction
import load
import optimization
import job
import sketch
import visualization
import xyPlot
import displayGroupOdbToolset as dgo
import connectorBehavior

def getXYZ_min_max(I):
    #Given a list of index values I, this looks at each element index by I
    #to find the min and max x,y,z values

    #For example:
    #Inputing I=[237] will find the min/max x/y/z for the element[237]

    #or I=range(0,nel) will find the min/max x/y/z for all the elements index
    #up to nel.
    xCoordsList=[]
    yCoordsList=[]
    zCoordsList=[]
    p = mdb.models[modelName].parts['Part-1']
    nNodesElem=len(p.elements[0].getNodes()) #The number of nodes per element
    for i in I:
        elementNodes=p.elements[i].getNodes()
        for j in range(0,nNodesElem):
            x=elementNodes[j].coordinates[0]
            y=elementNodes[j].coordinates[1]
            z=elementNodes[j].coordinates[2]
            xCoordsList.append(x)
            yCoordsList.append(y)
            zCoordsList.append(z)
    Xmin=min(xCoordsList)
    Xmax=max(xCoordsList)
    Ymin=min(yCoordsList)
    Ymax=max(yCoordsList)
    Zmin=min(zCoordsList)
    Zmax=max(zCoordsList)
    return (Xmin, Xmax, Ymin, Ymax, Zmin, Zmax)
def createBCset(part, axis, locValue, lim, setName):
    axis=axis.upper()
    axisCoordDict={}

```

```

axisCoordDict['X']=0
axisCoordDict['Y']=1
axisCoordDict['Z']=2

p = part
nodes=[]
nds = p.nodes # nds is a list
for i, nd in enumerate(nds):
    coord_i = axisCoordDict[axis]
    if round(nd.coordinates[coord_i],lim)==round(locValue,lim) :
        #print 'true'
        #print nd.coordinates[coord_i]- locValue
        if len(nodes)==0:
            nodes = nds[i:i+1]
        else:
            nodes += nds[i:i+1]

p.Set(nodes=nodes, name=setName)
del nodes
return
def createSurfacesAndConstrains(modelName):
# -*- coding: utf-8 -*-
    """
    Created on Wed Mar 07 15:13:43 2018
    Given an meshed rectangular part with brick elements (linear or cubic), create
    surface sets on the outer boundaries of the part.

    This code assumes that the outer faces normals of the part are parallel to the
    global coordinates.

    Assumes all elements are of the same order (linear or cubic)
    @author: ecamaren
    """
    partName = 'Part-1'
    instName = partName+'-1'
    refP1 = 'RefPoint1'
    refP2 = 'RefPoint2'
    refP3 = 'RefPoint3'
    #currentTime1 = time.asctime(time.localtime(time.time()))
    tol=0.0001 #Tolarence value to see if a node likes on the Min or Max X,Y,or Z plane
    lim = 5 # the accuracy limit digit for seeking the corresponding node pairs
    print 'Min and Max of domain and creating surface sets...'
    #####

    p = mdb.models[modelName].parts[partName]
    nel=p.elements[-1].label #The total number of elements in the model
    nNodesElem=len(p.elements[0].getNodes()) #The number of nodes per element

    minMax=getXYZ_min_max(range(0,nel)) #find the Min/Max values for all elements
    Xmin=minMax[0]
    Xmax=minMax[1]
    Ymin=minMax[2]
    Ymax=minMax[3]
    Zmin=minMax[4]
    Zmax=minMax[5]
    print '*****'

```

```

print 'Xmin=%1.5f' %(Xmin)
print 'Xmax=%1.5f' %(Xmax)
print 'Ymin=%1.5f' %(Ymin)
print 'Ymax=%1.5f' %(Ymax)
print 'Zmin=%1.5f' %(Zmin)
print 'Zmax=%1.5f' %(Zmax)

#Find the index values, i that correspond to elements on the boundary of
#the model
boundaryElem_i=[]
elLabels=[]
for i in range(0,nel):
    nAdjElem = len(p.elements[i].getAdjacentElements())
    if nAdjElem < 6:
        boundaryElem_i.append(i)
        elLabels.append(p.elements[i].label)
Elements = tuple(elLabels) #Can be deleted Later
setName='External-Elements' #Can be deleted Later
p.SetFromElementLabels(name=setName,elementLabels=Elements) #Can be deleted Later
#For each element on the RVE boundary, determine if is on the Xmax, Xmin
#Ymax, Ymin, Zmin, or Zmax. Create the list of index values for each of the
#6 cases: xMinList, yMinList, zMinList,xMaxList,yMaxList,zMaxList
xMinList=[]
yMinList=[]
zMinList=[]
xMaxList=[]
yMaxList=[]
zMaxList=[]

xMinElLabels=[] #Can be deleted Later
xMaxElLabels=[] #Can be deleted Later
yMinElLabels=[] #Can be deleted Later
yMaxElLabels=[] #Can be deleted Later
zMinElLabels=[] #Can be deleted Later
zMaxElLabels=[] #Can be deleted Later

for I in boundaryElem_i:
    minMaxI=getXYZ_min_max([I])
    iel=p.elements[I].label
    XminI=minMaxI[0]
    XmaxI=minMaxI[1]
    YminI=minMaxI[2]
    YmaxI=minMaxI[3]
    ZminI=minMaxI[4]
    ZmaxI=minMaxI[5]
    if abs(XminI - Xmin) < tol:
        xMinList.append(I)
        xMinElLabels.append(iel) #Can be deleted Later
    if abs(XmaxI - Xmax) < tol:
        xMaxList.append(I)
        xMaxElLabels.append(iel) #Can be deleted Later
    if abs(YminI - Ymin) < tol:
        yMinList.append(I)
        yMinElLabels.append(iel) #Can be deleted Later
    if abs(YmaxI - Ymax) < tol:
        yMaxList.append(I)

```

```

        yMaxElLables.append(iel) #Can be deleted later
    if abs(ZminI - Zmin) < tol:
        zMinList.append(I)
        zMinElLables.append(iel) #Can be deleted later
    if abs(ZmaxI - Zmax) < tol:
        zMaxList.append(I)
        zMaxElLables.append(iel) #Can be deleted later
#Given the face number (1,2,3,4,5,or 6) and the list of elements that have that face
#on the outer boundary create a set of elements
def FaceSet(face,faceElements):
    Elements = tuple(faceElements)
    setName='face'+str(face)
    p.SetFromElementLabels(name=setName,elementLabels=Elements)
    elset=p.sets[setName].elements
    return elset
#Find what faces (1,2,3,4,5,or 6) are on the outer boundary
#MinMax is either Xmin,Xmax,Ymin,Ymax,Zmin,Zmax
#MinMaxList is either xMinList=[],yMinList=[],zMinList=[],xMaxList=[]
#yMaxList=[],or zMaxList=[]
#Axis is either 1,2, or 3 for x,y,or z

def FindOutwardFaces(MinMax,MinMaxList,Axis):
    lim = 5 # the accuracy limit digit for searching nodal coordinates
    for I in MinMaxList:
        face=[] #Face will hold the node order for the face that is on the Min/Max
        #It changes for each element
        iel=p.elements[I].label
        for j in range(0,8):
            node=p.elements[I].getNodes()[j] #Cycle through each corner node
            if Axis==1:
                xcoord=node.coordinates[0]
                if round(xcoord,lim)==round(MinMax,lim):
                    face.append(j+1)
            if Axis==2:
                ycoord=node.coordinates[1]
                if round(ycoord,lim)==round(MinMax,lim):
                    face.append(j+1)
            if Axis==3:
                zcoord=node.coordinates[2]
                if round(zcoord,lim)==round(MinMax,lim):
                    face.append(j+1)
            if face==[1, 2, 3, 4]:
                face1Elements.append(iel)
            if face==[5, 6, 7, 8]:
                face2Elements.append(iel)
            if face==[1, 2, 5, 6]:
                face3Elements.append(iel)
            if face==[2, 3, 6, 7]:
                face4Elements.append(iel)
            if face==[3, 4, 7, 8]:
                face5Elements.append(iel)
            if face==[1, 4, 5, 8]:
                face6Elements.append(iel)
        faces=[face1Elements,face2Elements,face3Elements,face4Elements,face5Elements,face6Elements]
    allelset=[]

```

```

    for i in range(0,6):
        if len(faces[i])>0:
            elset=FaceSet(i,faces[i])
            allelset.append(elset)
        else:
            allelset.append([])

    return (allelset)
    face1Elements=[]
    face2Elements=[]
    face3Elements=[]
    face4Elements=[]
    face5Elements=[]
    face6Elements=[]
    allelset=FindOutwardFaces(Xmin,xMinList,1)
    p.Surface(face1Elements=allelset[0],
face2Elements=allelset[1],face3Elements=allelset[2],
            face4Elements=allelset[3],face5Elements=allelset[4],face6Elements=allelset
[5],name='xN-Surf')
    face1Elements=[]
    face2Elements=[]
    face3Elements=[]
    face4Elements=[]
    face5Elements=[]
    face6Elements=[]
    allelset=FindOutwardFaces(Xmax,xMaxList,1)
    p.Surface(face1Elements=allelset[0],
face2Elements=allelset[1],face3Elements=allelset[2],
            face4Elements=allelset[3],face5Elements=allelset[4],face6Elements=allelset
[5],name='xP-Surf')
    face1Elements=[]
    face2Elements=[]
    face3Elements=[]
    face4Elements=[]
    face5Elements=[]
    face6Elements=[]
    allelset=FindOutwardFaces(Ymin,yMinList,2)
    p.Surface(face1Elements=allelset[0],
face2Elements=allelset[1],face3Elements=allelset[2],
            face4Elements=allelset[3],face5Elements=allelset[4],face6Elements=allelset
[5],name='yN-Surf')
    face1Elements=[]
    face2Elements=[]
    face3Elements=[]
    face4Elements=[]
    face5Elements=[]
    face6Elements=[]
    allelset=FindOutwardFaces(Ymax,yMaxList,2)
    p.Surface(face1Elements=allelset[0],
face2Elements=allelset[1],face3Elements=allelset[2],
            face4Elements=allelset[3],face5Elements=allelset[4],face6Elements=allelset
[5],name='yP-Surf')
    face1Elements=[]
    face2Elements=[]
    face3Elements=[]
    face4Elements=[]

```

```

face5Elements=[]
face6Elements=[]
allelset=FindOutwardFaces(Zmin,zMinList,3)
p.Surface(face1Elements=allelset[0],
face2Elements=allelset[1],face3Elements=allelset[2],
        face4Elements=allelset[3],face5Elements=allelset[4],face6Elements=allelset
[5],name='zN-Surf')
face1Elements=[]
face2Elements=[]
face3Elements=[]
face4Elements=[]
face5Elements=[]
face6Elements=[]

allelset=FindOutwardFaces(Zmax,zMaxList,3)
p.Surface(face1Elements=allelset[0],
face2Elements=allelset[1],face3Elements=allelset[2],
        face4Elements=allelset[3],face5Elements=allelset[4],face6Elements=allelset
[5],name='zP-Surf')
print 'Implementing periodic constrains...'
#####
## Create the boundary sets for prepare to generate the periodic constraints by
equations
xP = 'XP'
xN = 'XN'
yP = 'YP'
yN = 'YN'
zP = 'ZP'
zN = 'ZN'
#####
## Create the boundary sets for prepare to generate the periodic constraints by
equations
part      = mdb.models[modelName].parts[partName]
geo_info   = part.queryGeometry()

createBCset(part, 'X', Xmin, lim, xN)
createBCset(part, 'X', Xmax, lim, xP)
createBCset(part, 'Y', Ymin, lim, yN)
createBCset(part, 'Y', Ymax, lim, yP)
createBCset(part, 'Z', Zmin, lim, zN)
createBCset(part, 'Z', Zmax, lim, zP)
#####

refP1Loc=3.0 # refP1Loc should be not equal to any location coord of the UnitCell

#build the reference point instances
mdb.models[modelName].Part(dimensionality=THREE_D, name=refP1, type=
    DEFORMABLE_BODY)
mdb.models[modelName].parts[refP1].ReferencePoint(point=(refP1Loc, 0.0, 0.0))
mdb.models[modelName].Part(dimensionality=THREE_D, name=refP2, type=
    DEFORMABLE_BODY)
mdb.models[modelName].parts[refP2].ReferencePoint(point=(0.0, refP1Loc, 0.0))
mdb.models[modelName].Part(dimensionality=THREE_D, name=refP3, type=
    DEFORMABLE_BODY)
mdb.models[modelName].parts[refP3].ReferencePoint(point=(0.0, 0.0, refP1Loc))

```

```

# create sets for the reference points
mdb.models[modelName].parts[refP1].Set(name='SetRefPoint1',
    referencePoints=(mdb.models[modelName].parts[refP1].referencePoints[1], ))
mdb.models[modelName].parts[refP2].Set(name='SetRefPoint2',
    referencePoints=(mdb.models[modelName].parts[refP2].referencePoints[1], ))
mdb.models[modelName].parts[refP3].Set(name='SetRefPoint3',
    referencePoints=(mdb.models[modelName].parts[refP3].referencePoints[1], ))
mdb.models[modelName].rootAssembly.regenerate()

## Creat instance for the 3 reference point parts
mdb.models[modelName].rootAssembly.Instance(dependent=ON, name='RefPoint1-1',
    part=mdb.models[modelName].parts['RefPoint1'])
mdb.models[modelName].rootAssembly.Instance(dependent=ON, name='RefPoint2-1',
    part=mdb.models[modelName].parts['RefPoint2'])
mdb.models[modelName].rootAssembly.Instance(dependent=ON, name='RefPoint3-1',
    part=mdb.models[modelName].parts['RefPoint3'])
mdb.models[modelName].rootAssembly.regenerate()
mdb.models[modelName].rootAssembly.regenerate()
# X-Faces
xPN=[]
for i in mdb.models[modelName].parts[partName].sets[xP].nodes:
    xPN=xPN+[(i.coordinates[0],i.coordinates[1],i.coordinates[2],i.label)]
xMax = xPN[0][0]
xNN=[]
for i in mdb.models[modelName].parts[partName].sets[xN].nodes:
    xNN=xNN+[(i.coordinates[0],i.coordinates[1],i.coordinates[2],i.label)]
# Constraints X-Faces
rep = 1
for m in xPN:
    c=0
    for n in xNN:
        if (abs(m[1]-n[1])<10**-lim) and (abs(m[2]-n[2])<10**-lim):
            c=c+1
            mdb.models[modelName].parts[partName].Set(name='Node-'+str(rep),
nodes=mdb.models[modelName].parts[partName].nodes[m[3]-1:m[3]])
            rep = rep+1
            mdb.models[modelName].parts[partName].Set(name='Node-'+str(rep),
nodes=mdb.models[modelName].parts[partName].nodes[n[3]-1:n[3]])
            rep = rep+1
            mdb.models[modelName].Equation(name='Constraint-x-'+str(rep-2),
terms=((1.0, instName+'.Node-'+str(rep-2),
1),
(-1.0, instName+'.Node-'+str(rep-1), 1),
(-1.0, 'RefPoint1-1.SetRefPoint1', 1)))
            mdb.models[modelName].Equation(name='Constraint-y-'+str(rep-2),
terms=((1.0, instName+'.Node-'+str(rep-2),
2),
(-1.0, instName+'.Node-'+str(rep-1), 2),
(-1.0, 'RefPoint1-1.SetRefPoint1', 2)))
            mdb.models[modelName].Equation(name='Constraint-z-'+str(rep-2),
terms=((1.0, instName+'.Node-'+str(rep-2),
3),
(-1.0, instName+'.Node-'+str(rep-1), 3),
(-1.0, 'RefPoint1-1.SetRefPoint1', 3)))
            mdb.models[modelName].Equation(name='Constraint-c-'+str(rep-2),
terms=((1.0, instName+'.Node-'+str(rep-2),

```

```

9),

                                (-1.0, instName+'.Node-'+str(rep-1), 9),
                                (-1.0, 'RefPoint1-1.SetRefPoint1', 9)))

    if (c==0):
        print 'no corresponding node for node label %d' %m[3]
# Y-Faces
yPN=[]
for i in mdb.models[modelName].parts[partName].sets[yP].nodes:
    yPN=yPN+[(i.coordinates[0],i.coordinates[1],i.coordinates[2],i.label)]
yMax = yPN[0][1]
yNN=[]
for i in mdb.models[modelName].parts[partName].sets[yN].nodes:
    yNN=yNN+[(i.coordinates[0],i.coordinates[1],i.coordinates[2],i.label)]
# Constraints Y-Faces
for m in yPN:
    c=0
    for n in yNN:
        if (abs(m[0]-n[0])<10**-lim) and (abs(m[2]-n[2])<10**-lim):
            c=c+1
            if (abs(m[0]-xMax)<10**-lim) and (abs(m[1]-yMax)<10**-lim):
                print 'skip'
            else:
                mdb.models[modelName].parts[partName].Set(name='Node-'+str(rep),
nodes=mdb.models[modelName].parts[partName].nodes[m[3]-1:m[3]])
                rep = rep+1
                mdb.models[modelName].parts[partName].Set(name='Node-'+str(rep),
nodes=mdb.models[modelName].parts[partName].nodes[n[3]-1:n[3]])
                rep = rep+1
                mdb.models[modelName].Equation(name='Constraint-x-'+str(rep-2),
                                                terms=((1.0, instName
+'.Node-'+str(rep-2), 1),
                                                (-1.0, instName
+'.Node-'+str(rep-1), 1),
                                                (-1.0,
'RefPoint2-1.SetRefPoint2', 1)))
                mdb.models[modelName].Equation(name='Constraint-y-'+str(rep-2),
                                                terms=((1.0, instName
+'.Node-'+str(rep-2), 2),
                                                (-1.0, instName
+'.Node-'+str(rep-1), 2),
                                                (-1.0,
'RefPoint2-1.SetRefPoint2', 2)))
                mdb.models[modelName].Equation(name='Constraint-z-'+str(rep-2),
                                                terms=((1.0, instName
+'.Node-'+str(rep-2), 3),
                                                (-1.0, instName
+'.Node-'+str(rep-1), 3),
                                                (-1.0, 'RefPoint2-1.SetRefPoint2',
3)))
                mdb.models[modelName].Equation(name='Constraint-c-'+str(rep-2),
                                                terms=((1.0, instName+'.Node-'+str(rep-2),
9),
                                                (-1.0, instName+'.Node-'+str(rep-1), 9),
                                                (-1.0, 'RefPoint2-1.SetRefPoint2', 9)))

    if c==0:
        print 'no corresponding node for node label %d' %m[3]

```



```

# Z-Faces
zPN=[]
for i in mdb.models[modelName].parts[partName].sets[zP].nodes:
    zPN=zPN+[(i.coordinates[0],i.coordinates[1],i.coordinates[2],i.label)]

zMax = zPN[0][2]

zNN=[]
for i in mdb.models[modelName].parts[partName].sets[zN].nodes:
    zNN=zNN+[(i.coordinates[0],i.coordinates[1],i.coordinates[2],i.label)]

def Set9StepBCs_MIX(modelName,LX,LY,LZ,Ha,SF,MFC_flag):
    step1='Step-1'
    step2='Step-2'
    step3='Step-3'
    step4='Step-4'
    step5='Step-5'
    step6='Step-6'
    step7='Step-7'
    step8='Step-8'
    step9='Step-9'
    a = mdb.models[modelName].rootAssembly
    m=mdb.models[modelName]
    mdb.models[modelName].StaticStep(name=step1, previous='Initial')
    mdb.models[modelName].StaticStep(name=step2, previous=step1)
    mdb.models[modelName].StaticStep(name=step3, previous=step2)
    mdb.models[modelName].StaticStep(name=step4, previous=step3)
    mdb.models[modelName].StaticStep(name=step5, previous=step4)
    mdb.models[modelName].StaticStep(name=step6, previous=step5)
    mdb.models[modelName].StaticStep(name=step7, previous=step6)
    mdb.models[modelName].StaticStep(name=step8, previous=step7)
    mdb.models[modelName].StaticStep(name=step9, previous=step8)
    a = mdb.models[modelName].rootAssembly
    region = a.instances['RefPoint1-1'].sets['SetRefPoint1']
    mdb.models[modelName].DisplacementBC(name='BC-ref1', createStepName=step1,
        region=region, u1=0.0, u2=0.0, u3=0.0, ur1=UNSET, ur2=UNSET, ur3=UNSET,
        amplitude=UNSET, fixed=OFF, distributionType=UNIFORM, fieldName='',
        localCsys=None)
    mdb.models[modelName].ElectricPotentialBC(name='BC-ref1E', createStepName=step1,
        region=region,fieldName='',magnitude=0.0,
distributionType=UNIFORM,amplitude=UNSET, fixed=OFF)
    a = mdb.models[modelName].rootAssembly
    region = a.instances['RefPoint2-1'].sets['SetRefPoint2']
    mdb.models[modelName].DisplacementBC(name='BC-ref2', createStepName=step1,
        region=region, u1=0.0, u2=0.0, u3=0.0, ur1=UNSET, ur2=UNSET, ur3=UNSET,
        amplitude=UNSET, fixed=OFF, distributionType=UNIFORM, fieldName='',
        localCsys=None)
    mdb.models[modelName].ElectricPotentialBC(name='BC-ref2E', createStepName=step1,
        region=region,fieldName='',magnitude=0.0,
distributionType=UNIFORM,amplitude=UNSET, fixed=OFF)
    #Step 1
    mdb.models[modelName].boundaryConditions['BC-ref1'].setValues(u1=LX)
    #Step 2
    mdb.models[modelName].boundaryConditions['BC-ref1'].setValuesInStep(
        stepName=step2, u1=0.0)
    mdb.models[modelName].boundaryConditions['BC-ref2'].setValuesInStep(

```

```

        stepName=step2, u2=LY)
#Step 3
mdb.models[modelName].boundaryConditions['BC-ref2'].setValuesInStep(
    stepName=step3, u2=0.0)
region = a.instances['Part-1-1'].surfaces['zN-Surf']
m.SurfaceTraction(name='zN', createStepName='Step-3',
    region=region, magnitude=-1, directionVector=((0.0, 0.0, 0.0), (0.0,
    0.0, 1.0)), distributionType=UNIFORM, field='', localCsys=None,
    traction=GENERAL, follower=OFF)
region = a.instances['Part-1-1'].surfaces['zP-Surf']
m.SurfaceTraction(name='zP', createStepName='Step-3',
    region=region, magnitude=1, directionVector=((0.0, 0.0, 0.0), (0.0,
    0.0, 1.0)), distributionType=UNIFORM, field='', localCsys=None,
    traction=GENERAL, follower=OFF)
#Step 4
m.loads['zN'].deactivate('Step-4')
m.loads['zP'].deactivate('Step-4')
region = a.instances['Part-1-1'].surfaces['zN-Surf']
m.SurfaceTraction(name='zNshear32', createStepName='Step-4',
    region=region, magnitude=-1, directionVector=((0.0, 0.0, 0.0), (0.0,
    1.0, 0.0)), distributionType=UNIFORM, field='', localCsys=None,
    traction=GENERAL, follower=OFF)
region = a.instances['Part-1-1'].surfaces['zP-Surf']
m.SurfaceTraction(name='zPshear32', createStepName='Step-4',
    region=region, magnitude=1, directionVector=((0.0, 0.0, 0.0), (0.0,
    1.0, 0.0)), distributionType=UNIFORM, field='', localCsys=None,
    traction=GENERAL, follower=OFF)
#Step 5
m.loads['zNshear32'].deactivate('Step-5')
m.loads['zPshear32'].deactivate('Step-5')
region = a.instances['Part-1-1'].surfaces['zN-Surf']
m.SurfaceTraction(name='zNshear13', createStepName='Step-5',
    region=region, magnitude=-1, directionVector=((0.0, 0.0, 0.0), (1.0,
    0.0, 0.0)), distributionType=UNIFORM, field='', localCsys=None,
    traction=GENERAL, follower=OFF)
region = a.instances['Part-1-1'].surfaces['zP-Surf']
m.SurfaceTraction(name='zPshear13', createStepName='Step-5',
    region=region, magnitude=1, directionVector=((0.0, 0.0, 0.0), (1.0,
    0.0, 0.0)), distributionType=UNIFORM, field='', localCsys=None,
    traction=GENERAL, follower=OFF)
#Step 6
mdb.models[modelName].boundaryConditions['BC-ref1'].setValuesInStep(
    stepName=step6, u2=0.5*LX, u3=0.0)
mdb.models[modelName].boundaryConditions['BC-ref2'].setValuesInStep(
    stepName=step6, u1=0.5*LY)
m.loads['zNshear13'].deactivate('Step-6')
m.loads['zPshear13'].deactivate('Step-6')

if MFC_flag=='P1':
    a = mdb.models[modelName].rootAssembly
    region = a.instances['Part-1-1'].sets['Electrode-Geom-Inner']
    mdb.models[modelName].ElectricPotentialBC(name='Gamma_minus',
        createStepName=step1, region=region, distributionType=UNIFORM,
        fieldName='', magnitude=0.0)

    a = mdb.models[modelName].rootAssembly

```

```

region = a.instances['Part-1-1'].sets['Electrode-Geom-Outer']
mdb.models[modelName].ElectricPotentialBC(name='Gamma_plus',
    createStepName=step1, region=region, distributionType=UNIFORM,
    fieldName='', magnitude=0.0)
#Step 7
mdb.models[modelName].boundaryConditions['BC-ref1'].setValuesInStep(
    stepName=step7, u2=0, u3=0.0)
mdb.models[modelName].boundaryConditions['BC-ref2'].setValuesInStep(
    stepName=step7, u1=0)
mdb.models[modelName].boundaryConditions['Gamma_minus'].setValuesInStep(
    stepName=step7, magnitude=-LX/2)
#Step 8
m.boundaryConditions['Gamma_plus'].deactivate('Step-8')
m.boundaryConditions['Gamma_minus'].deactivate('Step-8')
mdb.models[modelName].boundaryConditions['BC-ref1E'].setValuesInStep(
    stepName=step8, magnitude=0.0)
mdb.models[modelName].boundaryConditions['BC-ref2E'].setValuesInStep(
    stepName=step8, magnitude=-LY)
#Step 9
mdb.models[modelName].boundaryConditions['BC-ref2E'].setValuesInStep(
    stepName=step9, magnitude=0)
a = mdb.models[modelName].rootAssembly
region = a.instances['Part-1-1'].sets['Electrode-Geom-Bottom']
mdb.models[modelName].ElectricPotentialBC(name='Gamma_minusb',
    createStepName=step9, region=region, distributionType=UNIFORM,
    fieldName='', magnitude=0.0)
a = mdb.models[modelName].rootAssembly
region = a.instances['Part-1-1'].sets['Electrode-Geom-Top']
mdb.models[modelName].ElectricPotentialBC(name='Gamma_plusb',
    createStepName=step9, region=region, distributionType=UNIFORM,
    fieldName='', magnitude=-Ha)
elif MFC_flag=='P2':
    a = mdb.models[modelName].rootAssembly
    region = a.instances['Part-1-1'].sets['Electrode-Geom-Bottom']
    mdb.models[modelName].ElectricPotentialBC(name='Gamma_minus',
        createStepName=step1, region=region, distributionType=UNIFORM,
        fieldName='', magnitude=0.0)
    a = mdb.models[modelName].rootAssembly
    region = a.instances['Part-1-1'].sets['Electrode-Geom-Top']
    mdb.models[modelName].ElectricPotentialBC(name='Gamma_plus',
        createStepName=step1, region=region, distributionType=UNIFORM,
        fieldName='', magnitude=0.0)
#Step 7
m.boundaryConditions['Gamma_plus'].deactivate('Step-7')
m.boundaryConditions['Gamma_minus'].deactivate('Step-7')
a = mdb.models[modelName].rootAssembly
region = a.instances['Part-1-1'].sets['Electrode-Geom-Inner']
mdb.models[modelName].ElectricPotentialBC(name='Gamma_minusE1',
    createStepName=step7, region=region, distributionType=UNIFORM,
    fieldName='', magnitude=-LX/2)
a = mdb.models[modelName].rootAssembly
region = a.instances['Part-1-1'].sets['Electrode-Geom-Outer']
mdb.models[modelName].ElectricPotentialBC(name='Gamma_plusE1',
    createStepName=step7, region=region, distributionType=UNIFORM,
    fieldName='', magnitude=0)
mdb.models[modelName].boundaryConditions['BC-ref1'].setValuesInStep(

```

```

        stepName=step7, u2=0, u3=0.0)
mdb.models[modelName].boundaryConditions['BC-ref2'].setValuesInStep(
    stepName=step7, u1=0)
#Step 8
m.boundaryConditions['Gamma_plusE1'].deactivate('Step-8')
m.boundaryConditions['Gamma_minusE1'].deactivate('Step-8')
mdb.models[modelName].boundaryConditions['BC-ref2E'].setValuesInStep(
    stepName=step8, magnitude=-LY)
#Step 9
mdb.models[modelName].boundaryConditions['BC-ref2E'].setValuesInStep(
    stepName=step9, magnitude=0)
a = mdb.models[modelName].rootAssembly
region = a.instances['Part-1-1'].sets['Electrode-Geom-Bottom']
mdb.models[modelName].ElectricPotentialBC(name='Gamma_minusb',
    createStepName=step9, region=region, distributionType=UNIFORM,
    fieldName='', magnitude=0.0)

a = mdb.models[modelName].rootAssembly
region = a.instances['Part-1-1'].sets['Electrode-Geom-Top']
mdb.models[modelName].ElectricPotentialBC(name='Gamma_plusb',
    createStepName=step9, region=region, distributionType=UNIFORM,
    fieldName='', magnitude=-Ha)
else:
    print 'BC Definition error. Check MFC_flag'

#Get Field Output
#session.viewports['Viewport: 1'].assemblyDisplay.setValues(step='Step-1')
mdb.models[modelName].FieldOutputRequest(name='F-Output-1',
    createStepName='Step-1', variables=('S', 'E', 'U', 'RF', 'EPOT', 'EPG',
    'RCHG', 'EFLX', 'IVOL'))
#Set-up Job
mdb.models[modelName].HistoryOutputRequest(name='H-Output-2',
    createStepName='Step-1', variables=('ETOTAL', ))

def constrainsPBC(modelName):
    partName = 'Part-1'
    instName = partName+'-1'
    refP1 = 'RefPoint1'
    refP2 = 'RefPoint2'
    refP3 = 'RefPoint3'
    import time
    currentTime1 = time.asctime(time.localtime(time.time()))
    lim = 5 # the accuracy limit digit for seeking the corresponding node pairs

    #####
    ## Create the boundary sets for prepare to generate the periodic constraints by
    equations
    xP = 'XP'
    xN = 'XN'
    yP = 'YP'
    yN = 'YN'
    zP = 'ZP'
    zN = 'ZN'
    #####
    ## Create the boundary sets for prepare to generate the periodic constraints by
    equations

```

```

part      = mdb.models[modelName].parts[partName]
geo_info  = part.queryGeometry()
p = mdb.models[modelName].parts[partName]
nel=p.elements[-1].label #The total number of elements in the model

minMax=getXYZ_min_max(range(0,nel)) #find the Min/Max values for all elements
Xmin=minMax[0]
Xmax=minMax[1]
Ymin=minMax[2]
Ymax=minMax[3]
Zmin=minMax[4]
Zmax=minMax[5]

print '*****'
print 'Xmin=%1.5f' %(Xmin)
print 'Xmax=%1.5f' %(Xmax)
print 'Ymin=%1.5f' %(Ymin)
print 'Ymax=%1.5f' %(Ymax)
print 'Zmin=%1.5f' %(Zmin)
print 'Zmax=%1.5f' %(Zmax)

createBCset(part, 'X', Xmin, lim, xN)
createBCset(part, 'X', Xmax, lim, xP)
createBCset(part, 'Y', Ymin, lim, yN)
createBCset(part, 'Y', Ymax, lim, yP)
createBCset(part, 'Z', Zmin, lim, zN)
createBCset(part, 'Z', Zmax, lim, zP)

#####
refP1Loc=3.0 # refP1Loc should be not equal to any location coord of the UnitCell

#build the reference point instances
mdb.models[modelName].Part(dimensionality=THREE_D, name=refP1, type=
    DEFORMABLE_BODY)
mdb.models[modelName].parts[refP1].ReferencePoint(point=(refP1Loc, 0.0, 0.0))
mdb.models[modelName].Part(dimensionality=THREE_D, name=refP2, type=
    DEFORMABLE_BODY)
mdb.models[modelName].parts[refP2].ReferencePoint(point=(0.0, refP1Loc, 0.0))
mdb.models[modelName].Part(dimensionality=THREE_D, name=refP3, type=
    DEFORMABLE_BODY)
mdb.models[modelName].parts[refP3].ReferencePoint(point=(0.0, 0.0, refP1Loc))

# create sets for the reference points
mdb.models[modelName].parts[refP1].Set(name='SetRefPoint1',
    referencePoints=(mdb.models[modelName].parts[refP1].referencePoints[1], ))
mdb.models[modelName].parts[refP2].Set(name='SetRefPoint2',
    referencePoints=(mdb.models[modelName].parts[refP2].referencePoints[1], ))
mdb.models[modelName].parts[refP3].Set(name='SetRefPoint3',
    referencePoints=(mdb.models[modelName].parts[refP3].referencePoints[1], ))
mdb.models[modelName].rootAssembly.regenerate()

## Creat instance for the 3 reference point parts
mdb.models[modelName].rootAssembly.Instance(dependent=ON, name='RefPoint1-1',
    part=mdb.models[modelName].parts['RefPoint1'])
mdb.models[modelName].rootAssembly.Instance(dependent=ON, name='RefPoint2-1',
    part=mdb.models[modelName].parts['RefPoint2'])

```

```

mdb.models[modelName].rootAssembly.Instance(dependent=ON, name='RefPoint3-1',
    part=mdb.models[modelName].parts['RefPoint3'])
mdb.models[modelName].rootAssembly.regenerate()
mdb.models[modelName].rootAssembly.regenerate()
# X-Faces
xPN=[]
for i in mdb.models[modelName].parts[partName].sets[xP].nodes:
    xPN=xPN+[(i.coordinates[0],i.coordinates[1],i.coordinates[2],i.label)]
xMax = round(xPN[0][0],lim)
xNN=[]
for i in mdb.models[modelName].parts[partName].sets[xN].nodes:
    xNN=xNN+[(i.coordinates[0],i.coordinates[1],i.coordinates[2],i.label)]
# Constraints X-Faces
rep = 1
for m in xPN:
    c=0
    for n in xNN:
        if (abs(m[1]-n[1])<10**-lim) and (abs(m[2]-n[2])<10**-lim):
            c=c+1
            mdb.models[modelName].parts[partName].Set(name='Node-'+str(rep),
nodes=mdb.models[modelName].parts[partName].nodes[m[3]-1:m[3]])
            rep = rep+1
            mdb.models[modelName].parts[partName].Set(name='Node-'+str(rep),
nodes=mdb.models[modelName].parts[partName].nodes[n[3]-1:n[3]])
            rep = rep+1
            mdb.models[modelName].Equation(name='Constraint-x-'+str(rep-2),
terms=((1.0, instName+'.Node-'+str(rep-2),
1),
            (-1.0, instName+'.Node-'+str(rep-1), 1),
            (-1.0, 'RefPoint1-1.SetRefPoint1', 1)))
            mdb.models[modelName].Equation(name='Constraint-y-'+str(rep-2),
terms=((1.0, instName+'.Node-'+str(rep-2),
2),
            (-1.0, instName+'.Node-'+str(rep-1), 2),
            (-1.0, 'RefPoint1-1.SetRefPoint1', 2)))
            mdb.models[modelName].Equation(name='Constraint-z-'+str(rep-2),
terms=((1.0, instName+'.Node-'+str(rep-2),
3),
            (-1.0, instName+'.Node-'+str(rep-1), 3),
            (-1.0, 'RefPoint1-1.SetRefPoint1', 3)))
            mdb.models[modelName].Equation(name='Constraint-c-'+str(rep-2),
terms=((1.0, instName+'.Node-'+str(rep-2),
9),
            (-1.0, instName+'.Node-'+str(rep-1), 9),
            (-1.0, 'RefPoint1-1.SetRefPoint1', 9)))
            if (c==0):
                print 'no corresponding node for node label %d' %m[3]
# Y-Faces
yPN=[]
for i in mdb.models[modelName].parts[partName].sets[yP].nodes:
    yPN=yPN+[(i.coordinates[0],i.coordinates[1],i.coordinates[2],i.label)]
yMax = yPN[0][1]
yNN=[]
for i in mdb.models[modelName].parts[partName].sets[yN].nodes:
    yNN=yNN+[(i.coordinates[0],i.coordinates[1],i.coordinates[2],i.label)]
# Constraints Y-Faces

```

```

for m in yPN:
    c=0
    for n in yNN:
        if (abs(m[0]-n[0])<10**-lim) and (abs(m[2]-n[2])<10**-lim):
            c=c+1
            if (abs(m[0]-xMax)<10**-lim) and (abs(m[1]-yMax)<10**-lim):
                print 'skip'
            else:
                mdb.models[modelName].parts[partName].Set(name='Node-'+str(rep),
nodes=mdb.models[modelName].parts[partName].nodes[m[3]-1:m[3]])
                rep = rep+1
                mdb.models[modelName].parts[partName].Set(name='Node-'+str(rep),
nodes=mdb.models[modelName].parts[partName].nodes[n[3]-1:n[3]])
                rep = rep+1
                mdb.models[modelName].Equation(name='Constraint-x-'+str(rep-2),
terms=((1.0, instName
+'.Node-'+str(rep-2), 1),
(-1.0, instName
+'.Node-'+str(rep-1), 1),
(-1.0,
'RefPoint2-1.SetRefPoint2', 1)))
                mdb.models[modelName].Equation(name='Constraint-y-'+str(rep-2),
terms=((1.0, instName
+'.Node-'+str(rep-2), 2),
(-1.0, instName
+'.Node-'+str(rep-1), 2),
(-1.0,
'RefPoint2-1.SetRefPoint2', 2)))
                mdb.models[modelName].Equation(name='Constraint-z-'+str(rep-2),
terms=((1.0, instName
+'.Node-'+str(rep-2), 3),
(-1.0, instName
+'.Node-'+str(rep-1), 3),
(-1.0, 'RefPoint2-1.SetRefPoint2',
3)))
                mdb.models[modelName].Equation(name='Constraint-c-'+str(rep-2),
terms=((1.0, instName+'.Node-'+str(rep-2),
9),
(-1.0, instName+'.Node-'+str(rep-1), 9),
(-1.0, 'RefPoint2-1.SetRefPoint2', 9)))
            if c==0:
                print 'no corresponding node for node label %d' %m[3]
# Z-Faces
zPN=[]
for i in mdb.models[modelName].parts[partName].sets[zP].nodes:
    zPN=zPN+[(i.coordinates[0],i.coordinates[1],i.coordinates[2],i.label)]
zMax = zPN[0][2]
zNN=[]
for i in mdb.models[modelName].parts[partName].sets[zN].nodes:
    zNN=zNN+[(i.coordinates[0],i.coordinates[1],i.coordinates[2],i.label)]
# Constraints Z-Faces
for m in zPN:
    c=0
    for n in zNN:
        if (abs(m[0]-n[0])<10**-lim) and (abs(m[1]-n[1])<10**-lim):
            c=c+1

```

```

        if (abs(m[0]-xMax)<10**(-lim) and (abs(m[2]-zMax)<10**(-lim) or (abs(m[1]-
yMax)<10**(-lim) and (abs(m[2]-zMax)<10**(-lim):
            print 'skip2'
        else:
            mdb.models[modelName].parts[partName].Set(name='Node-'+str(rep),
nodes=mdb.models[modelName].parts[partName].nodes[m[3]-1:m[3]])
            rep = rep+1
            mdb.models[modelName].parts[partName].Set(name='Node-'+str(rep),
nodes=mdb.models[modelName].parts[partName].nodes[n[3]-1:n[3]])
            rep = rep+1
            mdb.models[modelName].Equation(name='Constraint-x-'+str(rep-2),
terms=((1.0, instName
+'.Node-'+str(rep-2), 1),
(-1.0, instName
+'.Node-'+str(rep-1), 1),
(-1.0,
'RefPoint3-1.SetRefPoint3', 1)))
            mdb.models[modelName].Equation(name='Constraint-y-'+str(rep-2),
terms=((1.0, instName
+'.Node-'+str(rep-2), 2),
(-1.0, instName
+'.Node-'+str(rep-1), 2),
(-1.0,
'RefPoint3-1.SetRefPoint3', 2)))
            mdb.models[modelName].Equation(name='Constraint-z-'+str(rep-2),
terms=((1.0, instName
+'.Node-'+str(rep-2), 3),
(-1.0, instName
+'.Node-'+str(rep-1), 3),
(-1.0, 'RefPoint3-1.SetRefPoint3',
3)))
            #Periodicity of Z faces in unconstrained due to internal electrodes
            mdb.models[modelName].Equation(name='Constraint-c-'+str(rep-2),
terms=((1.0, instName+'.Node-'+str(rep-2),
9),
(-1.0, instName+'.Node-'+str(rep-1), 9),
(-1.0, 'RefPoint3-1.SetRefPoint3', 9)))
            if c==0:
                print 'no corresponding node for node label %d' %m[3]

def Set9StepBCs_PBC_equipot(modelName,LX,LY,LZ,Ha,SF,MFC_flag):
    step1='Step-1'
    step2='Step-2'
    step3='Step-3'
    step4='Step-4'
    step5='Step-5'
    step6='Step-6'
    step7='Step-7'
    step8='Step-8'
    step9='Step-9'

    a = mdb.models[modelName].rootAssembly

    mdb.models[modelName].StaticStep(name=step1, previous='Initial')
    mdb.models[modelName].StaticStep(name=step2, previous=step1)
    mdb.models[modelName].StaticStep(name=step3, previous=step2)

```



```

mdb.models[modelName].StaticStep(name=step4, previous=step3)
mdb.models[modelName].StaticStep(name=step5, previous=step4)
mdb.models[modelName].StaticStep(name=step6, previous=step5)
mdb.models[modelName].StaticStep(name=step7, previous=step6)
mdb.models[modelName].StaticStep(name=step8, previous=step7)
mdb.models[modelName].StaticStep(name=step9, previous=step8)

a = mdb.models[modelName].rootAssembly
region = a.instances['RefPoint1-1'].sets['SetRefPoint1']
mdb.models[modelName].DisplacementBC(name='BC-ref1', createStepName=step1,
    region=region, u1=0.0, u2=0.0, u3=0.0, ur1=UNSET, ur2=UNSET, ur3=UNSET,
    amplitude=UNSET, fixed=OFF, distributionType=UNIFORM, fieldName='',
    localCsys=None)
mdb.models[modelName].ElectricPotentialBC(name='BC-ref1E', createStepName=step1,
    region=region, fieldName='', magnitude=0.0,
distributionType=UNIFORM, amplitude=UNSET, fixed=OFF)

a = mdb.models[modelName].rootAssembly
region = a.instances['RefPoint2-1'].sets['SetRefPoint2']
mdb.models[modelName].DisplacementBC(name='BC-ref2', createStepName=step1,
    region=region, u1=0.0, u2=0.0, u3=0.0, ur1=UNSET, ur2=UNSET, ur3=UNSET,
    amplitude=UNSET, fixed=OFF, distributionType=UNIFORM, fieldName='',
    localCsys=None)
mdb.models[modelName].ElectricPotentialBC(name='BC-ref2E', createStepName=step1,
    region=region, fieldName='', magnitude=0.0,
distributionType=UNIFORM, amplitude=UNSET, fixed=OFF)

a = mdb.models[modelName].rootAssembly
region = a.instances['RefPoint3-1'].sets['SetRefPoint3']
mdb.models[modelName].DisplacementBC(name='BC-ref3', createStepName=step1,
    region=region, u1=0.0, u2=0.0, u3=0.0, ur1=UNSET, ur2=UNSET, ur3=UNSET,
    amplitude=UNSET, fixed=OFF, distributionType=UNIFORM, fieldName='',
    localCsys=None)

mdb.models[modelName].boundaryConditions['BC-ref1'].setValues(u1=LX)

mdb.models[modelName].boundaryConditions['BC-ref1'].setValuesInStep(
    stepName=step2, u1=0.0)
mdb.models[modelName].boundaryConditions['BC-ref2'].setValuesInStep(
    stepName=step2, u2=LY)

mdb.models[modelName].boundaryConditions['BC-ref2'].setValuesInStep(
    stepName=step3, u2=0.0)
mdb.models[modelName].boundaryConditions['BC-ref3'].setValuesInStep(
    stepName=step3, u3=LZ)

mdb.models[modelName].boundaryConditions['BC-ref2'].setValuesInStep(
    stepName=step4, u3=0.5*LY)
mdb.models[modelName].boundaryConditions['BC-ref3'].setValuesInStep(
    stepName=step4, u2=0.5*LZ, u3=0.0)

mdb.models[modelName].boundaryConditions['BC-ref1'].setValuesInStep(
    stepName=step5, u3=0.5*LX)
mdb.models[modelName].boundaryConditions['BC-ref2'].setValuesInStep(
    stepName=step5, u3=0.0)
mdb.models[modelName].boundaryConditions['BC-ref3'].setValuesInStep(

```

```

stepName=step5, u1=0.5*LZ, u2=0.0)

mdb.models[modelName].boundaryConditions['BC-ref1'].setValuesInStep(
    stepName=step6, u2=0.5*LX, u3=0.0)
mdb.models[modelName].boundaryConditions['BC-ref2'].setValuesInStep(
    stepName=step6, u1=0.5*LY)
mdb.models[modelName].boundaryConditions['BC-ref3'].setValuesInStep(
    stepName=step6, u1=0.0)
if MFC_flag=='P1':
    a = mdb.models[modelName].rootAssembly
    region = a.instances['Part-1-1'].sets['Electrode-Geom-Inner']
    mdb.models[modelName].ElectricPotentialBC(name='Gamma_minus',
        createStepName=step1, region=region, distributionType=UNIFORM,
        fieldName='', magnitude=0.0)
    a = mdb.models[modelName].rootAssembly
    region = a.instances['Part-1-1'].sets['Electrode-Geom-Outer']
    mdb.models[modelName].ElectricPotentialBC(name='Gamma_plus',
        createStepName=step1, region=region, distributionType=UNIFORM,
        fieldName='', magnitude=0.0)
    #Step 7
    mdb.models[modelName].boundaryConditions['BC-ref1'].setValuesInStep(
        stepName=step7, u2=0, u3=0.0)
    mdb.models[modelName].boundaryConditions['BC-ref2'].setValuesInStep(
        stepName=step7, u1=0)
    mdb.models[modelName].boundaryConditions['Gamma_minus'].setValuesInStep(
        stepName=step7, magnitude=-LX/2)
    #Step 8
    m.boundaryConditions['Gamma_plus'].deactivate('Step-8')
    m.boundaryConditions['Gamma_minus'].deactivate('Step-8')
    mdb.models[modelName].boundaryConditions['BC-ref1E'].setValuesInStep(
        stepName=step8, magnitude=0.0)
    mdb.models[modelName].boundaryConditions['BC-ref2E'].setValuesInStep(
        stepName=step8, magnitude=-LY)
    #Step 9
    mdb.models[modelName].boundaryConditions['BC-ref2E'].setValuesInStep(
        stepName=step9, magnitude=0)
    a = mdb.models[modelName].rootAssembly
    region = a.instances['Part-1-1'].sets['Electrode-Geom-Bottom']
    mdb.models[modelName].ElectricPotentialBC(name='Gamma_minusb',
        createStepName=step9, region=region, distributionType=UNIFORM,
        fieldName='', magnitude=0.0)
    a = mdb.models[modelName].rootAssembly
    region = a.instances['Part-1-1'].sets['Electrode-Geom-Top']
    mdb.models[modelName].ElectricPotentialBC(name='Gamma_plusb',
        createStepName=step9, region=region, distributionType=UNIFORM,
        fieldName='', magnitude=-Ha)

elif MFC_flag=='P2':
    a = mdb.models[modelName].rootAssembly
    region = a.instances['Part-1-1'].sets['Electrode-Geom-Bottom']
    mdb.models[modelName].ElectricPotentialBC(name='Gamma_minus',
        createStepName=step1, region=region, distributionType=UNIFORM,
        fieldName='', magnitude=0.0)
    a = mdb.models[modelName].rootAssembly
    region = a.instances['Part-1-1'].sets['Electrode-Geom-Top']
    mdb.models[modelName].ElectricPotentialBC(name='Gamma_plus',

```

```

        createStepName=step1, region=region, distributionType=UNIFORM,
        fieldName='', magnitude=0.0)
#Step 7
m.boundaryConditions['Gamma_plus'].deactivate('Step-7')
m.boundaryConditions['Gamma_minus'].deactivate('Step-7')
a = mdb.models[modelName].rootAssembly
region = a.instances['Part-1-1'].sets['Electrode-Geom-Inner']
mdb.models[modelName].ElectricPotentialBC(name='Gamma_minusE1',
        createStepName=step7, region=region, distributionType=UNIFORM,
        fieldName='', magnitude=-LX/2)
a = mdb.models[modelName].rootAssembly
region = a.instances['Part-1-1'].sets['Electrode-Geom-Outer']
mdb.models[modelName].ElectricPotentialBC(name='Gamma_plusE1',
        createStepName=step7, region=region, distributionType=UNIFORM,
        fieldName='', magnitude=0)
mdb.models[modelName].boundaryConditions['BC-ref1'].setValuesInStep(
        stepName=step7, u2=0, u3=0.0)
mdb.models[modelName].boundaryConditions['BC-ref2'].setValuesInStep(
        stepName=step7, u1=0)
#Step 8
m.boundaryConditions['Gamma_plusE1'].deactivate('Step-8')
m.boundaryConditions['Gamma_minusE1'].deactivate('Step-8')

mdb.models[modelName].boundaryConditions['BC-ref2E'].setValuesInStep(
        stepName=step8, magnitude=-LY)
#Step 9
mdb.models[modelName].boundaryConditions['BC-ref2E'].setValuesInStep(
        stepName=step9, magnitude=0)
a = mdb.models[modelName].rootAssembly
region = a.instances['Part-1-1'].sets['Electrode-Geom-Bottom']
mdb.models[modelName].ElectricPotentialBC(name='Gamma_minusb',
        createStepName=step9, region=region, distributionType=UNIFORM,
        fieldName='', magnitude=0.0)
a = mdb.models[modelName].rootAssembly
region = a.instances['Part-1-1'].sets['Electrode-Geom-Top']
mdb.models[modelName].ElectricPotentialBC(name='Gamma_plusb',
        createStepName=step9, region=region, distributionType=UNIFORM,
        fieldName='', magnitude=-Ha)
else:
    print 'BC Definition error. Check MFC_flag'

#Get Field Output
#session.viewports['Viewport: 1'].assemblyDisplay.setValues(step='Step-1')
mdb.models[modelName].FieldOutputRequest(name='F-Output-1',
        createStepName='Step-1', variables=('S', 'E', 'U', 'RF', 'EPOT', 'EPG',
        'RCHG', 'EFLX', 'IVOL'))

#Set-up Job
mdb.models[modelName].HistoryOutputRequest(name='H-Output-2',
        createStepName='Step-1', variables=('ETOTAL', ))

def DeffUpdateTransverseShearStrain(LX,
LY,LZ,partName,jobName,modelName,flag,transform):
    # -*- coding: utf-8 -*-
    """
    Created on Wed Dec 19 17:45:07 2018

```

```

@author: ecamaren
"""
#Begin Post Processing
#Open the Output Data Base for the current Job
from visualization import *
from odbAccess import *
from abaqusConstants import *
from odbMaterial import *
from odbSection import *
from textRepr import *

Tot_Vol=LX*LY*LZ
BC='PBC'
if BC=='PBC':
    BCflag=1
elif BC=='SUBC':
    BCflag=2
elif BC=='KUBC':
    BCflag=3
#####
odbName=jobName+'.odb'

odb = openOdb(path=odbName);
myAssembly = odb.rootAssembly;
C=[[0.0 for x in range(9) ] for y in xrange(9)]
S=[[0.0 for x in range(9) ] for y in xrange(9)]
if flag==1:
    O=[[0.0 for x in range(9) ] for y in xrange(2)]
    datum0=session.odbs[odbName].rootAssembly.datumCsyses[ 'ASSEMBLY_PART-1-1_ORI-
POLINGFIELD' ]
    setName='Unit-Cell'
    setName='CenterRVE'
    # #Get only the last frame [-1]
    PARTNAME=partName.upper() + str(-1)
    SETNAME=setName.upper()
    # frameRepository = odb.steps['Step-1'].frames;
    elSet=myAssembly.instances[PARTNAME].elementSets[SETNAME]
    setName='Unit-Cell-ActiveVolume'
    setName='ActiveVolume'
    # #Get only the last frame [-1]
    SETNAMEa=setName.upper()
    # frameRepository = odb.steps['Step-1'].frames;
    elSeta=myAssembly.instances[PARTNAME].elementSets[SETNAMEa]

step=['Step-1','Step-2','Step-3','Step-4','Step-5','Step-6','Step-7','Step-8','Step-
9']
for i in range(0,9):
    #Creating a temporary variable to hold the frame repository provides the same
    #functionality and speeds up the process
    frameRepository = odb.steps['Step-'+str(i+1)].frames;

    frameS=[];
    frameE=[];
    frameP=[];
    frameF=[];

```

```

frameIVOL=[];
framePa=[];
frameFa=[];
frameIVOLa=[];

#Get only the last frame [-1]

if transform == 'full':
    framePi=frameRepository[-1].fieldOutputs['EPG'].getTransformedField(datumCsys=datum0);
    frameP.insert(0,framePi.getSubset(position=INTEGRATION_POINT,region=elSet));
    framePa.insert(0,framePi.getSubset(position=INTEGRATION_POINT,region=elSeta));
);

    frameFi=frameRepository[-1].fieldOutputs['EFLX'].getTransformedField(datumCsys=datum0);
    frameF.insert(0,frameFi.getSubset(position=INTEGRATION_POINT,region=elSet));
    frameFa.insert(0,frameFi.getSubset(position=INTEGRATION_POINT,region=elSeta));
);

elif transform == 'mechOnly':
    framePi=frameRepository[-1].fieldOutputs['EPG'];
    frameP.insert(0,framePi.getSubset(position=INTEGRATION_POINT,region=elSet));
    framePa.insert(0,framePi.getSubset(position=INTEGRATION_POINT,region=elSeta));
);

    frameFi=frameRepository[-1].fieldOutputs['EFLX'];
    frameF.insert(0,frameFi.getSubset(position=INTEGRATION_POINT,region=elSet));
    frameFa.insert(0,frameFi.getSubset(position=INTEGRATION_POINT,region=elSeta));
);

#Get only the last frame [-1]
frameSi=frameRepository[-1].fieldOutputs['S'].getTransformedField(datumCsys=datum0);
frameS.insert(0,frameSi.getSubset(position=INTEGRATION_POINT,region=elSet));

frameEi=frameRepository[-1].fieldOutputs['E'].getTransformedField(datumCsys=datum0);
frameE.insert(0,frameEi.getSubset(position=INTEGRATION_POINT,region=elSet));

frameIVOL.insert(0,frameRepository[-1].fieldOutputs['IVOL'].getSubset(position=INTEGRATION_POINT,region=elSet));
frameIVOLa.insert(0,frameRepository[-1].fieldOutputs['IVOL'].getSubset(position=INTEGRATION_POINT,region=elSeta));

Tot_Stress=0;
Tot_Strain=0;
Tot_E_Flux=0;
Tot_EPG=0;
#
Tot_EPGa=0;
Tot_E_Fluxa=0;

Tot_Vol=0;
Tot_Vola=0;
for II in range(0,len(frameS[-1].values)):
    Tot_Vol=Tot_Vol+frameIVOL[0].values[II].data;

```

```

        Tot_Stress=Tot_Stress+frameS[0].values[II].data *
frameIVOL[0].values[II].data;
        Tot_Strain=Tot_Strain+frameE[0].values[II].data *
frameIVOL[0].values[II].data;
        Tot_EPG=Tot_EPG+frameP[0].values[II].data * frameIVOL[0].values[II].data;
        Tot_E_Flux=Tot_E_Flux+frameF[0].values[II].data *
frameIVOL[0].values[II].data;
        for III in range(0,len(frameFa[-1].values)):
            Tot_Vola=Tot_Vola+frameIVOLa[0].values[III].data;
            Tot_EPGa=Tot_EPGa+framePa[0].values[III].data *
frameIVOLa[0].values[III].data;
            Tot_E_Fluxa=Tot_E_Fluxa+frameFa[0].values[III].data *
frameIVOLa[0].values[III].data;

    #Calculate Average
    Avg_Stress = Tot_Stress/Tot_Vol;
    Avg_Strain = Tot_Strain/Tot_Vol;
    Avg_EPG = Tot_EPG/Tot_Vol;
    Avg_E_Flux = Tot_E_Flux/Tot_Vol;

    Avg_EPGa = Tot_EPGa/Tot_Vola;
    Avg_E_Fluxa = Tot_E_Fluxa/Tot_Vola;
    print Avg_EPG;

    C[1-1][i] = Avg_Stress[0]          #stress11
    C[2-1][i] = Avg_Stress[1]          #stress22
    C[3-1][i] = Avg_Stress[2]          #stress33
    C[6-1][i] = Avg_Stress[3]          #stress12
    C[5-1][i] = Avg_Stress[4]          #stress13
    C[4-1][i] = Avg_Stress[5]          #stress23
    C[7-1][i] = Avg_E_Flux[0]
    C[8-1][i] = Avg_E_Flux[1]
    C[9-1][i] = Avg_E_Fluxa[2]
    S[1-1][i] = Avg_Strain[0]          #strain11
    S[2-1][i] = Avg_Strain[1]          #strain22
    S[3-1][i] = Avg_Strain[2]          #strain33
    S[6-1][i] = Avg_Strain[3]          #strain12
    S[5-1][i] = Avg_Strain[4]          #strain13
    S[4-1][i] = Avg_Strain[5]          #strain23
    S[7-1][i] = Avg_EPG[0]
    S[8-1][i] = Avg_EPG[1]
    S[9-1][i] = Avg_EPG[2]

    if flag==1:
        mdb.models[modelName].boundaryConditions['BC-ref1'].setValuesInStep(
            stepName=step[i], u3=Avg_Strain[4]*LX/2)
        mdb.models[modelName].boundaryConditions['BC-ref2'].setValuesInStep(
            stepName=step[i], u3=Avg_Strain[5]*LY/2)
        O[1-1][i] = Avg_Strain[4]*LX/2    #strain13 (X1 faces, BC)
        O[2-1][i] = Avg_Strain[5]*LY/2    #strain23 (X1 faces, BC)

    odb.close()

    print('-----')
    C-----')
    for i in range(0,len(C)):

```

```

        print('{0[0]:>16.7E} {0[1]:>16.7E} {0[2]:>16.7E}{0[3]:>16.7E}{0[4]:>16.7E}
{0[5]:>16.7E} {0[6]:>16.7E}{0[7]:>16.7E}{0[8]:>16.7E}'.format(C[i]))
        print('-----')
S-----')
    for i in range(0,len(C)):
        print('{0[0]:>16.7E} {0[1]:>16.7E} {0[2]:>16.7E}{0[3]:>16.7E}{0[4]:>16.7E}
{0[5]:>16.7E} {0[6]:>16.7E}{0[7]:>16.7E}{0[8]:>16.7E}'.format(S[i]))

    if flag==1:
        print('-----')
0-----')
        for i in range(0,len(O)):
            print('{0[0]:>16.7E} {0[1]:>16.7E} {0[2]:>16.7E}{0[3]:>16.7E}{0[4]:>16.7E}
{0[5]:>16.7E} {0[6]:>16.7E}{0[7]:>16.7E}{0[8]:>16.7E}'.format(O[i]))

import numpy as np
from numpy import matrix
from numpy import linalg
from numpy.linalg import inv

sAVG = matrix(C)
eAVG = matrix(S)

print "*****"
#print "jobName= %s"
print odbName
print "total volume= %f" %Tot_Vol
print "*****"

import numpy as np
#
#np.savetxt(jobName+"-O.txt", eeAVG)
if transform == 'full':
    np.savetxt(jobName+"-fullTransform-sAVG.txt", sAVG)
    np.savetxt(jobName+"-fullTransform-eAVG.txt", eAVG)
elif transform == 'mechOnly':
    np.savetxt(jobName+"-mechTransform2-sAVG.txt", sAVG)
    np.savetxt(jobName+"-mechTransform2-eAVG.txt", eAVG)

MFC_flag='P1'      #Can be P1 or P2
BC_flag='MIX'      #Can be MIX or PBCMIXe

transform='mechOnly' #Can be mechOnly or full

nCPUs=4 #Number of CPUs for analyses
partName = 'Part-1' # Make sure the Abaqus part name is Part-1
SF = 10e9          # Scale factor to scale the loads
LX=2*0.529166667   #RVE edge lengths
LY=0.4113704645
Ha=0.18 #Active layer thickness

CT=1 #Not really needed since only 1 height and volume fraction are computed
for LZ in [0.296]: #RVE height(s)
    for VF in [0.8654]: #RVE Volume fractions
        modelName = 'Model-' +str(CT)+'-LinearEL'

```

```

m=mdb.models[modelName]
jobName=MFC_flag+'-medium-'+str(CT) + '-1-' +BC_flag

if BC_flag == 'MIX':
    createSurfacesAndConstrains(modelName)
    Set9StepBCs_MIX(modelName,LX,LY,LZ,Ha,SF,MFC_flag)
elif BC_flag == 'PBCMIXe':
    constrainsPBC(modelName)
    Set9StepBCs_PBC_equipot(modelName,LX,LY,LZ,Ha,SF,MFC_flag)
# elif BC_flag == 'MIXPBCe':
#     createSurfacesAndConstrains(modelName)
#     Set9StepBCs_MIXPBCe(modelName,LX,LY,LZ, SF)
# elif BC_flag == 'MIX_Q':
#     createSurfacesAndConstrains(modelName)
#     Set9StepBCs_MIX_ALL_Q(modelName,LX,LY,LZ, SF)
# elif BC_flag == 'PBC':
#     constrainsPBC(modelName)
#     Set9StepBCs_PBC(modelName,LX,LY,LZ, SF)

odbName=jobName+'.odb'
m.HistoryOutputRequest(name='H-Output-1',
    createStepName='Step-1', variables=('ETOTAL', ))
#Create Job
myJob=mdb.Job(name=jobName, model=modelName, description='', type=ANALYSIS,
    atTime=None, waitMinutes=0, waitHours=0, queue=None, memory=75,
    memoryUnits=PERCENTAGE, getMemoryFromAnalysis=False,
    explicitPrecision=SINGLE, nodalOutputPrecision=SINGLE, echoPrint=OFF,
    modelPrint=OFF, contactPrint=OFF, historyPrint=OFF, userSubroutine='',
    scratch='', resultsFormat=ODB, multiprocessingMode=DEFAULT, numCpus=nCPUs,
    numDomains=nCPUs, numGPUs=0)
#Run Job
myJob.submit()
myJob.waitForCompletion() # Wait for the job to complete.
shearStrainUpdateFlag=0 #Set this equal to 1 if you want the shear strain avg.
to update the BCs.

#Compute volume averages
DeffUpdateTransverseShearStrain(LX,
LY,LZ,partName,jobName,modelName,shearStrainUpdateFlag,transform)
#Update the PBCs with shear average shear strains
if (BC_flag == 'MIX') or (BC_flag == 'MIXPBCe') or (BC_flag == 'MIX_Q'):
    jobName=MFC_flag+'-medium-'+str(CT) + '-1-' +BC_flag
    myJob=mdb.Job(name=jobName, model=modelName, description='', type=ANALYSIS,
        atTime=None, waitMinutes=0, waitHours=0, queue=None, memory=75,
        memoryUnits=PERCENTAGE, getMemoryFromAnalysis=False,
        explicitPrecision=SINGLE, nodalOutputPrecision=SINGLE, echoPrint=OFF,
        modelPrint=OFF, contactPrint=OFF, historyPrint=OFF, userSubroutine='',
        scratch='', resultsFormat=ODB, multiprocessingMode=DEFAULT, numCpus=nCPUs,
        numDomains=nCPUs, numGPUs=0)
    myJob.submit()
    myJob.waitForCompletion() # Wait for the job to complete.
    shearStrainUpdateFlag=0
    DeffUpdateTransverseShearStrain(LX,
LY,LZ,partName,jobName,modelName,shearStrainUpdateFlag,transform)
    CT=CT+1

```


C. SCRIPTS FOR POLARIZING THE P1 MFC

Python script to polarize the P1 FE models. This and many other files can be downloaded from <https://cdmhub.org/projects/ernestocamarena>.

"""

Created on Thu Apr 19 09:07:36 2018

This script is an extension of polarize9 but with a more efficient way to modified to handle a composite

Also added code to facilitate data transverse to SwiftComp (SC) input files at the final iteration. Print element orientations at the final iteration and for every iteration create and update scaled material properties for piezoelectric analysis in SC. 5/8/2018

Updated unpoled material properties.

New permittivity, new Poisson ratio (in C_{ij}) 8/20/2018

This script has partial polarized material deactivated. A break in the loop was also implemented. 8/27/2018

Must create a geometry set named 'PZT-Geom' before running program

This code simulations starts with in initially uniform material and element direction and then over the number of Iterations, will update the element orientations based on the field output (EPG). Old directions are deleted for each loop. Creation of new sections, assignments, and materials are skipped until the element directions converge.

This code is based on polarize11_fullypoled but initial loop was removed that was too time consuming and not even needed. Unused function definitions were also deleted 11/24/18

@author: ecamaren

"""

#Begin Post Processing

#Open the Output Data Base for the current Job

```
from visualization import *
from odbAccess import *
from abaqusConstants import *
from odbMaterial import *
from odbSection import *
from textRepr import *
from mesh import *
from part import *
from material import *
from section import *
from assembly import *
from step import *
import job
```

Iterations=15 *#The numer of iterations for the main Loop*

jobNameAppend='-fine-MIX'

jobNameAppend='-medium-MIX'

jobNameAppend='-M2814-P1-activeArea'

nCPUs=160 *#The numer of CPUs to use for all jobs*

modelName = 'Model-1'

partName = 'Part-1'

PZTsetName='PZT-Geo'

```

m=mdb.models[modelName]
p = m.parts[partName]
nel=len(p.sets[PZTsetName].elements)
nelT=len(p.elements) #The total number of elements in the model
print 'Number Elements to modify sections, materials, and orientations: %1.1f'
    %(nel)
print 'Total Number of elements in model: %1.1f' %(nelT)

PZTregion =p.sets[PZTsetName]
defaultOrientation = tuple([1,0,0,0,1,0]) #Define OrientVectors for first Loop

elemList=[] #This variable is an ordered list of element numbers
            #and will be used to assign element orientation.
            #It can change for each iteration

orientVectors=[] # This will hold the components of the unit vectors
                #that will define the element orientation. It will
                #change for each iteration

orientVectorsOld=[] #Orientation vectors from the previous iteration

dnmax=1
for ct in range(0,Iterations):
    print '***** Iteration: %1.1f'
        %(ct+1)
    if ct > 0:
        elemList=tuple(elemList)

        elemList=tuple(elemList)
#Create Default Orientation Field aligned with Global Coords
        orientVectors = tuple(orientVectors)

# print 'dnmax: %1.4f' %(dnmax)
        if dnmax < 0.05:
            print 'Converged! Breaking Loop!'
            break

    m.DiscreteField(name='PolingField', description='',
                    location=ELEMENTS, fieldType=ORIENTATION, dataWidth=6,
                    defaultValues=defaultOrientation,
                    data=('', 6, elemList, orientVectors), ),
                    orientationType=CARTESIAN, partLevelOrientation=True)

#Assign Orientation
    p.MaterialOrientation(region=PZTregion,
                        orientationType=FIELD, axis=AXIS_1, fieldName='PolingField',
                        localCsys=None, additionalRotationType=ROTATION_NONE, angle=0.0,
                        additionalRotationField='', stackDirection=STACK_3)

#Set-up Job
    jobName='Polarize-'+str(ct+1) + jobNameAppend
# jobName='Job' + jobNameAppend
    odbName=jobName+'.odb'

    m.HistoryOutputRequest(name='H-Output-1',
                          createStepName='Step-1', variables=('ETOTAL', ))

```

```

myJob=mdb.Job(name=jobName, model='Model-1', description='', type=ANALYSIS,
              atTime=None, waitMinutes=0, waitHours=0, queue=None, memory=95,
              memoryUnits=PERCENTAGE, getMemoryFromAnalysis=False,
              explicitPrecision=SINGLE, nodalOutputPrecision=SINGLE,
              echoPrint=OFF, modelPrint=OFF, contactPrint=OFF, historyPrint=OFF,
              userSubroutine='', scratch='', resultsFormat=ODB,
              multiprocessingMode=DEFAULT, numCpus=nCPUs, numDomains=nCPUs,
              numGPUs=0)
myJob.submit()
myJob.waitForCompletion()           # Wait for the job to complete.

odb = openOdb(path=odbName);
myAssembly = odb.rootAssembly;
frameRepository = odb.steps['Step-1'].frames;
frameP=[];

datum0=session.odbs[odbName].rootAssembly.
              datumCsyses['ASSEMBLY_PART-1-...1_ORI-POLINGFIELD']

PARTNAME=partName.upper() + str(-1) #Make uppercase
SETNAME=PZTsetName.upper()
elSet=myAssembly.instances[PARTNAME].elementSets[SETNAME]

#Get only the last frame [-1]. And in the Global Coordinates System
# (IMPORTANT)
framePi=frameRepository[-1].fieldOutputs['EPG'].
              getTransformedField(datumCsys=datum0);
frameP.insert(0,framePi.getSubset(position=CENTROID,region=elSet));

if ct > 0:
    orientVectorsOld=orientVectors
    orientVectors=[]
    elemList=[]
    directionList=[]

for i in range(0,nel):
    elem_no=frameP[0].values[i].elementLabel
    elemList.append(elem_no)
    E1=frameP[0].values[i].data[0]
    E2=frameP[0].values[i].data[1]
    E3=frameP[0].values[i].data[2]
    mag = sqrt(E1**2+E2**2+E3**2)

    tolDir=4 #number of decimal places to round directions
    n1=round(E1/mag,tolDir)
    n2=round(E2/mag,tolDir)
    n3=round(E3/mag,tolDir)

    orientVectors.append(n1)
    orientVectors.append(n2)
    orientVectors.append(n3)
    orientVectors.append(0.0)
    orientVectors.append(1.0)
    orientVectors.append(0.0)

```

*#Find the difference vector and magnitude between the current direction and the
#previous iteration*

```

if ct > 0:
    c1=orientVectors[6*i]-orientVectorsOld[6*i]
    c2=orientVectors[6*i+1]-orientVectorsOld[6*i+1]
    c3=orientVectors[6*i+2]-orientVectorsOld[6*i+2]
    dnmag=sqrt(c1**2+c2**2+c3**2)

```

#Seach for abs(max(dn))

```

if i==0:
    dnmax=abs(dnmag)
    print 'i= %1.1f : dnmax=%1.5f' %(i,dnmax)
elif dnmag > dnmax:
    dnmax=abs(dnmag)
    print 'i= %1.1f  dnmax=%1.5f' %(i,dnmax)

```

REFERENCES

- [1] W. Yu. An Introduction to Micromechanics. *Applied Mechanics and Materials*, 828:3–24, 2016.
- [2] W. Yu. *Multiscale Structural Mechanics: Top-down Modeling of Composite Structures Using Mechanics of Structure Genome*. John Wiley, 2017.
- [3] W. Yu. A Unified Theory for Constitutive Modeling of Composites. *Journal of Mechanics of Materials and Structures*, 11(4):379–411, 2016.
- [4] R. S. Dahiya, M. Valle, G. Metta, L. Lorenzelli, and S. Pedrotti. Deposition, Processing and Characterization of P(VDF-TrFE) Thin Films for Sensing Applications. In *2008 IEEE Sensors*, pages 490–493. IEEE, 2008.
- [5] J. F. Tressler, S. Alkoy, and R. E. Newnham. Piezoelectric Sensors and Sensor Materials. *Journal of Electroceramics*, 2(4):257–272, 1998.
- [6] C. B. Eom and S. Trolier-McKinstry. Thin-film Piezoelectric MEMS. *MRS Bulletin*, 37(11):1007–1017, 2012.
- [7] N. W. Hagood and A. Bent. Development of Piezoelectric Fiber Composites for Structural Actuation. In *34th Structures, Structural Dynamics and Materials Conference*, pages 3625–3638, La Jolla, CA, 1993. AIAA/ASME/ASCE/AHS/ASC.
- [8] C. R. Bowen, R. Stevens, L. J. Nelson, A. C. Dent, G. Dolman, B. Su, T. W. Button, M. G. Cain, and M. Stewart. Manufacture and Characterization of High Activity Piezoelectric Fibres. *Smart Materials and Structures*, 15(2):295–301, 2006.
- [9] J.-S. Park and J.-H. Kim. Analytical Development of Single Crystal Macro Fiber Composite Actuators for Active Twist Rotor Blades. *Smart Materials and Structures*, 14(4):745–753, 2005.
- [10] D. J. Leo. *Engineering Analysis of Smart Material Systems*. John Wiley & Sons, Hoboken, NJ, 2007.
- [11] Y. Shindo, F. Narita, and T. Watanabe. Nonlinear Electromechanical Fields and Localized Polarization Switching of Piezoelectric Macrofiber Composites. *Journal of Mechanics of Materials and Structures*, 29(4):647–653, 2011.
- [12] K. C. Le. *Vibrations of Shells and Rods*. Springer Berlin Heidelberg, 1999.
- [13] S. Katzir. Who Knew Piezoelectricity? Rutherford and Langevin on Submarine Detection and the Invention of Sonar. *Notes and Records of the Royal Society*, 66(2):141–157, 2012.

- [14] J. Sirohi and I. Chopra. Fundamental Understanding of Piezoelectric Strain Sensors. *Journal of Intelligent Material Systems and Structures*, 11(4):246–257, 2000.
- [15] Y. Bian, Y. Zhang, K. Sun, H. Jin, L. Dai, and H. Shen. A Biomimetic Vibration Sensor Using a Symmetric Electrodes Metal Core Piezoelectric Fiber. *Journal of Intelligent Material Systems and Structures*, 29(6):1015–1024, 2018.
- [16] P. Tan and L. Tong. Micro-Electromechanics models for Piezoelectric-Fiber-Reinforced Composite Materials. *Composites Science and Technology*, 61(5):759–769, 2001.
- [17] N. W. Hagood, R. Kindel, K. Ghandi, and P. Gaudenzi. Improving Transverse Actuation of Piezoceramics Using Interdigitated Surface Electrodes. *SPIE Smart Structures and Intelligent Systems*, 1917:341–352, 1993.
- [18] C. R. Bowen, L. J. Nelson, R. Stevens, M. G. Cain, and M. Stewart. Optimisation of Interdigitated Electrodes for Piezoelectric Actuators and Active Fibre Composites. *Journal of Electroceramics*, 16(4):263–269, 2006.
- [19] B. B. Nielsen, M. S. Nielsen, and I. F. Santos. A Layered Shell Containing Patches of Piezoelectric Fibers and Interdigitated Electrodes: Finite Element Modeling and Experimental Validation. *Journal of Intelligent Material Systems and Structures*, 28(1):78–96, 2017.
- [20] Abaqus®, Release 6.14, Documentation Collection. 2018.
- [21] ANSYS® Academic Research Mechanical, Release 16.2.3, Help System, Coupled Field Analysis Guide, System of Units, ANSYS, Inc. 2018.
- [22] V. L. Berdichevsky. *Variational Principles of Continuum Mechanics*. Springer Berlin, 2009.
- [23] B. Peng, J. Goodsell, R. B. Pipes, and W. Yu. Generalized Free-Edge Stress Analysis Using Mechanics of Structure Genome. *Journal of Applied Mechanics*, 83(10):101013, 2016.
- [24] M. Augusta Neto, W. Yu, and S. Roy. Two Finite Elements for General Composite Beams With Piezoelectric Actuators and Sensors. *Finite Elements in Analysis and Design*, 45(5):295–304, 2009.
- [25] L. Liao and W. Yu. Asymptotical Construction of a Fully Coupled, Reissner–Mindlin Model for Piezoelectric Composite Plates. *Smart Materials and Structures*, 17(1):015010, 2008.
- [26] L. Liao and W. Yu. An electromechanical Reissner-Mindlin model for laminated piezoelectric plates. *Composite Structures*, 88(3):394–402, 2009.
- [27] W. Yu and T. Tang. Variational Asymptotic Method for Unit Cell Homogenization of Periodically Heterogeneous Materials. *International Journal of Solids and Structures*, 44(11-12):3738–3755, 2007.
- [28] T. Tang and W. Yu. Variational asymptotic micromechanics modeling of heterogeneous piezoelectric materials. *Mechanics of Materials*, 40(10):812–824, 2008.

- [29] J. Bravo-Castillero, R. Guinovart-Diaz, F. J. Sabina, and R. Rodriguez-Ramos. Closed-form Expressions for the Effective Coefficients of a Fiber-reinforced Composite With Transversely Isotropic Constituents II. Piezoelectric and Square Symmetry. *Mechanics of Materials*, 33(4):1463–1479, 2001.
- [30] A. L. Kalamkarov and A. V. Georgiades. Micromechanical Modeling of Smart Composite Structures. *Smart Materials and Structures*, 11(3):313, 2002.
- [31] F. Biscani, H. Nasser, S. Belouettar, and E. Carrera. Equivalent Electro-Elastic Properties of Macro Fiber Composite (MFC) Transducers Using Asymptotic Expansion Approach. *Composites Part B: Engineering*, 42(3):444–455, 2011.
- [32] A. C. Cook and S. S. Vel. Multiscale Analysis of Laminated Plates with Integrated Piezoelectric Fiber Composite Actuators. *Composite Structures*, 94(2):322–336, 2012.
- [33] H. Berger, S. Kari, U. Gabbert, R. Rodriguez-Ramos, R. Guinovart, J. A. Otero, and J. Bravo-Castillero. An Analytical and Numerical Approach for Calculating Effective Material Coefficients of Piezoelectric Fiber Composites. *International Journal of Solids and Structures*, 42(21-22):5692–5714, 2005.
- [34] S. Kuznetsov and J. Fish. Mathematical Homogenization Theory for Electroactive Continuum. *International Journal for Numerical Methods in Engineering*, 91(11):1199–1226, 2012.
- [35] H. E. Pettermann and S. Suresh. A Comprehensive Unit Cell Model: A Study of Coupled Effects in Piezoelectric 1–3 Composites. *International Journal of Solids and Structures*, 37(39):5447–5464, 2000.
- [36] H. Berger, S. Kari, U. Gabbert, R. Rodriguez-Ramos, J. Bravo-Castillero, R. Guinovart-Diaz, F. J. Sabina, and G. A. Maugin. Unit Cell Models of Piezoelectric Fiber Composites for Numerical and Analytical Calculation of Effective Properties. *Smart Materials and Structures*, 15(2):451–458, 2006.
- [37] G. M. Odegard. Constitutive Modeling of Piezoelectric Polymer Composites. *Acta Materialia*, 52(18):5315–5330, 2004.
- [38] J. Pastor. Homogenization of Linear Piezoelectric Media. *Mechanics Research Communications*, 24(2):145–150, 1997.
- [39] R. de Medeiros, M. E. Moreno, F. D. Marques, and V. Tita. Effective Properties Evaluation for Smart Composite Materials. *Journal of the Brazilian Society of Mechanical Sciences and Engineering*, 34(spe):362–370, 2012.
- [40] W. Qi and W. Cao. Finite Element Analysis and Experimental Studies on the Thickness Resonance of Piezocomposite Transducers. *Ultrasonic Imaging*, 18(1):1–9, 1996.
- [41] C. V. Madhusudhana Rao and G. Prasad. Characterization of 1–3 Piezoelectric Polymer Composites – A Numerical and Analytical Evaluation Procedure for Thickness Mode Vibrations. *Condensed Matter Physics*, 13(1):13703–13712, 2010.
- [42] R. Kar-Gupta and T. A. Venkatesh. Electromechanical Response of (2–2) Layered Piezoelectric Composites. *Smart Materials and Structures*, 22(2):025035, 2013.

- [43] J. Schröder and M.-A. Keip. Two-scale Homogenization of Electromechanically Coupled Boundary Value Problems. *Computational Mechanics*, 50(2):229–244, 2012.
- [44] M.-A. Keip, P. Steinmann, and J. Schröder. Two-scale computational homogenization of electro-elasticity at finite strains. *Computer Methods in Applied Mechanics and Engineering*, 278:62–79, 2014.
- [45] R. Kiran, A. Kumar, V. S. Chauhan, R. Kumar, and R. Vaish. Finite Element Study on Performance of Piezoelectric Bimorph Cantilevers Using Porous/Ceramic 0–3 Polymer Composites. *Journal of Electronic Materials*, 47(1):233–241, 2018.
- [46] J. Calogero, H. B. Atitallah, N. Wyckoff, Z. Ounaies, and M. Frecker. Non-linear Piezoelectric Material Properties and Non-Uniform Poling in a Flexible Electro-Active Composite Finite Element Model. In *ASME. Smart Materials, Adaptive Structures and Intelligent Systems, Volume 1: Multifunctional Materials; Mechanics and Behavior of Active Materials; Integrated System Design and Implementation; Structural Health Monitoring ():V001T01A015*. ASME, 2016.
- [47] A. Deraemaeker, S. Benelechi, A. Benjeddou, and A. Preumont. Analytical and Numerical Computation of Homogenized Properties of MFCS: Application to a Composite Boom with MFC Actuators and Sensors. In *Proceedings of the III ECCOMAS Thematic Conference on Smart Structures and Materials*, pages 1–22, 2007.
- [48] A. Deraemaeker, H. Nasser, A. Benjeddou, and A. Preumont. Mixing Rules for the Piezoelectric Properties of Macro Fiber Composites. *Journal of Intelligent Material Systems and Structures*, 20(12):1475–1482, 2009.
- [49] A. Deraemaeker and H. Nasser. Numerical Evaluation of the Equivalent Properties of Macro Fiber Composite (MFC) Transducers Using Periodic Homogenization. *International Journal of Solids and Structures*, 47(24):3272–3285, 2010.
- [50] H. Nasser, F. Biscani, and S. Belouettar. Effect of Matrix Properties on the Overall Piezoelectric Constants of Piezocomposite Transducers. *Mechanics of Advanced Materials and Structures*, 18(7):531–539, 2011.
- [51] M. A. Trindade and A. Benjeddou. Finite Element Homogenization Technique for the Characterization of d15 Shear Piezoelectric Macro-fibre Composites. *Smart Materials and Structures*, 20(7), 2011.
- [52] M. A. Trindade and A. Benjeddou. Finite Element Characterisation of Multi-layer d31 Piezoelectric Macro-Fibre Composites. *Composite Structures*, 151:47–57, 2015.
- [53] S. S. Prasath and A. Arockiarajan. Analytical, Numerical and Experimental Predictions of the Effective Electromechanical Properties of Macro-Fiber Composite (MFC). *Sensors and Actuators A: Physical*, 214:31–44, 2014.
- [54] S. S. Prasath and A. Arockiarajan. Influence of bonding layer on effective electromechanical properties of macro-fiber composites (MFCs). *Smart Materials and Structures*, 23(9):095046, 2014.

- [55] S. S. Prasath and A. Arockiarajan. Effect of interphase and thermal environment on the effective properties of Macro-Fiber Composites (MFC). *Composites Part B: Engineering*, 75:327–335, 2015.
- [56] C. Dumoulin and A. Deraemaeker. A Study on the Performance of Piezoelectric Composite Materials for Designing Embedded Transducers for Concrete Assessment. *Smart Materials and Structures*, 27(3):035008, 2018.
- [57] H. Brito-Santana, R. de Medeiros, R. Rodriguez-Ramos, and V. Tita. Different Interface Models for Calculating the Effective Properties in Piezoelectric Composite Materials with Imperfect Fiber-Matrix Adhesion. *Composite Structures*, 151:70–80, 2016.
- [58] A. Jafari, A. A. Khatibi, and M. M. Mashhadi. Comprehensive Investigation on Hierarchical Multiscale Homogenization Using Representative Volume Element for Piezoelectric Nanocomposites. *Composites Part B: Engineering*, 42(3):553–561, 2011.
- [59] A. C. Dent, C. R. Bowen, R. Stevens, M. G. Cain, and M. Stewart. Effective Elastic Properties for Unpoled Barium Titanate. *Journal of the European Ceramic Society*, 27(13-15):3739–3743, 2007.
- [60] K. Terada, M. Hori, T. Kyoya, and N. Kikuchi. Simulation of the Multi-scale Convergence in Computational Homogenization Approaches. *International Journal of Solids and Structures*, 37(16):2285–2311, 2000.
- [61] S. Saeb, P. Steinmann, and A. Javili. Aspects of Computational Homogenization at Finite Deformations: A Unifying Review From Reuss’ to Voigt’s Bound. *Applied Mechanics Reviews*, 68(5):050801, 2016.
- [62] J. Schröder. Derivation of the Localization and Homogenization Conditions for Electro–mechanically Coupled Problems. *Computational Materials Science*, 46(3):595–599, 2009.
- [63] K. Y. Hashimoto and M. Yamaguchi. Elastic, Piezoelectric, and Dielectric Properties of Composite Materials. In *IEEE Transactions On Ultrasonics Ferroelectrics And Frequency Control*, pages 697–702, 1986.
- [64] R. E. Newnham, D. P. Skinner, and L. E. Cross. Connectivity and Piezoelectric-Pyroelectric Composites. *Materials Research Bulletin*, 13(5):525–536, 1978.
- [65] D. P. Skinner, R. E. Newnham, and L. E. Cross. Flexible Composite Transducers. *Materials Research Bulletin*, 13(6):599–607, 1978.
- [66] A. Bent, N. W. Hagood, and J. P. Rogers. Anisotropic Actuation with Piezoelectric Fiber Composites. *Journal of Intelligent Material Systems and Structures*, 6(3):338–349, 1995.
- [67] R. Kar-Gupta and T. A. Venkatesh. Electromechanical Response of 1–3 Piezoelectric Composites: An Analytical Model. *Acta Materialia*, 55(3):1093–1108, 2007.
- [68] F. Levassort, M. Lethiecq, D. Certon, and F. Patat. A Matrix Method for Modeling Electroelastic Moduli of 0-3 Piezo-composites. *IEEE Transactions on Ultrasonics, Ferroelectrics and Frequency Control*, 44(2):445–452, 1997.

- [69] F. Biscani, H. Nasser, and S. Belouettar. Directional Dependence of the Static Response of Layered Piezoelectric Transducers. *Journal of Intelligent Material Systems and Structures*, 23(12):1311–1322, 2012.
- [70] S. S. Prasath and A. Arockiarajan. Experimental and Theoretical Investigation on the Thermo-Electro-Elastic Properties of Macro-Fiber Composites (MFC). *Composite Structures*, 122:8–22, 2015.
- [71] A. Bent. *Active Fiber Composites for Structural Actuation*. PhD thesis, MIT, 1997.
- [72] E. Lenglet, A.-C. Hladky-Hennion, and J.-C. Debus. Numerical Homogenization Techniques Applied to Piezoelectric Composites. *The Journal of the Acoustical Society of America*, 113(2):826–833, 2003.
- [73] S. Raja and T. Ikeda. Concept and Electro-elastic Modeling of Shear Actuated Fiber Composite using Micro-mechanics Approach. *Journal of Intelligent Material Systems and Structures*, 19(10):1173–1183, 2008.
- [74] K. Veerannan and A. Arockiarajan. Analytical, Numerical and Experimental Studies on Effective Properties of Layered (2–2) Multiferroic Composites. *Sensors and Actuators A: Physical*, 236:380–393, 2015.
- [75] H. L. W. Chan and J. Unsworth. Simple Model for Piezoelectric Ceramic/Polymer 1-3 Composites Used in Ultrasonic Transducer Applications. *IEEE Transactions on Ultrasonics, Ferroelectrics, and Frequency Control*, 36(4):434–441, 1989.
- [76] W. A. Smith and B. A. Auld. Modeling 1–3 Composite Piezoelectrics: Thickness-Mode Oscillations. *IEEE Transactions on Ultrasonics, Ferroelectrics and Frequency Control*, 38(1):40–47, 1991.
- [77] W. A. Smith, A. Shaulov, and B. A. Auld. Tailoring the Properties of Composite Piezoelectric Materials for Medical Ultrasonic Transducers. In *IEEE 1985 Ultrasonics Symposium*, pages 642–647. IEEE, 1985.
- [78] J. D. Eshelby. The Determination of the Elastic Field of an Ellipsoidal Inclusion, and Related Problems. *Proceedings of the Royal Society A: Mathematical, Physical and Engineering Sciences*, 241(1226):376–396, 1957.
- [79] M. L. Dunn and M. Taya. Micromechanics Predictions of the Effective Electroelastic Moduli of Piezoelectric Composites. *International Journal of Solids and Structures*, 30(2):161–175, 1993.
- [80] T. Mori and K. Tanaka. Average Stress in Matrix and Average Elastic Energy of Materials With Misfitting Inclusions. *Acta Metallurgica*, 21(5):571–574, 1973.
- [81] A. R. Aguiar, J. Bravo-Castillero, and U. P. da Silva. Application of Mori–Tanaka Method in 3–1 Porous Piezoelectric Medium of Crystal Class 6. *International Journal of Engineering Science*, 123:36–50, 2018.
- [82] J. Elouafi, L. Azrar, and A. A. Aljinaidi. Closed-form Expressions for the Effective Moduli of Heterogeneous Piezoelectric Materials. *International Journal of Solids and Structures*, 52:19–32, 2015.

- [83] R. E. Newnham, L. J. Bowen, K. A. Klier, and L. E. Cross. Composite Piezoelectric Transducers. *Materials & Design*, 2(2):93–106, 1980.
- [84] N. Mallik and M. C. Ray. Effective Coefficients of Piezoelectric Fiber-Reinforced Composites. *AIAA Journal*, 41(4):704–710, 2003.
- [85] L. Li and N. R. Sottos. Improving Hydrostatic Performance of 1–3 Piezocomposites. *Journal of Applied Physics*, 77(9):4595–4603, 1995.
- [86] R. E. Montgomery and C. Richard. A Model for the Hydrostatic Pressure Response of a 1–3 Composite. *IEEE Transactions on Ultrasonics, Ferroelectrics and Frequency Control*, 43(3):457–466, 1996.
- [87] N. Rajapakse and Y. Chen. A Coupled Analytical Model for Hydrostatic Response of 1–3 Piezocomposites. *IEEE Transactions on Ultrasonics, Ferroelectrics and Frequency Control*, 55(8):1847–1858, 2008.
- [88] J. Aboudi. Micromechanical Prediction of the Effective Coefficients of Thermo-Piezoelectric Multiphase Composites. *Journal of Intelligent Material Systems and Structures*, 9(9):713–722, 1998.
- [89] M. Avellaneda and P. J. Swart. Calculating the Performance of 1–3 Piezoelectric Composites for Hydrophone Applications: An Effective Medium Approach. *The Journal of the Acoustical Society of America*, 103(3):1449, 1998.
- [90] L. V. Gibiansky and S. Torquato. Optimal Design of 1–3 Composite Piezoelectrics. *Structural Optimization*, 13(1):23–28, 1997.
- [91] M. Eynbeygi and M. M. Aghdam. A Micromechanical Study on the Electro-elastic Behavior of Piezoelectric Fiber-reinforced Composites Using the Element-free Galerkin Method. *Acta Mechanica*, 226(9):3177–3194, 2015.
- [92] Y. Sapsathiarn, R. Tippyaphalapholgul, and T. Senjuntichai. Effective Properties of Piezoelectric Fiber-Reinforced Composites with Imperfect Interface. *Journal of Engineering Mechanics*, 143(3):B4016001, 2017.
- [93] P. L. Bishay, L. Dong, and S. N. Atluri. Multi-Physics Computational Grains (MPCGs) for Direct Numerical Simulation (DNS) of Piezoelectric Composite/Porous Materials and Structures. *Computational Mechanics*, 54(5):1129–1139, 2014.
- [94] C.-W. Nan and F.-S. Jin. Multiple-scattering Approach to Effective Properties of Piezoelectric Composites. *Physical Review B*, 48(12):8578–8582, 1993.
- [95] J. C. Michel, H. Moulinec, and P. Suquet. Effective Properties of Composite Materials With Periodic Microstructure: A Computational Approach. *Computer Methods in Applied Mechanics and Engineering*, 172(1-4):109–143, 1999.
- [96] S. Iyer and T. A. Venkatesh. Electromechanical Response of (3–0, 3–1) Particulate, Fibrous, and Porous Piezoelectric Composites with Anisotropic Constituents: A Model Based on the Homogenization Method. *International Journal of Solids and Structures*, 51(6):1221–1234, 2014.
- [97] D. Zäh and C. Miehe. Computational Homogenization in Dissipative Electromechanics of Functional Materials. *Computer Methods in Applied Mechanics and Engineering*, 267:487–510, 2013.

- [98] C. P. Jiang and Y. K. Cheung. An Exact Solution for the Three-phase Piezoelectric Cylinder Model Under Antiplane Shear and Its Applications to Piezoelectric Composites. *International Journal of Solids and Structures*, 38(28-29):4777–4796, 2001.
- [99] Z. Xue, L. Li, M. N. Ichchou, and C. Li. Hysteresis and the Nonlinear Equivalent Piezoelectric Coefficient of MFCs for Actuation. *Chinese Journal of Aeronautics*, 30(1):88–98, 2017.
- [100] R. Paradies and M. M. Melnykowycz. State of Stress in Piezoelectric Elements With Interdigitated Electrodes. *Journal of Electroceramics*, 24(3):137–144, 2010.
- [101] S. Hensel, W.-G. Drossel, M. Nestler, and R. Müller. Modeling of the Performance Reduction of Macro Fiber Composites for Use in Numerical Forming Simulation of Piezoceramic-metal-compounds. *CIRP Journal of Manufacturing Science and Technology*, 7(2):129–138, 2014.
- [102] E. Merkel and A. Ricoeur. Effective Properties of Cracked Piezoelectrics with Non-trivial Crack Face Boundary Conditions. *Archive of Applied Mechanics*, 86(7):1325–1340, 2016.
- [103] W. Chen and C. S. Lynch. Finite Element Analysis of Cracks in Ferroelectric Ceramic Materials. *Engineering Fracture Mechanics*, 64(5):539–562, 1999.
- [104] T. Tang and W. Yu. Variational Asymptotic Homogenization of Heterogeneous Electromagnetoelastic Materials. *International Journal of Engineering Science*, 46(8):741–757, 2008.
- [105] X. Wang, E. Pan, J. D. Albrecht, and W. J. Feng. Effective Properties of Multilayered Functionally Graded Multiferroic Composites. *Composite Structures*, 87(3):206–214, 2009.
- [106] K. S. Challagulla and A. V. Georgiades. Micromechanical Analysis of Magneto-electro-thermo-elastic Composite Materials With Applications to Multilayered Structures. *International Journal of Engineering Science*, 49(1):85–104, 2011.
- [107] E. F. Crawley and J. De Luis. Use of Piezoelectric Actuators as Elements of Intelligent Structures. *AIAA Journal*, 25(10):1373–1385, 1987.
- [108] T. Zhang and Z. Shi. Two-dimensional Exact Analysis for Piezoelectric Curved Actuators. *Journal of Micromechanics and Microengineering*, 16(3):640–647, 2006.
- [109] K. Chandrashekhara and A. N. Agarwal. Active Vibration Control of Laminated Composite Plates Using Piezoelectric Devices: A Finite Element Approach. *Journal of Intelligent Material Systems and Structures*, 4(4):496–508, 1993.
- [110] P. Heyliger. Static Behavior of Laminated Elastic/Piezoelectric Plates. *AIAA Journal*, 32(12):2481–2484, 1994.
- [111] C.-H. Hong and I. Chopra. Modeling and Validation of Induced Strain Actuation of Composite Coupled Plates. *AIAA Journal*, 37(3):372–377, 1999.

- [112] R. Zemcik, R. Rolfes, M. Rose, and J. Tessmer. High-Performance 4-Node Shell Element with Piezoelectric Coupling. *Mechanics of Advanced Materials and Structures*, 13(5):393–401, 2006.
- [113] O. Polit, M. D’Ottavio, and P. Vidal. High-Order Plate Finite Elements for Smart Structure Analysis. *Composite Structures*, 151:81–90, 2016.
- [114] E. Carrera and S. Valvano. Analysis of Laminated Composite Structures With Embedded Piezoelectric Sheets by Variable Kinematic Shell Elements. *Journal of Intelligent Material Systems and Structures*, 28(20):2959–2987, 2017.
- [115] G. Rama, D. Marinković, and M. Zehn. Efficient Three-node Finite Shell Element for Linear and Geometrically Nonlinear Analyses of Piezoelectric Laminated Structures. *Journal of Intelligent Material Systems and Structures*, 29(3):345–357, 2018.
- [116] H. A. Sodano, J. Lloyd, and D. J. Inman. An Experimental Comparison Between Several Active Composite Actuators for Power Generation. *Smart Materials and Structures*, 15(5):1211–1216, 2006.
- [117] W. K. Wilkie, R. G. Bryant, J. W. High, R. L. Fox, R. F. Hellbaum, A. Jalink, B. D. Little, and P. H. Mirick. Low-Cost Piezocomposite Actuator for Structural Control Applications. In *Proceedings, SPIE’s 7th International Symposium on Smart Structures and Materials, Newport Beach, California*, volume March, pages 323–334, 2000.
- [118] Smart-Materials Corp. <http://www.smart-material.com>, 2018.
- [119] J. W. Sohn, S.-B. Choi, and H. S. Kim. Vibration Control of Smart Hull Structure with Optimally Placed Piezoelectric Composite Actuators. *International Journal of Mechanical Sciences*, 53(8):647–659, 2011.
- [120] B. W. LaCroix and P. G. Ifju. Investigating Potential Substrates to Maximize Out-of-Plane Deflection of Piezoelectric Macro-Fiber Composite Actuators. *Journal of Intelligent Material Systems and Structures*, 26(7):781–795, 2014.
- [121] S. Q. Zhang, Y. X. Li, and R. Schmidt. Modeling and Simulation of Macro-Fiber Composite Layered Smart Structures. *Composite Structures*, 126(2015):89–100, 2015.
- [122] S.-Q. Zhang, Z.-X. Wang, X.-S. Qin, G.-Z. Zhao, and R. Schmidt. Geometrically Nonlinear Analysis of Composite Laminated Structures with Multiple Macro-Fiber Composite (MFC) Actuators. *Composite Structures*, 150:62–72, 2016.
- [123] Y.-X. Li, S.-Q. Zhang, R. Schmidt, and X.-S. Qin. Homogenization for Macro-Fiber Composites Using Reissner-Mindlin Plate Theory. *Journal of Intelligent Material Systems and Structures*, 2016.
- [124] G. Molinari, A. F. Arrieta, and P. Ermanni. Aero-Structural Optimization of Three-Dimensional Adaptive Wings with Embedded Smart Actuators. *AIAA Journal*, 0(0):1–12, 2014.
- [125] G. Molinari, M. Quack, A. F. Arrieta, M. Morari, and P. Ermanni. Design, Realization and Structural Testing of a Compliant Adaptable Wing. *Smart Materials and Structures*, 24(10):105027, 2015.

- [126] A. C. Henry, G. Molinari, and A. F. Arrieta. Smart Morphing Wing: Optimization of Distributed Piezoelectric Actuation. In *25th AIAA/AHS Adaptive Structures Conference*, Reston, Virginia, 2017. American Institute of Aeronautics and Astronautics.
- [127] A.-M. R. McGowan, W. K. Wilkie, R. W. Moses, R. C. Lake, J. L. Pinkerton-Flornance, C. D. Weiseman, M. C. Reaves, B. K. Taleghani, P. H. Mirick, and M. L. Wilbur. Aeroservoelastic and Structural Dynamics Research on Smart Structures Conducted at NASA Langley Research Center. In *Proceedings of Smart Structures and Materials 1998: Industrial and Commercial Applications of Smart Structures Technologies*, volume 3326, page 188, San Diego, CA, United States, 1998. International Society for Optics and Photonics.
- [128] A. J. Lee, A. Moosavian, and D. J. Inman. Control and Characterization of a Bistable Laminate Generated with Piezoelectricity. *Smart Materials and Structures*, 26(8):085007, 2017.
- [129] A. Pandey and A. Arockiarajan. Performance Studies on Macro Fiber Composite (MFC) Under Thermal Condition Using Kirchhoff and Mindlin Plate Theories. *International Journal of Mechanical Sciences*, 130:416–425, 2017.
- [130] A. Pandey and A. Arockiarajan. Actuation Performance of Macro-Fiber Composite (MFC): Modeling and Experimental Studies. *Sensors and Actuators A: Physical*, 248:114–129, 2016.
- [131] M.-L. Dano, M. Gakwaya, and B. Jullière. Compensation of Thermally Induced Distortion in Composite Structures using Macro-fiber Composites. *Journal of Intelligent Material Systems and Structures*, 19(2):225–233, 2008.
- [132] C. Bowen and H. A. Kim. Modeling and Characterization of Piezoelectrically Actuated Bistable Composites. *IEEE Trans Ultrasonics Ferroelectrics Freq Control*, 58(9):131–168, 2011.
- [133] D. Upadrashta and Y. Yang. Finite Element Modeling of Nonlinear Piezoelectric Energy Harvesters with Magnetic Interaction. *Smart Materials and Structures*, 24(4):045042, 2015.
- [134] S. Aimmanee and K. Tichakorn. Piezoelectrically Induced Snap-through Buckling in a Buckled Beam Bonded with a Segmented Actuator. *Journal of Intelligent Material Systems and Structures*, 29(9):1862–1874, 2018.
- [135] X. Wang, W. Zhou, Z. Wu, and W. Wu. Optimal Unimorph and Bimorph Configurations of Piezocomposite Actuators for Bending and Twisting Vibration Control of Plate Structures. *Journal of Intelligent Material Systems and Structures*, page 1045389X1774273, 2017.
- [136] X. Wang, W. Zhou, G. Xun, and Z. Wu. Dynamic Shape Control of Piezocomposite-actuated Morphing Wings With Vibration Suppression. *Journal of Intelligent Material Systems and Structures*, 29(3):358–370, 2018.
- [137] R. B. Williams, D. J. Inman, M. R. Schultz, M. W. Hyer, and W. K. Wilkie. Nonlinear Tensile and Shear Behavior of Macro Fiber Composite Actuators. *Journal of Composite Materials*, 38(10):855–869, 2004.

- [138] J. M. Lloyd. *Electrical Properties of Macro-Fiber Composite Actuators and Sensors*. PhD thesis, jul 2004.
- [139] R. B. Williams, B. W. Grimsley, D. J. Inman, and W. K. Wilkie. Manufacturing and Mechanics-Based Characterization of Macro Fiber Composite Actuators. In *Proceedings of IMECE2002 Adaptive Structures and Materials Systems*, pages 79–89, New Orleans, Louisiana, 2002. ASME.
- [140] X. Liu, K. Rouf, B. Peng, and W. Yu. Two-step Homogenization of Textile Composites Using Mechanics of Structure Genome. *Composite Structures*, 171:252–262, 2017.
- [141] R. Paradies and M. Melnykowycz. Numerical Stress Investigation for Piezoelectric Elements with a Circular Cross Section and Interdigitated Electrodes. *Journal of Intelligent Material Systems and Structures*, 18(9):963–972, 2007.
- [142] H. Nasser, A. Deraemaeker, and S. Belouettar. Electric Field Distribution in Macro Fiber Composite Using Interdigitated Electrodes. *Advanced Materials Research*, 47-50:1173–1176, 2008.
- [143] S. J. Kim, K. H. Ji, and S. H. Paik. Numerical Simulation of Mechanical Behavior of Composite Structures by Supercomputing Technology. *Advanced Composite Materials*, 17(4):373–407, 2008.
- [144] H. F. Tiersten. *Linear Piezoelectric Plate Vibrations*. Springer US, Boston, MA, 1969.
- [145] W. Yu. An Exact Solution for Micromechanical Analysis of Periodically Layered Composites. *Mechanics Research Communications*, 46:71–75, 2012.
- [146] O. Rique, J. E. Goodsell, W. Yu, and R. B. Pipes. Three-dimensional Thermoelastic Properties of General Composite Laminates. *Journal of Composite Materials*, page 002199831773403, 2017.
- [147] Wolfram Research, Inc. Mathematica, Version 9.0. Champaign, IL, 2012.
- [148] W. K. Wilkie, D. Inman, J. Lloyd, and J. High. Anisotropic Piezocomposite Actuator Incorporating Machined PMN-PT Single Crystal Fibers. In *45th AIAA/ASME/ASCE/AHS/ASC Structures, Structural Dynamics & Materials Conference*, number April 2004, pages 1–17, 2004.
- [149] J. J. Espadas-Escalante, N. P. van Dijk, and P. Isaksson. A Study on the Influence of Boundary Conditions in Computational Homogenization of Periodic Structures with Application to Woven Composites. *Composite Structures*, 160:529–537, 2017.
- [150] T. R. Gururaja, W. A. Schulze, L. E. Cross, R. E. Newnham, B. A. Auld, and Y. J. Wang. Piezoelectric Composite Materials for Ultrasonic Transducer Applications. Part I: Resonant Modes of Vibration of PZT Rod-Polymer Composites. *IEEE Transactions on Sonics and Ultrasonics*, 32(4):481–498, 1985.
- [151] J. Lv, H. Zhang, X. Gao, and Y. Huang. A New Multiscale Computational Method for Electromechanically Coupled Analysis of Heterogeneous Piezoelectric Composites. *Journal of Intelligent Material Systems and Structures*, 26(4):434–449, 2015.

- [152] B. Kranz, A. Benjeddou, and W. G. Drossel. Numerical and Experimental Characterizations of Longitudinally Polarized Piezoelectric d_{15} Shear Macro-fiber Composites. *Acta Mechanica*, 224(11):2471–2487, 2013.
- [153] J. A. Gallagher, D. M. Pisani, B. Smith-Stewart, and C. S. Lynch. Stress and Electric Field Gradient Contributions to Dielectric Loss in Ferroelectrics With Interdigitated Electrodes. *Journal of Intelligent Material Systems and Structures*, 26(5):573–581, 2015.

VITA

Ernesto was born in El Paso, TX. After graduating from Franklin High School, he completed one year of college at the University of Texas at El Paso. At which point he transferred to Purdue University in 2008. In 2012 he earned a Bachelor of Science in Civil Engineering (Structures) and then in 2014 a Master of Science in Civil Engineering (also Structures). His research interests are micromechanics, multiscale structural mechanics, and smart materials and structures. He loves his wife, family, church, and spending time outdoors.